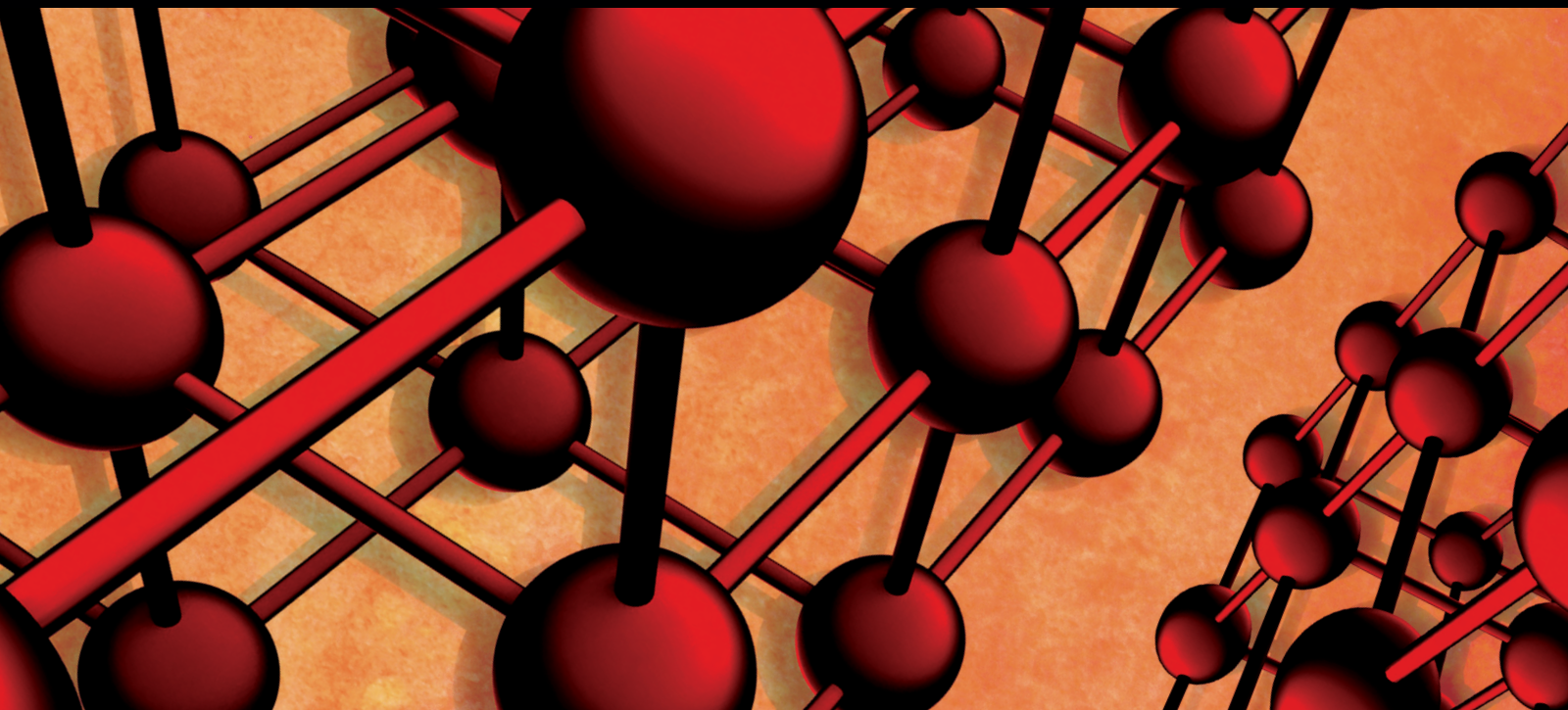


Advances in Materials Science and Engineering

Simulation and Optimization in Materials Technology

Guest Editors: Martha Guerrero, Caner Simsir, Augusto Deus, and Bozidar Sarler





Simulation and Optimization in Materials Technology

Advances in Materials Science and Engineering

Simulation and Optimization in Materials Technology

Guest Editors: Martha Guerrero, Caner Simsir, Augusto Deus,
and Bozidar Sarler



Copyright © 2014 Hindawi Publishing Corporation. All rights reserved.

This is a special issue published in “Advances in Materials Science and Engineering.” All articles are open access articles distributed under the Creative Commons Attribution License, which permits unrestricted use, distribution, and reproduction in any medium, provided the original work is properly cited.

Editorial Board

K. G. Anthymidis, Greece
Robert S. Averbach, USA
Amit Bandyopadhyay, USA
Zoe Barber, UK
Yucel Birol, Turkey
Susmita Bose, USA
Steve Bull, UK
Peter Chang, Canada
Daolun Chen, Canada
Manish U. Chhowalla, USA
S. Chinnappanadar, India
Martin Crimp, USA
Jie Dai, Singapore
Chapal K. Das, India
João P. Davim, Portugal
Seshu B. Desu, USA
Yong Ding, USA
Sergi Gallego, Spain
John W. Gillespie, USA
Hiroki Habazaki, Japan
Richard Hennig, USA
Dachamir Hotza, Brazil
Chun-Hway Hsueh, Taiwan
Shyh-Chin Huang, Taiwan
Rui Huang, USA
Wei Huang, China
Jacques Huot, Canada
William A. Jesser, USA
Jaehwan Kim, Korea

Sridhar Komarneni, USA
Prashant Kumta, USA
Jui-Yang Lai, Taiwan
Pavel Lejcek, Czech Republic
Markku Leskela, Finland
Bin Li, China
Hai Lin, China
Yuanhua Lin, China
Zhimin Liu, China
Tao Liu, China
Jun Liu, China
Ying Liu, USA
Meilin Liu, Georgia
Yuan Liu, China
Gang Liu, China
Maria A. Loi, The Netherlands
Hai Lu, China
Peter Majewski, Australia
Shuichi Miyazaki, Japan
Paul Munroe, Australia
Ali Nazari, Iran
Luigi Nicolais, Italy
Tsutomu Ohzuku, Japan
Xiaoqing Pan, USA
Ganapathiraman Ramanath, USA
Raju V. Ramanujan, Singapore
Manijeh Razeghi, USA
Mohd Sapuan Salit, Malaysia
Jainagesh A. Sekhar, USA

Jiangbo Sha, China
Liyuan Sheng, China
You Song, China
Aloysius Soon, Korea
Charles C. Sorrell, Australia
Steven L. Suib, USA
Sam-Shajing Sun, USA
Weihua Tang, China
Achim Trampert, Germany
Vladimir Tsukruk, USA
Krystyn Van Vliet, USA
Rui Vilar, Portugal
Min Wang, China
Jörg M. K. Wiezorek, USA
Wei Wu, USA
Gongnan Xie, China
Aiguo Xu, China
Jianqiao Ye, UK
Yadong Yin, USA
Ming-Xing Zhang, Australia
Jian Zhang, Singapore
Kai Zhang, China
Kai Zhang, China
Rui Zhang, China
Tao Zhang, China
Bin Zhang, China
Jun Zhang, China
Yufeng Zhang, China
Jing Zhang, China

Contents

Simulation and Optimization in Materials Technology, Martha Guerrero, Caner Simsir, Augusto Deus, and Bozidar Sarler

Volume 2014, Article ID 947319, 1 pages

Molecular Dynamics Simulation of Solidification of Pd-Ni Clusters with Different Nickel Content,

Chen Gang, Zhang Peng, and Liu Hongwei

Volume 2014, Article ID 926206, 7 pages

Fatigue Durability Analysis of Collecting Rapping System in Electrostatic Precipitators under Impact Loading, Ali Akbar Lotfi Neyestanak, Saeed Adib Nazari, Ali Imam, and Cyrus Aghanajafi

Volume 2014, Article ID 136059, 9 pages

Experimental Investigation on Material Transfer Mechanism in WEDM of Pure Titanium (Grade-2),

Anish Kumar, Vinod Kumar, and Jatinder Kumar

Volume 2013, Article ID 847876, 20 pages

Numerical Analysis of Hot Cracking in Laser-Hybrid Welded Tubes, Moritz Oliver Gebhardt,

Andrey Gumenyuk, and Michael Rethmeier

Volume 2013, Article ID 520786, 8 pages

Arc Interference Behavior during Twin Wire Gas Metal Arc Welding Process, Dingjian Ye, Xueming Hua, and Yixiong Wu

Volume 2013, Article ID 937094, 5 pages

Effective Thermal Conductivity of Open Cell Polyurethane Foam Based on the Fractal Theory,

Kan Ankang and Han Houde

Volume 2013, Article ID 125267, 7 pages

Effect of Process Parameters on Gas Nitriding of Grey Cast Iron, Nana Wang and Jinxiang Liu

Volume 2013, Article ID 217848, 6 pages

Integrating the TRIZ and Taguchi's Method in the Optimization of Processes Parameters for SMT,

Yung-Tsan Jou, Wen-Tsann Lin, Wei-Cheng Lee, and Tsu-Ming Yeh

Volume 2013, Article ID 830891, 10 pages

Modelling of Ballistic Impact over a Ceramic-Metal Protection System, Leandro Neckel,

Dachamir Hotza, Daniel Stainer, Rolf Janssen, and Hazim Ali Al-Qureshi

Volume 2013, Article ID 698476, 8 pages

Modelling the Influence of Manufacturing Process Variables on Dimensional Changes of Porcelain Tiles, Dolly Santos-Barbosa, Dachamir Hotza, Juan Boix, and Gustavo Mallol

Volume 2013, Article ID 142343, 12 pages

Geometry Optimization Calculations for the Elasticity of Gold at High Pressure, E. Güler and M. Güler

Volume 2013, Article ID 525673, 5 pages

Modelling of Hybrid Materials and Interface Defects through Homogenization Approach for the Prediction of Effective Thermal Conductivity of FRP Composites Using Finite Element Method,

C. Mahesh, K. Govindarajulu, and V. Balakrishna Murthy

Volume 2013, Article ID 147693, 7 pages

Calculation of Liquidus Temperature for Aluminum and Magnesium Alloys Applying Method of Equivalency, Mile B. Djurdjević, Srećko Manasijević, Zoran Odanović, and Natalija Dolić
Volume 2013, Article ID 170527, 8 pages

Effect of Mandrel on Cross-Section Quality in Numerical Control Bending Process of Stainless Steel 2169 Small Diameter Tube, Jun Fang, Shiqiang Lu, Kelu Wang, Jianmei Xu, Xiaomei Xu, and Zhengjun Yao
Volume 2013, Article ID 849495, 9 pages

Neuro-Fuzzy Model for the Prediction and Classification of the Fused Zone Levels of Imperfections in Ti6Al4V Alloy Butt Weld, Giuseppe Casalino, Sabina Luisa Campanelli, and Fabrizio Memola Capece Minutolo
Volume 2013, Article ID 952690, 7 pages

Editorial

Simulation and Optimization in Materials Technology

Martha Guerrero,¹ Caner Simsir,² Augusto Deus,³ and Bozidar Sarler⁴

¹ *Universidad Autonoma de Nuevo Leon, Facultad de Ingenieria Mecanica y Electrica, Avenida Universidad S/N, Cd. Universitaria, CP 66451, San Nicolas de los Garza, NL, Mexico*

² *Atilim University, Metal Forming Center of Excellence (MFCE), Atilim University Campus, Kizilcasar Mahallesi, 06836 Incek-Golbasi, Ankara, Turkey*

³ *Universidade de Lisboa, Instituto Superior Tecnico, Departamento de Engenharia Mecanica e ICEMS, Avenida Rovisco Pais, 1049-001 Lisboa, Portugal*

⁴ *University of Nova Gorica, Laboratory for Multiphase Processes, Vipavska 13, 5000 Nova Gorica, Slovenia & Institute of Metals and Technology, Laboratory for Simulation of Materials and Processes, Lepi pot 11, 1000 Ljubljana, Slovenia*

Correspondence should be addressed to Martha Guerrero; martha.guerreromt@uanl.edu.mx

Received 11 February 2014; Accepted 11 February 2014; Published 12 March 2014

Copyright © 2014 Martha Guerrero et al. This is an open access article distributed under the Creative Commons Attribution License, which permits unrestricted use, distribution, and reproduction in any medium, provided the original work is properly cited.

The interdisciplinary field of materials technology is crucial for development of new materials, facing a huge spectrum of challenges in the area of natural resources, energy, new functionality, environmental impact, and so forth.

Computational modelling and simulation on quantum mechanics, molecular dynamics, and continuum mechanics levels play an ever increasing role in materials technology. Together with automatic computer optimization of different materials technology aspects, they form a framework for virtual design of new materials and processes. This framework is built on multiscale, multiphysics, and multiobjective components. New numerical methods and parallelization on large computers give this research field an additional acceleration. The virtual design avoids many expensive experiments and prototyping. In addition, completely new materials and production processes can be tested well before actual materials synthesis or production process construction.

The present special issue is dedicated to the contemporary efforts in the described field.

Chen Gang et al. present molecular dynamics simulation of solidification, Ali Akbar Lotfi Neyestanak et al. present finite element method analysis of fatigue durability, Anish Kumar et al. present experiments and statistical model of an electrothermal production process, Andrey Gumenyuk and Michael Retheimer present a numerical model of hot cracking, Xueming Hua and Yixiong Wu present a model

for arc interference in welding process, Kan Ankang and Han Houde investigate the effective thermal conductivity of polyurethane foams, Nana Wang and Jinxiang Liu investigate the effect of process parameters of nitriding of cast iron, Yung-Tsan Jou et al. computationally optimize the assembly technology for core circuit board parts, Leandro Neckel et al. model the ballistic impact of a ceramic-metal protection system, Dolly Santos-Barbosa et al. model the influence of process parameters on dimensions of porcelain tiles, E. Güler and M. Güler explore the mechanical properties of Au by using geometry optimization approach, C. Mahesh et al. model thermal conductivity of composite materials, Mile B. Djurdjević et al. use the method of equivalency to describe the liquidus temperature of aluminium and magnesium alloys, Jun Fang et al. model the bending of the steel tubes, and Giuseppe Casalino et al. use neurofuzzy model to predict defects in titanium alloys.

The selected 15 papers for the present special issue demonstrate the power of simulation and optimization in diverse aspects of materials technology.

*Martha Guerrero
Caner Simsir
Augusto Deus
Bozidar Sarler*

Research Article

Molecular Dynamics Simulation of Solidification of Pd-Ni Clusters with Different Nickel Content

Chen Gang, Zhang Peng, and Liu Hongwei

School of Materials Science and Engineering, Harbin Institute of Technology at Weihai, 2 Wenhuxi Road, Weihai 264209, China

Correspondence should be addressed to Zhang Peng; pzhang@hit.edu.cn

Received 17 May 2013; Accepted 5 December 2013; Published 6 February 2014

Academic Editor: Martha Guerrero

Copyright © 2014 Chen Gang et al. This is an open access article distributed under the Creative Commons Attribution License, which permits unrestricted use, distribution, and reproduction in any medium, provided the original work is properly cited.

Molecular dynamics simulation has been performed for investigating the glass transition of Pd-Ni alloy nanoparticles in the solidification process. The results showed that the Pd-Ni nanoparticles with composition far from pure metal should form amorphous structure more easily, which is in accordance with the results of the thermodynamic calculation. There are some regular and distorted fivefold symmetry in the amorphous Pd-Ni alloy nanoparticles. The nanoclusters with bigger difference value between formation enthalpies of solutions and glasses will transform to glass more easily than the other Pd-Ni alloy nanoclusters.

1. Introduction

In the past decades, because of the high special surface area and its excellent catalytic performance, pure metal or its alloy nanoparticles have been studied and used widely in catalytic chemistry [1–4]. It is well known that the structure of nanocatalyst particle affects the catalytic activity and selectivity evidently. However, in most experimental cases some restricted conditions were required normally, which blocks the studies on nanostructure of catalyst profoundly. As an economical research method, the computer simulation of molecular dynamics (MD) has been applied to study the metal cluster structure or properties by many researchers successfully [5–11].

Considering the structure stability of catalyst nanoparticles, many MD simulations have been done for researching the melting process of the metal clusters [8–11]. Nevertheless, there are few studies about structure transformation in solidification of the melted clusters. The atomic configuration, which affects the catalyst efficiency, should be different with altering the atomic ratio in the clusters or the solidification process.

Pd-Ni alloy clusters, synthesized by many methods, have been used as catalyst in many reactions, especially in hydrogenation [1]. The melting and solidifying process of Pd-Ni

nanoparticles will occur in some preparation or application, such as supporting the cluster on the carbon nanotubes or other catalytic reactions. Therefore, the solidification of melted Pd-Ni nanoparticles has been simulated by molecular dynamics in the present work, and the tendency to forming noncrystalline structure of Pd-Ni alloy with different element content has been also studied here by thermodynamic calculation method.

2. Method of Simulation

The parallel code LAMMPS was used for all MD simulations in this work [12]. The embedded-atom method (EAM), a set of n -body potentials, has been proved to accurately describe various dynamic properties of transition and noble metals. The EAM potential data used here was obtained from the literature [13]. The Newtonian equations of motion are integrated using the Verlet method with a time step of 5×10^{-4} ps.

The calculation is performed in two steps. Firstly, the melting models for simulating solidification process were obtained after the initial models were heated to 2300 K and relaxed enough time (50 ps). Then, the melting models were subjected to cooling process consisting of a series of dropping

TABLE 1: Content of nickel of every cluster model.

Model	Ni (at.%)	Model	Ni (at.%)
Pd	0	Ni800	58.3
Ni200	14.6	Ni1000	72.9
Ni400	29.2	Ni1200	87.5
Ni600	43.7	Ni	100

and keeping temperature MD simulations with temperature decrements of 100 K. The cooling rate of 4 K/ps and the equilibration simulation time of 10 ps were used in the present study. The cooling process of nanoclusters was simulated with constant temperature and constant volume (NVT) molecular dynamic in enough large box with a periodic boundary condition.

The initial models with 1372 atoms (diameter about 2 nm) started with geometries constructed from a FCC block of Pd. Through replacing the Pd atom with Ni atom randomly, the alloy models with different nickel atom content can be created. The exponent of all models can be found in Table 1.

The radial distribution function (RDF) shown as in (1), being regarded as one of the most important parameters, is used to describe the structure characterization of solid, amorphous and liquid states [14]. Consider

$$g(r) = \frac{\Omega}{N^2} \cdot \left\langle \frac{\left(\sum_{i=1}^{N_i} n_i \right)}{4\pi r^2 \Delta r} \right\rangle, \quad (1)$$

where $g(r)$ is the probability of finding an atom in a distance ranging from r to $\Delta r + r$ (Δr is the step of calculation), Ω is the simulated volume of unit cell, N is the number of atoms in the system, and N_i is the average number of atoms around the i th atom in the sphere shell ranging from r to $r + \Delta r$.

Besides MD simulation, Miedema's thermodynamic theory was used for calculating the forming energies of binary transition metal alloy system, which can explain the glass-forming ability of Pd-Ni alloy with different Ni content. On the basis of Miedema's thermodynamic theory [15–19], the formation enthalpy of Pd-Ni solid solution is expressed as

$$\Delta H_{\text{PdNi}} = \Delta H_{\text{PdNi}}^{\text{chem}} + \Delta H_{\text{PdNi}}^{\text{eles}} + \Delta H_{\text{PdNi}}^{\text{stru}}, \quad (2)$$

where $\Delta H_{\text{PdNi}}^{\text{chem}}$ results from the electronic redistribution occurring when the alloy forms, $\Delta H_{\text{PdNi}}^{\text{eles}}$ is the size-mismatch contribution to the formation enthalpy in a binary system, and $\Delta H_{\text{PdNi}}^{\text{stru}}$ accounts for the difference in valence and crystal structure of the component metals. However, the structure of palladium is close to that of nickel. That is to say, the $\Delta H_{\text{PdNi}}^{\text{stru}}$ can be ignored here.

Then the Gibbs free energy of Pd-Ni solid can be expressed as

$$\Delta G_{\text{PdNi}} = \Delta H_{\text{PdNi}}^{\text{chem}} + \Delta H_{\text{PdNi}}^{\text{elec}} - T \cdot \Delta S_{\text{PdNi}}^{\text{ideal}}, \quad (3)$$

where $\Delta S_{\text{PdNi}}^{\text{ideal}}$ is the ideal mixing entropy. Consider

$$\Delta S_{\text{PdNi}}^{\text{ideal}} = X_{\text{Pd}} \cdot \ln X_{\text{Pd}} + X_{\text{Ni}} \cdot \ln X_{\text{Ni}},$$

$$\Delta H_{\text{PdNi}}^{\text{chem}} = X_{\text{Pd}} \cdot X_{\text{Ni}}$$

$$\cdot (f_{\text{NiPd}} \cdot \Delta H_{\text{NiinPd}}^{\text{amp}} + f_{\text{PdNi}} \cdot \Delta H_{\text{PdinNi}}^{\text{amp}})$$

$$f_{\text{NiPd}} = X_{\text{Pd}}^S \cdot \left[1 + K_r \cdot (X_{\text{Pd}}^S \cdot X_{\text{Ni}}^S)^2 \right], \quad (4)$$

$$f_{\text{PdNi}} = X_{\text{Ni}}^S \cdot \left[1 + K_r \cdot (X_{\text{Pd}}^S \cdot X_{\text{Ni}}^S)^2 \right],$$

$$X_{\text{Pd}}^S = \frac{X_{\text{Pd}} \cdot V_{\text{Pd}}^{2/3}}{X_{\text{Pd}} \cdot V_{\text{Pd}}^{2/3} + X_{\text{Ni}} \cdot V_{\text{Ni}}^{2/3}}, \quad X_{\text{Pd}}^S + X_{\text{Ni}}^S = 1,$$

where X_{Pd} , X_{Ni} , V_{Pd} , and V_{Ni} are the mole ratio and atomic volume of Pd and Ni, respectively. The factor K_r takes the values 8, 5, and 0 for intermetallics, metallic glasses, and solid solutions, respectively; $\Delta H_{\text{NiinPd}}^{\text{amp}}$ is given by

$$\Delta H_{\text{NiinPd}}^{\text{amp}} = \frac{2V_{\text{Ni}}^{2/3}}{\left[(n_{\text{WS}}^{1/3})_{\text{Ni}}^{-1} + (n_{\text{WS}}^{1/3})_{\text{Pd}}^{-1} \right]} \cdot \left\{ -P \cdot (\phi_{\text{Ni}} - \phi_{\text{Pd}})^2 + Q \cdot \left[(n_{\text{WS}}^{1/3})_{\text{Ni}} - (n_{\text{WS}}^{1/3})_{\text{Pd}} \right]^2 - R \right\}. \quad (5)$$

The parameters, such as P , Q , and R , were shown in Table 2. The $\Delta H_{\text{PdNi}}^{\text{amp}}$ can also be calculated by this kind of formula.

Similar to the form of $\Delta H_{\text{PdNi}}^{\text{chem}}$, the $\Delta H_{\text{PdNi}}^{\text{eles}}$ can be expressed as

$$\Delta H_{\text{PdNi}}^{\text{eles}} = X_{\text{Pd}} \cdot X_{\text{Ni}} \cdot (X_{\text{Pd}} \cdot \Delta H_{\text{NiinPd}}^{\text{eles}} + X_{\text{Ni}} \cdot \Delta H_{\text{PdinNi}}^{\text{eles}}),$$

$$\Delta H_{\text{NiinPd}}^{\text{eles}} = \frac{2K_{\text{Ni}} \cdot \tau_{\text{Pd}} \cdot (V_{\text{Ni}} - V_{\text{Pd}})^2}{3K_{\text{Ni}} \cdot V_{\text{Pd}} + 4\tau_{\text{Pd}} \cdot V_{\text{Ni}}},$$

$$\Delta H_{\text{PdinNi}}^{\text{eles}} = \frac{2K_{\text{Pd}} \cdot \tau_{\text{Ni}} \cdot (V_{\text{Ni}} - V_{\text{Pd}})^2}{3K_{\text{Pd}} \cdot V_{\text{Ni}} + 4\tau_{\text{Ni}} \cdot V_{\text{Pd}}}, \quad (6)$$

where K_{Ni} and K_{Pd} are bulk moduli of Ni and Pd, respectively, τ_{Ni} and τ_{Pd} are shear moduli of Ni and Pd, respectively.

The Gibbs free energy of formatting amorphous Pd-Ni alloy is

$$\Delta G_{\text{PdNi}}^{\text{amor}} = \Delta H_{\text{PdNi}}^{\text{chem}} - T \cdot \Delta S_{\text{PdNi}}^{\text{ideal}} + X_{\text{Ni}} \cdot \Delta G_{\text{Ni}}^{a-s} + X_{\text{Pd}} \cdot \Delta G_{\text{Pd}}^{a-s}. \quad (7)$$

The $\Delta G_{\text{PdNi}}^{\text{amor}}$ contains the free energy of the mixing of the pure liquid metals (the first two terms) plus the free energy difference between the amorphous state and the crystalline state of the pure components. The difference can be expressed as

$$\Delta G^{a-s} = \Delta H_m^i \cdot \left[\frac{(T_m^i - T)}{T_m^i} \right] \cdot \left[\frac{2T}{(T_m^i + T)} \right], \quad i = \text{Pd or Ni}, \quad (8)$$

TABLE 2: Parameters for calculating forming energy of Pd-Ni binary alloy [24–26].

	T_m (K)	ΔH_m (kJ/mol)	P	Q/P	R/P
Pd	1828.0	16.74	14.2	9.4	14.2
Ni	1728.3	17.48			
	Φ (volt)	$V^{2/3}$ (cm ²)	$N_{WS}^{1/3}$ (d.u.)	K (GPa)	τ (GPa)
Pd	5.45	4.29	1.67	183.3	43.5
Ni	5.2	3.52	1.75	193.0	83.9

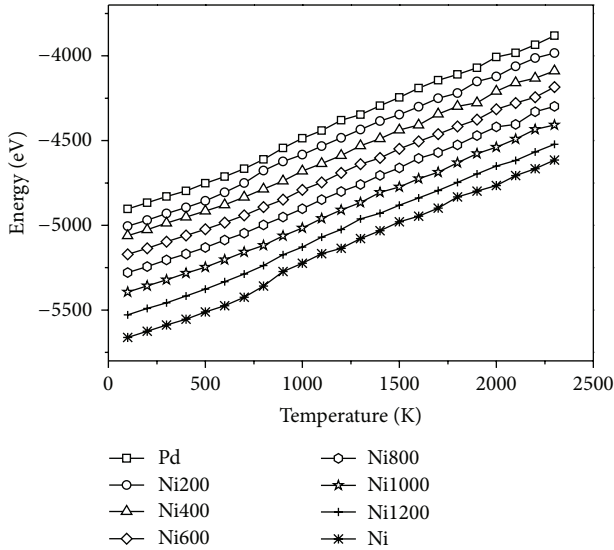


FIGURE 1: Total energy versus temperature curve for Pd-Ni clusters during cooling process.

where the ΔH_m is the molar heat of fusion, T_m is the melting points of metal.

For Pd-Ni cluster, surface energy should be considered in the forming energy. For the same size of the clusters and simplifying calculation, the surface energies of noncrystalline and crystalline clusters were considered as equal approximately. Then the term of surface energy was neglected in this study.

3. Results and Discussion

When liquid nanocluster translates to crystal cluster, the jump should appear in caloric curve. However, the cluster only has 1372 atoms, which leads to less energy decrease as crystallization. Therefore, the visible jump is not found in the Figure 1.

Figure 2 shows the radial distribution function (RDF) curves of Pd-Ni alloy clusters at 300 K. Crystalline states are visible through the well-defined peaks, which represent positions of the first, second, third, and n th nearest neighbor atoms. It proves the presence of an FCC crystal structure in Pd, Ni200, Ni1200, and Ni models. Because of the equilibrium distance of Pd atom bigger than that of Ni, the Pd atom content increasing, the first neighbor distance generally increasing, which is found in Figure 2. For Ni400, Ni600,

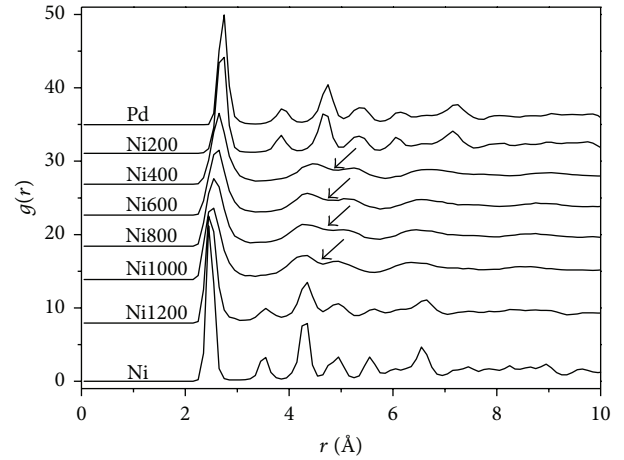
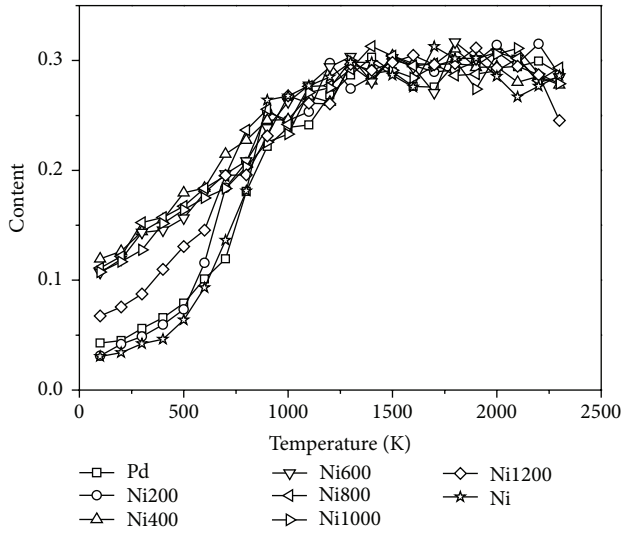


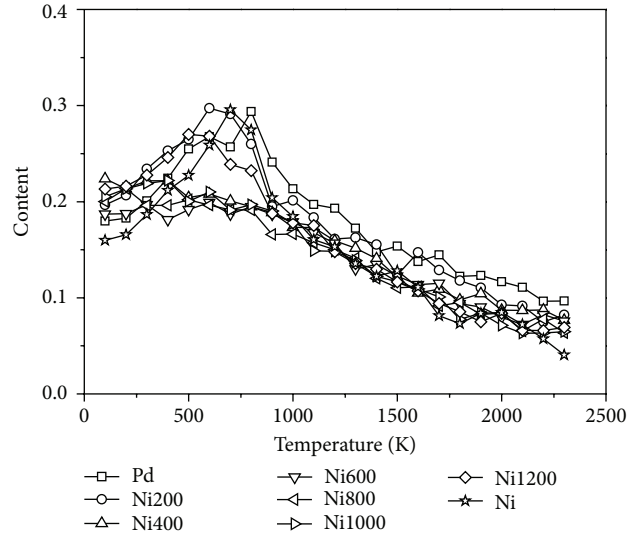
FIGURE 2: Radial distribution function (RDF) of Pd-Ni clusters at 300 K with the cooling rate of 4 K/ps.

Ni800, and Ni1000 clusters, the number of the first neighbor atoms is fewer than that of Pd, Ni200, Ni1200, and Ni, while the splitting of the second peak, denoted in Figure 2 by single arrow line, appears in the RDF curves of Ni400, Ni600, Ni800, and Ni1000 clusters. The splitting of the second peak is a well-known characteristic feature of solid amorphous structure of metallic glass, and the number of the first neighbor atoms is fewer, which can effectively describe the characteristics of the geometric structural evolvement [20–22].

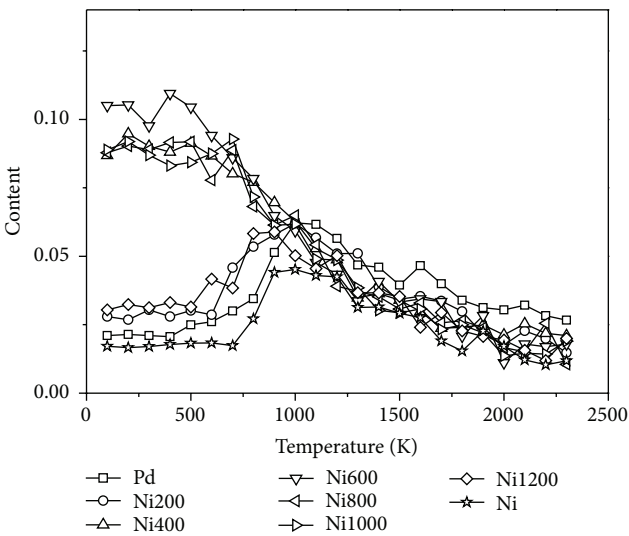
Pair analysis (PA) technique, which can effectively describe the characteristics of the geometric structural evolvement, was used for the analysis of the geometric features of the atomic cluster [20–22]. In this study, PA method was used to analyze the structural changes accompanying the solidification process of melting Pd-Ni clusters. Based on the regulation of bond pair, two atoms are within a specified cutoff distance of each other and they are called a bonded pair of clusters [22, 23]. In RDF curves, if $g(r_c)$ is the first minimum value, then r_c was defined as cutoff distance for PA. Four-index number $ijkl$ is used to express bonded pairs of atomic clusters by Honeycutt and Andersen [20]. If any atomic pair A-B forms a bond, $i = 1$ and otherwise $i = 2$; j refers to the number of near neighbors which form bonds with both atom A and atom B; k stands for the number of pairs among the neighboring atoms forming bonds; l is a special distinguished index parameter. Based on the PA technique, the 1201 and 1311 bond pairs represent



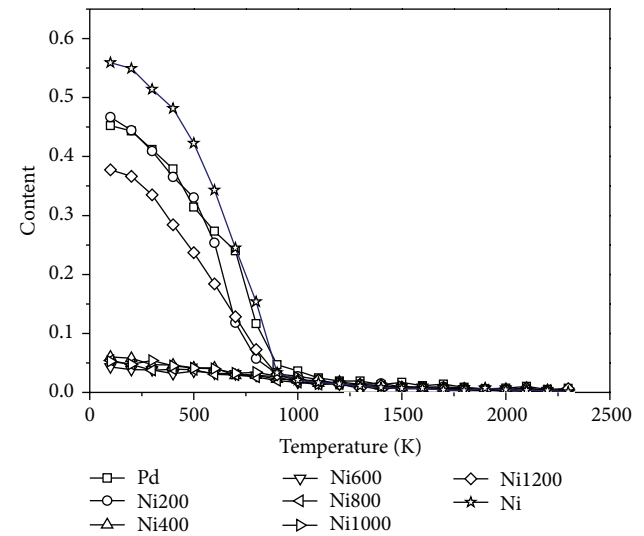
(a)



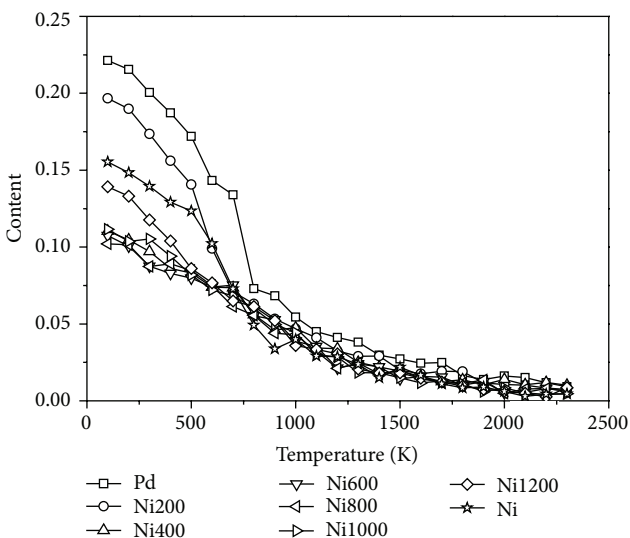
(b)



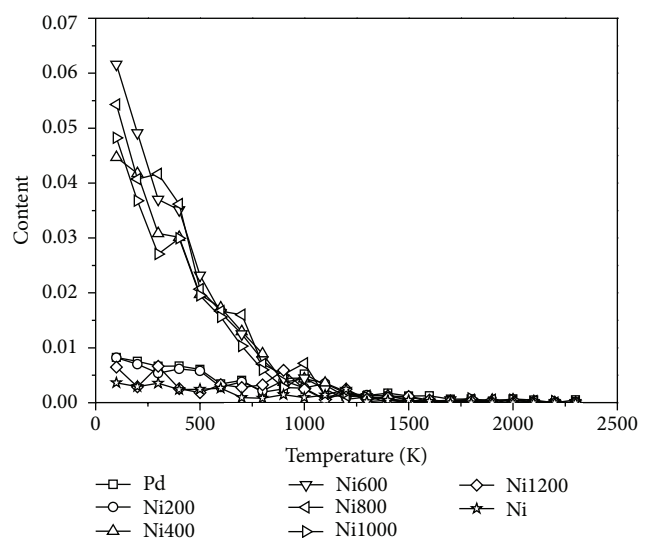
(c)



(d)



(e)



(f)

FIGURE 3: Continued.

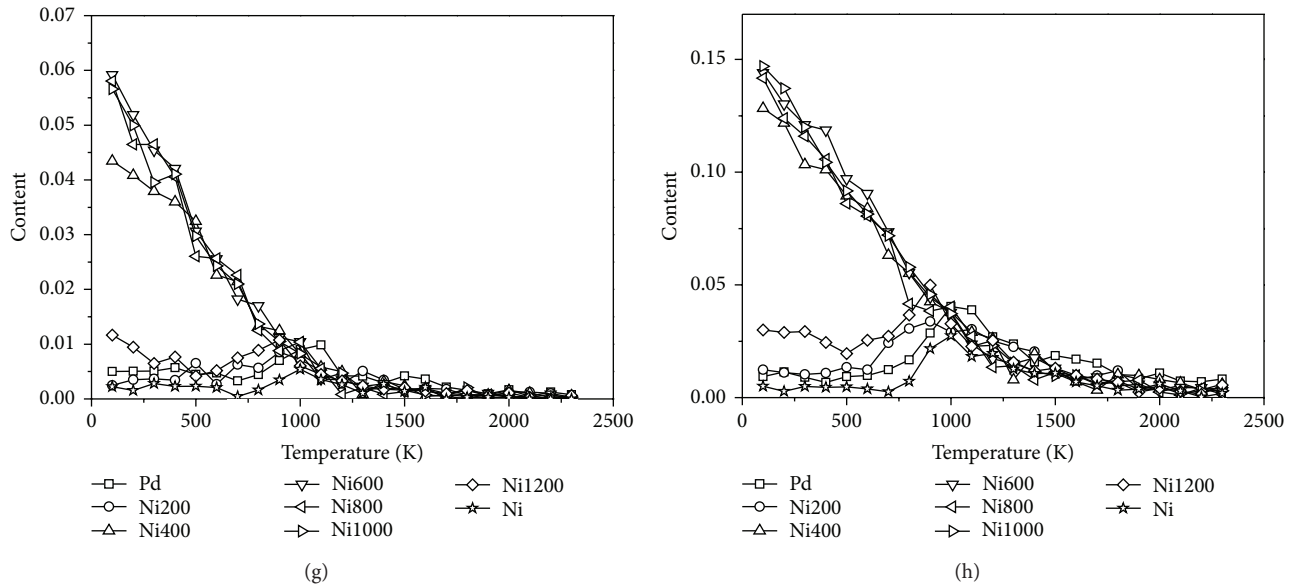


FIGURE 3: Relative amount of various atomic-bonded pairs includes (a) 1201, (b) 1311, (c) 1321, (d) 1421, (e) 1422, (f) 1551, (g) 1541, and (h) 1431 in Pd-Ni clusters at different temperatures during cooling.

the rhombus symmetrical features of short-range order. The FCC structure has the type of 1421 bond pairs, whereas the HCP crystal has the equal number of 1421 and 1422 bond pairs. The difference between 1421 and 1422 bond pairs is the topological arrangement of the two bonds between the four neighbors. The bond pair 1551, corresponding to a pentagonal bipyramid, is the characteristic of icosahedral order.

Figure 3 shows the normalized abundance of selected pairs and polyhedra in the Pd-Ni clusters simulation in the present study. The results indicate that the number of the 1201, 1311, 1321, 1421, 1422, 1551, 1541, and 1431 pairs will change with temperature dropping, especially when the temperature lower than 1000 K. Because all the clusters are in the liquid state at high temperature, the 1201 and 1311 pairs with relative high proportion shown in Figures 3(a) and 3(b), indicating short-range order structure, exist in all the clusters. According to the case of proportion of every type pair, all the clusters calculated in present work can be assorted into two kinds. The change tendency of the Ni, Ni1200, Ni200, and Pd, labeled with the first type, is different with the second type clusters including Ni400, Ni600, Ni800, and Ni1000. With the temperature dropping, solidification process leads to the proportion of 1201 pairs in all Pd-Ni clusters decreasing gradually. For the first type clusters, the proportion of 1421 and 1422 pairs increased observably to the relative high value shown in Figures 3(c) and 3(d), which indicates that most atoms in Ni, Ni1200, Ni200, and Pd are arranged mainly as FCC or HCP structure. And this result is in accordance with characteristic peaks shown in Figure 3. There are also 15–20% 1311 pairs in the first type clusters due to the surface atoms packing for the small surface energy. It can estimate the crystalline point where the 1421 pair number is evaluated abruptly. And the crystalline temperature of Ni, Ni1200, Ni200, and

Pd nanoclusters was about 800 K, 700 K, 600 K, and 800 K, respectively.

Relative amount of various bonded pairs in the second type Pd-Ni clusters was different from that of the first kind of clusters. In these clusters, the notable increase of 1311, 1321, 1551, 1541, and 1431 pairs was presented as the temperature dropping took place. These results suggested that the main atom structure of the second Pd-Ni clusters was short-range order at low temperature; namely, Ni400, Ni600, Ni800, and Ni1000 clusters are in amorphous states. In addition, the three types of pairs (1551, 1541, and 1431) corresponding to inherent structures with regular and distorted fivefold symmetries account for about 25% of all pairs, which implies that part of short-range order is local icosahedral order, meaning the order characteristic of a 13-atom icosahedron. There is also small proportion of 1421 and 1422 bond pairs in the second type clusters which indicates that crystalline short-range order exists in the disorder system [20, 21].

The results of MD simulation, which indicate that the clusters were easier to form amorphous structure when the number of Pd was close to that of Ni atom, can also be explained by thermodynamic calculation. Figure 4(a) shows the formation enthalpies of glasses (ΔG^{amor}) and solutions (ΔG^{cty}) of Pd-Ni alloy clusters calculated by the Miedema's model [16]. It is commonly regarded that the alloys could be vitrified into glass more easily only when the enthalpies of glasses are bigger than those of solution. So the compositions of a possible amorphous structure former should be ranging from about Pd75Ni25 to Pd28Ni72, being marked by dash line in Figure 4(a). In this composition region, the difference value between formation enthalpies of solutions and glasses has been used for expressing the glass formation ability (GFA) of Pd-Ni alloy clusters.

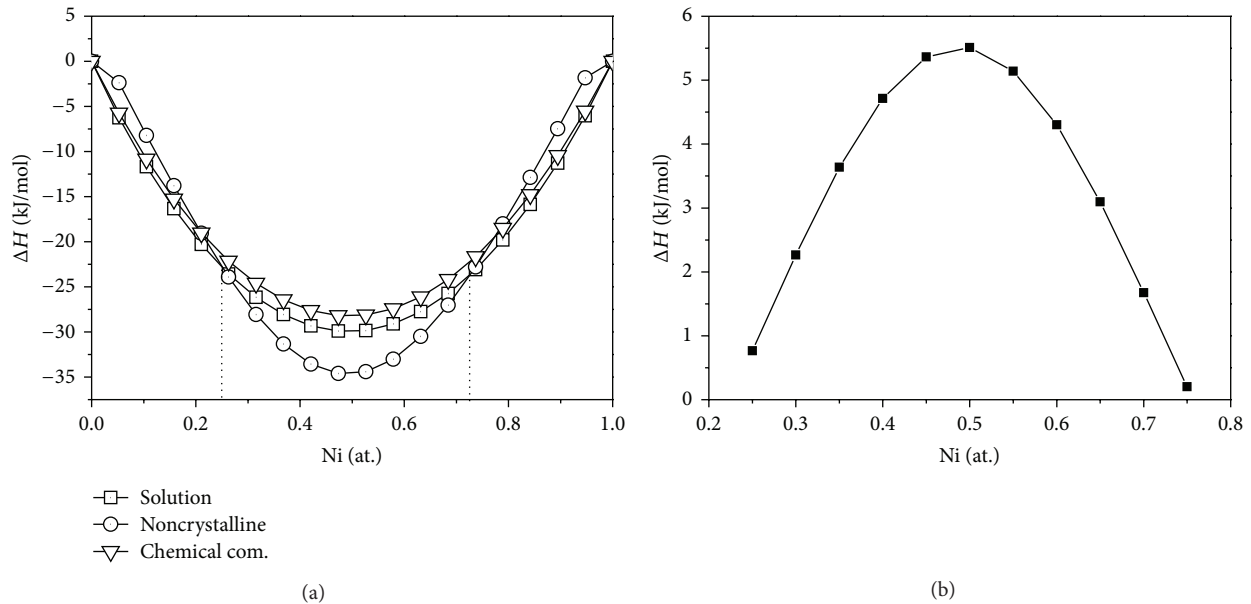


FIGURE 4: The formation enthalpies as function of the composition of Ni.

Evidently, in the curve of $\Delta G^{\text{cry}} - \Delta G^{\text{amor}}$ versus nickel atom content, shown in Figure 4(b), the cluster with about 50 percent of nickel can form glass more easily than other clusters. More leaving away from this composition point the value of the difference is much smaller, which suggested that the GFA increases firstly and then decreases with more nickel atoms in the cluster. For the verification of this law, the slower cooling process, in which the cooling rate was 0.8 K/ps and the equilibration simulation time was 100 ps, has also been used to simulate solidification of Pd-Ni alloy clusters. Figure 5 shows that the Pd, Ni200, Ni1200, and Ni clusters were presenting more perfect crystal structure and Ni1000 cluster showed the crystalline structure after the solidification process with slower cooling rate.

4. Conclusion

In summary, the solidification of Pd-Ni clusters with different nickel content has been studied in the present work. The results of molecule dynamic simulation and thermodynamic study certified that Pd-Ni clusters with composition close to 50 at.% will form noncrystal structure more easier than other Pd-Ni clusters.

Conflict of Interests

The authors declare that there is no conflict of interests regarding the publication of this paper.

Acknowledgments

This study was financially supported by the National Natural Science Foundation of China (nos. 51207031 and 51177022), China Postdoctoral Science Foundation (Grant no.

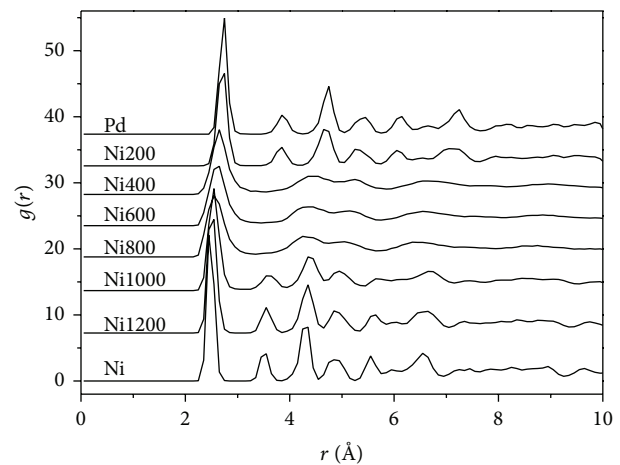


FIGURE 5: Radial distribution function (RDF) of Pd-Ni clusters at 300 K with the cooling rate of 0.8 K/ps.

2013M541368), the Promotive Research Fund for Excellent Young and Middle-Aged Scientists of Shandong Province (no. BS2011NJ002), the Science Foundation of HIT at Weihai (Grant no. IMJQ10080026), and the Natural Scientific Research Innovation Foundation of HIT (Grant no. IMXK57080026).

References

- [1] Z. J. Wu, M. H. Zhang, Z. F. Zhao, W. Li, and K. Tao, "Synthesis of a Pd on Ni-B nanoparticle catalyst by the replacement reaction method for hydrodechlorination," *Journal of Catalysis*, vol. 256, no. 2, pp. 323–330, 2008.

- [2] C.-H. Lu and F.-C. Chang, "Polyhedral oligomeric silsesquioxane-encapsulating amorphous palladium nanoclusters as catalysts for heck reactions," *ACS Catalysis*, vol. 1, no. 5, pp.481–488, 2011.
- [3] G. Z. Hua, T. Sharifi, F. Nitze, H. R. Barzegar, C.-W. Tai, and T. Wagberg, "Phase-transfer synthesis of amorphous palladium nanoparticle-functionalized 3D helical carbon nanofibers and its highly catalytic performance towards hydrazine oxidation," *Chemical Physics Letters*, vol. 543, pp. 96–100, 2012.
- [4] S. Y. Shen, T. S. Zhao, J. B. Xu, and Y. S. Li, "Synthesis of PdNi catalysts for the oxidation of ethanol in alkaline direct ethanol fuel cells," *Journal of Power Sources*, vol. 195, no. 4, pp.1001–1006, 2010.
- [5] D. H. Kim, H. Y. Kim, H. G. Kim, J. H. Ryu, and H. M. Lee, "The solid-to-liquid transition region of an Ag-Pd bimetallic nanocluster," *Journal of Physics Condensed Matter*, vol. 20, no. 3, Article ID 035208, 2008.
- [6] L. Miao, V. R. Bhethanabotla, and B. Joseph, "Melting of Pd clusters and nanowires: a comparison study using molecular dynamics simulation," *Physical Review B*, vol. 72, no. 13, Article ID 134109, 12 pages, 2005.
- [7] L. Zhu, K. S. Liang, B. Zhang, J. S. Bradley, and A. E. DePristo, "Bimetallic Pd-Cu catalysts: X-ray diffraction and theoretical modeling studies," *Journal of Catalysis*, vol. 167, no. 2, pp. 412–416, 1997.
- [8] S. Valkealahti and M. Manninen, "Melting of copper clusters," *Computational Materials Science*, vol. 1, no. 2, pp.123–134, 1993.
- [9] Y. Qi, T. Çain, W. L. Johnson, and W. A. Goddard III, "Melting and crystallization in Ni nanoclusters: the mesoscale regime," *Journal of Chemical Physics*, vol. 115, no. 1, pp. 385–394, 2001.
- [10] Y. N. Zhang, L. Wang, W. M. Wang, X. F. Liu, X. L. Tian, and P. Zhang, "Pressure effect on the structural transition of liquid Au," *Physics Letters A*, vol. 320, no. 5-6, pp. 452–458, 2004.
- [11] L. Wang, Y. N. Zhang, X. F. Bian, and Y. Chen, "Melting of Cu nanoclusters by molecular dynamics simulation," *Physics Letters A*, vol. 310, no. 2-3, pp. 197–202, 2003.
- [12] S. J. Plimpton, "Fast parallel algorithms for short-range molecular dynamics," *Journal of Computational Physics*, vol. 117, no. 1, pp. 1–19, 1995.
- [13] X. W. Zhou, R. A. Johnson, and H. N. G. Wadley, "Misfit-energy-increasing dislocations in vapor-deposited CoFe/NiFe multilayers," *Physical Review B*, vol. 69, no. 14, Article ID 144113, 10 pages, 2004.
- [14] S. Sengul and S. S. Dalgic, "Size dependence of melting process of ZnSe nanowires: molecular dynamics simulations," *Journal of Optoelectronics and Advanced Materials*, vol. 13, no. 11-12, pp. 1542–1547, 2011.
- [15] D. Kim, B.-J. Lee, and N. J. Kim, "Thermodynamic approach for predicting the glass forming ability of amorphous alloys," *Intermetallics*, vol. 12, no. 10-11, pp. 1103–1107, 2004.
- [16] F. R. de Boer, R. Boom, W. C. M. Mattens, A. R. Miedema, and A. K. Niessen, *Cohesion in Metals: Transition Metals Alloys*, North-Holland, Amsterdam, The Netherlands, 1988.
- [17] J. A. V. Butler, "The thermodynamics of the surfaces of solutions," *Proceedings of the Royal Society A*, vol. 135, no. 827, pp. 348–375, 1932.
- [18] Z. Y. Qiao, L. J. Yan, Z. M. Cao, and G. R. Liu, "Surface tension calculation of undercooled alloys," *Rare Metals*, vol. 20, no. 1, pp. 58–61, 2001.
- [19] J. Brillo, Y. Plevachuk, and I. Egry, "Surface tension of liquid Al-Cu-Ag ternary alloys," *Journal of Materials Science*, vol. 45, no. 19, pp. 5150–5157, 2010.
- [20] J. D. Honeycutt and H. C. Andersen, "Molecular dynamics study of melting and freezing of small Lennard-Jones clusters," *The Journal of Physical Chemistry*, vol. 91, no. 19, pp. 4950–4963, 1987.
- [21] L. Hui, F. Pederiva, G. H. Wang, and B. L. Wang, "Local clusters and defects in one-dimensional gold wires," *The Journal of Chemical Physics*, vol. 119, no. 18, pp. 9771–9776, 2003.
- [22] H. Li, F. Ding, J. L. Wang, X. F. Bian, and G. H. Wang, "Structural studies of clusters in melt of FeAl compound," *The Journal of Chemical Physics*, vol. 114, no. 14, pp. 6413–6416, 2001.
- [23] H. Li, G. Wang, F. Ding, J. L. Wang, and W. F. Shen, "Molecular dynamics computation of clusters in liquid Fe-Al alloy," *Physics Letters A*, vol. 280, no. 5-6, pp. 325–332, 2001.
- [24] J. A. Dean, *Lange's Handbook of Chemistry*, R. R. Donnelley & Sons, New York, NY, USA, 15th edition, 1999.
- [25] A. K. Niessen, F. R. de Boer, R. Boom, P. F. de Châtel, W. C. M. Mattens, and A. R. Miedema, "Model predictions for the enthalpy of formation of transition metal alloys II," *Calphad*, vol. 7, no. 1, pp. 51–70, 1983.
- [26] W. Martienssen and H. Warlimont, *Springer Handbook of Condensed Matter and Materials Data*, Springer, Berlin, Germany, 2005.

Research Article

Fatigue Durability Analysis of Collecting Rapping System in Electrostatic Precipitators under Impact Loading

Ali Akbar Lotfi Neyestanak, Saeed Adib Nazari, Ali Imam, and Cyrus Aghanajafi

Department of Mechanical and Aerospace Engineering, Science and Research Branch, Islamic Azad University, Tehran 14778 93855, Iran

Correspondence should be addressed to Ali Akbar Lotfi Neyestanak; aaklotfi@yahoo.com

Received 29 July 2013; Revised 24 November 2013; Accepted 2 December 2013; Published 12 January 2014

Academic Editor: Martha Guerrero

Copyright © 2014 Ali Akbar Lotfi Neyestanak et al. This is an open access article distributed under the Creative Commons Attribution License, which permits unrestricted use, distribution, and reproduction in any medium, provided the original work is properly cited.

Due to the importance of collecting rapping system in electrostatic precipitators (ESP) and controlling the relevant damage under impact loading, fatigue durability of this system is analyzed in the present study based on the numerical and experimental results considering fatigue damage growth and vibration acceleration in the collecting system because of the successive impact of rapping hammers. By microscopic examination of the fracture surface of rapping hammer, beach marks obviously show typical fatigue failure in the rapping hammer arm. In addition, the microscopic examination of the cross section of the collecting plates indicates the corrosion voids which cause crack and eventually fatigue failure. The finite element method is applied to determine both the stress and concentration positions of dynamic stress on the rapping system under impact loading. The paper results can be utilized in system optimization and new material selection for the system by evaluating rapping system durability.

1. Introduction

Dust particles of combustion gases produced in various industries such as cement industry, copper melting, and iron melting play a significant role in environmental pollution [1, 2]. Therefore, to prevent emitting the dust into the environment, electrostatic precipitators (Figure 1) have been utilized in which a strong electrostatic field is applied to migrate dust particles and produced gas through the plates and electrodes. Then the gas and particles become ionized in the field (corona formation) and charged dust particles immigrate toward the collecting plates [3–5]. Finally by depositing a portion of dust particles on the discharge electrodes and according to the viscosity and the dust type of different industries a rapping system will be needed to make a vibration with proper acceleration and amplitude on the collecting plates (Figure 2) [6].

According to the investigations, the minimum acceleration to separate a dust cake of deposited dust particles on the collecting plates from these plates is 100 g (980 m/s^2) (g is gravitational acceleration). The minimum and maximum accelerations caused by rapping on the collecting plates are illustrated in Figure 2. So, with the parameters like thickness,

frame dimension, and material of collecting plates, the sufficient energy obtained by rapping should be provided in order to make such an acceleration throughout the frame. Then the produced acceleration in the collecting plates is given in (1) by considering fundamental frequency and displacement made in the collecting plates resulting from rapping hammer [6, 7]. Consider

$$\text{acceleration} = 4\pi^2 f^2 d, \quad (1)$$

where d is displacement caused by rapping on the collecting plates (meter) and f is fundamental frequency (Hz). Fundamental frequency is given in relation (2) considering the dimension, weight, and material of the collecting plates. Consider

$$f = \frac{K}{2} \times \left(\frac{D}{wL^4} \right)^{1/2}, \quad (2)$$

where K is constant, L is the width of the collecting plate (m), w is weight per unit area, and D is the stiffness of the collecting plate which is given in relation (3). Consider

$$D = \frac{Et^3}{12(1-\nu^2)}, \quad (3)$$

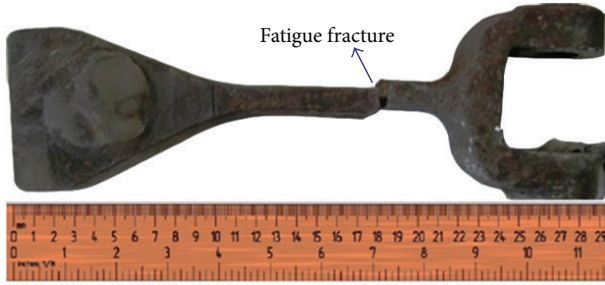


FIGURE 3: Hammer fatigue fracture location.



FIGURE 4: The location of collecting plate ruptures.

hammer arm. Therefore, in the experimental investigations rapping hammer will be fractured (by fatigue) in a600000 impact cycle because of dynamic loads of rapping. The fracture location of rapping hammer is shown in Figure 3. The aim of the present study in such a case is to analyze the fracture in order to determine and describe the main factors in the fracture of hammer and to use appropriate analysis techniques which can be suitable to design optimum production method for these hammers.

2.2. Second Case: Ruptures Investigation of Collecting Plates. A portion of energy is also devoted to vibration in the plate and eventually leads to elastic deformation. By considering the wave propagation through the plates created by the impact, the vibration acceleration of the collecting plates causes frequent deformations on the plate. If this amount is considered in the stress analysis of the collecting plates, it can produce dynamic stresses on the plates. The location of these dynamic stresses concentration in the plates is close to the locations which are restricted. So, according to Figure 4 durability rupture of collecting plates exactly occurs in such a place where there is the maximum stress. In this case, the aim of the paper is to analyze rupture fracture in order to determine and describe the main parameters of the collecting

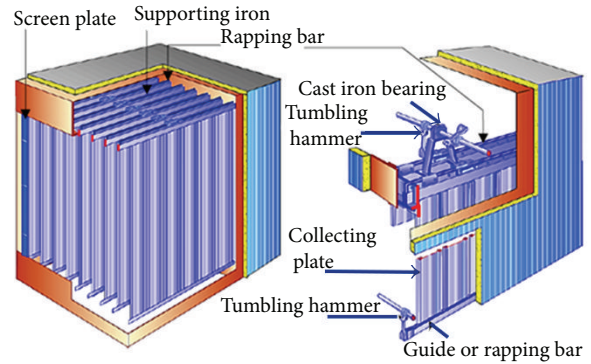


FIGURE 5: Rapping system, collecting plates (FLS Group, Inc.) [9].

TABLE 1: Profile parameters of collecting rapping system.

Profile	Hammer	Collecting plate
Heights H (m)	0.29	12.5
Mass m (kg)	6.9	98
Thickness t (mm)	40	1.5
Length L (m)	—	0.5

plates rupture, in addition to affording achieving a proper vibration in the plates without any damage and fracture.

3. Characteristics and Properties of the Rapping System Materials

Collecting plates and rapping hammer are the principle elements of EPS. The height of the collecting plates varies between 1 and 15 meters according to the desired collecting efficiency and input gas volume; in addition, the weight of the rapping hammer changes from 4 to 8 kg considering the plate height and necessary vibration acceleration. Rapping system including the collecting plates besides rapping hammer and all its elements is illustrated in Figure 5. The geometrical characteristics of the collecting plate and rapping hammer which are studied in this work are given in Table 1. Both XRF (X-ray fluorescence spectrometry) and optical emission spectrometry methods (quantometer) were applied to do precise chemical analysis of hammer and collecting plates. The results are shown in Table 2(a).

On the other hand, their mechanical properties were obtained by means of Gotech universal tensile testing machine with the capacity of 30 tons; in addition, preparing the sample with a flat cross section and a gage length of 80 mm was done according to standard EN10002-1 (DIN EN 10130). Furthermore, Impact value Charpy v Notch test was done for the hammer according to standard En 10045. The results are given in Table 2(b) gives. But, in the condition of more intensive corrosive environment more corrosion-resistant steel like SS316 will be used. The manufacturing process of these plates is rolling. The collecting plates inside the electrofilter shell are suspended and they are restricted at the top of the plates in a steel frame. Rapping hammer material done by chemical analysis and tensile mechanical

TABLE 2: Characteristics of examined collecting plates and rapping hammer.

(a) Chemical specifications								
Element	Composition (%)							
	C	Si	Mn	P	S	Cr	Ni	Mo
Collecting	0.131	0.202	0.889	0.0167	0.005	0.0081	0.0344	0.0050
Hammer	0.332	0.28	0.561	0.007	0.022	0.082	0.081	0.01

(b) Mechanical properties					
	Yield strength (Mpa)	Tensile strength (Mpa)	Elongation (%)	Impact value Charpy v Notch (long.)	Modulus of elasticity (Gpa)
Collecting	253	324	36	—	200
Hammer	314	562	16	41	210

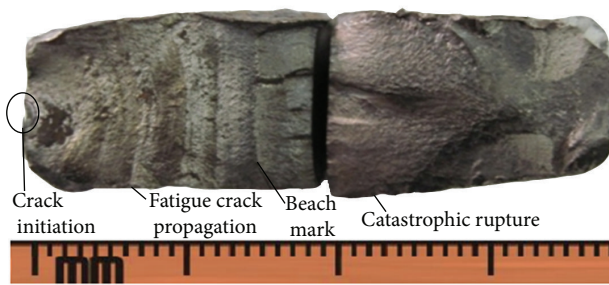


FIGURE 6: Fatigue fracture cross section of rapping hammer arm.

test is given in Table 2. The hammer material is steel Ck35 and formed and produced by forging operation.

4. Study of Fracture Surface

4.1. Visual Investigation into Fatigue Damage of Rapping Hammer. Cross section of the fracture is seen in two sections in Figure 6. The left one with a flat surface and half part of fracture surface shows fatigue damage. On this section, fatigue fracture surface without any plastic deformation has a flat surface and the fracture surface is approximately perpendicular to the principle stress-strain axis on the hammer. Fatigue fracture initiates from the pints of stress concentration on the rapping hammer arm and continues to reduce cross section of hammer arm up to the point that cross section is so small that the relevant stress of this cross section exceeds the allowable stress. Then, according to Figure 6 the hammer undergoes sudden fatigue rupture. On the right section of Figure 6, the reason of final fracture is the fact that the remaining cross section cannot bear the applied load.

4.2. Steps of Fatigue Fracture in Rapping Hammer. Fatigue crack initiates in the first step and as seen in Figure 6, it (this crack can be created because of the hammer contact with the rapping shaft at the surface besides the remaining stresses and scratches caused by forging operation at the surface) initiates from the points of stress concentration on the surface of rapping hammer arm and extends toward the center of hammer arm. After reaching the center, because of the cracks

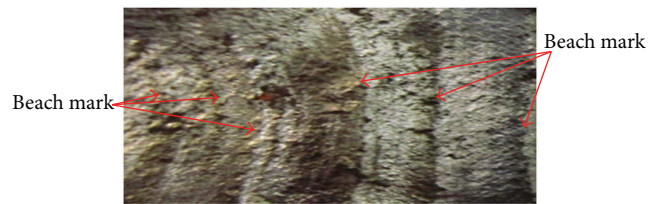


FIGURE 7: On fatigue fracture surface of hammer.

caused by hammer trim and after forging operation, fracture route will differ by 90 degrees and eventually because of the concentration of dynamic stresses, the hammer undergoes the catastrophic uterine rupture [12–17].

4.3. Optical Microscopy Investigation on Fatigue Fracture of Rapping Hammer. The presence of beach marks, clearly shown in Figure 7, is one of the main characteristics of fatigue. According to Figure 7, with microscopic investigation into the fracture surface of hammer, a group of concentric circles are seen at the cross section of fatigue fracture by the use of an optical microscope with 100x magnification in which their curvature is toward the initial point of fatigue crack. These circular lines called beach mark or arrest mark obviously show fatigue fracture of hammer at the plate perpendicular to the hammer axis. Beach marks show high cycle fatigue in the rapping hammer before reaching the middle axis of the hammer. Furthermore, hammer vibration in consecutive impacts which cause consecutive dynamic stresses is probably formed by propagation of initial crack which resulted from the production process and leads to failure of rapping hammer. A main area of the fracture surface presents high stress failure facies. A more detailed analysis of the fractured surface concludes that the surface that failed by fatigue is clearly less than the one that failed by overload; this measuring capacity allows the investigator to consider that failure occurred by fatigue but in the presence of high stress levels at the initiation zone. The fatigue area was relatively small, 20% of the whole fracture area.

4.4. Scanning Electron Microscopy/Fractography of Fatigue Rupture of Collecting Plates. Figure 8 shows the image of

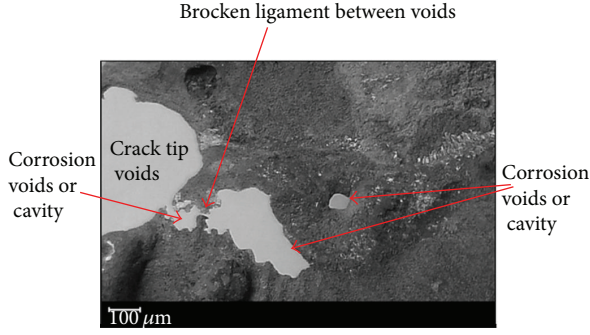


FIGURE 8: Crack tip voids formation and coalescence in a ductile fracture process of collecting plate.

rupture surface in the collecting plate. As seen in this figure, according to the mechanical properties of the collecting plates, they are characterized by flexible and not brittle material behavior. So, considering the effects produced by corrosion or other elements of the metallic matrix (as illustrated in Figure 8), final collapse is followed by cavities or voids growth, coalescence, and fracture of collecting plates.

Also SEM image of rupture surface in the collecting plate with high resolution is indicated in Figure 9. This image illustrates the primary defects of corrosion; in addition, fracture surface clearly shows the fatigue rupture perpendicular to the axis of collecting plate and in direction of impact. Moreover, rims and striation marks at a noticeably flat surface imply fatigue rupture and very small distance between rims indicates small distance between striation marks and finally shows high cycle fatigue rupture in the collecting plates.

It is noteworthy that collecting plates bear high dynamic stresses because of the vibration caused by consecutive rapping on these plates and the weight of the plates which leads to static stresses.

5. Dynamic Stresses Analysis of Rapping System

In this section, dynamic stress on the collecting plate and rapping system body, produced by frequent impacts on the rapping system to remove deposited dust cake of the collecting plates, is analyzed with numerical method, utilizing finite element technique and Abaqus software (version 6.10-1) [18]. The results of the finite element analysis are verified by applying experimental results, vibration analysis of the system, and rupture location of the piece.

5.1. The Dynamics of Rotational Motion of Hammer. Besides applying experimental results, dynamic motion of hammer before rapping, angular velocity, and kinetic energy of the hammer just before the impact are calculated to verify the finite element results. Finally, return angle after rapping as well as angular velocity and kinetic energy of the hammer after rapping is obtained with practical experiments. This measurement is done by calculating the amount of energy which includes the dissipated sound energy of all the energies causing elastic deformation and vibration in the rapping

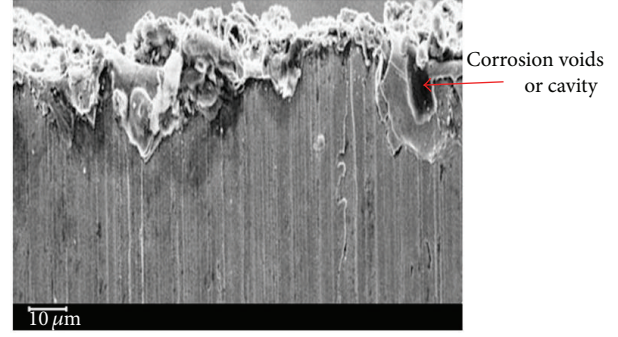


FIGURE 9: SEM image of a cross-section rupture of the collecting plate (corrosion pits near fracture surface).

system. Eventually, by doing practical experiments, it is possible to determine the energy which causes vibration in the collecting plates and motion in the system. The accuracy of numerical results is proved by comparing the results of experimental and numerical analysis. Therefore, considering the dynamic motion of the hammer, it is possible to use relations (4) to (9) to validate the results obtained by the software and experimental results. Consider

$$\omega = \sqrt{\frac{2mg\bar{r}}{I_O}}, \quad (4)$$

where ω is the angular velocity of a hammer, m is the hammer Mass, \bar{r} is the distance centre of mass from the axis of hammer rotation, and I_O is the moment of inertia around an axis of hammer rotation. Consider

$$\begin{aligned} E^P &= mgh, \\ E^K &= 0.5I\omega^2, \end{aligned} \quad (5)$$

where I is the moment of inertia, h is the hammer height, E^P is the potential energy of the hammer before rapping, and E^K kinetic energy of the hammer before rapping.

Furthermore, according to energy conservation law, after rapping, kinetic energy of the hammer at the moment of rapping converts to the energies given in relation (6) so it is possible to have strain energy produced in the hammer and system. Consider

$$E^T = E_1^E + E_2^E + E^r + E^b + E^a, \quad (6)$$

where E^T is the total energy after hammer rapping and includes

E_1^E : strain energy produced in the system, E_2^E : strain energy produced in rapping hammer, E^r : return kinetic energy in the hammer, E^b : kinetic energy in the plates, and E^a : the energy dissipated as sound.

The strain energy produced in the system is

$$E_1^E = 0.5(\sigma_1\varepsilon_1 + \sigma_2\varepsilon_2 + \sigma_3\varepsilon_3) \quad (7)$$

and for the strain energy in the rapping hammer there is

$$E_2^E = 0.5(\sigma_1\varepsilon_1 + \sigma_2\varepsilon_2 + \sigma_3\varepsilon_3). \quad (8)$$

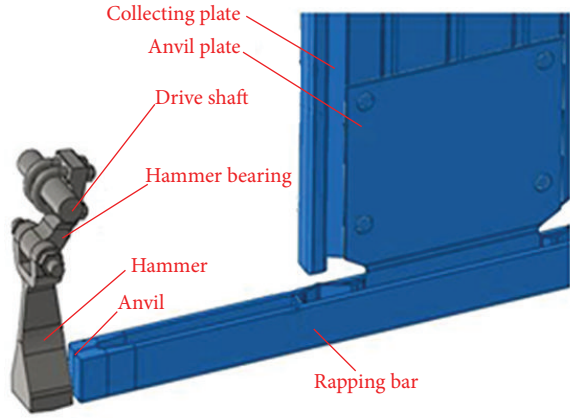


FIGURE 10: Numerical modeling relevant to all parts of the collecting plates and rapping system of the electrostatic filter (tumbling hammer, anvil plate rapping bar, and collecting plate).

According to relation (9), the equation of minimum potential energy in the case of dynamic matters also validates the results obtained by numerical analysis. Consider

$$\int_V (\delta \epsilon)^T \sigma dV = \int_V (\delta u)^T b dV + \int_s (\delta u)^T S dS + \sum_{p=1}^N (\delta u)^T f_p - \int_V (\delta u)^T \rho \ddot{u} dV - \int_V (\delta u)^T \mu \dot{u} dV. \quad (9)$$

5.2. Modeling the Rapping System of Electrostatic Precipitator. In this section, to analyze the dynamic stresses on the collecting plates and the body of the rapping hammer in order to remove deposited dust cake of the collecting plates by frequent impacts on the rapping system, 3D modeling of rapping hammer and dust collecting plates is done and then these 3D models are discussed by finite element method and Abaqus. Element C3D8R is applied to mesh the rapping system, shaft, anvil, and collecting plates. This element is used when there is no geometrical complication and more precise analysis is required. Conventional 3D elements have freedom degrees of rotation and displacement. The chosen elements of collecting plates are the conventional shell type or S4R. This element has both thick and thin shell together. Modeling of the system is shown in Figure 10.

5.3. Stress Analysis of the Rapping Hammer. Rapping and relevant dynamic stresses analysis is done after modeling the hammer. Rapping shaft is completely restricted in this analysis and the hammer has a rotational motion around the shaft axis because of its weight. According to this motion and considering the hammer and anvil surfaces as the contact surfaces, after reaching the hammer to the anvil they will contact because of the hammer weight and rotational motion around shaft axis. Therefore, because of rapping, a part of the energy of rotational motion of the hammer is converted to the strain energy in hammer and anvil so it creates stress in

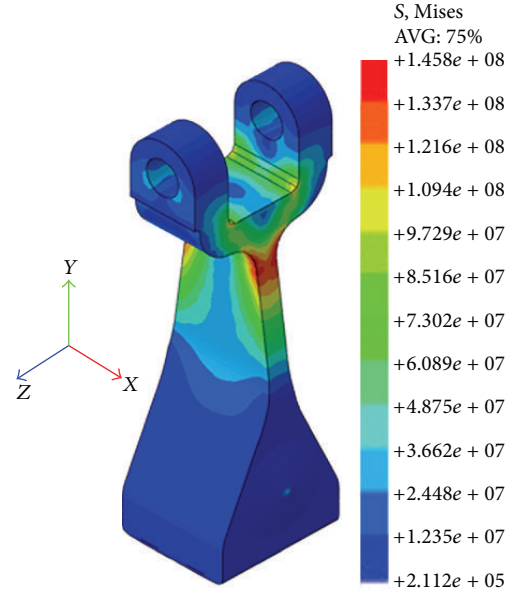


FIGURE 11: Maximum dynamic von Mises stresses in the hammers.

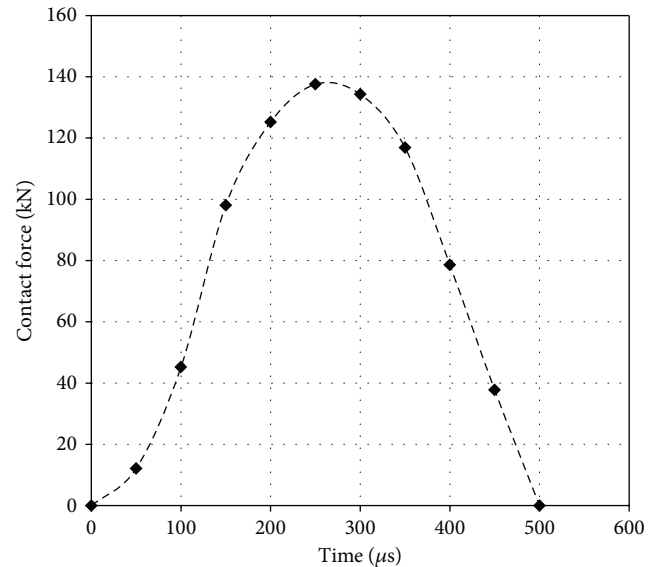


FIGURE 12: Impact force of the swing hammer on the bar supporting the electrodes.

them. According to the results of the analysis in Figure 11, it is possible to observe the maximum dynamic von Mises stress along y -axis and both sides of neutral axis in 3D model of the hammer.

So, as seen in Figure 11, the maximum von Mises stress on the arm of hammer, which is so effective in reducing the hammer life, is 145 Mpa. In addition, the maximum stress is exactly close to the fracture location so optimizing the rapping hammer profile is suggested to increase hammer life.

Figure 12 shows the dynamic force created after rapping along y -axis on the rapping bar. According to this diagram, the maximum amount of this force is 135 KN. So, by applying

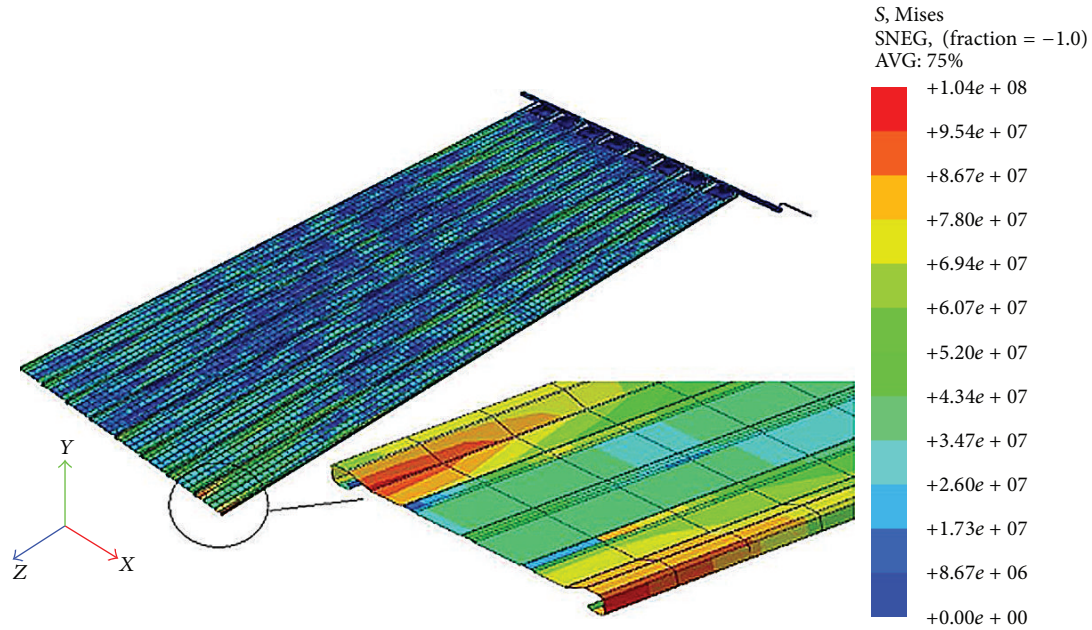


FIGURE 13: Maximum dynamic von Mises stresses in the collecting plate.

dynamic force caused by rapping, vibration with high acceleration is expectable on the plates [11, 19]; in addition, dynamic stresses resulting from plates vibration are evaluated [20].

5.4. Stress Analysis of Collecting Plate. The results of dynamic stresses because of rapper impact on the collecting plates are illustrated in Figure 13. According to the analysis, it is possible to observe maximum dynamic stress in 3D model of the system. Figure 13 shows the stress distribution in a group of collecting plates with mentioned material properties in Table 2. According to this figure, the noticeable part of stresses is below 100 megapascal. Also, it is indicated that the maximum stress distribution is just after impact and it is obviously seen that this maximum amount of von Mises stress on the plate is at the top of the plate and near the plate constraints; in addition, as seen in Figure 4 plates rupture also occurs in this location and in a place where there are the maximum dynamic stresses. Considering the maximum applied stress on the plates in addition to mechanical properties of them, given in Table 2, it is clearly seen that dynamic stresses are not the only reason for rupture but primary defects and holes caused by corrosion or rolling process of the plates and their fatigue during the frequent loading as well as.

Finally, since separating particles from the collecting plates acceleration is one of the main parameters in removing dust particles, it is observed by drawing the diagrams of acceleration variation with time that collecting plates system has an oscillation with short amplitude and high frequency. Acceleration variation of the plates with time because of the rapping hammer impact on these plates is shown in Figure 14 and the relevant results are given. According to the experiments, in order to prevent throwing the particles toward forward and creating dust particles between the collecting

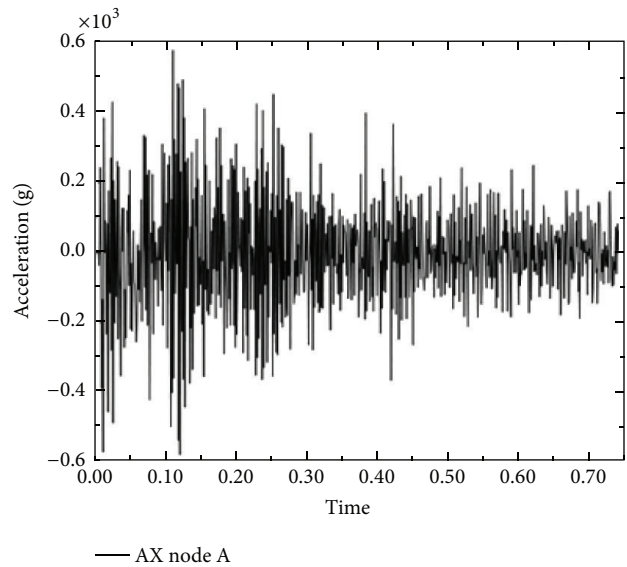


FIGURE 14: Amplitude of vibration acceleration of collecting plate at the measuring point A obtained from simulations.

plates, the acceleration perpendicular to the plates should be of small amount; on the other hand, the acceleration parallel to the plates should be of large amount to facilitate particle drops downwards. As seen in Figure 14, the acceleration parallel to the plates has the maximum amount, around 600 g, at point A (this point is schematically indicated in Figure 16). This diagram is also used to evaluate the results accuracy of analysis done by finite element method and compared with experimental results of accelerometer in a similar point (point A).



FIGURE 15: Test unit for measuring accelerations of collecting plate (JDEVS).

6. Experimental Study

6.1. *Description of Applied Equipment in the Test.* The acceleration is caused by rapping on a screen with six collecting plates with real dimensions in which the length and width of each plate are 12500 mm and 500 mm, respectively, and is measured in a pilot's tester constructed for this purpose in JDEVS (Figure 15 illustrates this pilot's tester). So, in order to measure the acceleration on these plates, accelerometer B&K type-2635 with a weight of 2/4 kg which calibrated with the accelerometer B&K type-4294 was utilized; besides, it was connected to a charge amplifier B&K type-2635. In the previous studies a similar pilot's tester was used.

6.2. *Measurement of the Acceleration Caused by Rapping on the Collecting Plates.* At first, as shown in Figure 16, the accelerometers are connected to the collecting plates at 2 m distance vertically and horizontally as the main accelerometer axis is perpendicular to the surface. (Figure 16 schematically shows the collecting plates and their distances from the accelerometers installed on the screens.) By releasing the hammer at degree 180 and impacting to anvil the energy resulting from hammers motion, which is about 38 J and includes strain energy produced in the hammer and collecting plates, kinetic energy converts to returning motion in hammer, collecting plate's motion, and sound energy. Transferred energy from hammer to collecting plates causes vibrations with very small amplitude and high frequency besides, high acceleration in the collecting plates. Figure 17 shows the results of the accelerometers. As seen in this 3D diagram, the maximum acceleration is obtained as it gets closer to the rapping location (the maximum measured acceleration on the second plate of the collecting screen is 850 g) and the acceleration is reduced as it gets further from this location toward the top of the plate or the end of the collecting plate screen. According to the diagram, the

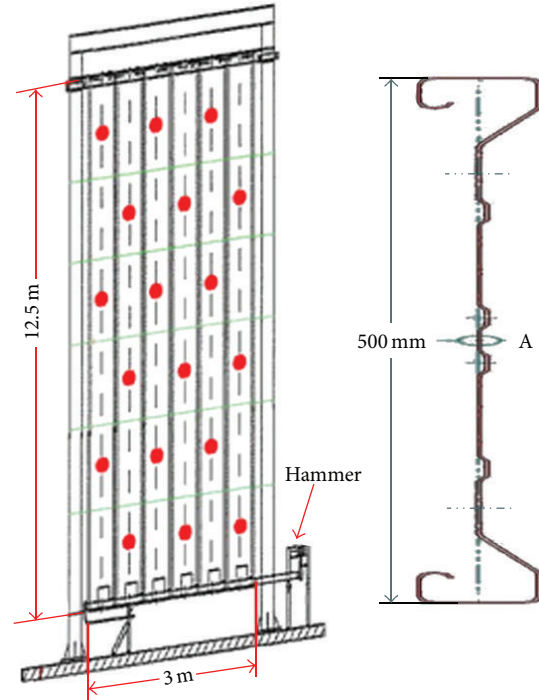


FIGURE 16: Schematic image for the frame consists of six collecting plate used for acceleration measurements (red points show the locations of the accelerometers).

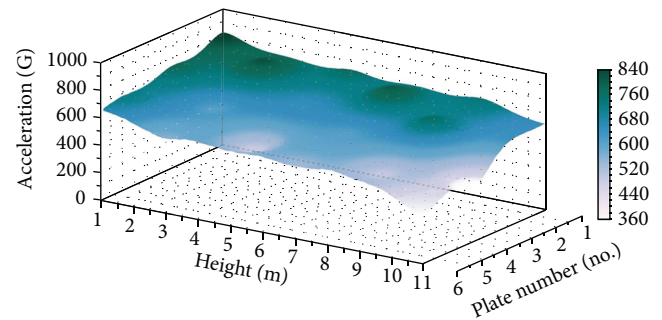


FIGURE 17: Result of accelerometer measurements at the points in which the accelerometers installed on the collecting plates (with six plates).

minimum acceleration equals 350 g at the height of 11000 mm and at the last plate of the collecting screen by noting the dimension of the collecting plates and their numbers in the screen. This amount can be proper considering the required energy to separate dust cake from the collecting plates.

7. Conclusion

The following results are obtained according to the investigations of the rapping system of the collecting plates besides the numerical and experimental analysis of the rapping hammer and collecting plates.

First Case: Rapping Hammer. By studying the remaining effects at the fracture surface of rapping hammer, it can

be mentioned that damage initiates in rapping hammer because of primary superficial defects caused by the hammer impact on the rapping shaft at the surface or because the scratches resulting from forging operation at the surface. Some observations such as beach mark indicate that the hammer bears high cycle fatigue after crack expansion. Therefore, fatigue crack extends from concentration location of dynamic stresses at the surface of rapping hammer arm towards the center of hammer arm. After reaching the arm center, because of the cracks caused by hammer hot trim followed by forging operation, fracture direction changes 90° and eventually rapping hammer bears catastrophic rupture because of the concentration of dynamic stresses there.

With changes in geometrical shape and optimizing the hammer design, it is possible to reduce the stress concentration on the hammer arm which leads to reducing the energy of elastic deformation in the hammer. This stress reduction significantly helps to increase rapping hammer life. Furthermore, to manufacture a hammer without any critical defects, it is necessary to observe design, control, and optimization of forging operation such as proper hot trim, superficial defects reduction, and removing the friction between hammer and rapping shaft.

Second Case: Studying the Collecting Plates Ruptures. Vibration and wave propagation in the collecting plate because of rapping produce frequent deformations on the surface and can cause dynamic stresses on the plates. Dynamic stress concentration is at the top of the plate and close to the locations where these plates are restricted. So, since fatigue rupture of the collecting plates occurs at the location where there is maximum stress, it can be validated on the analysis in FEM with noting the location of stress concentration. But, considering that both maximum dynamic stresses and mechanical properties of the plate materials can cause rupture, it confirms that the main factors of rupture are the primary defects and holes produced by corrosion or the defects created by rolling process and plates fatigue during frequent loading. Moreover, rupture surface of the plate obviously shows fatigue rupture perpendicular to the collecting plates axis and in the direction of rapping. The rim sand striation marks in a flat surface indicate soft fatigue rupture; in addition, very short distance of striation marks shows high cycle fatigue of the collecting plates.

Conflict of Interests

The authors declare that there is no conflict of interests regarding the publication of this paper.

Acknowledgments

The authors gratefully acknowledge financial and technical support by the Iranian Academic Center for Education, Culture and Research, Branch of Science and Technology University (JDEVS).

References

- [1] D. A. Lloyd, *Electrostatic Precipitator Handbook*, A. Hilger, Bristol, UK, 1988.
- [2] J. Harry, *Industrial Electrostatic Precipitation*, International Society of Electrostatic Precipitation (ISESP), Addison-Wesley, 1963.
- [3] A. Mizuno, "Electrostatic precipitation," *IEEE Transactions on Dielectrics and Electrical Insulation*, vol. 7, no. 5, pp. 615–624, 2000.
- [4] K. J. McLean, "Electrostatic precipitators," *IEE Proceedings A*, vol. 135, no. 6, pp. 347–361, 1988.
- [5] J. Katz, *The Art of Electrostatic Precipitation*, Precipitator Technology, Munhall, Pa, USA, 1979.
- [6] K. R. Parker, Ed., *Applied Electrostatic Precipitation*, Blackie Academic and Professional, London, UK, 1997.
- [7] K. Parker, *Electrical Operation of Electrostatic Precipitators*, 2007.
- [8] K. Darby, "An examination of the full electrostatic precipitation process for cleaning of gases," in *Proceedings 10th Particulate Control Symposium and 5th ICESP Conference on ESPs*, pp. 1–17, Washington, DC, USA, 1993, EPRI TR-103048 V2.
- [9] FLSmidth Airtech, *Electrostatic Precipitator*, Air Pollution Control, 2010.
- [10] A. Strehlow and M. Schmoch, "Comparison of techniques for electrode rapping in electrostatic precipitators," *Proceedings of the International Conference on Electrostatic Precipitation (ICESP '01)*, Birmingham, Ala, USA, May 2001.
- [11] L. Lillieblad, M. Thimanson, K. Porle, and H. Jacobson, "On dust cake removal in electrostatic precipitators," *Proceedings of the International Conference on Electrostatic Precipitation (ICESP '00)*, May 2000.
- [12] S. S. Manson and G. R. Halford, *Fatigue and Durability of Structural Materials*, ASM International, 2006.
- [13] R. Brooks, "Fatigue fracture of stainless steel wires in an electrostatic precipitator at a paper plant," in *Handbook of Case Histories in Failure Analysis*, vol. 1, ASM International, 1992.
- [14] L. Witek, "Numerical stress and crack initiation analysis of the compressor blades after foreign object damage subjected to high-cycle fatigue," *Engineering Failure Analysis*, vol. 18, no. 8, pp. 2111–2125, 2011.
- [15] F. Bagnoli, L. Allegrucci, M. Colavita, and M. Bernabei, "Fatigue failure of a stainless steel wires used in a hydraulic pressure line," *Engineering Failure Analysis*, vol. 16, no. 5, pp. 1404–1411, 2009.
- [16] L. Witek, M. Wierzbińska, and A. Poznańska, "Fracture analysis of compressor blade of a helicopter engine," *Engineering Failure Analysis*, vol. 16, no. 5, pp. 1616–1622, 2009.
- [17] V. Infante, J. M. Silva, M. de Freitas, and L. Reis, "Failures analysis of compressor blades of aeroengines due to service," *Engineering Failure Analysis*, vol. 16, no. 4, pp. 1118–1125, 2009.
- [18] ABAQUS 6.10-1 Software Dassault Systèmes Simulia Corporation, Providence, RI, USA, 2010.
- [19] A. P. Nowak, "Measurement verification of the hybrid finite element method," in *Proceedings of the 4th European Conference on Computational Mechanics (ECCM '10)*, Paris, France, May 2010.
- [20] A. Nowak and S. Wojciech, "Optimisation and experimental verification of a dust-removal beater for the electrodes of electrostatic precipitators," *Computers and Structures*, vol. 82, no. 22, pp. 1785–1792, 2004.

Research Article

Experimental Investigation on Material Transfer Mechanism in WEDM of Pure Titanium (Grade-2)

Anish Kumar,¹ Vinod Kumar,² and Jatinder Kumar³

¹ Department of Mechanical Engineering, M.M. University, Mullana, Ambala, Haryana 133207, India

² Department of Mechanical Engineering, Thapar University, Patiala, Punjab 147004, India

³ Department of Mechanical Engineering, National Institute of Technology, Kurukshetra, Haryana 136119, India

Correspondence should be addressed to Anish Kumar; anish_kaushik@rediffmail.com

Received 1 May 2013; Revised 7 October 2013; Accepted 9 October 2013

Academic Editor: Augusto Deus

Copyright © 2013 Anish Kumar et al. This is an open access article distributed under the Creative Commons Attribution License, which permits unrestricted use, distribution, and reproduction in any medium, provided the original work is properly cited.

This research work mainly focused on experimental investigation on material transfer mechanism in WEDM of pure titanium. The effects of machining parameters such as pulse on time, pulse off time, peak current, spark gap voltage, wire feed, and wire tension on the material removal rate (MRR), overcut, and surface roughness for pure titanium in WEDM process were explored. The selected machined samples were analyzed using energy dispersive X-ray analysis, scanning electron microscope, and X-ray diffraction techniques. It was observed from the results that a significant material transfer occurred from the dielectric, as well as tool, electrode on the work surface either in free form and/or in compound form. Also the multiresponse optimization of process parameters was done using desirability approach. The predictions from this model were validated by conducting experiments.

1. Introduction

The use of light, thin, and compact mechanical elements has recently become a global trend. The search for new, light-weight material with greater strength and toughness has led to the development of new generation of materials such as titanium. Having greater hardness and reinforcement strength, these materials are difficult to machine by the traditional methods. Although these materials can be machined conventionally, subsurface damages such as metallurgical alterations, work hardening, and microcracks can occur. Since the cost of using conventional machining is generally prohibitive, nonconventional machining such as wire electric discharge machining (WEDM) is the ideal technique in dealing with these materials [1]. Wire electrical discharge machining (WEDM) is a specialized thermal machining process capable of accurately machining parts with varying hardness or complex shapes, which have sharp edges that are very difficult to be machined by the main stream machining processes. This practical technology of the WEDM process is based on the conventional EDM sparking phenomenon utilizing the widely accepted noncontact technique of material removal. Since the introduction of the process, WEDM has evolved

from a simple means of making tools and dies to the best alternative of producing microscale parts with the highest degree of dimensional accuracy and surface finish quality. Some of the common applications of WEDM are including the fabrication of the stamping and extrusion tools and dies, fixtures and gauges, prototypes, aircraft and medical parts, and grinding wheel form tools [2]. The material removal mechanism of WEDM is very similar to the conventional EDM process involving the erosion effect produced by the electrical discharges (sparks). In WEDM, material is eroded from the work piece by a series of discrete sparks occurring between the work piece and the wire, separated by a stream of dielectric fluid, which is continuously fed to the machining zone. In case of WEDM, a wire electrode is trailing vertically through the work piece which usually is fed horizontally. This process utilizes a continuously traveling wire electrode made of thin copper, brass, or tungsten of diameter 0.05–0.3 mm, which is capable of achieving very small corner radii [3, 4]. The wire is kept in tension using a mechanical tensioning device reducing the tendency of producing inaccurate parts. During the WEDM process, the material is eroded from the work piece by a series of discrete sparks, ahead of the wire. The microprocessor used to continuously feed thin wire will

constantly maintain the gap (0.025 to 0.05) mm between the wire piece and the work piece. In WEDM process, there is no direct contact between the work piece and the wire piece thus eliminating the mechanical stresses during machining.

2. Background of Research Work

Miller et al. [5] presented a study for the optimization of cutting parameters which were effective for material removal rate and surface finish. The surface finish increased on with increasing the discharge current, pulse duration, and wire speed. Huang and Liao [6] studied the uses of grey relational and signal-to-noise ratio for demonstrating the influence of table feed and pulse on-time on the MRR. Hewidy et al. [7] modeled the machining parameters of wire electrical discharge machining of Inconel-601 using RSM. It was concluded that the volumetric metal removal rate generally increased with the increase of the peak current value and water pressure. Mahapatra and Patnaik [8] optimized the parameters using Taguchi method on D2 tool steel as work material in WEDM process. It was observed that discharge current, pulse duration, dielectric flow rate, and the interaction between discharge current and pulse duration were the most significant parameters for cutting operation. Mathematical models were developed for optimization of MRR and surface finish using nonlinear regression method. Ramakrishnan and Karunamoorthy [9] used Taguchi's robust design approach for WEDM. The three responses, namely, material removal rate, surface roughness, and wire wear ratio were considered. Manna and Bhattacharyya [10] optimized the machining parameters using the Taguchi and Gauss elimination method. The test results concluded that the voltage and pulse on time were the most significant parameters for controlling the metal removal rate. Sarkar et al. [11, 12] presented the modeling and optimization of wire electrical discharge machining of γ -TiAl in single and multipass cutting operation. A second-order mathematical model and ANN approach, in terms of machining parameters, were developed for cutting speed, surface roughness, and wire compensation using RSM. Yang et al. [13] analyzed the variations in metal removal rate, surface roughness average, and corner deviation (CD) of wire electrical discharge machining (WEDM) process in relation to the cutting of pure tungsten profiles. A hybrid method including response surface methodology (RSM) and back-propagation neural network (BPNN) integrated simulated annealing algorithm (SAA) was proposed to determine an optimal parameter setting. Kumar et al. [14] explored the study on WEDM in machining of commercially pure titanium (grade-2). The parameters such as pulse on time, pulse off time, peak current, spark gap set voltage, wire feed, and wire tension were varied to investigate their effects on the cutting rate, gap current, and surface roughness of the machined specimens. Shah et al. [15] investigated seven machining parameters in addition to varying material thickness on machining responses such as MRR, kerf, and surface roughness of tungsten carbide samples machined by WEDM. The design of experiments was based on Taguchi orthogonal designs. Results showed the little effect of material thickness on material removal rate and kerf. Sadeghi et al. [16] discussed

effects of process parameters on surface roughness and metal removal rate in WEDM of AISI D5 steel alloy. It was found that discharge current and pulse interval were more significant for MRR and surface roughness than open circuit voltage. Kung and Chiang [17] studied behavior of wire electric discharge machining of aluminum oxide-based ceramics. The effects of machining parameters on material removal rate and surface roughness were evaluated. Tzeng et al. [18] analyzed the dependence of the material removal rate and workpiece surface finish on process parameters during the manufacture of pure tungsten profiles by wire electrical discharge machining (WEDM). A hybrid method including a back-propagation neural network (BPNN), a genetic algorithm (GA), and response surface methodology (RSM) was proposed to determine optimal parameter settings of the WEDM process. The results showed that the RSM and BPNN/GA methods were both effective tools for the optimization of WEDM process parameters. Rao and Pawar [19] proposed the mathematical models using response surface modeling (RSM) for correlating the interrelationships of various WEDM parameters such as pulse on time, pulse off time, peak current, and servo feed setting on the machining speed and surface roughness. Yu et al. [20] explored the study on polycrystalline silicon material using WEDM process to optimize the groove width, surface roughness, and cutting speed. The results showed that pulse on time was the most significant factor for cutting speed, surface roughness, and groove width. Kuruvila and Ravindra [21] investigated the WEDM machining parameters on the hot die steel for dimensional error, surface roughness, and MRR. The study revealed that smaller pulse off time and pulse on time resulted in improving the overall performance with minimum dimensional error and good surface finish. The present study explores the machinability of pure titanium (grade-2) using WEDM process. The pure titanium (grade-2) is extensively used for sea water piping's, reactor vessels, and heat exchangers. The six parameters, that is, pulse on time, pulse off time, peak current, spark gap voltage, wire feed, and wire tension, were varied to investigate their effects on output responses, that is, MRR, overcut, and surface roughness. In addition, a second order mathematical model, in terms of machining parameters, was developed using response surface methodology. These responses were optimized using multiresponse optimization through desirability. The ANOVA was used to identify the significance of the process parameters involved during machining. The test results confirmed the validity and adequacy of the developed RSM model. The selected machined samples were analyzed using energy dispersive X-ray analysis, scanning electron microscope, and X-ray diffraction techniques.

3. Materials and Methods

The experiments were performed on a four-axis CNC type WEDM (Electronica Sprintcut, 734) as shown in Figure 1(a). The six parameters, that is, pulse on time, pulse off time, peak current, spark gap voltage, wire feed, and wire tension were varied to investigate their effect on output responses that is, the MRR, overcut, and surface roughness. The parameters kept constant during machining were electrode

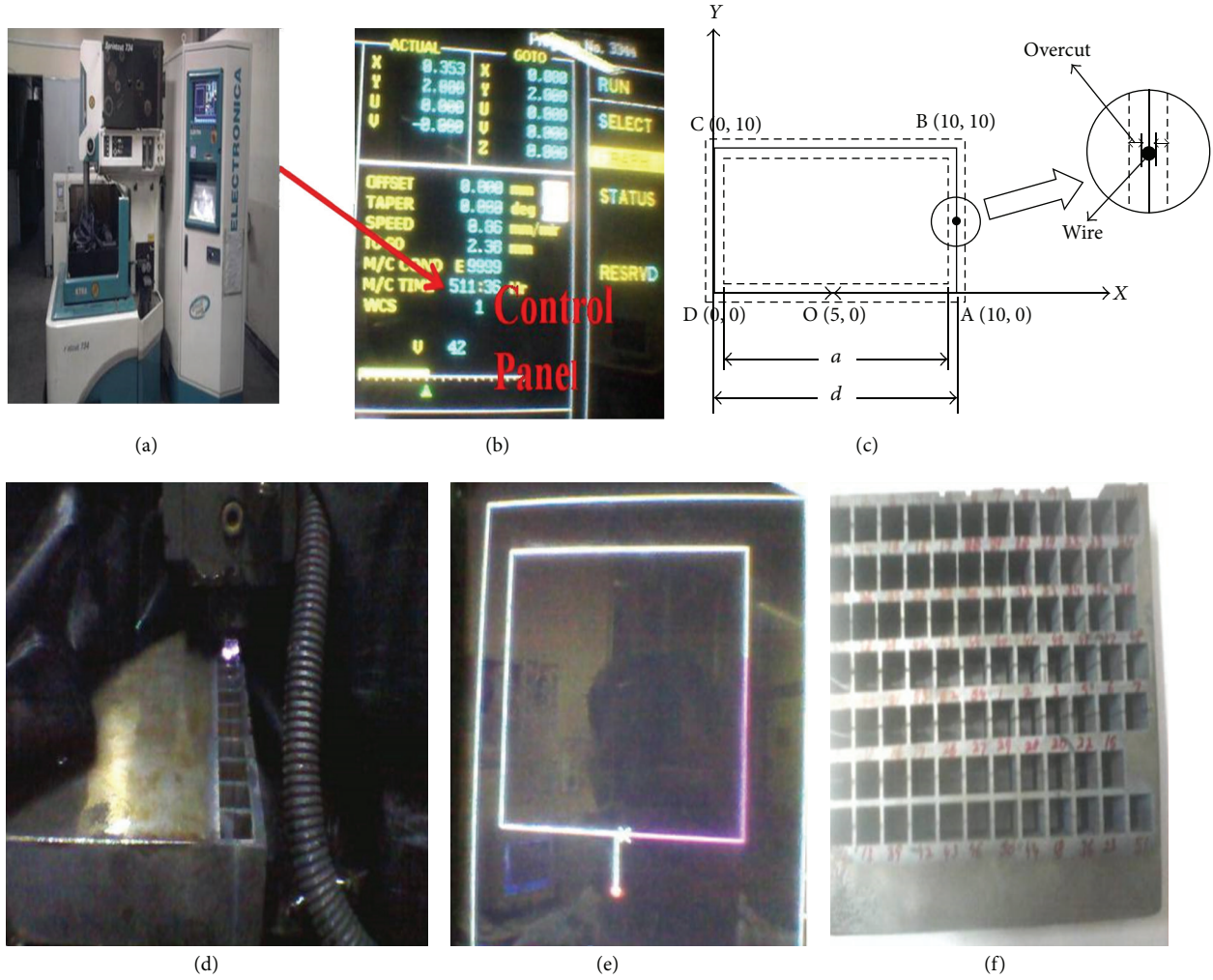


FIGURE 1: Job profile and experimental setup of WEDM machine tool (a) 4-axis WEDM CNC type, machine tool, (b) machine control panel, (c) work-path profile, (d) wire (tool) and workpiece (e) wire path on control panel, (f) square punch produced after WEDM.

(brass wire with $\varnothing 0.25$ mm), thickness of material 26 mm, and dielectric pressure 7 kg/cm^2 . The chemical composition of work material taken for experimentation was C: 0.10%, N: 0.03%, O_2 : 0.25%, H_2 : 0.015%, Fe: 0.30%, and Ti: 99.03%. The work material in the form of square plate having dimensions $148 \text{ mm} \times 148 \text{ mm} \times 26 \text{ mm}$ was taken for the experimentation work. The surface roughness of machined surface was measured in μm . The measurements were taken three times using the Mitutoyo's SURFTTEST (SJ-301). Figures 1(b)–1(d) show the work and wire path profiles during machining. The reference point taken was O (5, 0), and the wire tool traces the path OA-AB-BC-CD-DO. The CNC program for machining was generated using ELAPT software.

4. Design of Experiment

The process parameters and their levels for the main experiments were decided on the basis of the pilot experiments conducted using one factor at a time approach (OFTA) [14]. The main experiments were performed using RSM

based Box-Behnken design including pulse on time, pulse off time, peak current, spark gap voltage, wire feed, and wire tension machine parameters as shown in Table 1. In the present study, an attempt has been made to develop empirical models using statistical regression analysis. It provides a relationship between the input process parameters and output performance based on experimental results. Finally, the analysis was done to study the main effects and their interactions to explore the quadratic effect of parameters on the performance. The polynomial as the quadratic model relating the response to the factors for Box-Behnken design is given as

$$Y = \beta_0 + \sum_{i=1}^K \beta_i x_i + \sum_{i=1}^k \beta_{ii} x_i^2 + \sum_{i < j} \beta_{ij} x_i x_j, \quad (1)$$

where Y is the desired response and $x_i(1, 2, k)$ are the independent of k quantitative process variables. β_0 is constant, and β_i , β_{ii} , and β_{ij} are the coefficients of linear, quadratic, and cross-product terms.

TABLE 1: Factors and their levels.

S. no.	Symbols	Input factors	Level			Units
			I	II	III	
1	A	Pulse on time	0.7	0.9	1.1	μs
2	B	Pulse off time	17	26	38	μs
3	C	Peak current	120	160	200	Ampere
4	D	Spark gap voltage	40	50	60	Volt
5	E	Wire feed	4	7	10	m/min
6	F	Wire tension	500	950	1400	Grams

4.1. *Response Surface Methodology.* Response surface methodology is a collection of mathematical and statistical techniques for empirical model building. The RSM was applied for modeling of output responses such as material removal rate, overcut, and surface roughness. The general second-order model is defined as

$$Y = f(A, B, C, D, E, F), \quad (2)$$

where Y is the desired response and f is the response function. For the analysis purpose, the approximation of Y was proposed using the fitted second order polynomial regression model.

5. Results and Discussion

5.1. *Effect of Process Parameters on Material Removal Rate.* Consider

$$MRR = C_S \times b \times t \text{ mm}^3 / \text{min}, \quad (3)$$

where C_S = cutting speed in mm/min (taken from the machine control panel as shown in Figure 1(b)), b = width of cut in (10 mm), and t = thickness of work piece in (26 mm). The effect of the process parameters on the MRR has been determined by computing the values as shown in Table 2 using Design expert 6.0, software. The adequacy of model and effects of process parameters with their interactions for MRR are shown in ANOVA (Table 3). This model was developed at 95% confidence level. The model F value of 97.91 implied that the model is significant for MRR. It was observed from the F and P values that the factors A (pulse on time) and B (pulse off time) have a most significant effect on MRR. The values of "Prob. > F " less than 0.05 indicate that the model terms are significant. In this case A, B, C, D, BC, BD, B^2 , and C^2 were significant model terms. The lack of fit F value of 0.4750 implies that it is not significant compared to pure error. The "Pred. R -squared" of 0.9228 is in reasonable agreement with the "Adj. R -squared" of 0.9360. The model for MRR is given by

$$\begin{aligned} MRR = & 22.08597 + 10.23958 \times \text{Pulse on Time} \\ & - 1.00948 \times \text{Pulse off Time} \\ & - 0.070586 \times \text{Peak Current} \\ & - 0.17842 \times \text{Spark Gap Voltage} \end{aligned}$$

$$\begin{aligned} & + 0.00854025 \times \text{Pulse off Time}^2 \\ & + 0.000172852 \times \text{Peak Current}^2 \\ & + 0.00126488 \times \text{Pulse off Time} \\ & \times \text{Peak Current} + 0.00425 \\ & \times \text{Pulse off Time} \times \text{Spark Gap Voltage}. \end{aligned} \quad (4)$$

Figures 2(a) and 2(b) show the three-dimensional interaction plots for the response MRR. From Figure 2(a), it was observed that MRR increased from 4.91 mm³/min to 7.70 mm³/min with the increase in peak current from 120 to 200 amp and decrease of pulse off time from 38 to 17 μs . This result was concluded due to increase in peak current and decrease of pulse off time; the rate of discharge energy increases and pulse frequency decreases in wire electrode-work gap. The concentration of discharge energy in the spark gap leads to melting and vaporization of molten metal and floating metal suspended in the electrical discharge which leads to increase of MRR. High peak current and low pulse off time increased the debris in the spark gap, which leads to abnormal arcing. The abnormal arcing decreased discharge rate and the material removal rate [22]. Also abnormal arcing reduced the dielectric strength resulting in wire breakage. It was observed from Figure 2(b) that MRR increasing from 6.81 mm³/min to 8.93 mm³/min with the decrease of pulse off time 38 to 17 μs and spark gap voltage 60 to 40 V. This may reduce the gap between the work and wire electrodes during the spark. It was found that on decreasing the spark gap voltage, the wire speed increases which leads to increase the MRR. The present study revealed that higher MRR can be achieved at the lowest spark gap voltage, pulse off time, and high peak current. It was observed that WEDM surface produces the more irregular topography and defects included globules of debris, spherical particles, varying size craters, pockmarks, and microcracks as shown in Figures 5 and 6. An increase in discharge heat energy a pool of molten metal is formed and is overheated. The overheated molten metal evaporates forming gas bubbles that explode when the discharge ceases, taking molten metal material away. The result is the formation of crater. When the discharge ceases, these small gas bubbles will collapse containing lower pressure energy. The result is finer pockmarks, which also decrease the surface roughness. The spherical shape particles were reported due to surface tension of molten material. From the

TABLE 2: Design of experiments matrix and results.

Standard run no.	Factors					Response variables			
	Pulse on time T_{on} (μs)	Pulse off time T_{off} (μs)	Peak current I_p (Ampere)	Spark gap voltage SV (Volt)	Wire feed WF (m/min)	Wire tension WT (grams)	MRR (mm^3/min)	Overcut (μm)	Surface roughness (μm)
1	1.1	28	200	50	7	500	9.6	40	3.22
2	0.9	38	160	50	4	500	4.92	26	2.48
3	0.7	28	160	60	4	950	3.39	22	2.23
4	0.9	17	120	50	10	950	8.29	38	2.75
5	0.9	28	120	60	7	500	4.45	31	2.47
6	1.1	28	160	40	4	950	9.2	33	2.93
7	0.9	38	160	50	10	1400	4.77	25	2.48
8	0.9	28	160	50	7	950	5.19	30	2.65
9	0.9	17	160	50	4	500	8.81	33	2.81
10	1.1	28	160	40	10	950	8.59	33	2.94
11	1.1	38	160	40	7	950	8.3	32	2.91
12	1.1	28	160	60	4	950	7.03	35	2.83
13	0.9	17	160	50	10	500	8.19	32	2.79
14	0.9	28	160	50	7	950	4.67	30	2.61
15	0.7	28	120	50	7	500	3.28	25	2.49
16	0.9	28	160	50	7	950	5.51	31	2.68
17	0.9	28	120	60	7	1400	4.66	28	2.49
18	0.7	38	160	40	7	950	3.65	28	2.32
19	0.9	38	120	50	10	950	4.37	26	2.31
20	0.9	28	200	40	7	1400	6.72	38	2.89
21	0.9	28	200	60	7	500	6.67	32	2.69
22	0.9	38	200	50	10	950	6.54	35	2.57
23	0.9	28	120	40	7	1400	5.07	29	2.71
24	0.7	28	120	50	7	1400	3.3	24	2.51
25	0.9	38	200	50	4	950	7.07	35	2.56
26	1.1	28	160	60	10	950	6.77	37	2.82
27	1.1	28	120	50	7	500	7.1	33	2.77
28	0.7	28	160	40	10	950	4.27	30	2.35
29	0.7	28	200	50	7	500	4.49	31	2.48
30	0.7	17	160	40	7	950	6.9	33	2.70
31	0.7	28	200	50	7	1400	4.44	33	2.51
32	0.9	28	160	50	7	950	4.7	31	2.65
33	0.9	17	200	50	4	950	8.06	42	2.88
34	0.9	28	160	50	7	950	5.61	33	2.65
35	1.1	17	160	40	7	950	11.16	43	3.28
36	0.9	17	200	50	10	950	8.28	37	2.98
37	0.9	28	200	40	7	500	7.07	35	2.84
38	0.7	28	160	40	4	950	4.41	30	2.33
39	0.9	38	160	50	10	500	4.96	25	2.50
40	0.9	28	160	50	7	950	5.65	32	2.69
41	1.1	38	160	60	7	950	6.77	33	2.66
42	0.7	17	160	60	7	950	4.14	30	2.60
43	0.9	28	200	60	7	1400	6.57	32	2.68
44	0.9	17	120	50	4	950	7.61	35	2.75

TABLE 2: Continued.

Standard run no.	Factors						Response variables		
	Pulse on time T_{on} (μs)	Pulse off time T_{off} (μs)	Peak current I_p (Ampere)	Spark gap voltage SV (Volt)	Wire feed WF (m/min)	Wire tension WT (grams)	MRR (mm^3/min)	Overcut (μm)	Surface roughness (μm)
45	0.7	28	160	60	10	950	3.75	25	2.28
46	1.1	28	120	50	7	1400	7.11	35	2.75
47	0.7	38	160	60	7	950	3.28	24	2.15
48	0.9	17	160	50	4	1400	8.15	31	2.85
49	0.9	28	120	40	7	500	5.36	31	2.78
50	1.1	17	160	60	7	950	8.45	40	3.00
51	0.9	38	120	50	4	950	4.55	25	2.29
52	1.1	28	200	50	7	1400	8.37	35	3.12
53	0.9	17	160	50	10	1400	7.53	37	2.82
54	0.9	38	160	50	4	1400	4.92	25	2.49

TABLE 3: The analysis of variance for main and interaction effects of parameters on MRR.

Source	SS	DOF	MS	F -value	Prob. $> F$	At 95% CI	% Contribution
Model	180.93	8	22.62	97.91	<0.0001	significant	
Pulse on time	100.66	1	100.66	435.74	<0.0001	significant	52.61
Pulse off time	41.27	1	41.27	178.64	<0.0001	significant	21.57
Peak current	14.62	1	14.62	63.28	<0.0001	significant	7.64
Spark gap voltage	9.09	1	9.09	39.35	<0.0001	significant	4.75
Pulse off time ²	11.35	1	11.35	49.12	<0.0001	significant	5.93
Peak current ²	0.98	1	0.98	4.24	0.0453	significant	0.512
Pulse off time \times peak current	2.26	1	2.26	9.77	0.0031	significant	1.18
Lack of fit	9.40	40	0.24	1.18	0.4750	not significant	
$R^2 = 0.9457$							
R^2 adjusted = 0.9360							
Predicted $R^2 = 0.9228$							

SS: sum of square, DOF: degree of freedom, MS: mean square, F -value: Fisher value.

previous studies, some of the molten material was not flushed away from the gap by dielectric fluid and remained in the electrical discharge. This material resolidifies on the surface of machined samples, that is known as recast layer [23]. Appearance of significant recast layer as shown in Figure 8. Figures 2(c) and 2(d) present the normal probability plot of residuals and residual versus predicted plots for MRR. It was observed that the residuals following a straight line concluding that the errors are normally distributed. Based on experimental results as shown in Table 2, maximum MRR = $11.16 \text{ mm}^3/\text{min}$ was obtained when the parameters were set at pulse on time = $1.1 \mu s$, pulse off time = $17 \mu s$, peak current = 160 A, spark gap voltage = 40 V, wire feed = 7 m/min, and wire tension = 950 grams.

5.2. Effect of Process Parameters on the Overcut. The profile traced by wire and the job are not the same. The perpendicular distance between the actual profile and the profile traced by the wire is equal to half of the width of the cut. Thus, the actual job produced is either undersized or oversized depending upon whether the job is punch or die. In the present

study, the job has been considered as a square punch as shown in Figure 1(f). The dimensional deviation of square punch is equal to the half the width of the cut. The dimensional deviation is measured using a digimatic caliper (Mitutoyo) having least count 0.001 mm. The overcut as shown in (Figure 1(c)) was determined as

$$\begin{aligned} \text{Overcut } (\delta) &= \text{dimensional deviation } (D) - 0.5 \\ &\quad \times \text{wire diameter } (d), \end{aligned} \quad (5)$$

$$(D) = 0.5 (W_p - W_a),$$

where W_p = programmed path and W_a = actual job profile. The ANOVA and F -ratio test were performed to verify the adequacy of model. The model F value of 30.71 in Table 4 implied that the model is significant for overcut. There is only a 0.01% chance that the “model F value” could have largely occurred due to noise. The P value of this factor is 99%, which shows its strong influence with a contribution of 30.07% and 28.76%. The values of “Prob. $> F$ ” less than 0.05 indicate that the model terms are significant. In this case $A, B, C, D,$

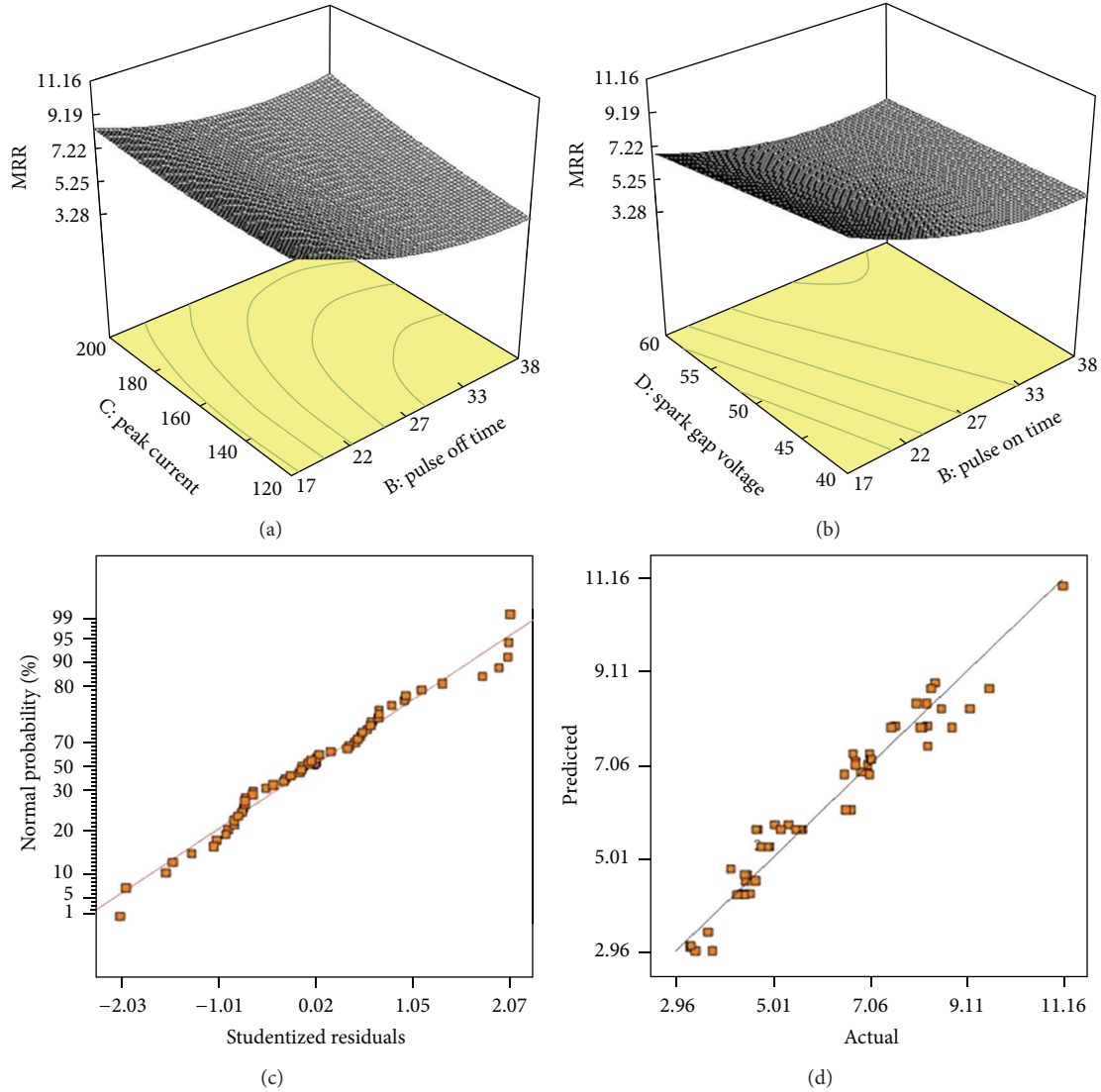


FIGURE 2: Response surface plot for MRR: (a) interaction plot between pulse off time and peak current, (b) interaction plot between pulse off time and spark gap voltage, (c) normal probability plot residuals, (d) actual versus predicted values.

B^2 , C^2 , E^2 , F^2 , and AD were significant model terms. The lack of fit F value of 0.1719 implies that it is not significant compared to pure error. The “Pred. R -squared” of 0.8191 is in reasonable agreement with the “Adj. R -squared” of 0.8706. This model can be used to navigate the design space. The regression model for overcut is given as

$$\begin{aligned} \text{Overcut} = & 102.82449 - 17.91667 \times \text{Pulse on Time} \\ & - 1.55367 \times \text{Pulse off Time} - 0.56702 \\ & \times \text{Peak Current} - 0.78333 \\ & \times \text{Spark Gap Voltage} + 1.83519 \\ & \times \text{Wire Feed} + 0.020770 \times \text{Wire Tension} \\ & + 0.010355 \times \text{Pulse off Time}^2 \\ & + 0.00165104 \times \text{Peak Current}^2 - 0.12315 \end{aligned}$$

$$\begin{aligned} & \times \text{Wire Feed}^2 - 0.0000110288 \\ & \times \text{Wire Tension}^2 + 0.75000 \\ & \times \text{Pulse on Time} \times \text{Spark Gap Voltage} \\ & + 0.00386905 \times \text{Pulse off Time} \\ & \times \text{Peak Current}. \end{aligned} \tag{6}$$

Figure 3(a) shows the three-dimensional response surface plots for the response overcut in terms of pulse on time and spark gap voltage. It was observed from these plots that the overcut is increased by increasing the pulse on time $0.7 \mu\text{s}$ to $1.1 \mu\text{s}$ and parallel decreasing of spark gap voltage. Due to increase in pulse on time, discharge energy in the spark gap increases. At high level of discharge energy in the spark gap leading to higher overcut [24], the overcut was observed

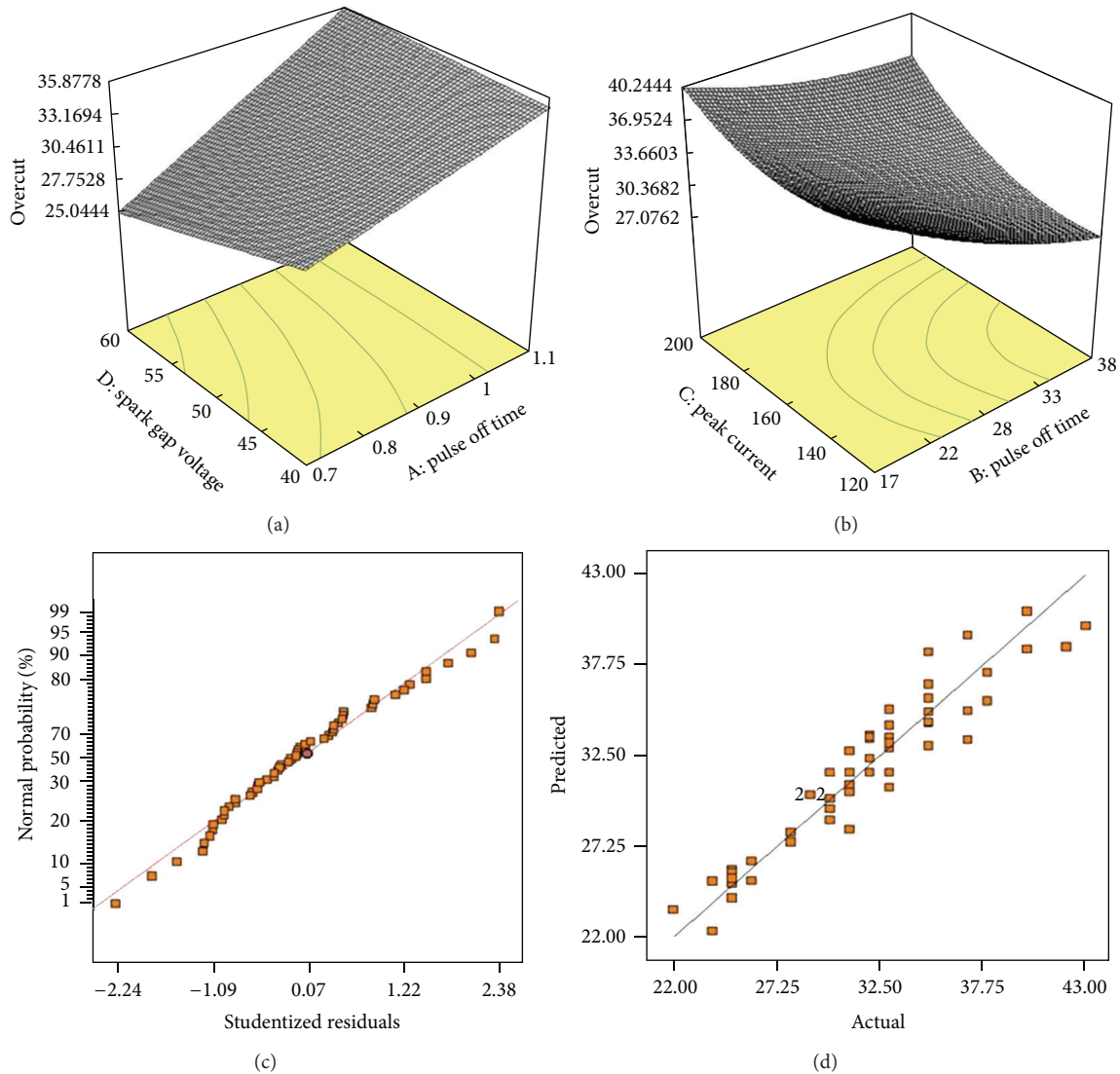


FIGURE 3: Response surface plot for overcut: (a) interaction plot between pulse on time and spark gap voltage, (b) interaction plot between pulse off time and peak current, (c) normal probability plot residuals, (d) actual versus predicted values.

during increasing pulse on time with value of $26.85 \mu\text{m}$ to $34.07 \mu\text{m}$. With further decrease of spark gap voltage 60 V to 40 V , the overcut also increased. It was found that decreasing the spark gap voltage lowers the spark gap and increases the molten metal in the gap due to its high thermal energy. The overcut was observed during decrease of spark gap voltage with value of $25.07 \mu\text{m}$ to $35.87 \mu\text{m}$. Figure 3(b) shows the three-dimensional response surface and contour plot between pulse off time and peak current. It was observed from these plots that the overcut is decreased by increasing the pulse off time from $17 \mu\text{s}$ to $38 \mu\text{s}$ simultaneously and decreasing peak current from 200 A to 120 A . It was found that by decreasing the peak current which leads to lesser discharge energy in the spark so that wire bending and vibration reduced may result in lesser overcut. By increasing the pulse off time and spark gap voltage means increasing the pulse frequency so that lesser amount of debris in the electrical

discharges which may result in lesser overcut. In order to obtain the lesser overcut, that is, $22 \mu\text{m}$ of the optimal parametric combination is pulse on time = $0.7 \mu\text{s}$, pulse off time = $28 \mu\text{s}$, peak current = 160 A , spark gap voltage = 60 V , wire feed = 4 m/min , and wire tension = 950 grams . Figures 3(c) and 3(d) display the normal probability plot of residuals and residual versus predicted plots for overcut. It is observed that the residuals generally fall on a straight line implying that the errors are normally distributed.

5.3. Effect of Process Parameters on the Surface Roughness. Surface roughness was an important process reaction, which dictates the condition of the surface component which has to be machined. If the surface finish of the machined work material was the decisive factor due to its application requirements, then the work material must be machined with low

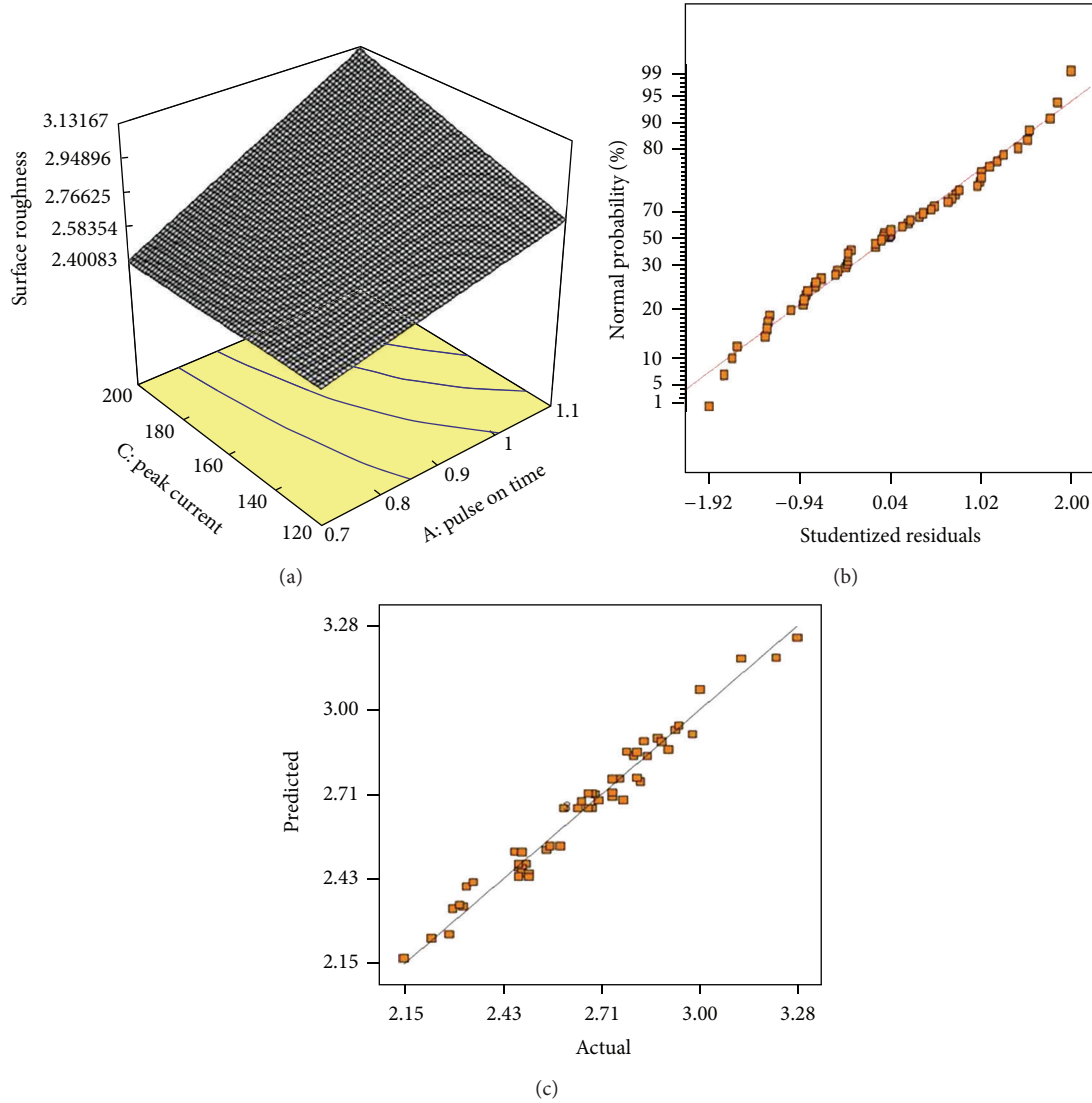


FIGURE 4: Response surface plot for surface roughness: (a) interaction plot between pulse on time and peak current, (b) normal probability plot residuals, (c) actual versus predicted values.

material removal rate. Equation represents the relationship between machining parameters and surface roughness, which is the result of developed statistical model for surface roughness

Surface Roughness

$$\begin{aligned}
 &= 3.86021 - 0.76667 \\
 &\times \text{Pulse on Time} - 0.035278 \\
 &\times \text{Pulse off Time} - 0.00922396 \\
 &\times \text{Peak Current} - 0.00866667 \\
 &\times \text{Spark gap Voltage} + 0.1247 \text{ Wire Feed} \\
 &- 0.000365432 \times \text{Wire Tension} \\
 &+ 0.00031746 \times \text{Pulse off Time}^2
 \end{aligned}$$

$$\begin{aligned}
 &- 0.00875 \times \text{Wire Feed}^2 \\
 &+ 0.000000191358 \times \text{Wire Tension}^2 \\
 &+ 0.012969 \times \text{Pulse on Time} \times \text{Peak Current}.
 \end{aligned}
 \tag{7}$$

Based on ANOVA as shown in Table 5, it implied that pulse on time, pulse off time, peak current, and spark gap voltage were significant to surface roughness. In addition to this normal plots of residuals and residual versus predicted has also been drawn. The data is normally distributed. It was observed from Figures 4(b) and 4(c) that all the experimental results are approximately very close to the predicted values, and hence the developed model can be effectively used to predict the surface roughness in WEDM of pure titanium. The *P* value for lack of fit is 0.1173 suggesting that this model adequately fits the data. The “Pred *R*-Squared” of 0.9527 is

TABLE 4: The analysis of variance for main and interaction effects of parameters on overcut.

Source	SS	DOF	MS	F-value	Prob. > F	At 95% CI	% Contribution
Model	1101.81	12	91.82	30.71	<0.0001	significant	
Pulse on time	368.17	1	368.17	123.16	<0.0001	significant	30.07
Pulse off time	352.67	1	352.17	117.97	<0.0001	significant	28.76
Peak current	176.04	1	176.04	58.89	<0.0001	significant	14.37
Spark gap voltage	28.17	1	28.17	9.42	<0.0038	significant	2.30
Pulse off time ²	14.22	1	14.22	4.76	0.0350	significant	1.16
Peak current ²	76.13	1	76.13	25.47	<0.0001	significant	6.21
Wire feed ²	13.40	1	13.40	4.48	0.0403	significant	1.09
Wire tension ²	54.41	1	54.41	18.20	<0.0001	significant	4.44
Pulse on time × spark gap voltage	36.00	1	36.00	12.04	0.0012	significant	2.94
Pulse off time × peak current	21.13	1	21.13	7.07	0.0111	significant	1.72
Lack of fit	115.73	36	3.21		0.1719	not significant	
$R^2 = 0.8999$							
R^2 adjusted = 0.8706							
Predicted $R^2 = 0.8191$							

SS: sum of square, DOF: degree of freedom, MS: mean square, F-value: Fisher value.

TABLE 5: The analysis of variance for main and interaction effects of parameters on surface roughness.

Source	SS	DOF	MS	F-Value	P > F	At 95% CI	% Contribution
Model	3.08	10	0.31	145.26	<0.0001	Significant	
Pulse on time	1.64	1	1.64	775.10	<0.0001	Significant	55.0
Pulse off time	0.84	1	0.84	396.22	<0.0001	Significant	28.0
Peak current	0.23	1	0.23	108.54	<0.0001	Significant	8.0
Spark gap voltage	0.18	1	0.18	85.03	<0.0001	Significant	6.0
Pulse off time ²	0.013	1	0.013	6.36	0.0155	Significant	0.41
Wire feed ²	0.068	1	0.068	32.18	<0.0001	Significant	2.15
Wire tension ²	0.019	1	0.019	8.90	0.0047	Significant	0.6
Pulse on time × peak current	0.086	1	0.086	40.62	<0.0001	Significant	2.71
Lack of fit	0.087	38	0.002295	2.91	0.1173	Not significant	
$R^2 = 0.9712$							
R^2 adjusted = 0.9646							
Predicted $R^2 = 0.9527$							

SS: sum of square, DOF: degree of freedom, MS: mean square, F-value: Fisher value.

in reasonable agreement with the “Adj R-Squared” of 0.9646. It was observed from Figure 4(a) that the surface roughness is affected by interaction between pulse on time and peak current with value of 2.41 to 2.72 μm . When pulse on time was increased from 0.7 to 1.1 μs with peak current of 200 A, the results surface roughness was increased from 2.40 to 3.13 μm . High pulsed current caused frequent cracking of dielectric fluid, causing more melt expulsions and larger tensile stresses. These effects were turned in poor surface finish. At higher pulse on time and peak current, the discharge energy per pulse increases which produces the deeper and wider overlapping craters, pockmarks, globules of debris, and microcracks on the machined samples as seen in SEM micrographs (Figures 5 and 6). The rapid cooling and heating effects generate gas bubbles that explode when the discharge ceases. It is clear from Figure 5(b) that the diameter and depth of crater were deeper and wider due to that high peak

current (200 A) and low pulse off time (17 μs) may result in increasing the surface roughness (2.98 μm). At higher peak current, the impact of discharge energy on the surface of workpiece becomes greater, and thus resulting erosion leads to the increase in deterioration of surface roughness [25]. It was observed from Figure 6(b) that some titanium particles were protruding and completely dislodged from the surface which may happen at higher pulse on time (1.1 μs) and peak current (200 A). The minimum surface roughness is obtained with value of 2.15 μm in experiment no. 15.

6. Crack Formation

Based on the previous research work done by Lee and Li [22], crack formation was usually associated with the development of high thermal stresses which exceed the fracture strength,

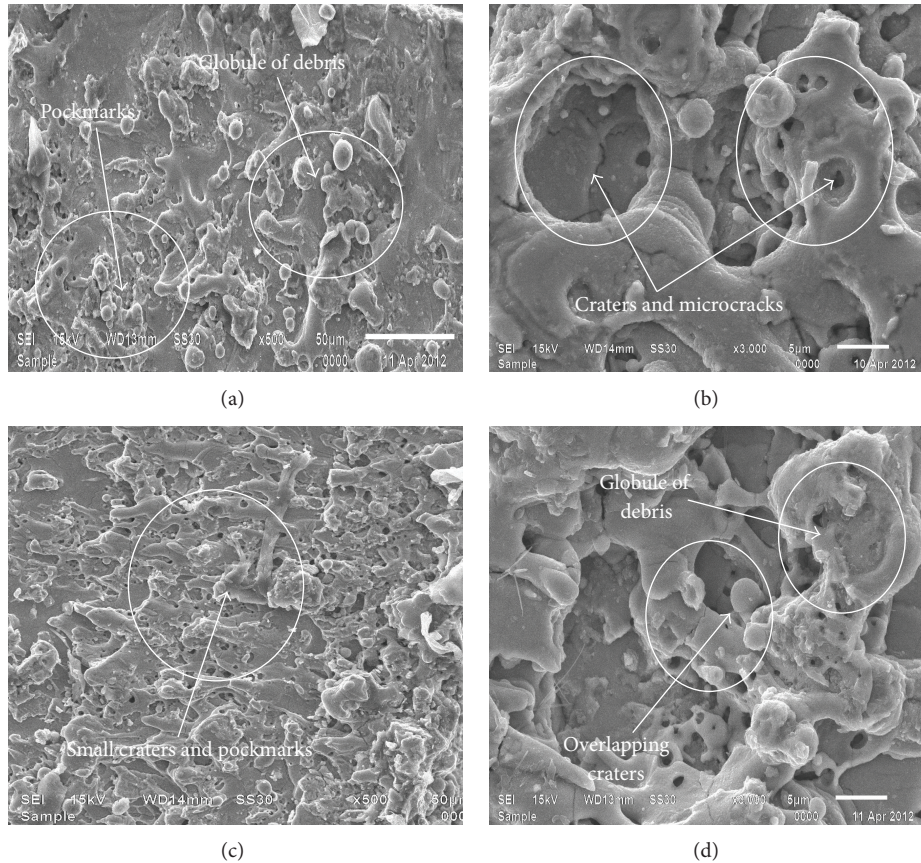


FIGURE 5: SEM micrograph (1000x, 2000x, 3000x, and 500x): (a) experiment no. 1, at $T_{on} = 1.1 \mu s$, $T_{off} = 28 \mu s$, $I_p = 200 A$, $SV = 50 V$, $WF = 7 m/min$, $WT = 500$ grams; (b) experiment no. 35, at $T_{on} = 1.1 \mu s$, $T_{off} = 17 \mu s$, $I_p = 160 A$, $SV = 40 V$, $WF = 7 m/min$, $WT = 950$ grams; (c) experiment no. 15, at $T_{on} = 0.7 \mu s$, $T_{off} = 28 \mu s$, $I_p = 120 A$, $SV = 50 V$, $WF = 7 m/min$, $WT = 500$ grams; (d) experiment no. 6, at $T_{on} = 1.1 \mu s$, $T_{off} = 28 \mu s$, $I_p = 160 A$, $SV = 40 V$, $WF = 4 m/min$, $WT = 950$ grams.

as well as with plastic deformation. In addition, the formation of microcracks not only was influenced by the setting of machining parameters but also depended on several materials properties such as tensile strength, thermal conductivity, thermal expansion coefficient, and Young modulus. In order to examine the subsurface cracks of machined samples by WEDM indicate that the material is amorphous either in free form and/or in compound form. The formation of microcracks is generally accompanied by rapid cooling and heating by dielectric fluid. The heating and cooling process was increasing the yield stress and the material plastically deformed during heating that build up the tensile stresses which leads to crack formation. The crack distribution on the surface was observed with evaluating the crack density and mean free path of the cracks [27, 28]. The surface crack densities at various peak current and pulse on time was observed in Figures 7(a)–7(d). It was observed that the cracks were developed due to high pulse on time and peak current. Due to increase of pulse on time and peak current leads to intense heat conditions on the work piece causing surface cracks developed on the material. The surface cracks density was observed wider due to free path of debris and also penetrates more deeply into original material. Overall,

the results show that the surface cracks were developed by increasing pulse on time and peak current. Cracks formed in crater continue to propagate when another discharge takes place in the neighborhood as shown in Figure 7(c). It can be noted that the intersection or inter-granular points of crack paths usually form perpendicular angles as shown in Figure 7(b). The penetrating cracks penetrate the entire subsurface to an extent into the parent material and are usually observed when machining is performed in deionized water as shown in Figure 7(a). Penetrating cracks tend to form a closed loop around the crater rim. These penetrating cracks at the subsurface mainly due to high stress concentrations are induced at crater rims during solidification.

7. Effect of Process Parameters on Recast Layer (RL)

The recast layer was observed at the cross-section of the WEDM surface. The recast layer is defined as the material melted by electrical discharge and resolidified on the work surface without being ejected nor removed by dielectric fluid [29]. It is very difficult to remove, and its appearance is

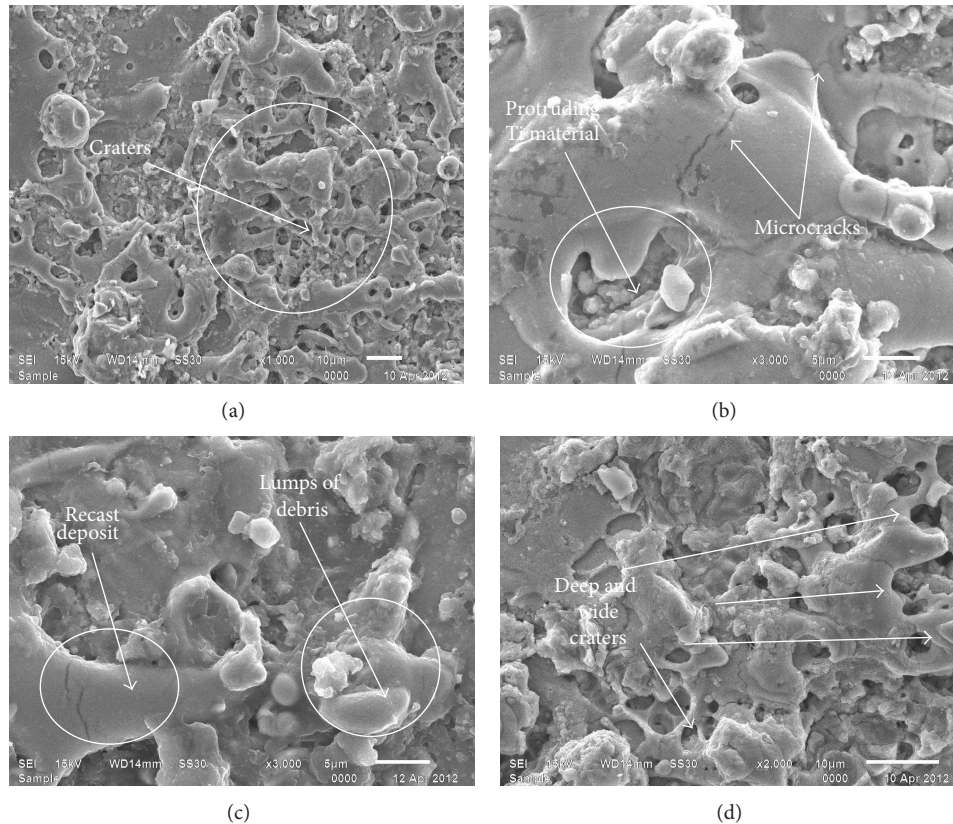


FIGURE 6: SEM micrograph (1000x, 2000x, 3000x, and 500x): (a) experiment no. 1, at $T_{on} = 1.1 \mu s$, $T_{off} = 28 \mu s$, $I_p = 200 A$, $SV = 50 V$, $WF = 7 m/min$, $WT = 500$ grams; (b) experiment no. 52, at $T_{on} = 1.1 \mu s$, $T_{off} = 28 \mu s$, $I_p = 200 A$, $SV = 50 V$, $WF = 7 m/min$, $WT = 1400$ grams; (c) experiment no. 50, at $T_{on} = 1.1 \mu s$, $T_{off} = 17 \mu s$, $I_p = 160 A$, $SV = 60 V$, $WF = 7 m/min$, $WT = 950$ grams; (d) experiment no. 36, at $T_{on} = 0.9 \mu s$, $T_{off} = 17 \mu s$, $I_p = 200 A$, $SV = 50 V$, $WF = 10 m/min$, $WT = 950$ grams.

observed through a scanning electron microscope at different levels of magnification. Below the recast layer there is the heat-affected zone. The recast layer thickness was changed due to superficial hardening of the work material by the discharge heat of electrical spark. The intensity of spark depends on peak current, pulse on time, and pulse off time. The thickness of recast layer of WEDM surface was increased due to increase of peak current and pulse on time and decrease of pulse off time as observed in Figures 8(a)–8(d). Due to increase of pulse on time and peak current, the melting of isothermals becomes more intense, which further penetrates into base metal, and the result extends the thickness of recast layer. It is clear that recast layers appear as nonuniform and have wave-like pattern. The average thickness of recast layer, as observed, is having a variation of $6 \mu m$ to $18 \mu m$.

8. Analyzing the Wire Wear Rate and Wire Rupture

In WEDM, the cutting is done by brass wire having tensile strength of $900 N/mm^2$. The occurrence of wire rupture would result in decrease of machining accuracy and the deterioration of quality of machined surface. Due to the thermal effects that develop at the interface zone between the tool

and work piece, a lot of material changes take place on the surface of tool and work piece [30]. In this regard, the material transfer characteristic of machined wire was investigated. The wire is fed through guide rolls causes abrasive action between wire and work piece may result in reduced the cross-section and also the surface characteristics of the work piece gets affected. Hence proper care should be taken in loading the spool to the machine to avoid wire deflection and breakage. In this study there are two types of wire rupture that was observed; one is due to high peak current and the other is increasing spark frequency. Figures 9(b)–9(e) show the micrograph of wear out wire. There are many different craters and residuals of debris adhered to the surface of wire electrode. The residuals of copper, carbon, oxygen, and titanium were detected in wire electrode which was observed by EDX shown in Figure 9(f). This may be due to the melting and resolidification of the titanium and brass wire electrode after WEDM. By increasing the peak current leads to generation of higher discharge energy in the spark gap may result increase the wire wear rate and wire breakage. When the debris in the gap cannot be flushed properly by dielectric may result the arcing was produced and wire breakage occurs. In addition, since the spark gap is too narrow, a portion of discharging energy was absorbed by wire electrode. Hence the surface of wire melts due to the induced high temperature.

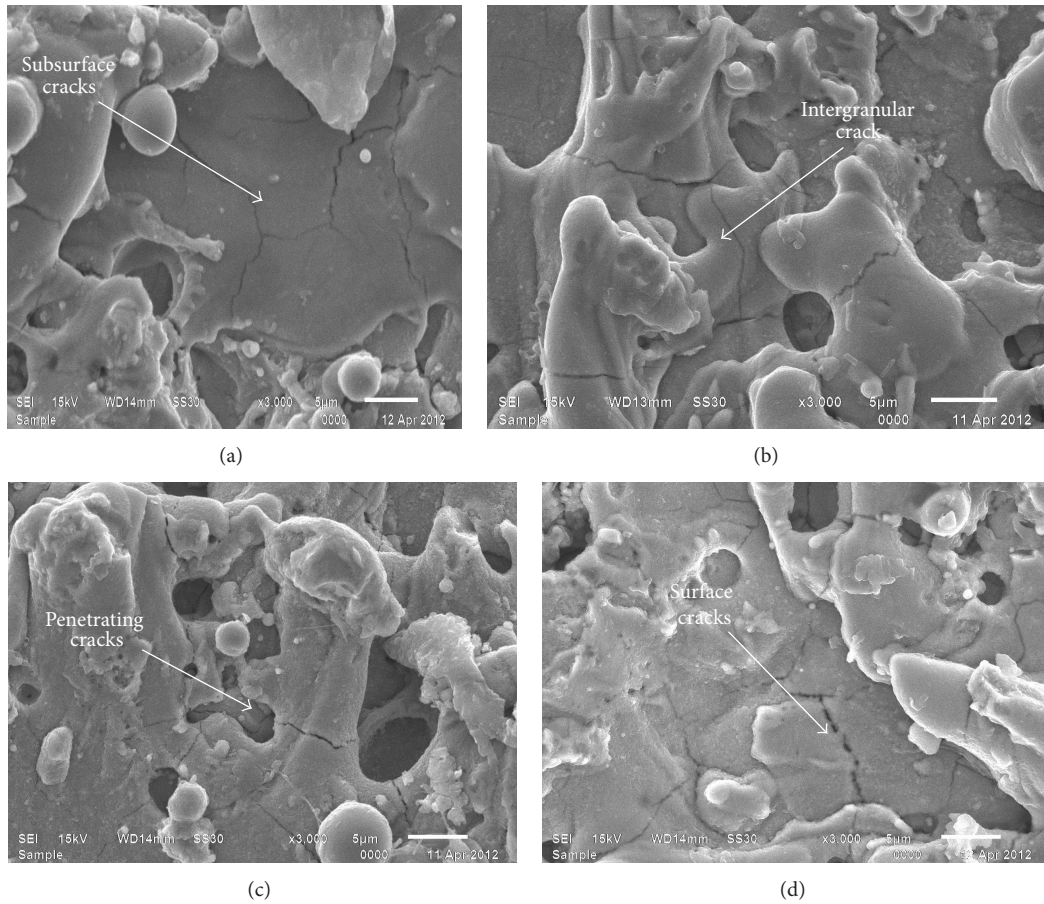


FIGURE 7: SEM micrographs of subsurface cracks at various pulse on time and peak current: (a) $T_{on} = 1.1 \mu s$, $I_p = 160 A$, (b) $T_{on} = 1.1 \mu s$, $I_p = 200 A$, (c) $T_{on} = 0.9 \mu s$, $I_p = 120 A$, (d) $T_{on} = 0.9 \mu s$, $I_p = 160 A$.

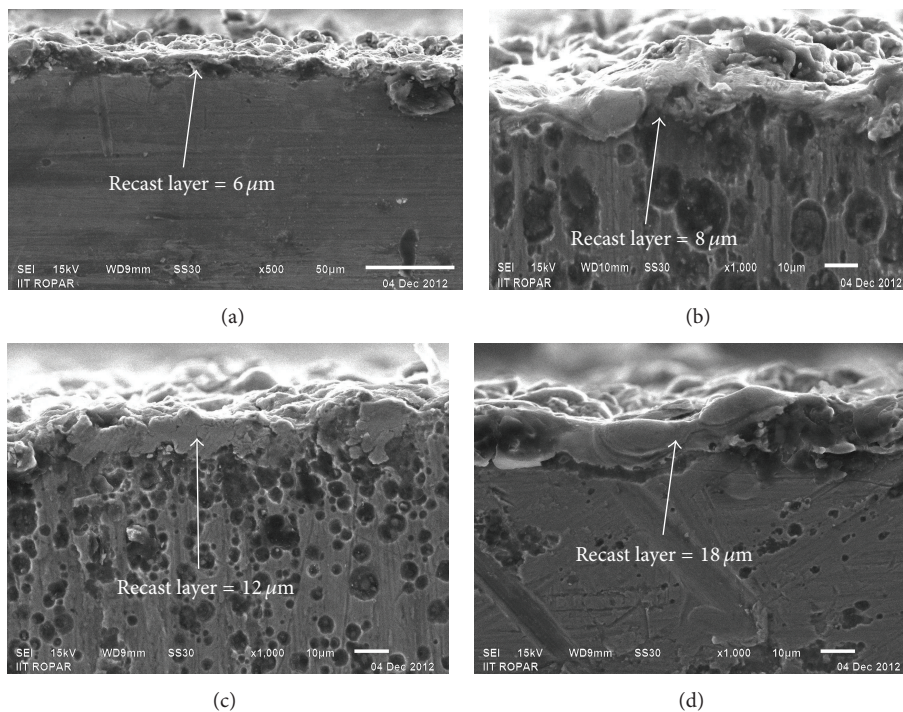


FIGURE 8: SEM micrographs of recast layer at various pulse on time and peak current: (a) $T_{on} = 1.1 \mu s$, $I_p = 160 A$, (b) $T_{on} = 1.1 \mu s$, $I_p = 200 A$, (c) $T_{on} = 0.9 \mu s$, $I_p = 120 A$, (d) $T_{on} = 0.9 \mu s$, $I_p = 160 A$.

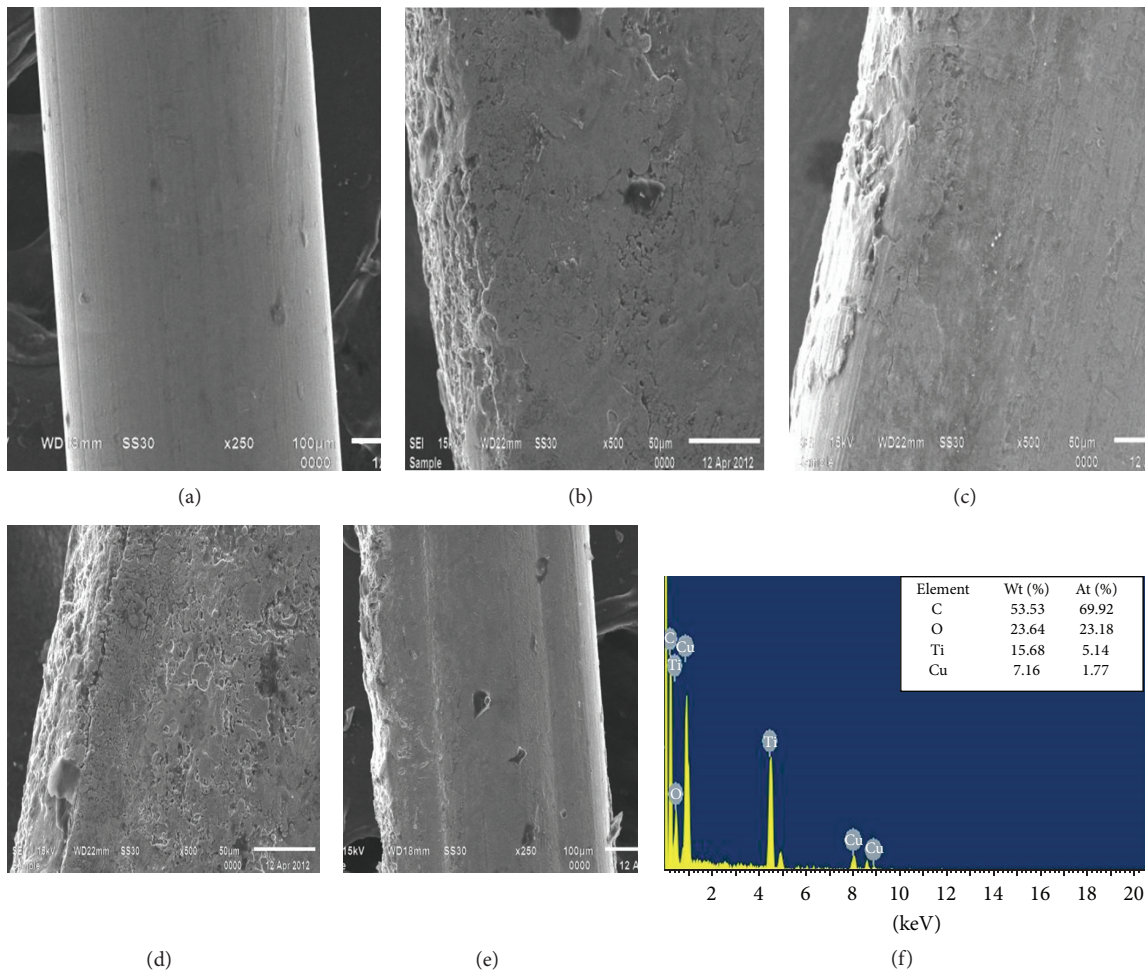


FIGURE 9: SEM micrographs (250x and 500x) of the machined wire electrode surface for machining of pure titanium at (a) fresh wire; (b) experiment no. 1, at $T_{on} = 1.1 \mu s$, $T_{off} = 28 \mu s$, $I_p = 200 A$, $SV = 50 V$, $WF = 7 m/min$, $WT = 500$ grams; (c) experiment no. 35, at $T_{on} = 1.1 \mu s$, $T_{off} = 17 \mu s$, $I_p = 160 A$, $SV = 40 V$, $WF = 7 m/min$, $WT = 950$ grams; ((d),(e)) experiment no. 15, at $T_{on} = 0.7 \mu s$, $T_{off} = 28 \mu s$, $I_p = 120 A$, $SV = 50 V$, $WF = 7 m/min$, $WT = 500$ grams; (f) EDX of machined wire electrode at $T_{on} = 0.9 \mu s$, $T_{off} = 38 \mu s$, $I_p = 160 A$, $SV = 50 V$, $WF = 4 m/min$, $WT = 500$ grams.

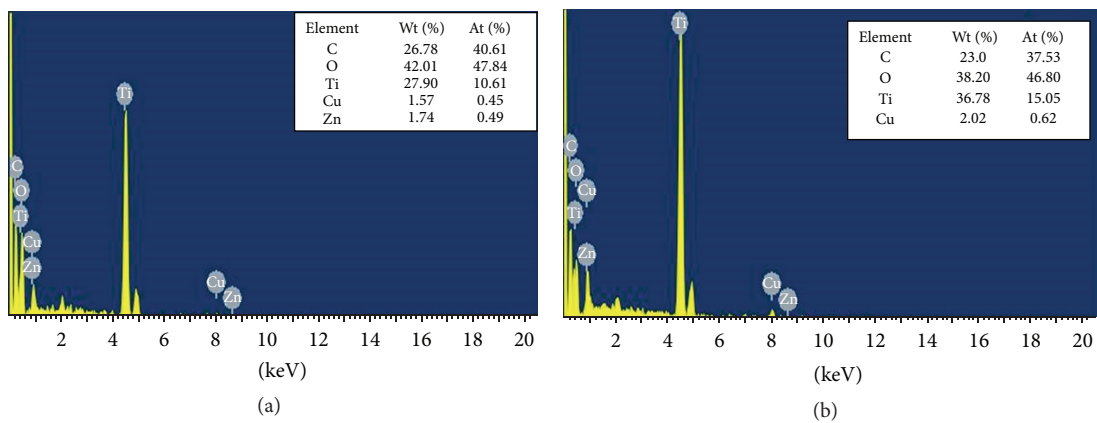


FIGURE 10: EDX analysis of pure titanium after WEDM.

9. EDX and XRD Analysis

The compositions of WEDM samples were detected through EDX. Figure 10 shows the energy dispersive X-ray (EDX) of affected surfaces, which are obtained by accelerating voltage of 3 kv. Through EDX technique, the residuals of copper and Zinc were also detected in the machined samples. This may be due to the melting, evaporation, and resolidification of the brass wire electrode and may result they were transferred to the work material. The presence of oxygen in the titanium probably was due to oxidation as a result of high temperature involved in the process. Although EDX result showed that carbon and oxygen also existed in the titanium, these elements were observed due to the fact that dielectric fluid with debris normally contains carbon and oxygen. Further, the XRD pattern analysis confirms the migration of tool elements (anode), and dielectric fluid elements were migrated to the work surface, and they formed different compounds like titanium dioxide (rutile) (TiO_2), ($\text{TiO}_{0.325}$), Ti_2O_3 , Ilmenite ($\text{Fe}_2\text{Ti}_4\text{O}$), and copper titanium dioxide (Cu_3TiO_4). The phases were identified in the form of peaks at 2θ scale. The plots of identified phases were shown in Table 6 and Figure 11.

10. Multiresponse Optimization Based on Desirability

Optimum selection of process parameters combinations is needed for obtaining higher MRR as well as minimum overcut and surface roughness. This is obtained by applying the multiresponse optimization through desirability function. The desirability approach is one of the useful approaches to optimize the multiple responses. This approach includes the concept of desirability functions. The general approach is to first convert each response (y_i) into an individual desirability function (d_i) and varied over the range $0 \leq d_i \leq 1$. Where if the response y_i is at its goal or target, then $d_i = 1$. The response is outside an acceptable region ($d_i = 0$). The weight of the desirability function for each response defines its shape. For each response, weights are assigned (r_i) to emphasize or de-emphasize the target. Finally, the individual desirability functions are combined to provide a measure of the overall desirability of the multiresponse system. This measure of composite desirability is the weighted geometric mean of the individual desirability for the responses. The optimal operating conditions are determined by maximizing the composite desirability [31]. Composite desirability is the weighted geometric mean of the individual desirabilities for the responses. The factor settings with maximum total desirability are considered to be the optimal parameter conditions. The simultaneous objective function is a geometric mean of all transformed responses. The optimization is accomplished by the following:

- (i) obtaining the individual desirability (d) for each response;
- (ii) combining the individual desirabilities to obtain the combined or composite desirability (D);
- (iii) maximizing the composite desirability and identifying the optimal input variable settings.

If it is desirable to maximize a response, the individual desirability is calculated as

$$d_i = \begin{cases} 0, & y_i < L_i, \\ \left(\frac{y_i - L_i}{T_i - L_i} \right)^w, & L_i \leq y_i \leq T_i, \\ 1, & y_i > T_i. \end{cases} \quad (8)$$

If the target (T_i) is to minimize a response, the individual desirability is calculated as

$$d_i = \begin{cases} 1, & y_i < T_i, \\ \left(\frac{U_i - y_i}{U_i - T_i} \right)^w, & T_i \leq y_i \leq U_i, \\ 0, & y_i > U_i, \end{cases} \quad (9)$$

where L_i = lower limit value of response y_i and

$$U_i = \text{upper limit value of response } y_i. \quad (10)$$

If the object for the response is a target value, then individual desirability is calculated as

$$d_i = \begin{cases} \left[\frac{(y_i - L_i)}{(T_i - L_i)} \right]^w, & L_i \leq y_i \leq T_i, \\ \left[\frac{(U_i - y_i)}{(U_i - T_i)} \right]^w, & T_i \leq y_i \leq U_i, \\ d_i = 0, & \text{if } y_i < L_i, \\ d_i = 0, & \text{if } y_i > U_i. \end{cases} \quad (11)$$

The factor settings with maximum total desirability are considered to be the optimal parameter conditions. The simultaneous objective function is a geometric mean of all transformed responses:

$$D = (d_1 \times d_2 \times d_3 \times \dots \times d_n)^{1/n} = \left(\prod_{i=1}^n d_i \right)^{1/n}, \quad (12)$$

where n is the number of responses in the measure. If any of the responses or factors falls outside the desirability range, the overall function becomes zero. It can be extended to reflect the possible difference in the importance of different responses, where the weight w_i satisfies $0 < w_i < 1$ and

$$w_1 + w_2 + \dots + w_n = 1, \quad (13)$$

$$D = (d_1^{w_1} \times d_2^{w_2} \times \dots \times d_n^{w_n})^{1/n}. \quad (14)$$

Desirability is an objective function that ranges from zero outside of the limits to one at the goal. The numerical optimization finds a point that maximizes the desirability

TABLE 6: XRD plot of identified phases.

Ref. code	Compound name	Crystal system	Displacement [$^{\circ}$ 2 θ .]	Chemical formula
01-073-1581	Titanium oxide	Hexagonal(225)	0.160	TiO _{0.325}
01-083-1284	Copper titanium oxide	Rhombohedra(167)	-0.391	Cu ₃ TiO ₄
00-010-0063	Titanium oxide	Cubic(227)	-0.270	Ti ₂ O ₃
01-075-0402	Ilmenite	Rhombohedral (148)	-0.668	Fe ₂ Ti ₄ O
01-085-0547	Zinc titanium oxide	Hexagonal(194)	0.000	ZnTiO ₃

TABLE 7: Constraints of input parameters and responses.

Parameters	Target	Lower limit	Upper limit	Lower weight	Upper weight	Importance
Pulse on time		0.7	1.1	1	1	3
Pulse off time		17	38	1	1	3
Peak current		120	200	1	1	3
Spark gap voltage		40	60	1	1	3
Wire feed		4	10	1	1	3
Wire tension		500	1400	1	1	3
MRR (mm ³ /min)	Maximize	3.28	11.16	1	1	3
Overcut (μ m)	Minimum	22	43	1	1	3
Surface roughness (μ m)	Minimum	2.15	3.28	1	1	3

function. The characteristics of a goal may be altered by adjusting the weight or importance. For several responses and factors, all goals get combined into one desirability function. For simultaneous optimization each response must have a low and high value assigned to each goal. The "Goal" field for responses must be one of five choices: "none," "maximum," "minimum," "target," or "in range." In the present investigation, the response parameters MRR, overcut, and surface roughness are chosen to maximize the overall desirability. The d_i for "in range" is included in the product of the desirability function " D " but is not counted in determining " n ": $D = (\prod d_i)^{1/n}$. Table 7 shows the constraints of input parameters and of responses and the goal and weights assigned to each parameter. Table 8 shows the values of 25 levels combinations of process parameters that will give high value of composite desirability (ranged from 0.603 to 0.527), and the values of predicted responses obtained are also given. The values of composite desirability for 54 performed experimental runs are also shown in Table 8. The value of composite desirability (D) was taken as 0.603. Table 9 gives the optimal input process parametric setting for multiresponse optimization. The current optimal process parameter settings are pulse on time of 1.1 μ s, pulse off time of 38 μ s, peak current of 128 A, spark gap voltage of 50 V, wire feed of 4 m/min, and wire tension of 1350 grams. To show the sensitivity of the results, contour plots for overall desirability and optimized histograms of the three responses MRR, overcut, and surface roughness are shown in Figures 12(a) and 12(b). The near-optimal region was located close to the right hand center region of the plot, which had a composite desirability value greater than 0.603 that gradually reduced as we moved left and upwards.

11. Confirmation Experiment

The confirmatory experiments were performed to verify the optimal input parametric setting for MRR, overcut, and surface roughness and were compared with optimal response values. The observed MRR, overcut, and surface roughness of the experimental results are 8.20 mm³/min, 31.17 μ m, and 2.43 μ m, respectively. Table 10 shows the error percentage for experimental validation of the developed models for the responses with optimal parametric setting. From the analysis it was concluded that the error between experimental and predicted values for MRR, overcut, and surface roughness lies within 6.95%, 6.32%, and 7.25%, respectively. Obviously, this confirms excellent reproducibility of the experimental conclusions.

12. Conclusions

In the present study, experimental investigation on material transfer mechanism in WEDM of pure titanium (grade 2) was done. Pulse on time, pulse off time, peak current, spark gap voltage, wire feed, and wire tension parameters were used to carry out the experimental study. The following conclusions were drawn.

- (1) The residuals of copper, carbon, and zinc were detected in the machined samples using EDX technique. This may be due to the melting, evaporation, and resolidification of the brass wire electrode and are transferred to the work material. XRD pattern analysis confirmed the migration of tool material and dielectric fluid elements on the work surface. The compounds like titanium dioxide (rutile) (TiO₂),

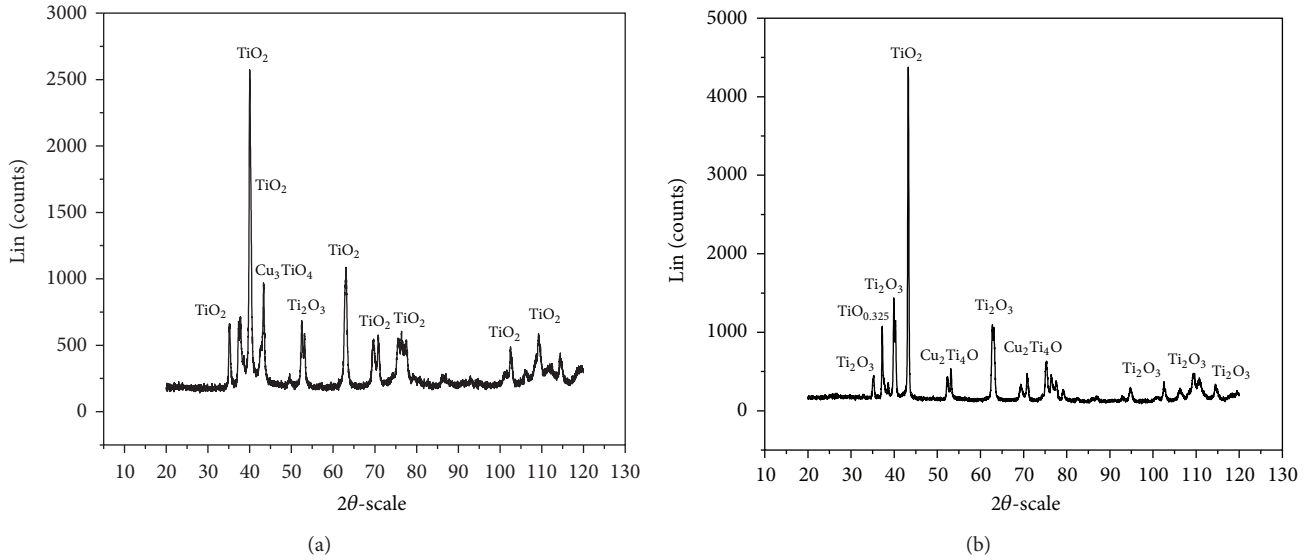


FIGURE 11: XRD pattern of the machined surface: (a) $T_{on} = 1.1 \mu s, T_{off} = 28 \mu s, I_p = 200 A, SV = 50 V, WF = 7 m/min, WT = 500$ grams; (b) $T_{on} = 0.7 \mu s, T_{off} = 28 \mu s, I_p = 120 A, SV = 50 V, WF = 7 m/min, WT = 500$ grams.

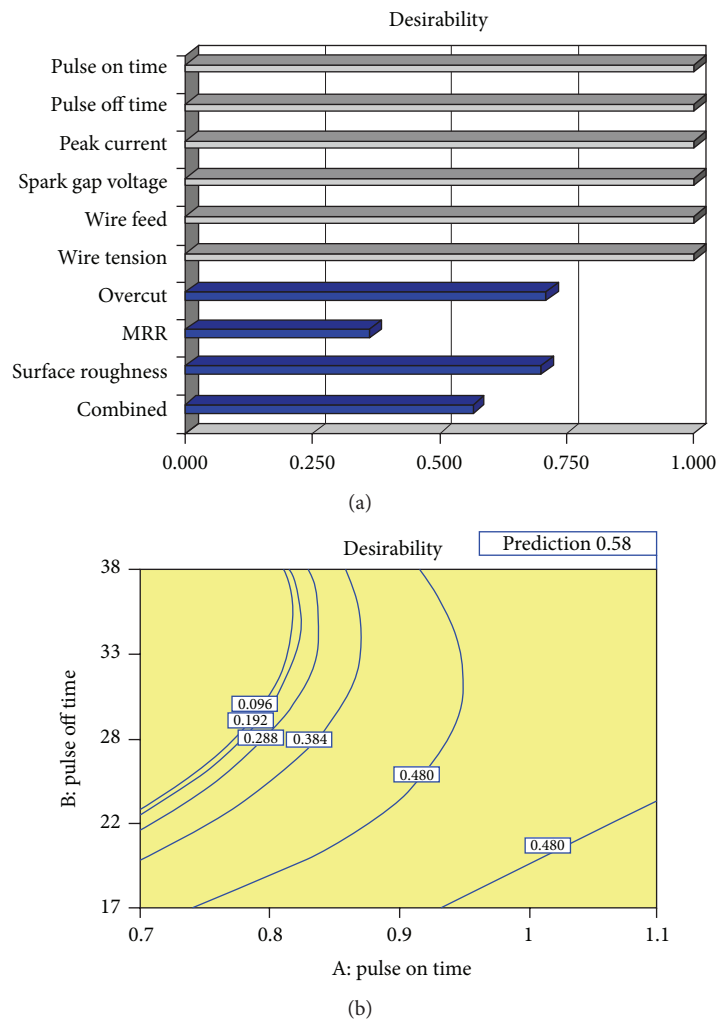


FIGURE 12: (a) Bar histograms and (b) contour plot for results of overall desirability functions (at $T_{on} = 1.1 \mu s, T_{off} = 38 \mu s, I_p = 165 A, SV = 40 V, WF = 4 m/min, WT = 1400$ grams).

TABLE 8: Process parameters combinations for high value of desirability.

Exp. no.	Factors						Predicted responses			Desirability
	T_{on} (μs)	T_{off} (μs)	I_p (Ampere)	SV (Volt)	WF (m/min)	WT (grams)	MRR (mm^3/min)	Overcut (μm)	Surface roughness (μm)	
1	1.1	38	165	40	4	1400	7.63	29.20	2.43	0.603
2	1.0	38	160	40	4	500	7.46	28.82	2.40	0.599
3	1.1	38	151	43	4	500	7.14	28.11	2.44	0.589
4	1.0	38	166	46	4	500	7.53	29.80	2.40	0.583
5	1.1	33	173	40	4	500	7.98	31.21	2.49	0.579
6	1.1	30	154	40	10	1394	7.79	30.79	2.53	0.577
7	1.1	38	144	40	5	1398	7.00	28.15	2.47	0.577
8	1.1	26	151	40	10	500	8.47	32.40	2.47	0.577
9	1.1	31	157	40	10	1393	7.79	30.81	2.39	0.576
10	1.0	21	130	40	4	1400	9.19	33.79	2.47	0.574
11	1.0	23	145	40	10	1400	8.87	33.28	2.37	0.573
12	1.1	24	146	40	10	500	8.84	33.23	2.41	0.573
13	0.9	21	154	40	4	1400	8.38	32.37	2.45	0.573
14	1.1	26	137	40	10	500	8.16	31.95	2.51	0.571
15	1.0	28	154	40	9	505	8.08	31.89	2.44	0.568
16	1.1	38	138	43	10	1400	6.78	27.87	2.43	0.566
17	0.9	18	149	40	4	1400	8.69	33.27	2.48	0.564
18	1.1	25	138	40	9	1400	8.41	32.76	2.45	0.563
19	0.9	17	162	40	4	1400	8.84	33.74	2.45	0.558
20	0.9	17	152	40	4	500	8.96	34.01	2.43	0.555
21	1.1	38	148	41	4	788	7.07	29.65	2.43	0.553
22	1.1	26	142	48	4	1400	7.64	31.45	2.49	0.552
23	1.0	38	156	48	4	1100	7.20	30.55	2.43	0.543
24	1.0	22	148	40	7	500	8.55	30.97	2.53	0.536
25	1.0	38	176	58	10	500	6.94	30.45	2.47	0.527

TABLE 9: Multioptimal parametric settings for MRR, overcut, and surface roughness.

Parameters	Units	Optimal parameter settings
Pulse on time	μs	1.1
Pulse off time	μs	38
Peak current	Ampere	128
Spark gap voltage	Volt	50
Wire feed	m/min	4
Wire tension	Grams	1350

($TiO_{0.325}$), Ti_2O_3 , Ilmenite (Fe_2Ti_4O), and copper titanium dioxide (Cu_3TiO_4) were formed.

- (2) Wire rupturing and wire wear rate were observed due to high peak current and more spark frequency. The formation of craters and the residuals of debris adhered to the surface of wire electrode. The cracks

were observed due to high pulse on time and peak current. The crack density was increased due to rapid cooling and heating in the spark zone.

- (3) This recast layer was developed due to high peak current. Also the minor cracks were observed that is may be due to high pulse on time and high peak current.
- (4) Pulse on time, peak current, and pulse off time were found to be the most significant factors affecting material removal rate. The wire feed and wire tension were found to be insignificant.
- (5) The overcut was found to vary from $26.85 \mu m$ to $34.07 \mu m$. Meanwhile, the interaction between pulse off time and peak current showed the most significant effect on overcut. The overcut was observed during the decrease of spark gap voltage with value of $25.07 \mu m$ to $35.87 \mu m$.

TABLE 10: Experimental validations of developed models with optimal parameter settings.

Responses	Predicted	Experimental	Error (%)	Desirability
MRR (mm ³ /min)	7.63	8.20	6.95	0.588
Overcut (μm)	29.20	31.17	6.32	0.573
Surface roughness (μm)	2.43	2.62	7.25	0.562

(6) The surface roughness varies between 2.48 μm and 2.62 μm . The surface roughness was mainly affected by interaction between pulse on time and peak current which ranged between 2.41 and 2.72 μm .

(7) It was observed that pulse on time and peak current deteriorate the integrity of machined samples which produces the deeper and wider overlapping craters, pockmarks, globules of debris, and microcracks.

References

- [1] S. Y. Hong, I. Markus, and W.-C. Jeong, "New cooling approach and tool life improvement in cryogenic machining of titanium alloy Ti-6Al-4V," *International Journal of Machine Tools and Manufacture*, vol. 41, no. 15, pp. 2245–2260, 2001.
- [2] A. B. Puri and B. Bhattacharyya, "An analysis and optimisation of the geometrical inaccuracy due to wire lag phenomenon in WEDM," *International Journal of Machine Tools and Manufacture*, vol. 43, no. 2, pp. 151–159, 2003.
- [3] K. H. Ho, S. T. Newman, S. Rahimifard, and R. D. Allen, "State of the art in wire electrical discharge machining (WEDM)," *International Journal of Machine Tools and Manufacture*, vol. 44, no. 12-13, pp. 1247–1259, 2004.
- [4] E. O. Ezugwu and Z. M. Wang, "Titanium alloys and their machinability—a review," *Journal of Materials Processing Technology*, vol. 68, no. 3, pp. 262–274, 1997.
- [5] S. F. Miller, A. J. Shih, and J. Qu, "Investigation of the spark cycle on material removal rate in wire electrical discharge machining of advanced materials," *International Journal of Machine Tools and Manufacture*, vol. 44, no. 4, pp. 391–400, 2004.
- [6] J. T. Huang and Y. S. Liao, "Optimization of machining parameters of Wire-EDM based on Grey relational and statistical analyses," *International Journal of Production Research*, vol. 41, no. 8, pp. 1707–1720, 2003.
- [7] M. S. Hewidy, T. A. El-Taweel, and M. F. El-Safty, "Modelling the machining parameters of wire electrical discharge machining of Inconel 601 using RSM," *Journal of Materials Processing Technology*, vol. 169, no. 2, pp. 328–336, 2005.
- [8] S. S. Mahapatra and A. Patnaik, "Optimization of wire electrical discharge machining (WEDM) process parameters using Taguchi method," *International Journal of Advanced Manufacturing Technology*, vol. 34, no. 9-10, pp. 911–925, 2007.
- [9] R. Ramakrishnan and L. Karunamoorthy, "Multi response optimization of wire EDM operations using robust design of experiments," *International Journal of Advanced Manufacturing Technology*, vol. 29, no. 1-2, pp. 105–112, 2006.
- [10] A. Manna and B. Bhattacharyya, "Taguchi and Gauss elimination method: a dual response approach for parametric optimization of CNC wire cut EDM of PRAISiCMMC," *International Journal of Advanced Manufacturing Technology*, vol. 28, no. 1-2, pp. 67–75, 2006.
- [11] S. Sarkar, S. Mitra, and B. Bhattacharyya, "Parametric optimisation of wire electrical discharge machining of γ titanium aluminide alloy through an artificial neural network model," *International Journal of Advanced Manufacturing Technology*, vol. 27, no. 5-6, pp. 501–508, 2006.
- [12] S. Sarkar, K. Ghosh, S. Mitra, and B. Bhattacharyya, "An integrated approach to optimization of WEDM combining single-pass and multipass cutting operation," *Materials and Manufacturing Processes*, vol. 25, no. 8, pp. 799–807, 2010.
- [13] R. T. Yang, C. J. Tzeng, Y. K. Yang, and M. H. Hsieh, "Optimization of wire electrical discharge machining process parameters for cutting tungsten," *International Journal of Advanced Manufacturing Technology*, vol. 60, no. 1–4, pp. 135–147, 2012.
- [14] A. Kumar, V. Kumar, and J. Kumar, "An investigation into machining characteristics of commercially pure titanium (Grade-2) using CNC WEDM," *Applied Mechanics and Materials*, vol. 159, pp. 56–68, 2012.
- [15] A. Shah, N. A. Mufti, D. Rakwal, and E. Bamberg, "Material removal rate, kerf, and surface roughness of tungsten carbide machined with wire electrical discharge machining," *Journal of Materials Engineering and Performance*, vol. 20, no. 1, pp. 71–76, 2011.
- [16] M. Sadeghi, H. Razavi, A. Esmailzadeh, and F. Kolahan, "Optimization of cutting conditions in WEDM process using regression modelling and Tabu-search algorithm," *Proceedings of the Institution of Mechanical Engineers B*, vol. 225, no. 10, pp. 1825–1834, 2011.
- [17] K.-Y. Kung and K.-T. Chiang, "Modeling and analysis of machinability evaluation in the wire electrical discharge machining (WEDM) process of aluminum oxide-based ceramic," *Materials and Manufacturing Processes*, vol. 23, no. 3, pp. 241–250, 2008.
- [18] C.-J. Tzeng, Y.-K. Yang, M.-H. Hsieh, and M.-C. Jeng, "Optimization of wire electrical discharge machining of pure tungsten using neural network and response surface methodology," *Proceedings of the Institution of Mechanical Engineers B*, vol. 225, no. 6, pp. 841–852, 2011.
- [19] R. V. Rao and P. J. Pawar, "Modelling and optimization of process parameters of wire electrical discharge machining," *Proceedings of the Institution of Mechanical Engineers B*, vol. 223, no. 11, pp. 1431–1440, 2009.
- [20] P.-H. Yu, H.-K. Lee, Y.-X. Lin, S.-J. Qin, B.-H. Yan, and F.-Y. Huang, "Machining characteristics of polycrystalline silicon by wire electrical discharge machining," *Materials and Manufacturing Processes*, vol. 26, no. 12, pp. 1443–1450, 2011.
- [21] N. Kuruvila and H. V. Ravindra, "Parametric influence and optimization of wire edm of hot die steel," *Machining Science and Technology*, vol. 15, no. 1, pp. 47–75, 2011.
- [22] S. H. Lee and X. Li, "Study of the surface integrity of the machined workpiece in the EDM of tungsten carbide," *Journal of Materials Processing Technology*, vol. 139, no. 1–3, pp. 315–321, 2003.
- [23] Y.-C. Lin, Y.-F. Chen, C.-T. Lin, and H.-J. Tzeng, "Electrical Discharge Machining (EDM) characteristics associated with

- electrical discharge energy on machining of cemented tungsten carbide,” *Materials and Manufacturing Processes*, vol. 23, no. 4, pp. 391–399, 2008.
- [24] K. P. Somashekhar, N. Ramachandran, and J. Mathew, “Material removal characteristics of microslot (kerf) geometry in μ -WEDM on aluminum,” *International Journal of Advanced Manufacturing Technology*, vol. 51, no. 5–8, pp. 611–626, 2010.
- [25] Y.-C. Lin, C.-H. Cheng, B.-L. Su, and L.-R. Hwang, “Machining characteristics and optimization of machining parameters of SKH 57 high-speed steel using electrical-discharge machining based on Taguchi method,” *Materials and Manufacturing Processes*, vol. 21, no. 8, pp. 922–929, 2006.
- [26] S. H. Lee and X. Li, “Study of the surface integrity of the machined workpiece in the EDM of tungstencarbide,” *Journal of Materials Processing Technology*, vol. 139, no. 1–3, pp. 315–321, 2003.
- [27] A. Kumar, S. Maheshwari, C. Sharma, and N. Beri, “Research developments in additives mixed electrical discharge machining (AEDM): a state of art review,” *Materials and Manufacturing Processes*, vol. 25, no. 10, pp. 1166–1180, 2010.
- [28] H. T. Lee and T. Y. Tai, “Relationship between EDM parameters and surface crack formation,” *Journal of Materials Processing Technology*, vol. 142, no. 3, pp. 676–683, 2003.
- [29] A. Hasçalik and U. Çaydaş, “Electrical discharge machining of titanium alloy (Ti-6Al-4V),” *Applied Surface Science*, vol. 253, no. 22, pp. 9007–9016, 2007.
- [30] N. G. Patil and P. K. Brahmkar, “Some studies into wire electro-discharge machining of alumina particulate-reinforced aluminum matrix composites,” *International Journal of Advanced Manufacturing Technology*, vol. 48, no. 5–8, pp. 537–555, 2010.
- [31] D. C. Montgomery, *Design and Analysis of Experiments*, Wiley, New York, NY, USA, 5th edition, 2001.

Research Article

Numerical Analysis of Hot Cracking in Laser-Hybrid Welded Tubes

Moritz Oliver Gebhardt,¹ Andrey Gumenyuk,² and Michael Rethmeier²

¹ *Linkage & Suspension, TRW Automotive GmbH, LEF, Hansaallee 190, 40547 Düsseldorf, Germany*

² *Division 9.3 Welding Technology, BAM Federal Institute for Materials Research and Testing, Unter den Eichen 87, 12205 Berlin, Germany*

Correspondence should be addressed to Andrey Gumenyuk; andrey.gumenyuk@bam.de

Received 30 August 2013; Accepted 18 November 2013

Academic Editor: Martha Guerrero

Copyright © 2013 Moritz Oliver Gebhardt et al. This is an open access article distributed under the Creative Commons Attribution License, which permits unrestricted use, distribution, and reproduction in any medium, provided the original work is properly cited.

In welding experiments conducted on heavy wall pipes, the penetration mode (full or partial penetration) occurred to be a significant factor influencing appearance of solidification cracks. To explain the observed phenomena and support further optimization of manufacturing processes, a computational model was developed, which used a sophisticated strategy to model the material. High stresses emerged in the models in regions which showed cracking during experiments. In partial penetration welding, they were caused by the prevention of weld shrinkage due to the cold and strong material below the joint. Another identified factor having an influence on high stress localization is bulging of the weld.

1. Introduction

Substitution of chipping for a welding process may help to save time and material, especially when high wall thicknesses need to be processed and/or high precision is demanded; as for example, in the production of hydraulics, a beam welding process is beneficial (see [1, 2] for details). A problem hindering intense industrial use is the occurrence of weld hot cracking, when the thickness of the weld exceeds 10 mm [3].

Welding trials conducted at BAM, using tubes with a wall thickness of 14.5 mm and a comparatively low outer diameter of 136.6 mm made from low-alloyed fine grain structural steel S460NH, revealed that cracking is closely connected to the penetration mode (full or partial) [2, 4]. Full penetration welds did not show any conspicuous features, as long as tack welds were omitted, but solidification cracks were detected in most welds using partial penetration. Cracks were either found at the lower end of the weld cross sections (from now on called the root) or in the middle of the weld, where a localized rise of the weld seam width (bulging) existed.

The report at hand tries to give an answer to (1) why partial penetration welds are more prone to hot cracking than full penetration welds and (2) which role the bulging plays in the content. A numerical model, using a sophisticated material modeling strategy, was employed to achieve this goal.

Solidification cracks emerge in the last stages of solidification when liquid is still present around the growing dendritic network. There is a stage between the start and end of solidification, where the material, even though ductile, shows brittle behavior [5]. The end of solidification in this content is the temperature where really all of the material is solidified which may be well below the point in time, when the body shows solid behavior macroscopically. Consequently low melting phases, like Fe-S (isothermal eutectic solidus temperature of 988°C [6]) play an important role in the content.

Important impact factors are the mechanical conditions encountered in the region under solidification, either via applied boundary conditions [7–10] or by the material itself.

In particular when welding high strength steel, the developing stresses can be high [9]. Their sway on the hot crack prone region needs close observation.

The reason for hot crack occurrence is not conclusively known [6]. Experimental evaluation at temperatures close to the solidus temperature is difficult and hence “an educated guess frequently replaces experimental proof” [11]. A common belief is that hot cracking is caused when the strains in the mushy zone [5, 12, 13] or the macroscopic outward movement of its edges [14, 15] exceeds a material dependent threshold value. Others linked crack nucleation to a pressure drop in the mushy interval [16–18]. Shibahara and coworkers [19–23] successfully used methods from structural fracture mechanics, which included evaluation of a bonding stress for the purpose of crack initiation and evolution. The influence of the triaxiality of the stress state is hardly taken into account in the discussion. But it was already remarked by Borland and Younger [24] in 1960 that the triaxiality may cause high stresses in the vulnerable zone, even though it is considerably soft.

When trying to understand the impact of mechanical and thermal boundary conditions on weld hot cracking, the mechanical reactions inside the vulnerable zone are of interest. Consequently, close attention must be taken when choosing material properties, particularly above 1000°C, including the liquid-solid transition and the liquid region. The purpose of the last point is not to simulate transport phenomena but to produce, at least qualitatively, a reasonable mechanical answer.

Steel melt is a liquid of the Newton type [25] with a viscosity comparable to water. Accordingly, three main features have to be modeled. The first one is a very low resistance against distortion. The second one is a considerable resistance against compression and expansion. When melting and solidification of a material are necessary to be evaluated, the third feature to model is a harsh drop in viscosity upon melting and a strong rise in viscosity during solidification.

2. Finite Element Model

2.1. Boundary Conditions. A rotational symmetry model was employed to allow usage of a fine mesh at a feasible computation time. Hence the computational domain was a cross section of the weld. Two models were built up. One model represented a partial penetration weld; the other one simulated a full penetration one. Both models used the same mesh made from parabolic quadrilaterals, with a maximum edge size of 0.11 mm at the weld symmetry line. The excess filler material of the full penetration model was deleted in the partial penetration one. The root in the full penetration model was constituted out of deformed weld metal.

Contact elements attached to the nodes at the symmetry line allowed retreat of the nodes from the symmetry line but prohibited its penetration. Nodes heated above solidus were bound to the symmetry to simulate the joining process. On the side of the tube far away the joint, spring elements represented the stiffness of the surrounding construction.

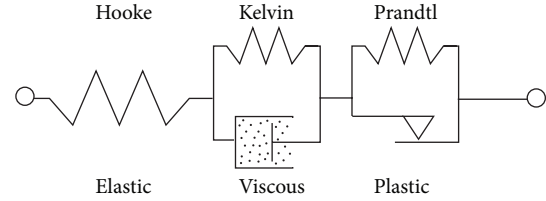


FIGURE 1: Simplified sketch for a material model ranging from ambient temperature up to the melt.

The welding heat was input using four double ellipsoidal shaped power density distributions. Heat transport across the free boundaries was neglected due to the high relation of volume versus surface of the tubes. A convection boundary condition at the clamping side of the model represented its heat sink.

The filler material was brought into the model using a dead/alive technology. It was revived, when the arc center crossed the computational plane.

2.2. Material Model. The material in the experiments was the low-alloyed high strength fine grain steel S460NH. It had an elastic limit $R_{p0.2}$ of 455 MPa and a tensile strength R_m of 625 MPa. While the thermophysical part of the applied material model was very much straight forward, the thermo-mechanical part of the model can be displayed as a sequential Hooke-Kelvin-Prandtl model (Figure 1). A limitation is that the picture is only valid for a one-dimensional test, without revolution of the force direction. As all three parts were arranged sequentially, it was always the softest part that defined the stress/strain state of the whole pattern. The Hooke part, on the left-hand side in Figure 1, was active for small strains, independent of the temperature. The Prandtl part represents the plastic part of the material model and was active for temperatures below 900°C only. A Kelvin model, symbolized by a damper parallel to a spring, stands for the viscoplastic part, which was active for temperatures >900°C only.

2.2.1. Material Properties Origin. The thermophysical material properties for the whole temperature range and the thermomechanical material properties for temperatures up to 900°C were taken from the SYSWELD material database [26] and were also published in [27]. The sources provide material properties for the solid phases ferrite, austenite, and martensite. Their values were originally designed to simulate S355J2G3. But despite the nominal difference in the yield strength of more than 100 MPa, the ferrite σ - ϵ -curve at 20°C fitted nearly perfectly the in-house measured curve of the tube material. The thermophysical and linear mechanical properties are within a narrow band for low-alloyed steels anyway [28, 29]. For this reason, the ferrite properties from the source were taken as base material values. The thermal strain data was provided by an author of [30] and originally measured at S690QL using heating and cooling rates typical for beam welding. Extra thermal strains during melting and solidification were also included.

TABLE 1: Parameters of the viscoplastic model used (see [31]).

	20°C	900°C-1440°C	1500°C
C_1	4.37×10^{-2}	$C^{(1/m+1)}$	8.83×10^1
C_2	8.92	$n/(m+1)$	1.10
C_3	-1.93	$m/(m+1)$	-5.85×10^{-2}
C_4	1.26×10^5	$Q/(m+1)$	1×10^{-4}

* C, n, m, Q from Kozlowski's fit.

2.2.2. Solid State Phase Transformation. In the beam welding processes modeled, the cooling rates are high and the resulting $t_{8/5}$ -times could readily be 1 s [10]. As a result, all the welded and heat affected material considered transform to martensite [30]. In this case a simple phase transformation model was applicable. The material of all elements which were heated above A_{C3} was exchanged when they started to cool down to a material that used martensitic material properties (σ - ϵ -curve, $E, \nu, \rho, \lambda,$ and h) below the martensite finish (M_F) temperature and austenitic properties above. To further enhance the model, a third material was included which was assigned to elements which had a peak temperature between A_{C1} and A_{C3} . It was composed of 50% each out of base material and martensite properties below M_F and of 50% each out of base material and austenite properties above M_F .

2.2.3. High-Temperature Region. The (austenite) σ - ϵ -curve from 900°C was retained for temperatures above. The Kelvin model from Figure 1 symbolizes a viscoplastic strain hardening model fitted by Kozlowski et al. [31] to measurements from Wray [32] and Suzuki et al. [33] on low-alloyed steels:

$$\dot{\epsilon} = C_1 \cdot \sigma^{C_2} \cdot \epsilon^{C_3} \exp\left(\frac{-C_4}{T}\right). \quad (1)$$

The constants C_1 to C_4 are given in Table 1. $C, m, n,$ and Q have to be taken from [31] and were evaluated for the presented model at a C -content of 0.2 wt.-%. For temperatures below 900°C, the value of C_4 was linearly increased at 20°C to 3.5 its value at 900°C. This allowed a smooth transition of the two models.

2.2.4. Molten State. From the solidus temperature up to the liquidus temperature, the material becomes a Newtonian fluid; that is, stresses based on deviatoric loads are solely dependent on the strain rate, and the stress versus strain rate curve crosses the origin. At the same time, the viscosity drops by several orders of magnitude, and distortions meet only little resistance. In contrast to the viscosity, the bulk modulus remains nearly constant at the solid-liquid transition [34] and the material keeps its resistivity against hydrostatic loads. When C_2 is set to zero and C_3 is set to one, the Kelvin model collapses to a Maxwell model [25, 35, 36] (a damper serial to a spring):

$$\sigma_{ij} = -p\delta_{ij} + 2\eta\epsilon_{ij}. \quad (2)$$

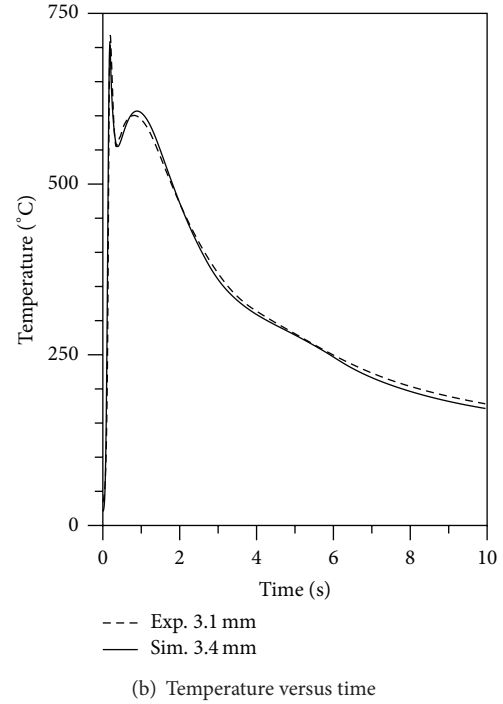
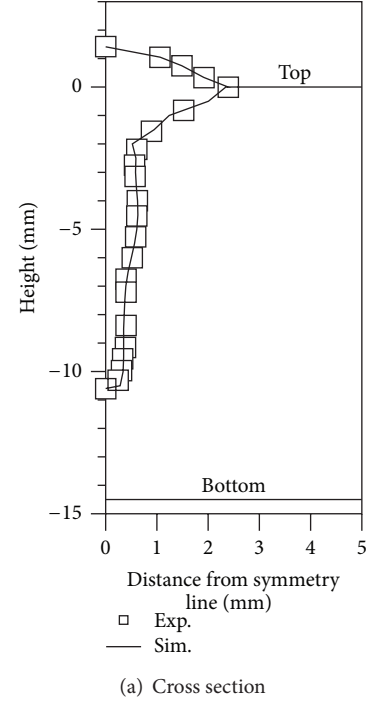


FIGURE 2: Comparison of the temperature field between experiments and the computational model for partial penetration.

The model can then be used to simulate a Newtonian fluid, with a viscosity of

$$\eta = \eta(T) = \frac{1}{C_1} \cdot \exp\left(\frac{C_4}{T}\right). \quad (3)$$

By a strong reduction of C_4 , the temperature dependence of the viscosity vanishes and is only controlled by C_1 . In trying to

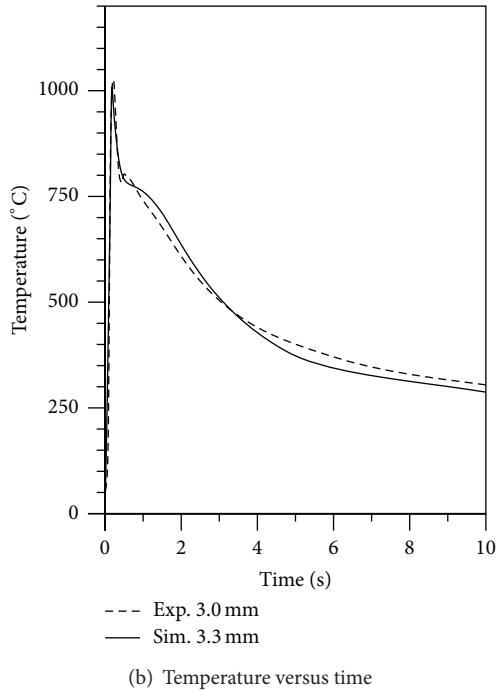
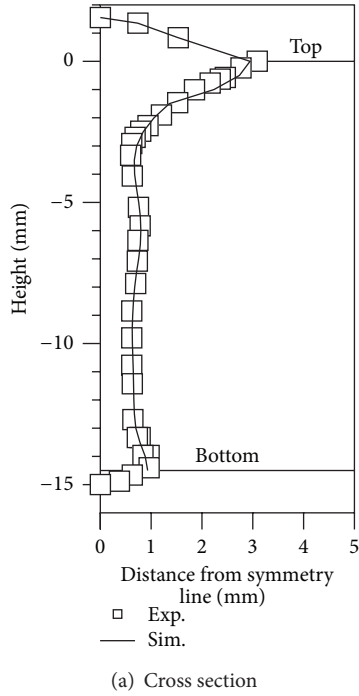


FIGURE 3: Comparison of the temperature field between experiments and the computational model for full penetration.

adjust C_1 , C_2 , C_3 , and C_4 to values as explained above while maintaining converged solutions, the parameters in Table 1 were determined.

2.3. Thermophysical Model Part Quality. The thermo-physical part of the numeric model was a load to the thermo-mechanical model, and so its quality is vital for the mechanic results. Figure 2 compares the computed

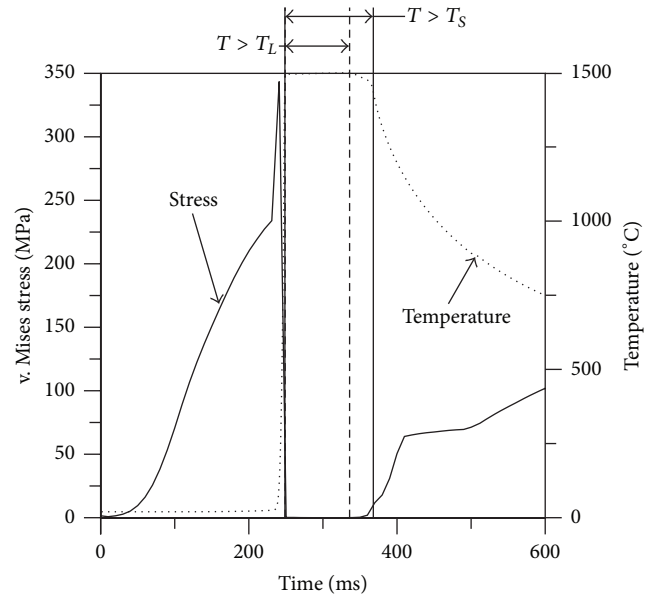


FIGURE 4: v. Mises stress and temperature of a node from the middle of the weld pool. In the figure, T_L stands for the liquidus temperature, while T_S denominates the solidus temperature.

temperature field in the partial penetration model against experimentally acquired values.

The left-hand side, Figure 2(a), makes a comparison between the maximum of the 1500°C isothermal and the experimental cross section. In Figure 2(b), the temperatures at the outer diameter in distance of 3.1 mm from the symmetry line are compared with experimental temperature measurements using thermocouples type K (Ni-CrNi) at the outer diameter in a distance of 3.4 mm from the symmetry line. The difference between the cross section areas was 0.37%, and the differences in the peak temperatures were 1.99%, 1.05%, and 1.05% for the global maximum and the smaller local maximum and minimum, respectively.

Figure 3 shows equal values for full joint penetration. The cross section areas differed by 2.6%; the peak temperatures and the temperatures to which the temperature field converged at a time of 10 s had differences of 1.8% and 5.6% of the experimental values, respectively.

Both cross sections displayed bulging around approximately -7 mm.

2.4. Mechanical Reproduction of the Molten State. Figure 4 shows the temperature and the v. Mises stresses at a point in the middle of the weld in the partial penetration model. The v. Mises stresses showed a harsh drop when the solidus temperature was reached and a strong rise after passing the liquidus temperature during cooling. During the molten stage (i.e. $T > T_L$), the stresses were approximately zero.

3. Results

The transversal stresses in the partial penetration model 10 ms after the laser passed the computational surface are displayed

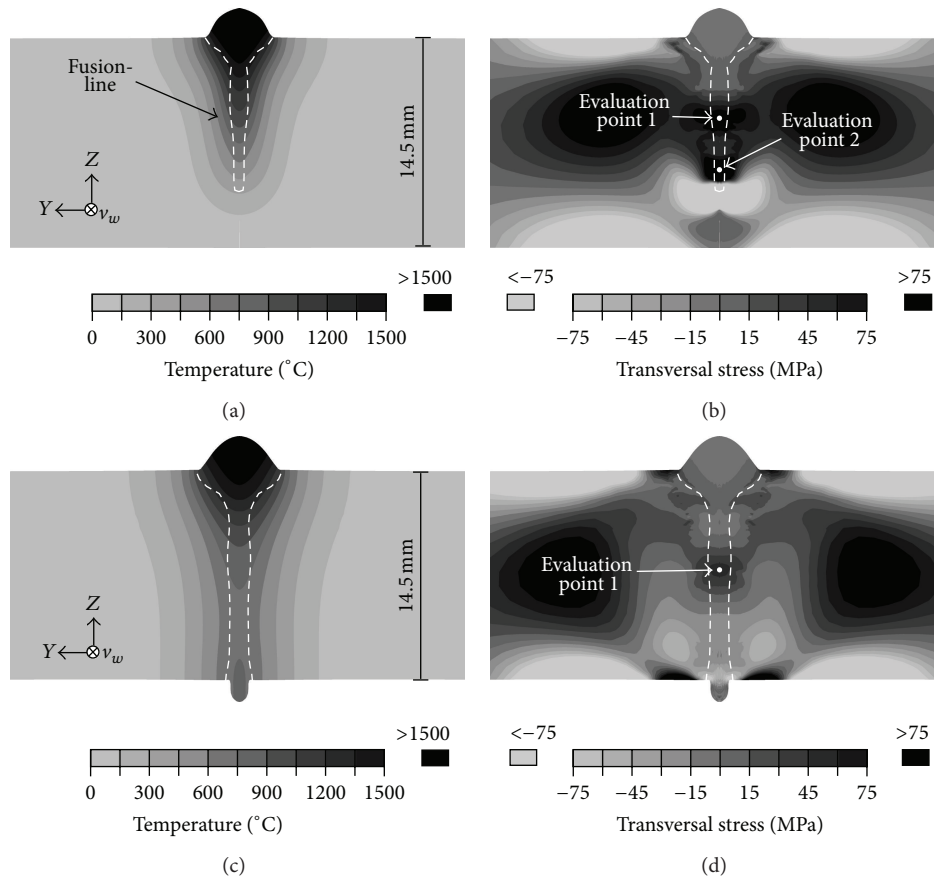


FIGURE 5: Temperature and v. Mises stresses in the computational model 10 ms after the laser beam center passed the computational domain. The figures show halves of cross sections reflected along the weld symmetry line.

in Figure 5(a). Two maxima, representing tensile stresses, could be found in the cross section. One was located in the bulging region and the other one in the root of the weld. This correlates with the spaces, in which cracks were found during experiments. Strong compressive stresses were visible in the region below the weld.

Obviously, the lower tensile maximum and the high levels of compressive stress below the weld were missing in the full penetration model (Figure 5(b)). But the maximum in the bulging region was retained, though, at a lower amplitude.

Figure 6 shows the evolution of the stresses during cooling in both models. The displayed values were taken from the respective evaluation points in Figure 5. Their orientation is given with respect to the welding direction.

The level of the computed stresses per se was striking. They easily overshoot 100 MPa, and the longitudinal stresses even reached 200 MPa. It is visible that the highest stresses were by far the stresses in the root of the partial penetration model. They were followed by the stresses in the bulging region. Despite a very short sequence in the vertical direction at about 1250 °C, the lowest stresses were found in the bulging region of the full penetration model. The stress levels in the bulging region of the two models differed widely when it came to lower temperatures, but they were of the same magnitude.

4. Interpretation

Due to the triaxiality of the stress state, the stresses can be high in the vulnerable zone, even though the material is soft. Since the hydrostatic part of the stress tensor is elastic, high levels of stress can exist, without the need for high strains. The existence of high stresses in the weld is in correlation with the compilation of Borland and Younger [24] and the works of Shibahara et al. [19–23].

The effect of the stresses can be pictured as follows. If rest of melt is trapped in the growing dendritic network, it will be subject to a negative pressure and may thus experience cavitation. Other than a liquid, the resulting gas can hardly sustain any stress and fails to support the dendrites, which become more vulnerable to applied loads.

The cold and strong material below the weld in partial penetration works like a local restraint and impedes weld shrinkage, causing the increased root side stress levels. If it is true that stresses cause crack emergence, then this is the root cause for the observed effect that partial penetration welds are more prone to solidification cracking than full penetration ones. This result corresponds to examinations by Quiroz et al. [9].

The bulging region is special as the molten pool has a local maximum in its width and as this region solidifies

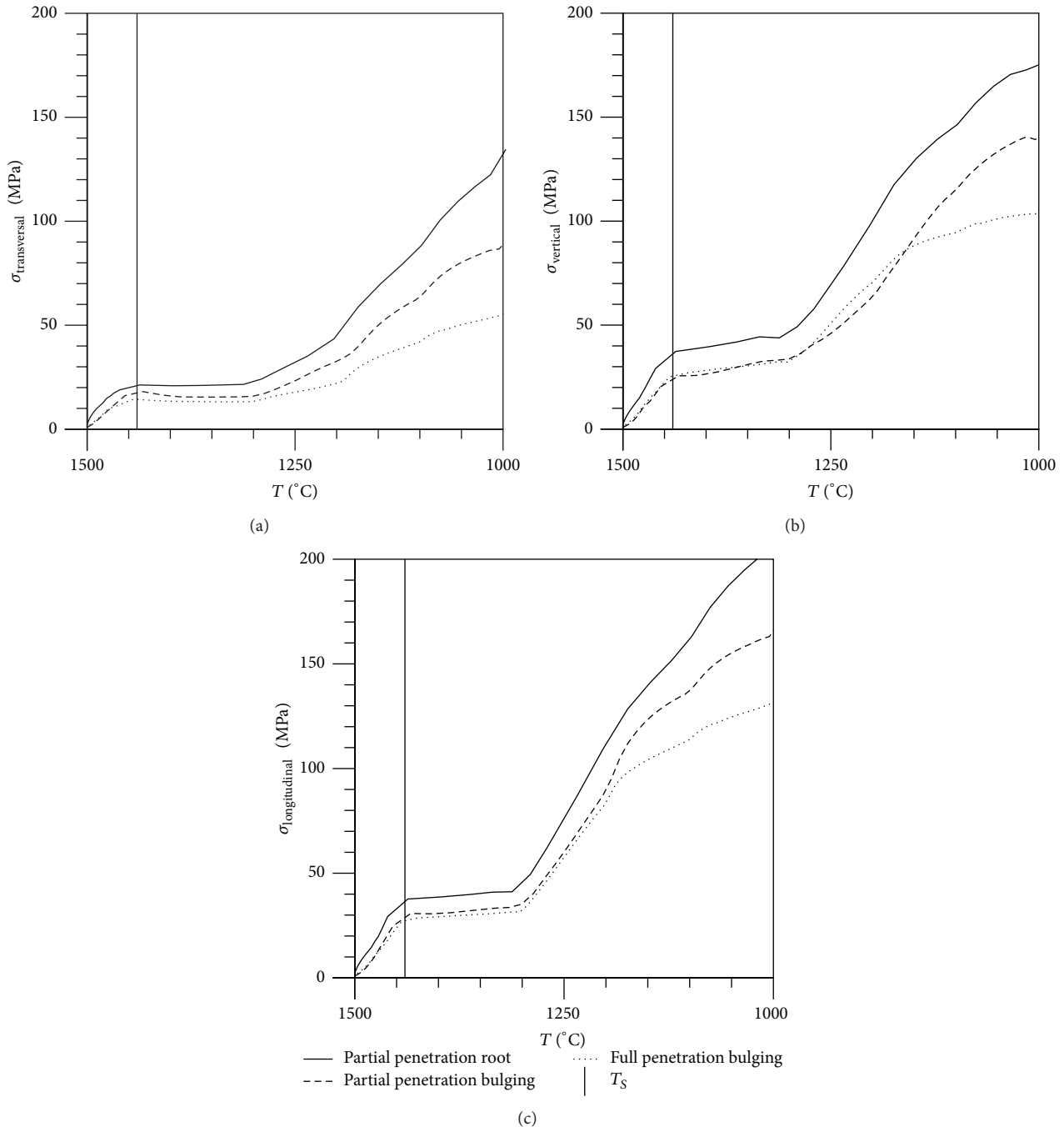


FIGURE 6: Stresses in the three spatial directions in both models. The figure gives values at the bulging region of both models and at the root of the partial penetration model.

after the parts of the weld above and below do. Weld hot cracks are regularly found in this zone. Both models displayed a maximum in the tensile stresses here. This is a strong indication that the correlation of hot cracks with bulging is not coincidental. The stresses are only caused by the interaction of the temperature field with the material. When the material in the weld solidifies, stresses caused by the thermal strains during solidification are relieved as long as connection to the melt is available. But when the bulging

region solidifies, the material around is already in the solid state and the whole amount of thermal strain adds to the stresses.

The stresses in the bulging region are higher in the partial penetration model, even though the bulging region and the height of the weld in the full penetration model are larger. The reason for this is most probably also found in the cold material below the weld. The material below the weld impedes the shrinkage, so the weld material is wider than it would

be without the extra boundary condition (hence the tensile stress). Consequently, tensile stresses are aggravated in a large part of the weld. Additionally, the stiffness of the cold material is bigger than that of warm weld material due to the temperature.

5. Conclusion and Outlook

Two models, representing partial and full penetration laser-GMA-hybrid welding experiments on thick-walled tubes, were built up to assess the mechanical reaction of the weld material at temperatures where solidification cracking happens. The reason was to understand why partial penetration welds were more prone to hot cracking than full penetration ones, during the experiments. A sophisticated material modeling strategy was developed, which used a viscoplastic model in the high temperature region and considered solid state phase transformation. By collapsing the viscoplastic part of the material model into a Maxwell model upon melting, the melt was modeled mechanically as a viscous Newton fluid.

The results showed high stresses in regions, where solidification cracks were found in the experiments, with higher levels in the partial penetration model. Those stresses are possible due to the triaxiality of the stress state. In the root of the partial penetration model, they were caused by the impedance of weld shrinkage due to the cold and strong material below the weld. The stress maximum in the bulging region, found in both models, was caused by the inhomogeneous cooling of the weld and presumably aggravated in partial penetration welding due to the cold material below the weld.

Further attention is needed to clarify the connection between partial penetration and the stress maximum in the bulging region. Other experimental results, for example, the influence of the laser beam power and the wire feed speed on hot cracking, have to be analyzed in future times.

References

- [1] M. Gebhardt, A. Gumenyuk, and M. Rethmeier, "Single-run high power laser-GMA-hybrid-welding of thick walled tubes," *Welding Journal*, vol. 91, no. 6, pp. 55–61, 2012.
- [2] M. Gebhardt, A. Gumenyuk, V. Quiroz, and M. Rethmeier, "Laser-MSG-hybridschweißen dickwandiger präzisionsrohre," *Schweißen und Schneiden*, vol. 64, no. 5, pp. 254–259, 2012.
- [3] J. Schuster, *Heißrisse in Schweißverbindungen*, DVS, Düsseldorf, Germany, 2004.
- [4] M. Gebhardt, A. Gumenyuk, and M. Rethmeier, "Laser-MSG-hybridschweißen dickwandiger präzisionsrohre," Final Report of the AiF-Project 15917N, BAM Bundesanstalt für Materialforschung und -prüfung, Berlin, Germany, 2011.
- [5] N. Prokhorov, "The technological strength of metals while crystallising during welding," Tech. Rep., 1965.
- [6] C. Cross, "On the origin of weld solidification cracking," in *Hot Cracking Phenomena in Welds*, H. Herold and T. Böllinghaus, Eds., pp. 3–18, Springer, Berlin, Germany, 2005.
- [7] C. E. Cross and T. Böllinghaus, "The effect of restraint on weld solidification cracking in aluminium," *Welding in the World*, vol. 50, no. 11-12, pp. 51–54, 2006.
- [8] T. Kannengiesser and A. Kromm, "Design-specific influences on local weld displacement and hot cracking," in *Proceedings of the 2nd International Conference on Welding and Joining of Materials (ICWJM '07)*, pp. 1–9, Cusco, Peru, 2007.
- [9] V. Quiroz, M. Gebhardt, S. Gook, A. Gumenyuk, and M. Rethmeier, "Hot cracking in high power laser beam welding of thick high strength structural steels under restraint conditions," in *Proceedings of the 29th International Congress on Applications of Lasers and Electro-Optics (ICALEO '10)*, pp. 225–232, Laser Institute of America, San Diego, Calif, USA, September 2010.
- [10] M. Gebhardt, V. Quiroz, A. Gumenyuk, and M. Rethmeier, "Restraint effects on stresses and strains in single-run high power laser beam welding of thick plates," in *Mathematical Modeling of Weld Phenomena 9*, H. Cerjak and N. Enzinger, Eds., pp. 1011–1033, Technischen Universität Graz, Styria, Austria, 2010.
- [11] D. G. Eskin and L. Katgerman, "A quest for a new hot tearing criterion," *Metallurgical and Materials Transactions A*, vol. 38, no. 7, pp. 1511–1519, 2007.
- [12] H. Bergmann and R. Hilbinger, "Numerical simulation of centreline hot cracks in laser beam welding of aluminium close to the sheet edge," in *Mathematical Modeling of Weld Phenomena 4*, H. Cerjak, Ed., pp. 658–668, Technischen Universität Graz, Styria, Austria, 1998.
- [13] R. Hilbinger, H. Bergmann, W. Köhler, and F. Palm, "Consideration of dynamic mechanical boundary conditions in the characterization of a hot cracking test by means of numerical simulation," in *Mathematical Modeling of Weld Phenomena 5*, H. Cerjak, Ed., pp. 847–862, Technischen Universität Graz, Styria, Austria, 2001.
- [14] V. Ploshikhin, A. Prikhodovsky, A. Ilin, C. Hermdinger, and F. Palm, "Mechanical-metallurgical approach for prediction of solidification cracking in welds," in *Mathematical Modeling of Weld Phenomena 8*, pp. 87–104, Technischen Universität Graz, Styria, Austria, 2007.
- [15] V. Ploshikhin, A. Prikhodovsky, and A. Ilin, "Experimental investigation of the hot cracking mechanism in welds on the microscopic scale," *Frontiers of Materials Science in China*, vol. 5, no. 2, pp. 135–145, 2011.
- [16] M. Rappaz, J.-M. Drezet, and M. Gremaud, "A new hot-tearing criterion," *Metallurgical and Materials Transactions A*, vol. 30, no. 2, pp. 449–455, 1999.
- [17] C. Monroe and C. Beckermann, "Development of a hot tear indicator for steel castings," *Materials Science and Engineering A*, vol. 413-414, pp. 30–36, 2005.
- [18] I. Farup and A. Mo, "Two-phase modeling of mushy zone parameters associated with hot tearing," *Metallurgical and Materials Transactions A*, vol. 31, no. 5, pp. 1461–1472, 2000.
- [19] M. Shibahara, H. Serizawa, and H. Murakawa, "Finite element method for hot cracking using interface element," *Transactions of the Japan Welding Research Institute*, vol. 28, no. 1, pp. 47–53, 1999.
- [20] M. Shibahara, H. Serizawa, and H. Murakawa, "Finite element analysis for hot cracking on transverse cross section using temperature dependent interface element (report ii)," *Transactions of the Japan Welding Research Institute*, vol. 29, no. 1, pp. 59–64, 2000.
- [21] M. Shibahara, H. Serizawa, and H. Murakawa, "Finite element analysis of hot cracking under welding using temperature-dependent interface element," in *Proceedings of the 11th International Offshore and Polar Engineering Conference*, I. Langen,

- T. Yao, J. Koo, R. Knapp, and J. Chung, Eds., vol. 4, pp. 297–303, The International Society of Offshore and Polar Engineers, Stavanger, Norway, June 2001.
- [22] M. Shibahara, H. Nagaki, S. Takaba, H. Serizawa, and H. Murakawa, “Prediction of hot cracks of T-joints in full-penetration welding process,” *Welding in the World*, vol. 53, no. 11-12, pp. 312–321, 2009.
- [23] M. Shibahara, T. Iwamoto, T. Osuki, K. Ogawa, H. Serizawa, and H. Murakawa, “Numerical analysis of hot cracking in welded pipe structure,” *Transactions of the Japan Welding Research Institute*, pp. 97–98, 2011.
- [24] J. Borland and R. Younger, “Some aspects of cracking in welded cr-ni austenitic steels,” *British Welding Journal*, vol. 7, no. 1, pp. 22–59, 1960.
- [25] B. Thomas and M. Bellet, “Modeling of stress, distortion and hot tearing,” in *ASM Handbook*, D. Stefanescu, Ed., vol. 15, pp. 449–461, American Society of Metals, 2008.
- [26] ESI Group, “Material database,” 2009.
- [27] J. Hildebrand, *Numerische schweißsimulation. bestimmung von temperatur, gefüge und eigenspannung an schweißverbindungen aus stahl- und glaswerkstoffen [Ph.D. thesis]*, Bauhaus-Universität Weimar, Weimar, Germany, 2009.
- [28] F. Richter, *Physikalische Eigenschaften von Stählen und Ihre Temperaturabhängigkeit*, Stahleisen-Sonderbericht, Stahleisen, Düsseldorf, Germany, 1983.
- [29] F. Richter, *Die Wichtigsten Physikalischen Eigenschaften Von 52 Eisenwerkstoffen*, Stahleisen-Sonderbericht, Stahleisen, Düsseldorf, Germany, 1973.
- [30] U. Dilthey, P. Seyffarth, A. Gumenyuk, K. Woeste, and A. Scharff, *Mathematische Simulation der Gefügeentwicklung und der Sich Einstellenden Mechanischen Eigenschaften Elektronenstrahlgeschweißter Verbindungen von Stahlwerkstoffen*, Deutsche Forschungsgemeinschaft, Bonn, Germany, 2001.
- [31] P. F. Kozlowski, B. G. Thomas, J. A. Azzi, and H. Wang, “Simple constitutive equations for steel at high temperature,” *Metallurgical Transactions A*, vol. 23, no. 3, pp. 903–918, 1992.
- [32] P. J. Wray, “Effect of carbon content on the plastic flow of plain carbon steels at elevated temperatures,” *Metallurgical Transactions A*, vol. 13, no. 1, pp. 125–134, 1982.
- [33] T. Suzuki, K.-H. Tacke, K. Wuennenberg, and K. Schwerdtfeger, “Creep properties of steel at continuous casting temperatures,” *Ironmaking and Steelmaking*, vol. 15, no. 2, pp. 90–100, 1988.
- [34] C. Li and B. G. Thomas, “Thermomechanical finite-element model of shell behavior in continuous casting of steel,” *Metallurgical and Materials Transactions B*, vol. 35, no. 6, pp. 1151–1172, 2004.
- [35] J. Lemaitre and J. L. Chaboche, *Mechanics of Solid Materials*, Cambridge University Press, Cambridge, UK, 2002.
- [36] H. E. Siekmann, *Strömungslehre—Grundlagen*, Springer, Berlin, Germany, 1st edition, 2000.

Research Article

Arc Interference Behavior during Twin Wire Gas Metal Arc Welding Process

Dingjian Ye, Xueming Hua, and Yixiong Wu

Shanghai Key Laboratory of Materials Laser Processing and Modification, Shanghai Jiao Tong University, Shanghai 200240, China

Correspondence should be addressed to Dingjian Ye; yedingjian@sjtu.edu.cn

Received 16 August 2013; Revised 11 November 2013; Accepted 11 November 2013

Academic Editor: Caner Simsir

Copyright © 2013 Dingjian Ye et al. This is an open access article distributed under the Creative Commons Attribution License, which permits unrestricted use, distribution, and reproduction in any medium, provided the original work is properly cited.

In order to study arc interference behavior during twin wire gas metal arc welding process, the synchronous acquisition system has been established to acquire instantaneous information of arc profile including dynamic arc length variation as well as relative voltage and current signals. The results show that after trailing arc (T-arc) is added to the middle arc (M-arc) in a stable welding process, the current of M arc remains unchanged while the agitation increases; the voltage of M arc has an obvious increase; the shape of M arc changes, with increasing width, length, and area; the transfer frequency of M arc droplet increases and the droplet itself becomes smaller. The wire extension length of twin arc turns out to be shorter than that of single arc welding.

1. Introduction

In recent years, numbers of researches have been focused on studying welding materials, welding technology, and welding equipment, especially the multiwire welding, to enhance the welding productivity [1, 2]. In twinwire or even multiwire MIG welding, the purpose is to increase the welding speed while the line energy remains constant. As several wires are melting at the same time, the deposition rate undoubtedly turns out to be higher than a single one.

As it can improve welding productivity and ameliorate the welding formation, twin wire welding has attracted extensive attention. Nowadays, the most frequently used twin wire welding mainly includes twin wire gas metal arc welding [3], TANDEM twin wire welding [4], and submerged arc welding (SAW) [5]. The primary problem in twin wire welding process is the interference between the two arcs which directly affects the welding quality [6]. The interference between the two arcs induces the variance of respective arc morphology which further leads to the change in thermal space allocation. In order to obtain ideal welding effect, pulse power supply is widely used. The control setups for adjusting two welding power supplies use three modes: synchronous, alternating, and random modes. It can control welding arc and relative timing relations of short circuit in order to reduce the mutual interference [7].

By far, researches about-arc interruption phenomenon of twin wire mostly focus on the P-GMAW TANDEM welding method. Ueyama and Ohnawa [8] utilized the pulse control method, while the phenomenon of arc interference and voltage instability still remained severe. Scotti et al. [7] took advantage of high-speed photography to analyze the two melting droplet transfer and arc behavior under different conditions by varying current level and different phase. Ueyama et al. [9] also found that the welding torch structure had an influence on welding formation during high-speed pulse TANDEM welding process. The result showed that using specifically constructed welding torches could obtain the stable burning arc, increase the welding speed and obtain better welding formation. Ueyama et al. [4] studied the effect of wire spacing and the shielding gas composition on arc interference during pulse TANDEM welding process. Yudodibroto et al. [10] came out with an index for assessment of TANDEM welding arc stability through statistics and calculation of welding current and voltage analysis. Ueyama et al. [11] showed how the state of the welding pool surface had an effect on the voltage of the abnormal arc by employing the minimum voltage principle.

In this paper, the arc interference of high strength low alloy steel in twin wire GMAW was investigated by observing the arc profile variation as well as measuring the electric signals variation.

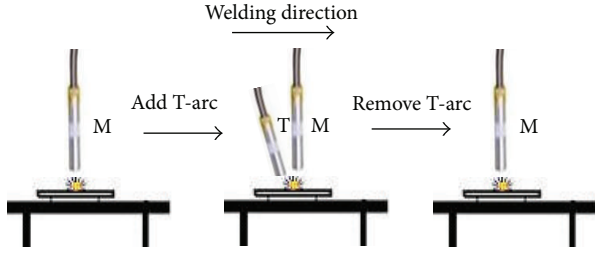


FIGURE 1: Experimental schematic model.

2. Experimental Procedure

During the experiment, the first wire is defined as M-arc along the welding direction; the following wire is defined as T-arc. The double arc welding is realized by adding T-arc to the system after M-arc is steadily burning. After M- and T-arcs steadily burn together for two seconds, T-arc is removed from the system. The arc interference is analyzed mainly in four aspects: the electrical signal, the arc shape, the droplet transfer frequency, and the wire extension length. The experimental process is shown in Figure 1. High-speed camera system and electrical signal acquisition system are employed to monitor the process so as to obtain the interference information. M-arc profile is taken by high-speed photography system. The whole experimental system of high-speed twin wire welding is displayed in Figure 2.

2.1. Materials. The sample employed in welding tests is high strength low alloy steel with the thickness of 15 mm. The chemical composition of the material is shown in Tables 1 and 2. The filler material used in this research is a super cored 70MXH welding wire with the diameter of 1.6 mm. The shielding gas used is pure CO₂, which is widely used in shipbuilding.

2.2. Welding Equipment. Experimental equipment system consisted of Panasonic YD-500GR3 welding power source, electrical signal acquisition card, high-speed camera system, and so forth.

2.3. Welding Parameters. The double electrode is all positive (welding torch is adjacent to the anode). The torch distance as well as the distance between nozzle and the base metal are both 20 mm. And the intersection angle between two adjacent torches is 10°. The flat welding is performed with CO₂ shielding gas flow of 20 L/min and the welding speed of 500 mm/min. The current and voltage of M- and T-arcs are 250 A/27.5 V and 200 A/25 V, respectively.

3. Results and Discussion

3.1. Analysis of Signals Waveform of Twin Wire GMAW. The double arc welding is realized by adding T-arc to the system after M-arc is steadily burning. In this process, the current and voltage of M- and T-arcs are measured during the experiment, which are shown in Figure 3. The diagram

TABLE 1: Chemical composition of base metal.

Steel no.	C (%)	Si (%)	Mn (%)	P (%)	S (%)	Cr (%)	Ni (%)	Cu (%)
AB-A	0.15	0.78	0.08	0.19	0.2	0.03	0.01	0.02

TABLE 2: Chemical composition of super cored 70MXH welding wire.

Steel no.	C (%)	Si (%)	Mn (%)	P (%)	S (%)	Cr (%)	Ni (%)	Cu (%)
AB-A	0.05	0.55	1.65	—	—	—	—	—

illustrates that both the average and effective current values of M-arc show no obvious change after adding the T-arc, while the voltage of M-arc has a remarkable increase and the voltage of T is also higher than the setting one. Moreover, the standard difference enlarges the agitation of the current and the voltage.

In the experiment both of the two wires are anode. Therefore, serious interference exists due to the electromagnetic force, which results in mutual offset in arc area. The arc length also changes slightly, which further leads to the arc voltage change. This phenomenon can be simply explained by the deviation formula simplification model derived in Figure 4.

The center offset of M- and L-arcs can be expressed using the following formulas:

$$l_T = \frac{I_M L_T^2}{2I_T D_E}, \quad (1)$$

$$l_M = \frac{I_T L_M^2}{2I_M D_E}.$$

The above offset expressions demonstrate that the offset of one arc is proportional to the other arc's current and the square of its own arc length, while being inversely proportional to its own current and the arc distance. Furthermore, the arc shifts due to the electromagnetic force.

3.2. Analysis of Arc Profile Characteristics of M-Arc. According to the arc image, the arc shape of M is more stable when it burns alone. The arc dragging effect results in a slight offset towards the opposite direction of welding. As is shown in Figure 5, After T-arc is introduced, the coupled arc stability changes. Due to the attraction between the two arcs, the M-arc has a more obvious offset towards T-arc. Using lab view software, the average values of the height, length, and area of M-arc are calculated. In the circumstance of single-wire welding, the width, length, and area of M-arc are 10.23 mm, 5.76 mm, and 39.17 mm², respectively. After adding T-arc to the system, the coupled arc shape changes into 12.17 mm in width, 6.73 mm in length, and 52.09 mm² in area.

According to the principle of minimum voltage, the energy consumption characterization of arc tends to be minimized and the arc is symmetry in axis when a certain condition of current and boundary is determined. As the arc is in a stable state, the arc column diameter (D) and

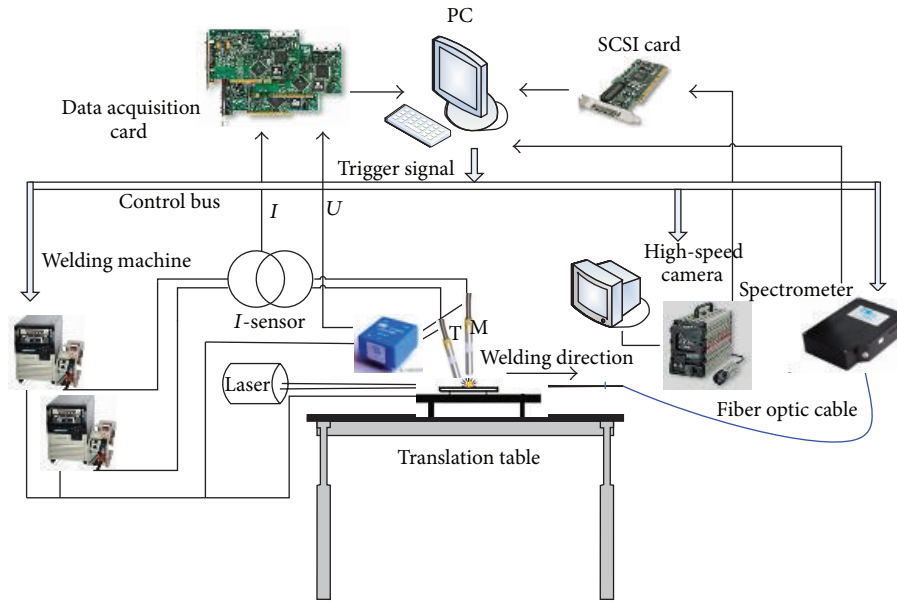


FIGURE 2: Experimental system of high-speed twin wire welding.

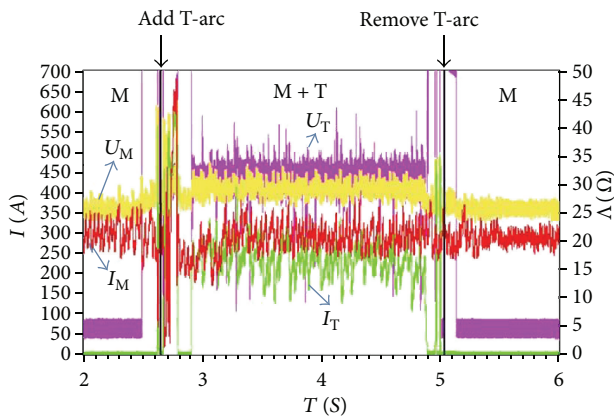


FIGURE 3: Electrical diagram of twin wire of GMAW.

temperature (T) should enable the electric field intensity of arc column (E) to own a minimum value.

When the T-arc approaches to M-arc, it can be considered as the fact that the arc is compelled to be heated by surrounding medium. According to the principle of minimum voltage, the cross-section area of the arc will be automatically increased, leading to the reduction of current density, electric field strength, and electric arc temperature. When the heat dissipation is eliminated, a little heat is produced by the arc for compensation. Therefore, the arc heat production is $I * E$, where current I keeps invariant and E is reduced. According to the principle of minimum voltage, the arc has an automatic dropping tendency to drive E to the minimum value, indicating the heat dissipating capacity reduction to present the maximum tendency. Therefore when the arc is being heated, the arc will automatically expand to a certain diameter, and then arc electric field strength E becomes the maximum reduction.

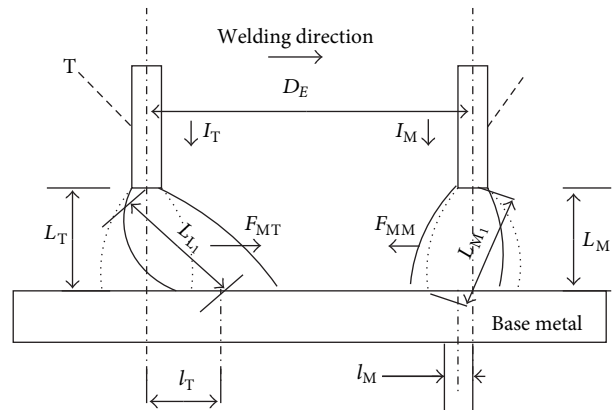


FIGURE 4: Schematic illustration of electromagnetic force acted on arc (D_E : the distance between M- and L-arcs; I_M , I_T : the current of M-arc and T-arc; L_M , L_T : the initial arc length of M-arc and T-arc; F_{ML} , F_{MT} : the Lorentz force).

3.3. Analysis of Droplet Transfer and Wire Extension Length of M-Arc. During the process of single arc welding, the droplet transfer frequency of M-arc is about 30 HZ. After adding T-arc, the droplet transfer frequency of M-arc reaches about 40 HZ. When T-arc is added, the droplet transfer mode of M-arc as well as the rejection transfer mode remains unchanged. The transfer frequency increases, while the droplet size becomes smaller, as is shown in Figure 6. The fact that no obvious change occurs in the current of M-arc after T-arc is added demonstrates that the wire feeding speed remains unchanged throughout the experiment. It is because welding wire feeding rate determines the current variation. Moreover, due to the heating effect of T-arc welding wire, the melting heat increases, which increases the welding wire melting rate. As wire feeding rate keeps unchanged, the droplet size becomes smaller.



FIGURE 5: Arc image of M-arc.

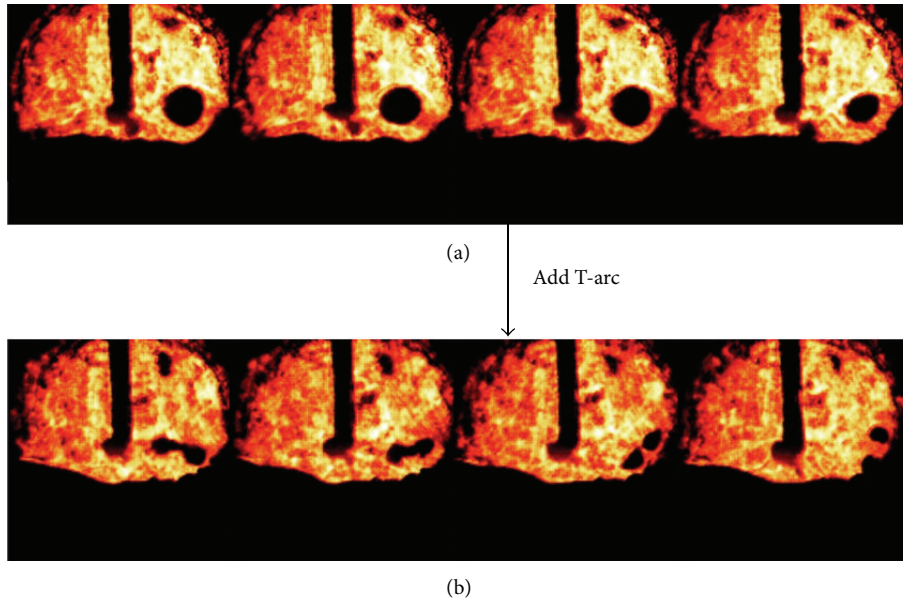


FIGURE 6: Droplet transfer of M-arc: (a) droplet transfer of M-arc simplex welding; (b) droplet transfer of M-arc welding after adding T-arc.

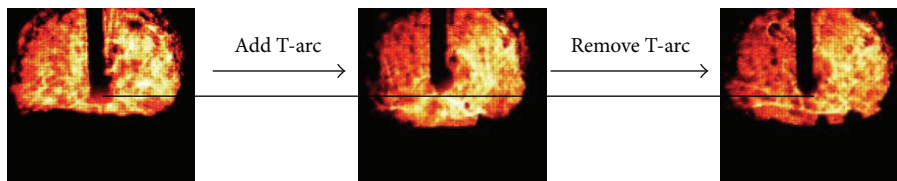


FIGURE 7: Wire extension length of M-arc.

The wire extension length of M-arc is calculated when it is burning alone and after adding T-arc using lab view, respectively. As shown in Figure 7, the wire extension length of M-arc decreases after T-arc is added. Wire extension length changed from 10.16 mm to 9.92 mm after T-arc is added under the condition of $I_M = 250$ A and $I_T = 200$ A, respectively.

The decrease of wire extension length can be explained in the wire heating source. Previous researches have widely studied the mechanism of heating in welding process and concluded a similar opinion. The total wire heat P_m causing heating and melting consists of two main parts: one is heat production of arc near electrode region and the other is the resistance heat. Tichella et al. [12] point out that the heat for heating and melting of welding wire mainly comes from the energy of the anode to absorb electrons (back), which means that the arc heat is the main energy for melting welding wire,

while Lesnewich [13] considers that the resistance heat of wire extension length is the main energy for melting welding wire, even in the case of low welding current. If there are an increase in the wire extension length and a reduction in wire cross-sectional area, it also leads to the increase of wire melting speed.

There is no doubt that wire melting heat comes from two parts: arc heat and resistance heat. However, for the twin wire welding being heated by the adjacent-arc, the heat for heating and melting of welding wire should consist of three parts. The expression is as follows:

$$\begin{aligned} P_m &= P_A + P_R + P_L = I_a (U_m + I_a R_s) + P_L \\ &= I_a \left(U_w + I_a \rho \frac{L_s}{S} \right) + P_L, \end{aligned} \quad (2)$$

where P_m is the total quantity of heat for heating and melting of welding wire; P_A is the arc near electrode region heat; P_R is the resistance heat; P_L is the second arc heat; I_a is the welding current; U_m is the equivalent voltage of arc melting of welding wire; U_w is the work voltage; R_s is the wire extension length resistance; ρ is the welding wire resistance; L_s is the wire extension length; S is the wire area.

The welding wire is connected to anode; thus the heat for melting welding wire mainly relies on the heat generated by resistance heat in anode area. U_m is similar to U_w (work voltage), and U_w is related to the materials. With a given material, the anode heat production is only related to the current. Due to the adding of welding wire, welding wire is provided with adjacent heat P_L , while the fuse rate and P_m remain unchanged. Since U_w and P_A keep invariant, P_R and L_s have a relative decrease. Hence, wire extension length decreases.

4. Conclusions

- (1) The experimental setup is established in order to study the interference behavior between twin wire arcs including measuring the synchronous signals of current and voltage and observing the arc profile, droplet transfer process, and wire extension length variation.
- (2) Because of the presence of arc pressure, the arc length and the voltage increase. The current remains unchanged, while the agitation increases in twin wire welding process.
- (3) Due to the effect of arc interaction, twin wire welding droplet transfer frequency increases quickly and the droplet size becomes smaller. At the same time, wire extension length decreases which indicates that the welding point changes.

Acknowledgment

This research is financially supported by the National Natural Science Foundation of China (Grant no. 51275299).

References

- [1] T. C. Nguyen, D. C. Weckman, D. A. Johnson, and H. W. Kerr, "High speed fusion weld bead defects," *Science and Technology of Welding and Joining*, vol. 11, no. 6, pp. 618–633, 2006.
- [2] A. Hiroshi, M. Tomokazu, and N. Shigeo, "Technical development of advanced 3-electrode MAG high speed horizontal fillet welding process," IIW Doc. No. XII-1898-06:92.
- [3] Y. Ruan, X. M. Qiu, W. B. Gong, D. Q. Sun, and Y. P. Li, "Mechanical properties and microstructures of 6082-T6 joint welded by twin wire metal inert gas arc welding with the SiO_2 flux," *Materials and Design*, vol. 35, pp. 20–24, 2012.
- [4] T. Ueyama, T. Ohnawa, M. Tanaka, and K. Nakata, "Occurrence of arc interaction in tandem pulsed gas metal arc welding," *Science and Technology of Welding and Joining*, vol. 12, no. 6, pp. 523–529, 2007.
- [5] D. V. Kiran, B. Basu, A. K. Shah, S. Mishra, and A. De, "Probing influence of welding current on weld quality in two wire tandem submerged arc welding of HSLA steel," *Science and Technology of Welding and Joining*, vol. 15, no. 2, pp. 111–116, 2010.
- [6] R. P. Reis, A. Scotti, J. Norrish, and D. Cuiuri, "Investigation on welding arc interruptions in the presence of magnetic fields: welding current influence," *IEEE Transactions on Plasma Science*, vol. 40, no. 3, pp. 870–876, 2012.
- [7] A. Scotti, C. O. Morais, and L. O. Vilarinho, "The effect of out-of-phase pulsing on metal transfer in twin-wire GMA welding at high current level," *Welding Journal*, vol. 85, no. 10, pp. 225–230, 2006.
- [8] T. Ueyama and T. Ohnawa, "Occurrence of arc interference and interruption in TANDEM pulsed GMA welding," IIW Doc, No. XII-1883-06.
- [9] T. Ueyama, T. Ohnawa, M. Tanaka, and K. Nakata, "Effects of torch configuration and welding current on weld bead formation in high speed tandem pulsed gas metal arc welding of steel sheets," *Science and Technology of Welding and Joining*, vol. 10, no. 6, pp. 750–759, 2005.
- [10] B. Yudodibroto, M. Hermans, and I. Richardson, "Process stability analysis during TANDEM wire arc welding," IIW Doc. XII-1876-06, 2006.
- [11] T. Ueyama, T. Ohnawa, T. Uezono, M. Tanaka, M. Ushio, and K. Nakata, "Solution to problems of arc interruption and stable arc length control in TANDEM pulsed GMA welding," *Welding International*, vol. 20, no. 8, pp. 602–611, 2006.
- [12] G. Tichella, G. Jelmorini, and V. Heuvel, "Droplet temperature measurement in arc welding," IIW Doc, 212-411-77, 1977.
- [13] A. Lesnewich, "Control of melting rate and metal transfer in gas-shielded metal-arc welding part I-Controlo of electrode melting rate," *Welding Journal*, no. 8, pp. 343–345, 1958.

Research Article

Effective Thermal Conductivity of Open Cell Polyurethane Foam Based on the Fractal Theory

Kan Ankang and Han Houde

Merchant Marine College, Shanghai Maritime University, Shanghai 201306, China

Correspondence should be addressed to Kan Ankang; ankang0537@126.com

Received 6 March 2013; Revised 13 September 2013; Accepted 19 November 2013

Academic Editor: Martha Guerrero

Copyright © 2013 K. Ankang and H. Houde. This is an open access article distributed under the Creative Commons Attribution License, which permits unrestricted use, distribution, and reproduction in any medium, provided the original work is properly cited.

Based on the fractal theory, the geometric structure inside an open cell polyurethane foam, which is widely used as adiabatic material, is illustrated. A simplified cell fractal model is created. In the model, the method of calculating the equivalent thermal conductivity of the porous foam is described and the fractal dimension is calculated. The mathematical formulas for the fractal equivalent thermal conductivity combined with gas and solid phase, for heat radiation equivalent thermal conductivity and for the total thermal conductivity, are deduced. However, the total effective heat flux is the summation of the heat conduction by the solid phase and the gas in pores, the radiation, and the convection between gas and solid phase. Fractal mathematical equation of effective thermal conductivity is derived with fractal dimension and vacancy porosity in the cell body. The calculated results have good agreement with the experimental data, and the difference is less than 5%. The main influencing factors are summarized. The research work is useful for the enhancement of adiabatic performance of foam materials and development of new materials.

1. Introduction

Because of distinguished adiabatic performance, open cell polyurethane foam, with small density and low thermal conductivity ($0.018\sim 0.032200\text{ W/(m}\cdot\text{K)}$), is applied in various fields such as building, food cold storage, and refrigerating cargo transportation, for heat conservation purpose. The irregular geometrical construction of open cell polyurethane foam makes it irregular in physical properties. And it makes the theoretic research difficult, especially in the accurate thermal performance. Actually, adiabatic materials' thermal conductivity can be measured by the plate thermal guarded device, but it is inconvenient for science research and the polyurethane foam development. It has been a considerable research project for thermophysics engineering and hylology to analyze and estimate the effective thermal conductivity of porous medium for a long time [1]. While the foam porous medium material is taken as the research project to calculate the thermal conductivity, it is always supposed as the connecting virtual medium in large-scale space, that is, "the average volume" in geometric distribution. Whitaker [2, 3] and Whitaker and Chou [4] took the virtual "average volume"

method to describe the procedure of the heat and mass transfer inside the porous medium. The view was taken that the porous medium was combined with solid phase material, liquid, and gas. The gas phase contains dry air and vapor. Supposed that all the phases in porous medium were balances of heat and the pores' dimensions were according to "average volume", a dozen of variables involved in the mathematical formula. Yu et al. [5, 6] also investigated experimentally their coupling and diffusing physical model and derived the relative mathematical formula.

There are two main methods to estimate the thermal conductivity of porous medium materials nowadays. One is that the thermal conductivity is illuminated as the complicated mathematical functions by the pore proportion and the microstructure parameters. Lagarde [7] derived the equivalent effective thermal conductivity λ_e function of the saturation porous materials. The equivalent effective thermal conductivity is obtain from

$$\lambda_e = \varphi\lambda_f + (1 - \varphi)\lambda_s, \quad (1)$$

where λ_f is the fluid phase thermal conductivity ($\text{Wm}^{-1}\text{K}^{-1}$) and λ_s is that of the solid phase ($\text{Wm}^{-1}\text{K}^{-1}$).

Here the supposition was made that heat fluxes through fluid in the pore and by the solid phase of the porous body were individual and took place simultaneously. However, the heat transfer was also proceeding between the fluid phase and the solid phase simultaneously. So the real model was more complicated than the expression in (1). So Williams and Dawe [8] developed the function as follows:

$$\lambda_e = \varepsilon \left[\varepsilon_1 \lambda_f + (1 - \varepsilon_1) \lambda_s \right] + \frac{(1 - \varepsilon)}{\varepsilon_2 / \lambda_f + (1 - \varepsilon_2) / \lambda_s}, \quad (2)$$

where $\varphi = \varepsilon \varepsilon_1 + (1 - \varepsilon) \varepsilon_2$. The factor ε is ratio that the heat flux transfers along with the temperature grads to the total heat flux, while ε_1 is the factor for inexistence of the solid-solid connection and ε_2 is for the existence of solid-solid connection and solid-fluid connection.

Actually, in the microspace structure of porous medium materials, the existence of ideal even distribution of the pores in the porous body is impossible. So there is a big error between the ideal model mentioned above and the real body. The available ideal models and empirical equations for foam thermal insulating materials are only generally related to pores proportion, which is the approximate reflection of the apparent thermal conductivity in the macrospace. But for the real foam material whose pore distribution is irregular, the available ideal models and empirical equations are not relative to the microstructure and cannot expose the actual heat and mass transfer procedure and the distribution of temperature and humidity. As a result, the big error is presence in the research work.

The other method involves fractal theory. Fractal theory, introduced into the estimation and research work to calculate the thermal conductivity of porous foam materials, is a new way for the theory development on thermal performance of porous medium materials. Fractal theory was first put forward in 1975 by Mandelbrot who was a professor from Harvard University in USA. Some experts, such as Pitchumani [9], Yu and Li [5], and Ma et al. [6], have done deep researches on the effective thermal conductivity of granular porous medium by fractal theory and have created corresponding mathematical equations. Based on the fractal theory, Thovert et al. [10], Zhang et al. [11], and so on developed the theoretical models for calculation of the effective thermal conductivity of irregular porous medium. According to the concept of Sierpinski carpet model, Pitchumani and Ramakrishnan [12, 13] created the pore distribution theoretical model, but the model and mathematical equations were very complicated in fractal dimension. Ma et al. [6] built a mathematical model of effective thermal conductivity for porous medium according to fractal theory, which manifested that the thermal conductivity of porous medium was a function of the pore ratio, the area ratio, the thermal conductivity ratio in components, and the thermal contact resistance all together. It had nothing to do with empirical constants and less parameters and simple to calculate in the formula. However, different porous media are not the same with each other in internal fractal essence. And it is also difficult to estimate the thermal contact resistance of porous medium in practice. The universality of the model still needs to be further verified. Thovert et al. [10] illuminated

the fractal porous medium by the percolation mathematical model, and did the solution by geometrical iteration. Whereafter, Adler, Thovert, and Thompson added empirical constants gotten by experiments into Adler's function. And the function is commonly described as

$$\lambda = \lambda_0 \phi^\alpha, \quad (3)$$

where λ_0 is the thermal conductivity of the liquid in the porous material pores ($\text{Wm}^{-1}\text{K}^{-1}$). And the superscript α here is defined as:

$$\alpha = \frac{d_s + D_f (2 - d_s)}{d_s (3 - D_f)}, \quad (4)$$

where, the fractal dimension factor $D_f = 2.5-2.85$, and spectral dimension d_s is used to describe the procedure of the percolation in the pores.

Yangsheng [14], based on the percolation theory, created the relationship between the pore diameters of various grain material and the thermal conductivity. But the pore porosity, the fractal dimension, and the microstructure are not involved in the model. Pitchumani and Yao [15] calculated the transverse and longitudinal fractal dimensions to illuminate the microstructure fibrous materials, and the thermal conductivity was derived based on the conventional heat transfer theory. But the model only serves some certain fibrous porous materials well.

So, it is considerably difficult and also unpractical to build a theoretically mathematical model of effective thermal conductivity that is universal for porous medium. Consequently, crating a mathematical model of thermal conductivity for one certain porous medium that reflects its structure characteristic in internality, is an important developing direction for the porous medium research work.

2. Microstructures of the Open Cell Polyurethane Foam and Fractal Description

2.1. Microstructures. The open cell polyurethane is composed of solid substrates and cells. By the effect of foaming agent and cell opening agent, great deals of cells are generated and continuously distributed inside the material. The cells connect with each other side by side, and the gas in pores can flow freely through one cell to another. That is really an advantage to expulse foaming agent and vapors that embraced in pores. Meanwhile, the gas in pores can easily be expelled as the thorough connection of cells. The solid substrate of open cell polyurethane has the certain intensity to support the material and to prevent the collapse in vacuum state. So the polyurethane foam with open cell structure can be used widely as the core material of the vacuum insulation panel.

Microstructures of the open cell polyurethane, consisting of skeleton of solid substrate (the white part in the picture) and cells (the black part in the picture), is shown in Figure 1 (taken by electron microscopy). Cells are generally cubed structurally in the space and continuously distributed in section plane, and the dimensions of the apertures are in

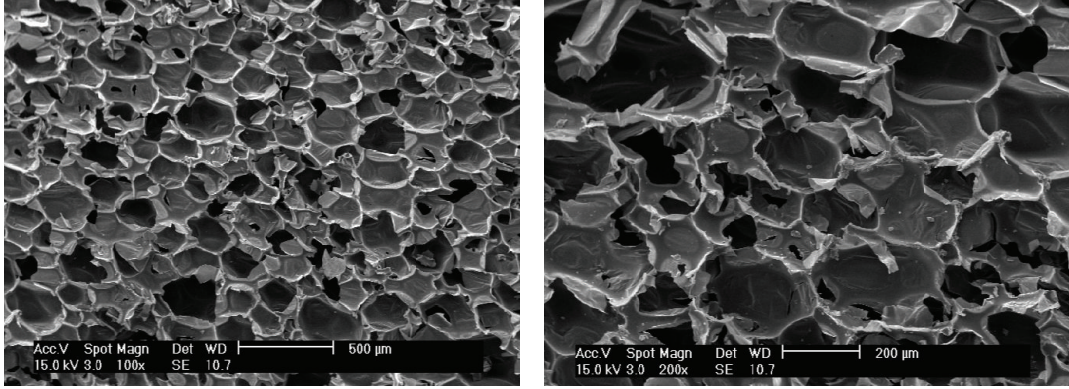


FIGURE 1: Microstructure section of the open cell polyurethane foam (magnified 500 and 200 times).

range of 140–220 μm and the length of average skeleton is 125 μm . The cells' dimensions are various and the distribution is random and irregular.

2.2. Fractal Description. Fractal theory, since it was born, has attracted lots of scientists' interest because of its unique advantages of research in irregular and complicated objects geometrically and success in dealing with many problems of geometry, physics, geology, hylology, and so on. Meanwhile, the various problems in the scientific subjects also enhanced the development of the fractal theory. Fractal theory is an effective approach to describe nonlinear phenomena in nature, complicated structures in geometry, and internal objects and spatial distribution. Fractal theory firstly committed research on nonlinear complex systems and analyzed the inner laws from the investigated subjects that were not simplified and abstract. That is essential distinction between fractal theory and linear way. Two subjects can be treated as the self-similarity, while the fractal dimension values are equal, according to the fractal theory. Various fractal models have been built for porous media materials by experts and researchers, and the famous models, such as Sierpinski carpet model, Menger sponge model, and Koch curve model, are adopted by many researchers. However, almost porous media materials in nature are not the same with the models mentioned above. They are not strict similarity but similar in mathematical calculation.

According to fractal theory, it is a self-similar scaling relationship between metric measure of objects δ and physical quantity $N(\delta)$ existed in D_f dimension Euclidean space including area and volume, or length of a porous fractal [16]:

$$N(\delta) \propto \delta^{D_f}. \quad (5)$$

For one fractal body, the fractal dimension value D_f is in the range from 2 to 3. But for the microstructure open cell polyurethane, the diameters of the pores are different. The structure is irregular, and the distribution is random. For the open cell polyurethane foam, the largest pore size of cells is $D_{\max} = 220 \mu\text{m}$, and the smallest one is $D_{\min} = 140 \mu\text{m}$; and supposing the measure length δ for the pace $D_{\max} \rightarrow D_{\min}$, the cell volume $V(\delta)$ can be described in the following:

$$V(\delta) \propto \delta^{D_f}. \quad (6)$$

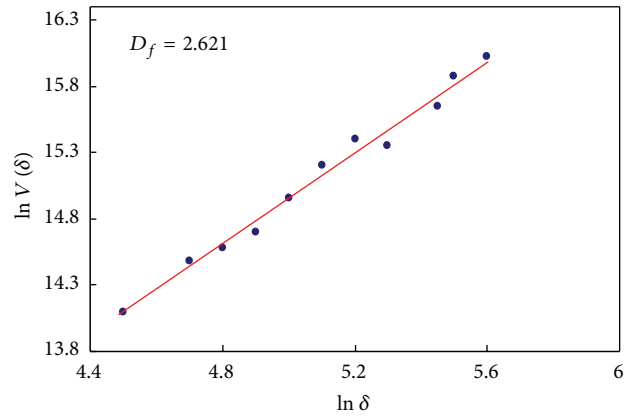


FIGURE 2: Fractal dimension calculation for cell body of the open cell polyurethane foam.

Based on fractal theory, the cell distribution has self-similarity statistically for the open cell polyurethane foam. Equation (6) can be replaced by the following:

$$V(\delta) = C\delta^{D_f}, \quad (7)$$

where C is constant. And taking the logarithm to (7), (8) can be gotten as

$$\ln V(\delta) = \ln C + D_f \ln \delta. \quad (8)$$

According to Sierpinski carpet's random fractal method, Figure 1 is fractal calculated and the result was shown in Figure 2. That is, the open cell polyurethane foam volume in this research has the fractal feature and the fractal dimension value is $D_f = 2.621$ for the sample.

However, the structure in the porous medium is irregular and the distribution of the pore is also random. The physical quantity $N(\delta)$, the pores' quantity, has the relationship with δ and the pore diameter D . So (5) can be rewritten as

$$N(\delta > D) = \left(\frac{D_{\max}}{D}\right)^{D_f} \quad (9)$$

or

$$N'(\delta > D_{\min}) = \left(\frac{D_{\max}}{D_{\min}}\right)^{D_f}. \quad (10)$$

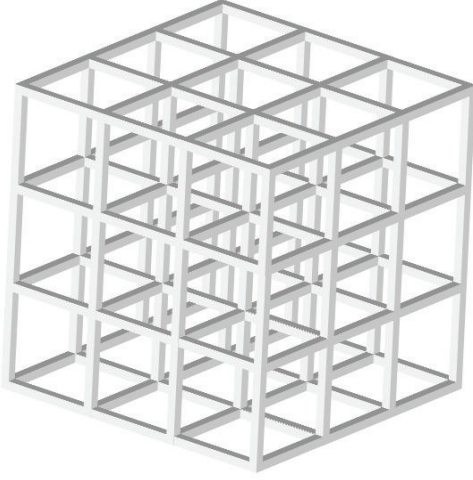


FIGURE 3: Simplified structure model of the open cell polyurethane foam.

Taking differential coefficient to (9), then

$$dN = -D_f D_{\max}^{D_f} D^{-D_f-1} dD. \quad (11)$$

So, combining with (10) and (12) can be gotten as

$$-\frac{dN}{N^f} = D_f D_{\min}^{D_f} D^{-(D_f+1)} dD. \quad (12)$$

Here, the pore distribution probability function $f(D) = D_f D_{\min}^{D_f} D^{-(D_f+1)}$ can be rewritten as

$$\int_{-\infty}^{\infty} f(D) dD = \int_{D_{\min}}^{D_{\max}} f(D) dD = 1 - \left(\frac{D_{\min}}{D_{\max}} \right)^{D_f}. \quad (13)$$

The fractal effective diameter L of the pores in the open cell polyurethane can be calculated according to the pore distribution probability function:

$$\begin{aligned} L &= \int_{D_{\min}}^{D_{\max}} D D_f D_{\min}^{D_f} D^{-(D_f+1)} dD \\ &= \frac{D_f}{D_f - 1} D_{\min} \left[1 - \left(\frac{D_{\min}}{D_{\max}} \right)^{D_f-1} \right]. \end{aligned} \quad (14)$$

Based on the inner structure of the open cell polyurethane form, we suppose that cells are cubed and well distributed, as in Figure 3.

3. The Equivalent Thermal Conductivity of Fractal Model

The equivalent thermal conductivity λ_e of the porous open cell medium materials is the function of the variable thermal conductivities of the phases, the inner structure, and the pores distribution [17]. So the equivalent thermal conductivity λ_e can be illuminated in the following:

$$\lambda_e = f\left(\sum \lambda_i, \varphi, D_f\right), \quad (15)$$

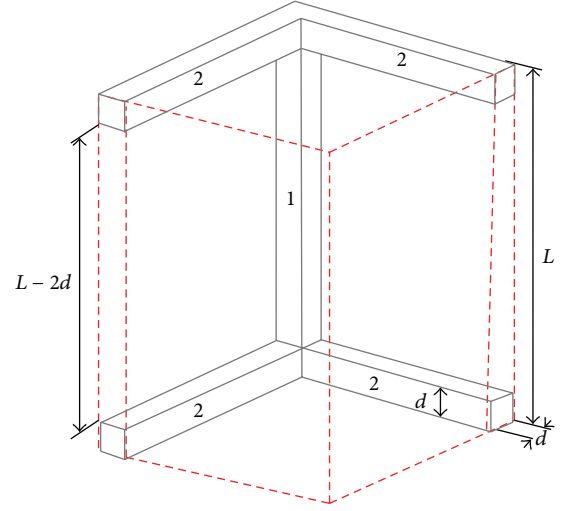


FIGURE 4: Thermal network sketch.

where λ_i is thermal conductivity of the phase i in the porous medium materials. For the solid phase, the conductivity is λ_s , while λ_g for the gas in the pores φ is the porosity of the average volume.

The mathematic model for the open cell polyurethane is developed on the basis of (15) in this paper. Neglecting the effect of heat radiation in cells and gas heat convection, we conclude that the heat transfer in one cell of open cell polyurethane form is only influent by adjacent cells. For one cell, we suppose that the structure is regular prism, the fractal diameter L ; the height is mentioned above in (14), while the solid substrates height d , just as in Figure 3. So, the whole heat transfer procedure in the cell can be analyzed as the electricity transfer in the electrocircuit. Suppose that heat current flow from top to underside through the cell body, then thermal resistance of the cell mainly consists of four parts.

R_1 is thermal resistance of vertical pillar, R_2 level pillar, R_3 gas among level pillars, and R_4 gas in cavity.

The thermal resistance simplified model can be described as in Figure 4.

According to interrelated heat transfer knowledge, we can easily get that

$$R_1 = \frac{L}{\lambda_s d^2}$$

$$R_2 = \frac{2d}{\lambda_s d (L - 2d)} = \frac{2}{\lambda_s (L - 2d)}$$

$$R_3 = \frac{(L - 2d)}{\lambda_g (L - 2d) d/2} = \frac{2}{\lambda_g d}$$

$$R_4 = \frac{4L}{\lambda_g (L - 2d)^2}$$

$$R_{\text{total}} = \frac{4L}{\lambda_e L^2} = \frac{4}{\lambda_e L}, \quad (16)$$

where R_{total} is entire thermal resistance; λ_s is thermal conductivity of foam's skeleton; λ_g is thermal conductivity of gas in cells; $\lambda_{e,\text{foam}}$ is effective thermal conductivity of the form.

From the analysis above, we can deduce that

$$R_{\text{total}} = \frac{R_1 R_4 (2R_2 + R_3)}{2R_1 R_4 + (2R_2 + R_3)(R_1 + R_4)}. \quad (17)$$

From (3) and (17), (18) can be easily gotten:

$$\lambda_{e,\text{foam}} = \frac{4\lambda_s d^2}{L^2} + \frac{\lambda_g (L - 2d)^2}{L^2} + \frac{4\lambda_g \lambda_s (L - 2d) d}{L(2\lambda_g d + L\lambda_s - 2\lambda_s d)}, \quad (18)$$

where $\lambda_{e,\text{foam}}$ in (18) is the effective thermal conductivity when there is static gas in pores of the open cell polyurethane.

The conception of porosity φ for porous polyurethane would be introduced here. Generally, it is the ratio of the summation of the vacancy volume V_i to the whole material block volume V . With the calculating methods by the fractal theory, the porosity φ can be easily illuminated as [18]

$$\varphi = \frac{\sum_{i=1}^n V_i}{V} = \left(1 - \frac{2d}{L}\right)^{D_f}. \quad (19)$$

Combining (18) with (19), the effective thermal conductivity will be gotten:

$$\lambda_{e,\text{foam}} = \lambda_s \left(1 - \varphi^{1/D_f}\right)^2 + \lambda_g \varphi^{2/D_f} + 2 \frac{\lambda_g \lambda_s \left(1 - \varphi^{1/D_f}\right) \varphi^{1/D_f}}{\lambda_g \left(1 - \varphi^{1/D_f}\right) + \lambda_s \varphi^{1/D_f}}. \quad (20)$$

From (20), we can conclude that the effective thermal conductivity of the open cell polyurethane form has relationship with the phases of the cell body and the fractal dimension and the cell structure, that is, the porosity.

The thermal conductivity would decrease with fractal dimension's increase of cells volume and increase of pore porosity, and that is in accordance with heat conducting performance. The bigger the fractal dimension and porosity are, the less the solid substrates are and the worse the heat conducting property is.

4. The Effective Thermal Conductivity of Thermal Radiation

Heat radiation is an important factor for the open cell polyurethane foam. It can be treated as a gray-body medium

to estimate the radiation heat flow in cells [10]. So the rate of radiation heat flow for a cell is

$$q_r = -\frac{4\sigma(T_1^4 - T_2^4)}{3\beta L}, \quad (21)$$

where σ is Stefn-Boltzmann constant, $\sigma = 5.6697 \times 10^{-8} \text{ W}/(\text{K}^4 \cdot \text{m}^2)$, β is radiation extinction coefficient for porous medium, and T_1 and T_2 are separately heat flow's temperature of entrance and exit.

So we can get the equivalent radiation thermal conductivity $\lambda_{e,r}$ for a porous medium:

$$\lambda_{e,r} = \frac{4\sigma(T_1^2 + T_2^2)(T_1 + T_2)}{3\beta}. \quad (22)$$

5. The Comparison between Results of Theoretical Calculation and Experiment

The entire equivalent thermal conductivity λ_e can be obtained in (23) on the condition of integrating the heat conducting and radiation-conduction heat transfer together:

$$\lambda_e = \lambda_{e,\text{foam}} + \lambda_{e,r}. \quad (23)$$

The certain open cell polyurethane foam above is selected as a sample to test in experiments, and its thermal conductivity of solid substrates is $\lambda_s = 0.5832 \text{ W}/(\text{m} \cdot \text{K})$, the thermal conductivity of gas in pore is $\lambda_g = 0.0229 \text{ W}/(\text{m} \cdot \text{K})$, and the decay coefficient tested is $\beta = 445 \text{ m}^{-1}$. The measurement way to test thermal conductivity of the sample is heat guarded plate method. And the standard of test refers to GB/T3399-2009. The results are collected in Table 1.

6. Conclusion

It can be found from Table 1 that there is little difference between the results calculated by the theoretical model present above and the experimental ones. Conclusions from the research work are as follows.

There is a good consistency between experimental and theoretical calculations presented in this paper. Error is less than 5%. Especially when taking the open cell polyurethane foam as the core of vacuum insulation panels, the gas thermal conductivity in (18) can be ignored, and calculations simplified and more accurate results can be obtained.

The effective thermal conductivity of the open cell polyurethane foam has a relationship with the material properties, inner microstructure, and the service environmental temperature. Thermal conductivity during heat conduction in entire effective thermal conductivity is predominant in normal temperature, while the effective thermal conductivity during radiation is a little undulating, but the value is not primary. So, increasing the porosity of the body can enhance its entire heat insulating property, on conditioning that its structural strength is enough for the open cell polyurethane foam.

The research work has manifestly established a connection between a thermophysical property and the internal

TABLE 1: The comparative table between results of calculation and experiment.

Sample	Density kg/m ³	Porosity %	Fractal dimension	Average temperature K	λ W/(m·K)				Difference %
					$\lambda_{e, \text{foam}}$	$\lambda_{e,r}$	λ_e	λ_{test}	
1	45	81	2.63	300	0.2804	0.0022	0.2826	0.280	-0.93%
				355	0.2804	0.0028	0.2832	0.287	1.3%
2	60	72	2.53	300	0.3186	0.0022	0.3208	0.330	2.8%
				355	0.3186	0.0028	0.3214	0.332	3.2%

microstructure of porous media by fractal theory. The theoretical work would be an important reference in enhancing heat insulating of porous media and useful in developing new material for environmental protection and energy conservation.

Nomenclature

C: Constant value
 D_{\min} : The smallest bore size in dimension
 D_{\max} : The biggest bore size in dimension
 D_f : Fractal dimension factor
 d_s : Spectral dimension
 d : Width of the model pillar
 L : Length of the model pillar
 $N(\delta)$: Physical quantity
 R : Thermal resistance (m²·K/W)
 T : Temperature (K)
 V : Volume (m³).

Greek Symbols

α : $\alpha = (d_s + D_f(2 - d_s))/d_s(3 - D_f)$
 σ : Stefn-Boltzmann constant,
 $\sigma = 5.6697 \times 10^{-8}$ W/(K⁴·m²)
 β : Radiation extinction coefficient
 λ : Thermal conductivity (W/(m·K))
 δ : Variable measure length(m)
 φ : Pore porosity in the average volume.

Subscripts and Superscripts

e : Effective
 r : Radiation
 g : Residual gaseous phase in the pore
 f : The fluid phase
 S : The solid phase
total: Total value
test: The value gotten from experiments.

Acknowledgment

This work was financially supported by Science & Technology Program of Shanghai Maritime University no. 20120091. We are grateful to Professor Wenzhe Sun and Professor Dan Cao for their advices and suggestions for this project. The authors also acknowledge Dr. Wenzhong Gao with valuable

discussion and contributions in mounting the experimental and installing the data acquisition devices.

References

- [1] Y. Chen and M. Shi, "Determination of effective thermal conductivity for porous media using fractal techniques," *Journal of Engineering Thermophysics*, vol. 20, no. 5, pp. 608–615, 1999.
- [2] S. Whitaker, "Diffusion and dispersion in porous media," *AIChE Journal*, vol. 13, no. 6, pp. 1066–1085, 1967.
- [3] S. Whitaker, "Advances in the theory of fluid motion in porous media," *Chemical Engineering*, vol. 61, pp. 14–28, 1969.
- [4] S. Whitaker and W. T.-H. Chou, "Drying granular porous media-theory and experiment," *Drying Technology*, vol. 1, no. 1, pp. 3–33, 1983.
- [5] B. Yu and J. Li, "Some fractal characters of porous media," *Fractals*, vol. 9, no. 3, pp. 365–372, 2001.
- [6] Y. Ma, B. Yu, D. Zhang, and M. Zou, "A self-similarity model for effective thermal conductivity of porous media," *Journal of Physics D*, vol. 36, no. 17, pp. 2157–2164, 2003.
- [7] A. Lagarde, "Consideration sur le transfert de chaleur en milieu poreux," *Institut Francais Du Petrole*, vol. 2, pp. 383–446, 1965.
- [8] J. K. Williams and R. A. Dawe, "Fractals—an overview of potential applications to transport in porous media," *Transport in Porous Media*, vol. 1, no. 2, pp. 201–209, 1986.
- [9] R. Pitchumani, "Evaluation of thermal conductivities of disordered composite media using a fractal model," *Journal of Heat Transfer*, vol. 121, no. 1, pp. 163–166, 1999.
- [10] J. F. Thovert, F. Wary, and P. M. Adler, "Thermal conductivity of random media and regular fractals," *Journal of Applied Physics*, vol. 68, no. 8, pp. 3872–3883, 1990.
- [11] D. Zhang, H. Yang, and M. Shi, "Important problems of fractal model in porous media," *Journal of Southeast University*, vol. 32, no. 5, pp. 692–697, 2002.
- [12] R. Pitchumani and B. Ramakrishnan, "A fractal geometry model for evaluating permeabilities of porous preforms used in liquid composite molding," *International Journal of Heat and Mass Transfer*, vol. 42, no. 12, pp. 2219–2232, 1999.
- [13] B. Ramakrishnan and R. Pitchumani, "Fractal permeation characteristics of preforms used in liquid composite molding," *Polymer Composites*, vol. 21, no. 2, pp. 281–296, 2000.
- [14] Z. Yangsheng, *Coupling Effect and Engineering Reflection of Porous Media Materials*, Science Press, Beijing, China, 2010.
- [15] R. Pitchumani and S. C. Yao, "Correlation of thermal conductivities of unidirectional fibrous composites using local fractal techniques," *Journal of Heat Transfer*, vol. 121, no. 1, pp. 788–796, 1991.
- [16] B. B. Mandelbrot, *The Fractal Geometry of Nature*, W.H. Freeman, New York, NY, USA, 1983.

- [17] A. K. Kan, T. T. Zhang, and H. J. Lou, "Fractal study of effective thermal conductivity of fiber glass materials," *Chinese Journal of Vacuum Science and Technology*, vol. 33, pp. 654–660, 2013.
- [18] Z. Donghui, J. Feng, and S. Mingheng, "Heat conduction in fractal porous media," *Journal of Applied Sciences*, vol. 21, no. 3, pp. 253–2257, 2003.

Research Article

Effect of Process Parameters on Gas Nitriding of Grey Cast Iron

Nana Wang and Jinxiang Liu

School of Mechanical Engineering, Beijing Institute of Technology, Beijing 100081, China

Correspondence should be addressed to Jinxiang Liu; liujx@bit.edu.cn

Received 2 August 2013; Revised 22 October 2013; Accepted 18 November 2013

Academic Editor: Martha Guerrero

Copyright © 2013 N. Wang and J. Liu. This is an open access article distributed under the Creative Commons Attribution License, which permits unrestricted use, distribution, and reproduction in any medium, provided the original work is properly cited.

Gas nitriding process parameters have significant effects on the nitriding layer of material. In the present work, a series of gas nitriding experiments on pearlitic grey cast iron specimens were carried out at different temperatures. To study the influence of nitriding process parameters on the nitriding layer, the numerical simulations of nitriding processing are performed, which take into account the threshold value of nitriding potential. The results show that the numerical simulations, incorporating the nitriding potential's threshold value, can accurately predict the case depth and nitrogen concentration profile. The nitriding layer increases with increasing nitriding time and temperature, whereas the nitrogen concentration on the surface decreases with increasing temperature. Besides, the results also reveal that the nitriding potential nearly has no effect on the case depth, whereas it has great influence on nitrogen concentration on the surface and chemical composition of the compound layer.

1. Introduction

Gas nitriding is a typical thermochemical surface treatment within the eutectoid temperature, in which the nitrogen is transferred from the ammonia gas into the workpiece surface, generating the gamma phase (γ' -Fe₄N) and epsilon phase (ϵ -Fe₃N) [1, 2]. After nitriding, the so-called compound layer and diffusion zone can be formed, which are capable of improving the wear and corrosion resistance of materials and enhancing the fatigue endurance [3, 4], respectively. The nitriding process parameters, such as nitriding time, nitriding temperature, and nitriding potential, have great influence on the forming of nitriding layer. The nitriding process parameters are mainly determined by experience in practical engineering applications. Their effects on nitriding layer are not very clear from a mathematical view. Therefore, considering the sensitivity of nitriding layer to the process parameters, there is an urgent demand to investigate the influence of the process parameters mathematically.

In recent years, a significant amount of experimental work has been conducted, aiming to investigate the nitriding process parameters' effect on nitriding process. Nevertheless, due to high time-consuming and economic costs, the experimental method is not very effective and feasible in practical applications, especially when the parameters vary in

a wide range. Under the circumstances, numerical analysis can be a good choice to study the processing parameters' influence. Arif et al. [5] investigated the effect of nitriding time, nitriding temperature, and nitriding potential on the nitrogen concentration and hardness depth profile by using finite element code. In their research, the influence of the compound layer on the nitrogen concentration distribution was not considered, so the calculated case depth was larger than the experimental data. To avoid the aforementioned shortcomings, Yang et al. [6, 7] proposed a compound layer growth model for an alloy steel. However, the difference between the critical value and threshold value of nitriding potential was ignored in Yang's research. Besides, Hu et al. [8, 9] simulated the nitriding process under multistage nitriding potential controlling. In their study, a nitriding layer without the compound layer was obtained by controlling nitriding process parameters. Furthermore, most of the researches published in the literature were focused on the nitriding process of pure iron or steels. For grey cast iron, a widely used material, related studies are lacking.

In the present work, a series of gas nitriding experiments on grey cast iron specimens were conducted at 550, 570, and 590°C. Afterwards, the numerical simulations were performed, which combined the influence of nitriding potential's threshold value on nitriding layer and Fick's second law. The

calculated thickness of diffusion zone was compared with the tested data to verify the numerical simulations. Finally, the effect of nitriding process parameters, including nitriding temperature, nitriding potential, and nitriding time, was further investigated.

2. Experimental Work

2.1. Material. The material tested in the study is pearlitic grey cast iron. The chemical composition of the material is shown in Table 1. Figure 1 depicts the microstructure of the grey cast iron. The graphite within the material is in a sheet form. Due to the large amount of graphite, the grey cast iron has good heat transfer ability, self-lubricating performance, and good casting property. It is a very suitable material for components operating under high temperature and friction condition.

2.2. Nitriding Process, Sample Preparation, and Equipment. Gas nitriding experiments were carried out on grey cast iron specimens. The specimens were divided into three groups, with two specimens in each group. The tested temperatures were set as 550, 570, and 590°C for each group, with the same total time of 24 hours and nitriding potential of 1.5 atm^{-1/2}.

After nitriding, the specimens were prepared by a standard grinding and polishing procedure, and microstructure observation was performed using JSM-5610LV SEM. Specimens were etched by 5% Nital in order to observe the nitriding layer by OLYMPUS PMG3. Hardness of the samples was also tested by applying a load of 1 N with holding time of 10 s. Besides, the hardness tests were conducted in 6 points of one sample and the average value was taken to represent the final hardness.

In order to obtain the composition of the nitriding layer, XRD analysis of the surface layer was performed using D8 ADVANCE X-ray diffractometer with CuK, at 40 kV and 40 mA. The scanned area was in the range of 15–90°.

3. Numerical Model of Gas Nitriding Process

3.1. Theoretical Background. In gas nitriding, the atomic nitrogen is dissociated from ammonia (NH₃) gas and then diffuses into the workpiece surface of component. The dissociation obeys the following rule:



where [N] represents N atom dissolved in the workpiece surface.

The above equation presumes that equilibrium has been established. The activated atomic nitrogen is dissolved in the iron crystal lattices, which not only promotes the nitriding of α -Fe, but also accelerates the formation and growth of compound layer. The solution of atomic nitrogen in pure iron is relatively fast, which does not affect the nitriding rate [10]. When building numerical model, for convenience, it is assumed that the graphite has no influence on the nitriding rate, although graphite is widely distributed in the iron matrix [11]. The resulting effect of this assumption will be discussed in detail in Section 5.1.

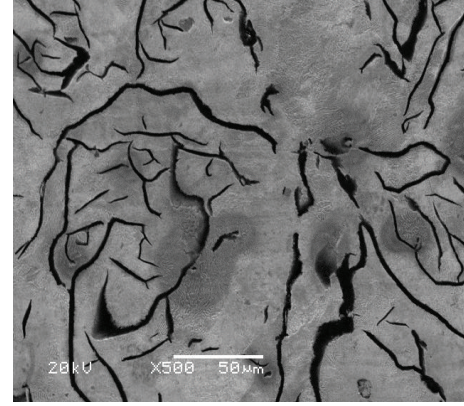


FIGURE 1: SEM analysis of the grey cast iron used in an engine cylinder liner.

The transformation of atomic nitrogen within grey cast iron is determined by the diffusion velocity, which is described by Fick's second law:

$$\frac{\partial c}{\partial t} = D \frac{\partial^2 c}{\partial x^2}, \quad (2)$$

where c represents the nitrogen concentration within the material and D is the diffusion coefficient of atomic nitrogen.

3.2. Numerical Model and Boundary Conditions. Nitriding potential is the measurement of nitriding ability of NH₃ gas. The phases and nitrogen concentration on the nitriding surface are closely related to the nitriding potential after local equilibrium is established. At the earliest, the well-known Lehrer diagram of pure iron, which was constructed by Lehrer through investigating the equilibrium conditions of NH₃-H₂ and Fe-N [12], was used to determine the relationship of the nitrided phases, nitrogen concentration, and nitriding potential.

The critical value of nitriding potential is defined as the turning point when the nucleation of γ' phase occurs at certain temperature. This value can be directly obtained from the Lehrer diagram. However, in engineering applications, the nitriding potential for compound layer nucleation is not completely equal to the critical value, since a minimal value, the so-called threshold value, has to be exceeded for certain nitriding time. The theoretical equation [13] for threshold value of nitriding potential is

$$K_{nt} = \frac{K_{nc}}{1 - \exp(\beta^2 t/D) \operatorname{erfc}(\beta\sqrt{t}/\sqrt{D})}, \quad (3)$$

where K_{nt} is the threshold value of nitriding potential for nitriding time t , K_{nc} is the critical value of nitriding potential, β is the mass transfer coefficient in gas-solid reaction, and erfc represents the complementary error function.

At a certain nitriding temperature, the time t_c , representing the nucleation starting time of compound layer, can be obtained by substituting the critical value of nitriding potential into (3). For accuracy, a two-stage process is defined

TABLE 1: Chemical composition (wt.%) of the studied grey cast iron.

C	S	Si	P	Mn	Cr	B	Cu	Ni	Ti	V	Mo	Nb	Fe
2.98	0.032	1.646	0.061	0.469	0.051	0.003	0.348	1.278	0.045	0.042	0.874	0.066	Bal.

in the current study. In the first stage, that is, $t \leq t_c$, the compound layer is not formed. In the second stage, that is $t > t_c$, the compound layer starts to nucleate and grow. The initial condition for stage I can be described as

$$t = 0, \quad c = c_0, \quad (4)$$

where c_0 is the initial nitrogen concentration within grey cast iron.

The boundary condition for stage I is

$$\begin{aligned} x = \infty, \quad c = 0, \quad x = 0, \\ -D_d \frac{\partial c}{\partial x} = \beta (c_g - c_s), \end{aligned} \quad (5)$$

where D_d represents the diffusion coefficient of atomic nitrogen in the diffusion zone, x is the depth from surface, c_g is the nitrogen concentration in the gas phase, and c_s is the nitrogen concentration on the surface of grey cast iron.

At the end of stage I, the compound layer begins to be formed and the nitrogen concentration in the interface between compound layer and diffusion zone is in equilibrium. In the diffusing process, the nitrogen concentration in the interface is set as unchanged. Therefore, the obtained nitrogen concentration on the surface of cast iron can be considered as the initial boundary condition for stage II. Since the thickness of compound layer is much less than that of the diffusion zone [7], the influence of the interface moving during the nitriding process is ignored in the study. Based on the hypothesis, the boundary condition for stage II is of the following form:

$$\begin{aligned} x = \infty, \quad c = 0, \\ x = 0, \quad c = c_d, \end{aligned} \quad (6)$$

where c_d is the nitrogen concentration on the workpiece surface after stage I.

The parameters needed to be calibrated are the diffusion coefficient D_d and mass transfer coefficient β . For parameter D_d , it is mainly influenced by the alloying element, which is capable of reacting with the atomic nitrogen. For grey cast iron, the governing alloying element is Cr, whereas it has little effect on the diffusion coefficient when its content is lower than 5% [14, 15]. The Cr element in the analyzed grey cast iron is 0.051%, so the influence can be ignored. The diffusion coefficient is determined by the following equation [16]:

$$D_d = 0.66 \exp\left(\frac{-77900}{RT}\right), \quad (7)$$

where R is the gas constant with a value of 8.314 J/mol·K and T is the nitriding temperature.

TABLE 2: The tested hardness of the compound layer at 550, 570, and 590°C.

Distance from the surface (μm)	Hardness value (Hv)		
	550	570	590
100	440	501	474
130	403	455	447

For parameter β , it is determined by the following equation [8]:

$$\beta = 0.0621 \exp\left(\frac{-6267}{T}\right). \quad (8)$$

In practice, since the compound layer is a multiphase composition, the diffusion coefficient of atomic nitrogen in this area is hard to be determined, and the thickness of compound layer can only be determined by experimental data. Therefore, the study is aimed at predicting the thickness of diffusion zone and analyzing the influence of nitriding process parameters.

4. Experimental Assessment

4.1. Optical Microscope. The cross-sectional observation through optical microscopes was made. Figure 2 shows the case depths after nitriding at 550, 570, and 590°C. As shown in the figure, the white layer is formed on the surface which is known as the compound layer. Beneath the compound layer, there is a diffusion zone, which is not so clear to be observed. It can be found that the compound layer increases with the increase in nitriding temperature, and the average thickness values at 550, 570, and 590°C are 4.50, 9.05, and 12.9 μm , respectively. The relationship between the compound layer thickness (h) and nitriding temperature is plotted in Figure 3, which exhibits a linear characteristic; that is, $h = -110.9 + 0.2T$.

4.2. Hardness Measurement. The tested hardness values in the depth of 100 and 130 μm are listed in Table 2. With the increase in distance from the surface, the hardness decreases to some degree. For both 100 and 130 μm , the hardness gets its maximum value at 570°C.

The case depth is determined by testing the microhardness of the nitrided samples. The depth is considered to be the distance between the workpiece surface and the location where the hardness is the same with the matrix material. For the analyzed grey cast iron, the obtained average case depths after nitriding are 79, 139, and 155 μm at 550, 570, and 590°C, respectively.

4.3. XRD Analysis. Figure 4 presents the XRD diffractogram of the sample's surface. The horizontal and longitudinal coordinate represents the diffractogram angle and diffractogram

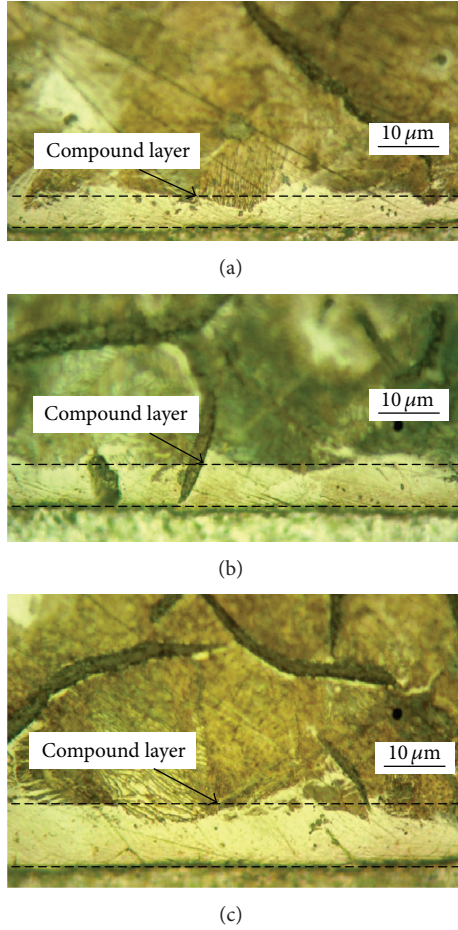


FIGURE 2: Cross-sectional scanning electron microscopy observation of the nitrided samples at (a) 550, (b) 570, and (c) 590°C.

strength, respectively. Due to the relative thinness of the compound layer, the reflection intensity of the γ' - Fe_4N phase is not distinct enough. Nevertheless, it can be found that after nitriding, the major phases on the surface are γ' - Fe_4N and ϵ - Fe_3N , which confirms the presence of superficial compound layer.

5. Numerical Results and Discussions

5.1. Numerical Results. The gas nitriding process in the study was simulated by using the model described in Section 3. The calculated nitrogen concentration of grey cast iron is depicted in Figure 5. It can be seen that with the increase in nitriding temperature, the thickness of diffusion zone increases. For a clear presentation, the experimental and calculated thickness values are listed in Table 3 and the calculation errors are also presented. It needs to be noted that the tested thickness of diffusion zone is determined by removing the compound layer from the tested case depth. The calculated thickness values are in good agreement with the experimental data, with an absolute maximal error value of 6.8%, which demonstrates the accuracy and feasibility of the numerical simulations.

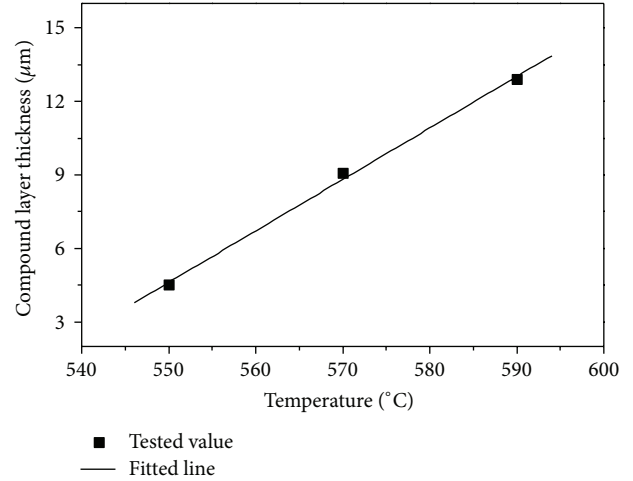


FIGURE 3: Experimental compound layer thickness as a function of nitriding temperature.

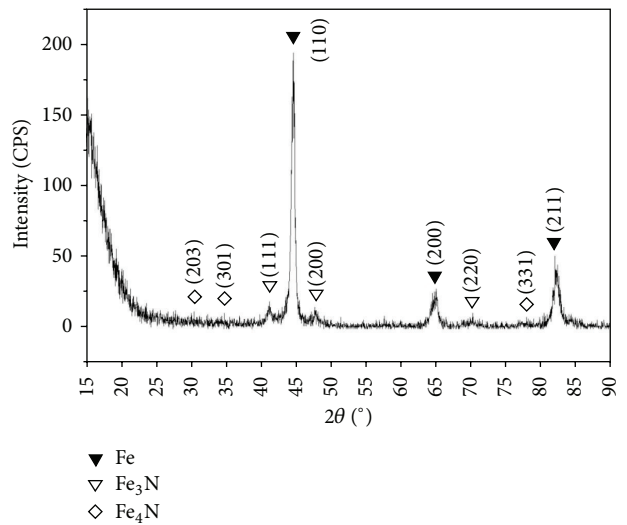


FIGURE 4: XRD diffractogram of the sample's surface for the analyzed grey cast iron after nitriding.

TABLE 3: The calculated and experimental case depths of the grey cast iron at 550, 570, and 590°C.

T (°C)	Tested (μm)	Calculated (μm)	Error (%)
550	74	79	6.8
570	129	125	-3.1
590	142	141	-0.7

For the presence of calculation error, it can be attributed to the following reasons. Firstly, during calculation, the influence of the interface's movement was not considered, which was a disadvantage of the present model. Secondly, the critical value of nitrogen potential, which was directly obtained from the Lehrer diagram of pure iron, may not be accurate for grey cast iron. Furthermore, for the analyzed grey cast iron, the largely distributed graphite may also have some uncertain effects on the nitriding potential value.

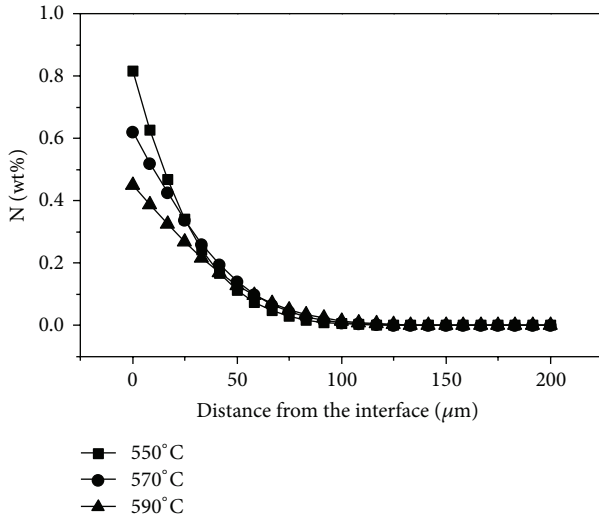


FIGURE 5: The calculated nitrogen concentration distribution at 550, 570, and 590°C.

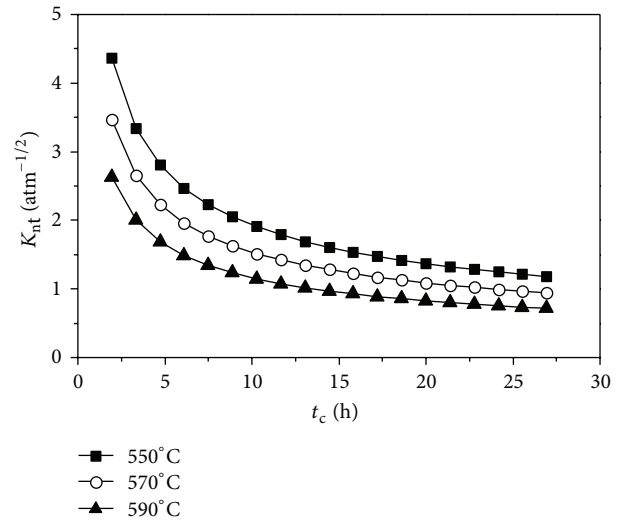


FIGURE 6: The threshold value of nitrogen potential at different temperatures.

Nevertheless, the accuracy of the numerical simulations is considered to be acceptable, which is a guarantee of the following effect analysis of nitriding process parameters.

5.2. Effect of Nitriding Temperature on the Threshold Value of Nitriding Potential. Nitriding temperature is a crucial process parameter which greatly affects the gas nitriding process. In the study, a threshold value of nitrogen potential is adopted instead of the traditional critical value, which is a significant advantage of the present model in comparison with the existing ones [5–7]. The relationship between the threshold value and temperature is given in Figure 6. As temperature increases, the threshold value decreases significantly. Under the circumstances, the time needed to form the compound layer decreases at higher nitriding temperature.

5.3. Effect of Nitriding Potential. Nitrogen potential, which represents the nitrogen activity on the workpiece surface, is used to control the compound layer’s thickness and phases. In order to investigate the influence of nitrogen potential, numerical simulations were conducted with respect to different nitriding potential values, that is, 0.32, 0.75, 1.5, and 3.5 atm^{-1/2}. Figure 7 presents the calculated nitrogen concentration profile for different nitriding potentials. It can be observed that the nitrogen potential has no effect on the case depth. However, the nitrogen concentration on the workpiece surface is of great difference, which exhibits the highest value for nitriding potential of 3.5 atm^{-1/2}. The analysis results directly demonstrate that the nitriding potential has great effect on the phase composition of compound layer, since it strongly influences the nitrogen concentration on the surface.

5.4. Effect of Nitriding Time. To investigate the influence of nitriding time on the case depth, numerical calculations were performed with different nitriding time of 7, 11, 24, and 40 hours. Figure 8 shows the calculated nitrogen concentration

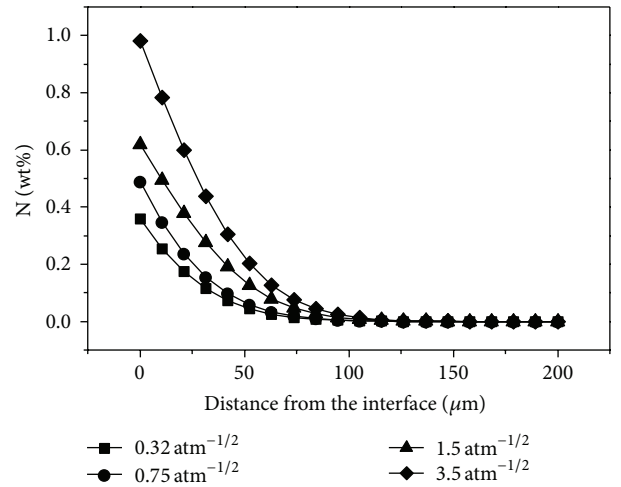


FIGURE 7: The nitrogen concentration distributions with different nitriding potentials.

profile for different nitriding time. Because the threshold values of nitriding potential at the nitriding time of 7 and 11 hours are higher than those of the present nitriding potential, no compound layer is formed on the surface. When nitriding time is 24 and 40 hours, the compound layer is formed and the nitrogen concentration on the workpiece surface turned into the same value. At the same time, the case depth increases as nitriding time increases from 24 to 40 hours.

6. Conclusions

Based on the gas nitriding experiments and numerical simulations, the following conclusions can be drawn.

- (1) The numerical simulations, taking into account the influence of threshold value of nitriding potential, can

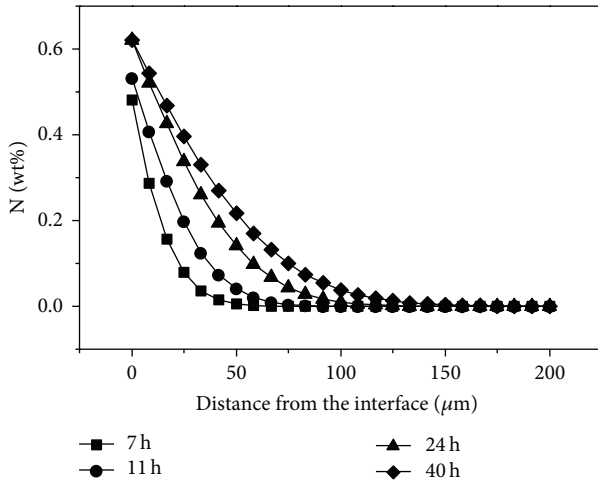


FIGURE 8: The nitrogen concentration distributions with different nitriding time.

precisely predict the thickness of diffusion zone and nitrogen concentration profile.

- (2) With the increase in nitriding temperature and time, the thickness of case depth increases to some degree, whereas the nitrogen concentration on the surface decreases as nitriding temperature increases.
- (3) For the analyzed grey cast iron, the nitriding potential has little effect on the thickness of case depth but has a relatively great influence on the nitrogen concentration of workpiece surface and composition of nitriding layer. The proposed numerical simulations for nitriding layer prediction and analysis can be a reference for practical engineering applications.

References

- [1] M. A. J. Somers, "Thermodynamics, kinetics and microstructural evolution of the compound layer; A comparison of the states of knowledge of nitriding and imitrocarburizing," *Heat Treatment of Metals*, vol. 27, no. 4, pp. 92–102, 2000.
- [2] D. Pye, *Practical Nitriding and Ferritic Nitrocarburizing*, Materials Park, Ohio, Ohio, USA, 2003.
- [3] M. A. J. Somers and E. J. Mittemeijer, "Layer-growth kinetics on gaseous nitriding of pure iron: evaluation of diffusion coefficients for nitrogen in iron nitrides," *Metallurgical and Materials Transactions A*, vol. 26, no. 1, pp. 57–74, 1995.
- [4] H. Du, M. A. J. Somers, and J. Agren, "Microstructural and compositional evolution of compound layers during gaseous nitrocarburizing," *Metallurgical and Materials Transactions A*, vol. 31, no. 1, pp. 195–211, 2000.
- [5] A. F. M. Arif, S. S. Akhtar, and B. S. Yilbas, "Effect of process variables on gas nitriding of H13 tool steel with controlled nitriding potential," *International Journal of Surface Science and Engineering*, vol. 4, no. 4–6, pp. 396–415, 2010.
- [6] M. Yang and R. D. J. Sisson, "Modeling the nitriding process of steels," *Advanced Materials and Processes*, vol. 170, no. 7, pp. 33–36, 2012.
- [7] M. Yang, C. Zimmerman, D. Donahue, and J. R. D. Sisson, "Modeling the gas nitriding process of low alloy steels," *Journal of Materials Engineering and Performance*, vol. 22, no. 7, pp. 1892–1898, 2013.
- [8] M. J. Hu, J. S. Pan, and Y. J. Li, "Mathematical modelling and computer simulation of nitriding," *Materials Science and Technology*, vol. 15, no. 6, pp. 547–550, 2000.
- [9] M. J. Hu and J. S. Pan, *Fundamentals of Thermochemical Surface Treatment of Steel*, Shanghai Jiao Tong University Press, Shanghai, China, 1996.
- [10] W. D. Jentzsch, F. Esser, and S. Boehmer, "Mathematical model for the nitriding of soft iron by ammonia-hydrogen mixtures," *Neue Hutte*, vol. 26, no. 1, pp. 19–23, 1981.
- [11] Z. X. Zhu and K. F. Yao, *Engineering Materials*, Tsinghua University Press, Beijing, China, 2011.
- [12] L. S. Darken and R. W. Gurry, *Physical Chemistry of Metals Istedition London*, McGraw-Hiu, 1953.
- [13] T. Bell, "Controlled nitriding in ammoniahydrogen mixturs," *Heat Treatment*, vol. 73, pp. 51–57, 1975.
- [14] Y. Sun and T. Bell, "A numerical model of plasma nitriding of low alloy steels," *Materials Science and Engineering A*, vol. 224, no. 1-2, pp. 33–47, 1997.
- [15] T. Spalvins, "Tribological and microstructural characteristics of ion-nitrided steels," *Thin Solid Films*, vol. 108, no. 2, pp. 157–163, 1983.
- [16] L. Torchane, P. Bilger, J. Dulcy, and M. Gantois, "Control of iron nitride layers growth kinetics in the binary Fe-N system," *Metallurgical and Materials Transactions A*, vol. 27, no. 7, pp. 1823–1835, 1996.

Research Article

Integrating the TRIZ and Taguchi's Method in the Optimization of Processes Parameters for SMT

Yung-Tsan Jou,¹ Wen-Tsann Lin,² Wei-Cheng Lee,¹ and Tsu-Ming Yeh³

¹ Department of Industrial and Systems Engineering, Chung Yuan Christian University, Chung Li 32023, Taiwan

² Department of Industrial Engineering and Management, National Chin-Yi University of Technology, Taichung 41170, Taiwan

³ Department of Industrial Engineering and Management, Dayeh University, Changhua 51591, Taiwan

Correspondence should be addressed to Tsu-Ming Yeh; tmyeh@mail.dyu.edu.tw

Received 12 August 2013; Accepted 27 October 2013

Academic Editor: Caner Simsir

Copyright © 2013 Yung-Tsan Jou et al. This is an open access article distributed under the Creative Commons Attribution License, which permits unrestricted use, distribution, and reproduction in any medium, provided the original work is properly cited.

SMT is an assembly technology for core circuit board parts. Unless process parameters are effectively controlled, poor solderability may result in a decline in product quality. This study looks at an SMT manufacturing process in a multinational company. First, the TRIZ contradiction matrix is revised to investigate the association between the 39 parameters in the contradiction matrix and 13 parameters that influence the unevenness of solder paste in the solder paste printing process. Expert verification is then used to screen the key factors affecting the quality of SMT, which are then combined with Taguchi's method to identify the optimal parameter set influencing the thickness of SMT solder paste. *Results.* TRIZ identifies squeegee pressure, ejection speed, squeegee speed, and squeegee angle as the four parameters with the greatest influence on SMT solder paste thickness. Taguchi's method is used to identify the optimum levels set for the experimental factors and carry out confirmation experiments. The *S/N* ratio improved from 21.732 db to 26.632 db, while the mean also improved from the current 0.163 mm to 0.155 mm, close to the target value of 0.15 mm. The results show that applying TRIZ and Taguchi's method for the purpose of product improvement is feasible.

1. Introduction

Today, product cycles are short and undergo rapid changes. Consumer electronic products, such as smart phones, notebook computers, and digital cameras, play an important role in our everyday lives. As consumers become more demanding, there is an increasing emphasis on lighter, thinner, high quality, and low-priced products that can be delivered to the consumer quickly. In addition, due to global competition, businesses are increasingly demanding rigorous quality standards to meet customer's demand [1, 2].

To meet the demand for light, thin, short, and small electronic products, print circuit boards (PCB) have evolved from single-layer to multilayer boards, with a consequent reduction in their size. As a result, most traditional plated-through hole parts are gradually falling out of use. An effective solution to this is to attach electronic components onto the PCB, resulting in the development of surface mount technology (SMT). However, unless process parameters are effectively controlled, poor solderability may result in a

decline in product quality. For example, if insufficient solder paste is deposited at the PCB printing stage, the strength of the solder joints may be inadequate or an empty solder phenomenon may occur. However, if too much solder paste is deposited, bridges may form between the solder joints, leading to short circuits.

Yang et al. [3] point out that SMT has become the primary tool for PCB assembly. An SMT quality problem may cause a significant production loss, and SMT quality issues are crucial to competition between companies. In the research on optimizing stencil printing, Tsai [4] offers a comparative perspective, finding that in the SMT manufacturing process 60% of stencil quality issues are caused by defects in solder paste printing. In their research using Taguchi's method to improve the parameters of solder paste printer processes, Lai and Wang [5] use optimized printing parameters, leading to an improvement of approximately 20% in solder paste printing quality. Recent studies on solder paste printing quality by Tsai [4] and Lai and Wang [5] have both produced significant improvements in solder paste printing quality.

Worsening feature \ Improving feature		1			7		39
		Weight of moving object	Volume of moving object	...	Productivity
4	Length of nonmoving object				↓		↓
5	Area of moving object	-----	-----	----->	4, 7, 14, 17		↓
...							↓
39	Productivity	-----	-----	-----	-----	----->	—

Source: <http://www.innovation-triz.com/TRIZ40/>

FIGURE 1: An example of the contradiction matrix.

However, they fail to explain how they selected their experimental variables. Many researchers, including Yildiz [6, 7], Durgun and Yildiz [8], and Yildiz and Solanki [9], have applied Taguchi's method or algorithms to plan experiments and parameter optimization in the past few years.

Andersen and Fagerhaug [10] argue that the TRIZ contradiction matrix is a tool for eliminating root causes of problems in the engineering process and can be used to identify engineering parameters that cause engineering problems or conflicts. This study randomly selected 30 sets of data from the process-site and measured and calculated the process capability index as $C_{pk} = 1.24$. This figure does not meet Kane's [11] recommended minimum acceptable process capability index of $C_{pk} \geq 1.33$, showing that there is still significant room for improvement in the quality of the solder paste printing process. Therefore, this study attempts to combine TRIZ and Taguchi's method to carry out empirical research. It is hoped that a predictive model of the manufacturing process outcomes can be used to identify optimized process parameters.

2. Literature Review

2.1. TRIZ. TRIZ is an abbreviation for the "theory of inventive problem solving" in the Russian language. The theory was developed by the Soviet inventor Altshuller [12] in 1946 with the aim of solving different types of contradictions.

Altshuller [12] developed the concept of the "technical contradiction" after observing a large number of invention proposals. The technical contradiction arises because improving one technical system parameter impacts negatively on another one. For example, making a product lighter by reducing its thickness also makes the product more prone to being easily damaged [13]. However, using better materials increases the cost of manufacturing the product. When confronted with a technical contradiction, a contradiction matrix can normally be used to analyze the problem. Thus, the contradiction matrix is the key analytical tool of TRIZ, as well as a basic technique for technical deconstruction and innovation.

The aim of TRIZ is to avoid conflicts between different elements. Hence, Altshuller identified 39 engineering parameters that often produce technical contradictions. In the matrix, each cell indicates the principles used to resolve

these contradictions. The matrix provides a fast and simple way to find solutions to technical contradictions. The matrix is a 39×39 matrix. To resolve the contradictions, Altshuller [14] proposed a set of 40 inventive principles. For each contradiction, several principles are suggested to resolve the contradiction. Selecting relevant inventive principles can help the user to produce a solution to the contradictions.

Loh et al. [15] argue that TRIZ is a method of knowledge extraction that can be applied systematically to resolve issues in the area of innovation and improvement. Nakagawa [16] argues that TRIZ is an advanced methodology, which uses a contradiction matrix and 40 inventive principles to provide clear answers to complex problems.

Figure 1 shows an example of a contradiction matrix. In the example, for the improving feature of the area of a moving object (5), the worsening feature is the volume of the moving object (7). From the contradiction matrix, we can identify four inventive principles (4, 7, 14, and 17) to resolve the contradiction. However, if we choose the improving and worsening parameters of productivity (39), we find that the contradiction matrix shows a blank cell, indicating the absence of inventive principles that can provide a solution to the problem. For information on the contradiction matrix and inventive principles, please see <http://www.innovation-triz.com/TRIZ40/>.

2.2. Taguchi's Method. Taguchi's method is derived from traditional experimental design methods. This method was developed by Genichi Taguchi in 1949. When applied in designing communication systems, it enables the number of experiments to be reduced and at the same time identifies problems in such systems [17]. The method advocates using the orthogonal array function combined with a simple function evaluation process to achieve improvements in the manufacturing process and product design [18].

Taguchi et al. [19] point out that Taguchi's method uses parameter design to improve quality; that is, for product target functions that need improvement, the factors and levels that affect the target functions are identified. Subsequently, orthogonal arrays are used to determine the configuration of the experimental factors and the number of experiments in order to obtain the same information provided by a full factorial experiment with a smaller number of experiments,

analyzing a small amount of experimental data to increase product quality effectively.

Zhang et al. [20] and Yildiz [21] point out that the main tools in Taguchi's method are orthogonal arrays and S/N ratios, emphasizing the importance of quality issues in the product or during the design and manufacturing process. A tolerance design is used to reduce product performance variation. ANOVA is then used to find the level of influence of each significant factor. The tolerance of each significant factor is set based on the costs of each factor, ensuring that product quality variation is minimal and achieving the most appropriate level of quality, thereby realizing robust design objectives.

Yildiz [22] points out that Taguchi's method applies engineering knowledge to experiment planning, focusing on solutions to achieve objectives. As the experimental results obtained by Taguchi's experimental design methods have a high degree of reproducibility, the configuration of experimental factors is straightforward, the number of experiments required is reduced, and the method of analysis is simple and easy to understand. Because of these advantages, Taguchi's method has been applied in many industries to improve and optimize design parameters. For instance, Su et al. [23] use Taguchi's dynamic approach to increase optical whiteness effectively. Hong [24] uses Taguchi's method to identify important factors in market segmentation. In addition, Celani de Souza et al. [25] have shown that Taguchi's method can improve the quality of dialysis. Yildiz [26] uses an immune algorithm and Taguchi's method to design a new design optimization framework.

Taguchi's method specifies the objective function as a certain signal-to-noise ratio (S/N ratio). According to this method, the S/N ratio for different quality characteristics can be separated into larger-the-better (LTB), nominal-the-best (NTB), and smaller-the-better (STB). This study is concerned with improving the uniformity of solder paste thickness in the solder paste printing process. Therefore, NTB is applied out of these quality characteristics. The calculation of the S/N ratio is shown in the following formula (1):

$$S/N_{\text{NTB}} = 10 \cdot \log_{10} \left(\frac{y^2}{s^2} \right), \quad (1)$$

where y is the sample mean and s is the sample standard deviation. The variability characteristic is inversely proportional to the S/N ratio. This means that a larger S/N ratio corresponds to a more robust system.

3. Research Methods

TRIZ and Taguchi's method are alternative experimental design methods used by enterprises to develop new products and improve product quality. The two approaches are often used separately. The TRIZ contradiction matrix enables technical variables that influence quality characteristics to be quickly identified. Although such an approach is able to identify inventive principles, it can only help users to speculate about solutions. The two methods show a wide variation in their experimental efficiency and additivity. Taguchi's

method can identify a more optimal value from preset factor levels. However, these variables do not necessarily have a significant effect on quality characteristics.

Therefore, this study attempts to combine TRIZ and Taguchi's method, screening variables that have a significant influence on quality characteristics by linking factors that cause uneven solder paste in the solder paste printing process to the 39 engineering parameters in the TRIZ contradiction matrix, before applying Taguchi's method to the screened variables to identify the optimum process parameter set. The steps are as follows.

- (1) Determine experimental variables: list the factors affecting the evenness of solder paste during the solder paste printing process, integrate the 39 engineering parameters in the TRIZ contradiction matrix to create a correlation table and produce a ranking, screening the variables that have a significant effect on quality characteristics.
- (2) Design and run experiment: use the orthogonal array function from Taguchi's method for experiment design, the number of repetitions, and conduct the experiment; calculate the S/N ratio and mean. Process managers, engineers, and quality assurance personnel select the levels based on the analysis and discussion of variables that have a significant influence and their range.
- (3) Optimization analysis: a two-phase optimization analysis is carried out on experimental data to identify the optimum combination and predict the optimum model for the manufacturing process.
- (4) Maximize the S/N ratio: this study uses the delta value and percent combination suggested by scholars to select important influence factors. We identified experiment factors with a delta value greater than the average effect value and a pooled error smaller than 15% as important influence factors and the point closest to the target level as the optimum level of influence factors.
- (5) Move the mean closer to the target value: at this stage, the selection has no effect on the S/N ratio. However, factors that have a significant effect on the mean are adjustable, moving the mean closer to the target value.
- (6) Forecast optimization: applying the additive model, the expected S/N ratio and estimated mean for the optimal combination condition are calculated based on the set levels of the significant influence factors.
- (7) Confirmation tests: confirmation experiments are run on the optimum combination produced using Taguchi's method. This result is then compared with the predicted results using Taguchi's method to confirm the improvement in results.

4. Case Study

4.1. Determine Experiment Variables. This study uses the SMT solder paste printing process for PCB production by

TABLE 1: Continued.

Technical parameters	Influence factors												
	1	2	3	4	5	6	7	8	9	10	11	12	13
	Work temperature	Work humidity	Solder paste type	Solder paste proportion	Squeegee angle	Squeegee pressure	Squeegee speed	Ejection speed	Solder paste poise	Stencil tensity	Squeegee stencil thickness	PCB flatness	Working platform flatness
37				V		V		V					V
38					V					V			V
39				V									V
Number of correlations	4	2	6	7	12	13	11	12	10	9	7	9	7
Ranking	12	13	11	8	2	1	4	2	5	6	8	6	8

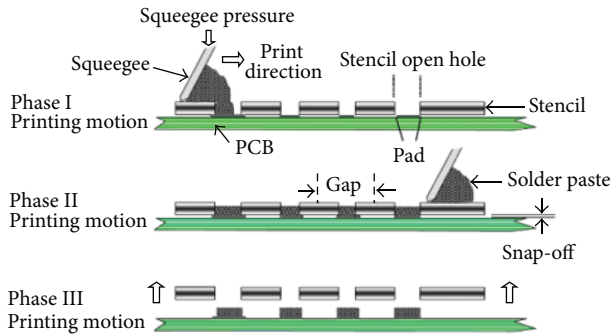


FIGURE 2: The solder paste printing process.

a multinational company as a case study to investigate the uniformity of solder paste application. The main purpose of solder paste in PCB is to fix parts to the PCB to ensure that the product functions normally. Solder paste printing is the first stage of the SMT manufacturing process. A stencil and solder paste printer squeeze are used to insert the solder paste onto corresponding pads in the PCB through holes in the board. After removing the stencil, the solder paste is left on the pad in the correct shape, completing the printing process, as shown in Figure 2.

Table 1 shows 13 factors that directly influence the thickness of solder paste during the SMT solder paste printing process used in the production of printed circuit boards as selected by process managers, engineers, and quality assurance personnel in the plant. These are then combined with 39 technical parameters in the TRIZ contradiction matrix to produce a correlation table showing the relationship between the 13 factors and 39 technical parameters. Finally, we screen the squeegee angle, squeegee pressure, squeegee speed, and ejection speed as the four variables that have a significant influence on quality characteristics.

4.2. Design and Run the Experiment. We carry out the experiment on the squeegee angle, squeegee pressure, squeegee speed, and ejection speed as the four variables that have a significant influence on quality characteristics. The experimental design uses the $L_9(3^4)$ orthogonal array function proposed by Taguchi's method. The process managers, engineers, and quality assurance personnel select the levels based on the analysis and discussion of their range. Because this study is aimed at improving the uniformity of solder paste thickness during the solder paste printing process, the quality characteristic applied is that of nominal-the-best (NTB). The calculation of the S/N ratio is shown in formula (1).

Based on the influence factor and level settings, nine sets of parameter values are input into the solder paste printer to carry out actual PCB printing. The experiment was repeated four times for each run order and the actual solder paste thickness data was recorded. The target value for solder paste thickness is set at 0.15 mm, with an upper limit of 0.20 mm and a lower limit of 0.10 mm. Table 2 shows the $L_9(3^4)$ orthogonal array and results for uniformity.

4.3. Optimization Analysis. Carry out optimization analysis on the experimental data and predict the optimal model for the experimental process.

4.3.1. Maximize the S/N Ratio. Analysis of the influence of each experiment factor (A , B , C , and D) on the uniformity was performed with an S/N response table, using a Minitab 16 software package.

Table 3 shows the orthogonal array and associated experimental results for uniformity with calculated S/N ratios. The S/N response table for uniformity is presented in Table 3. It shows the calculated S/N ratios for each level of experimental factors. The experimental factor that has the strongest influence is determined according to the value of delta as shown in Table 3. The value of delta equals the difference between maximum and minimum S/N ratios for a particular experimental factor. The higher the value of delta, the more influential the experimental factor. The experiment factors and their interactions are sorted in relation to the values of delta.

Following Lee [27], Sheu [28], and Yang's [29] recommendations, this study defines important influence factors as experimental factors that have a value of delta greater than the average effect size. It can be seen from Table 3 that the strongest influence was exerted by squeegee pressure (factor A), squeegee angle (factor B), and ejection speed (factor D).

The ANOVA procedure was used to investigate which design parameters significantly affect quality characteristics. The procedure is performed by separating the total variability of the S/N ratios into contributions by each of the design parameters and the errors. The total variability of the S/N ratio is measured by the sum of the squared deviations from the total mean S/N ratio.

Yildiz [30], Hong [24], Hsiang and Lin [31], and Su and Yeh [32] use percent contribution to carry out decision making. Percent contribution is the pure sum to squares (pure SS) for each factor as a ratio of the total sum to squares (total SS). When the pooled error percentage ($\rho_{err} \leq 15\%$), it can be assumed that no important factors have been omitted from the experiment; in other words, pooled error factors are not significant and can be neglected.

An examination of the calculated percent contribution for all experiment factors also shows a very high influence of factor A , factor B , and factor C on the S/N ratios (Table 4).

First, we find that the percent contributions of squeegee pressure (factor A), squeegee angle (factor B), and ejection speed (factor D) are 34.14%, 31.17%, and 19.81%, respectively. Second, the pooled error is less than 15% (14.88%). Therefore, we can assume that no important factors were missed. By analyzing the experiment factors and ANOVA, this study shows that squeegee pressure (factor A), squeegee angle (factor B), and ejection speed (factor D) have significant effects on the contraction rate.

Based on the above analysis, we are able to determine that squeegee pressure (factor A), squeegee angle (factor B), and ejection speed (factor D) are important influence factors in the present study.

TABLE 2: Experimental design using the $L_9(3^4)$ orthogonal array and results.

Run order	A Squeegee pressure	B Squeegee angle	C Squeegee speed	D Ejection speed	S/N ratio	Mean
1	1	1	1	1	21.2140	0.1725
2	1	2	2	2	21.5987	0.1700
3	1	3	3	3	25.8433	0.1600
4	2	1	2	3	23.3596	0.0850
5	2	2	3	1	19.8540	0.1475
6	2	3	1	2	25.8433	0.1600
7	3	1	3	2	18.1639	0.0775
8	3	2	1	3	20.8458	0.0900
9	3	3	2	1	20.1436	0.1525

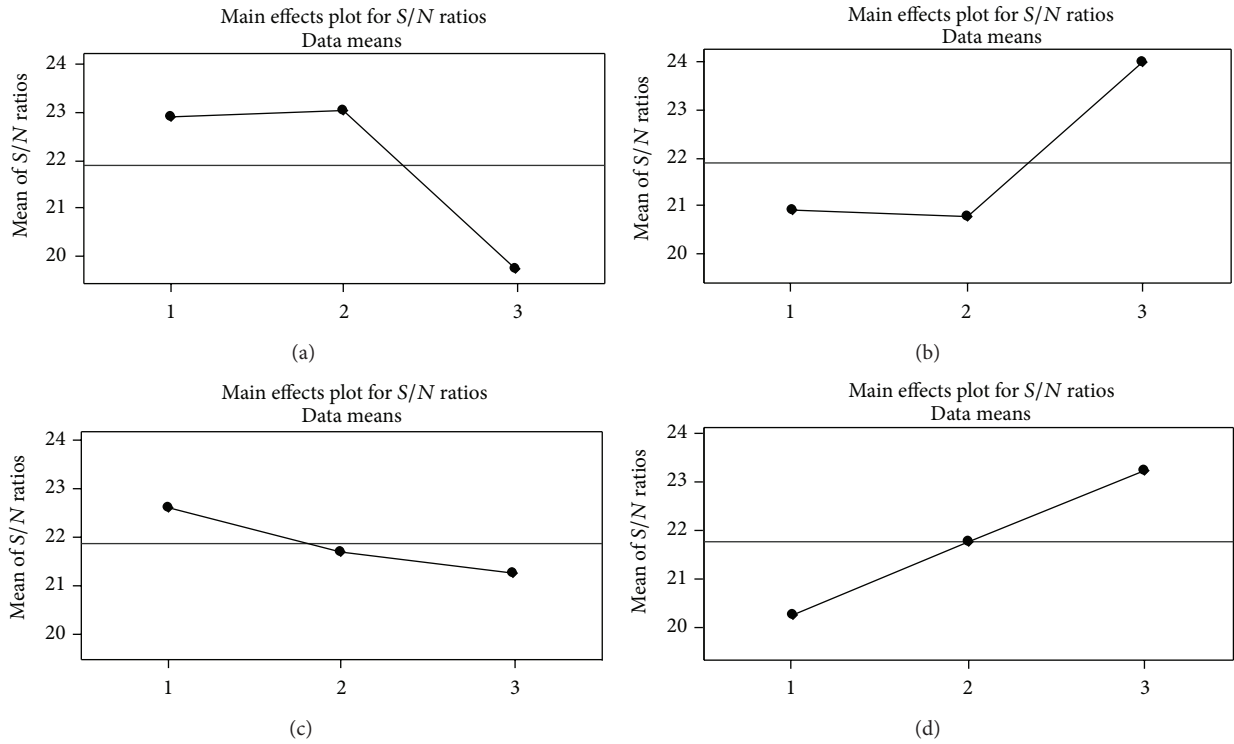


FIGURE 3: Main effect plots for S/N ratios. Signal-to-noise: nominal-the-best ($10 \cdot \log_{10}(y^2/s^2)$).

TABLE 3: S/N response table for uniformity.

Level	A	B	C	D
1	22.89	20.91	22.63	20.40
2	23.02	20.77	21.70	21.87
3	19.72	23.94	21.29	23.35
Delta	3.30	3.18	1.35	2.95
Average	2.695			
Rank	1	2	4	3

The plots for S/N ratios are shown in Figure 3. The optimal levels for each experiment factor can be easily determined from these graphs in accordance with Taguchi’s “nominal-the-best” performance characteristic. Response

graphs show a variation in the S/N ratios when the setting of the experimental factors is changed from one level to another. Figure 3 suggests that the optimum condition for the uniformity is the combination of A_2 , B_3 , and D_3 levels of the respective experiment factors.

4.3.2. *Moving the Mean Closer to the Target Value.* At this stage, we select appropriate adjustment factors (with no effect on the S/N ratio, but a significant effect on the mean) to move the mean closer to the target value. Table 5 shows the calculated mean for each level of experiment factors. Table 5 shows that squeegee pressure (factor A), squeegee angle (factor B), and ejection speed (factor D) should be selected as factors that have a significant influence on the mean. However, the above three factors also have a significant

TABLE 4: Results of the analysis of variance for S/N ratios.

Source	DF	SS	MS	F	Pure SS	Contribution (%)
A	2	20.949	10.475	7.33	18.891	34.14%
B	2	19.303	9.651	6.75	17.245	31.17%
D	2	13.016	6.508	4.55	10.958	19.81%
$C + \text{error}$	2	2.058	1.429	—	—	—
Pooled error	(2)	(2.058)	(1.429)	—	8.232	14.88%
Total	8	55.326	—	—	55.326	100%

TABLE 5: Means response table for uniformity.

Level	A	B	C	D
1	0.1675	0.1117	0.1408	0.1575
2	0.1478	0.1358	0.1358	0.1358
3	0.1067	0.1575	0.1283	0.1117
Delta	0.0608	0.0458	0.0125	0.0458

influence on the S/N ratio. Therefore, we do not select any adjustment factors in this step.

Examination of the calculated percent contribution for all experiment factors also shows a very high influence of factor A , factor B , and factor D on the means: see Table 6.

First, we find that the percent contributions of squeegee pressure (factor A), squeegee angle (factor B), and ejection speed (factor D) are 44.29%, 23.96%, and 23.96%, respectively. From the aforementioned analysis, we are able to determine that squeegee pressure (factor A), squeegee angle (factor B), and ejection speed (factor D) have significant effects on the contraction rate for means.

Based on the previous discussion, this study sets the optimal factor level to $A_2 B_3 C_1 D_3$.

4.3.3. Forecast Optimization. Based on the previous discussion, this study sets the optimal factor level to $A_2 B_3 C_1 D_3$. Therefore, the additive model is used to estimate the expected S/N ratio and mean under optimal conditions.

The mean S/N ratio for the nine experiments is $\bar{\eta} = 21.874$ db, and the predicted S/N ratio under optimal conditions is

$$\begin{aligned}\hat{\eta} &= \bar{\eta} + (A_2 - \bar{\eta}) + (B_3 - \bar{\eta}) + (D_3 - \bar{\eta}) \\ &= 23.02 + 23.94 + 23.35 - (2 * 21.874) \\ &= 26.562 \text{ db.}\end{aligned}\quad (2)$$

Similarly, the mean observation for the nine experiments is $\bar{y} = 0.1350$ mm, and the predicted mean under optimal conditions is

$$\begin{aligned}\hat{y} &= \bar{y} + (A_2 - \bar{y}) + (B_3 - \bar{y}) + (D_3 - \bar{y}) \\ &= 0.1478 + 0.1575 + 0.1117 - (2 * 0.1350) \\ &= 0.147 \text{ mm.}\end{aligned}\quad (3)$$

4.4. Confirmation Tests. The confirmation experiment under optimal conditions produced 25 individual values and 5 S/N

ratios. To confirm that optimal conditions can be reproduced, it is necessary to estimate the confidence interval of the S/N and mean. Su [33] recommends using the formula proposed by Ross [34] to calculate the confidence interval in order to facilitate confirmation experiments. Some scholars [35, 36] suggest that the S/N ratio should be within ± 3 db of the optimal value as the basis for assessing the confidence interval in reproduced experiments. Therefore, combining the aforementioned recommendations, this study uses Ross' proposed formula to calculate the confidence interval. However, when the calculated confidence interval exceeds ± 3 db, the level is set at ± 3 db:

$$CI = \sqrt{F_{\alpha,1,v_2} \times V_e \times \left[\frac{1}{n_{\text{eff}}} + \frac{1}{r} \right]}, \quad (4)$$

where CI is the confidence interval, $F_{\alpha,1,v_2}$ is value F at the significance level, α , α is the significance level, V_2 is the degree of freedom of the pooled error, V_e is the variance of the pooled error, n_{eff} is the effective number of observations, and r is the number of repeated confirmation experiments.

The S/N ratio and mean confidence intervals for confirmation experiments under optimal conditions are

$$\begin{aligned}CI_{S/N} &= \sqrt{F_{\alpha,1,v_2} \times V_e \times \left[\frac{1}{n_{\text{eff}}} + \frac{1}{r} \right]} \\ &= \sqrt{18.51 \times 1.429 \times \left[\frac{7}{9} + \frac{1}{5} \right]} \\ &= 5.09 \text{ db,}\end{aligned}\quad (5)$$

as $CI_{S/N} = 5.09$ db > 3 db; therefore the S/N ratio confidence interval is ± 3 db,

$$\begin{aligned}CI_{\text{mean}} &= \sqrt{F_{\alpha,1,v_2} \times V_e \times \left[\frac{1}{n_{\text{eff}}} + \frac{1}{r} \right]} \\ &= \sqrt{18.51 \times 0.000119 \times \left[\frac{7}{36} + \frac{1}{25} \right]} \\ &= 0.023 \text{ mm.}\end{aligned}\quad (6)$$

The average of the five confirmation experiments is as follows: S/N ratio = 26.632 db and mean = 0.155 mm. These two values fall entirely within the corresponding confidence intervals, indicating that the experiment achieved an improvement. The comparison of values before improvement

TABLE 6: Results of the analysis of variance for means.

Source	DF	SS	MS	F	Pure SS	Contribution (%)
A	2	0.005629	0.002815	23.70	0.005392	44.29%
B	2	0.003154	0.001577	13.28	0.002917	23.96%
D	2	0.003154	0.001577	13.28	0.002917	23.96%
C + error	2	0.000237	0.000119		—	—
Pooled error	(2)	(0.000237)	(0.000119)		0.000949	7.79%
Total	8	0.012175			0.012175	100%

TABLE 7: Comparison of values before improvement (current), forecast optimization, and confirmation experiments.

	Before improvement (current)	Forecast optimization	Confirmation experiment
S/N ratio	21.732db	26.562 db	26.632 db
Mean	0.163 mm	0.147 mm	0.155 mm

(current), forecast optimization, and confirmation experiments is shown in Table 7.

Confirmation experiments are run on the optimum combination produced using Taguchi's method. This result is then compared with the predicted results using Taguchi's method to confirm the improvement in results.

5. Conclusion

In this study, the S/N ratio improved from 21.732 db to 26.632 db, while the mean also improved from the current 0.163 mm to 0.155 mm, indicating a reduced variation. In addition, the mean was closer to the target value (0.15 mm), showing that applying TRIZ and Taguchi's method for improving the uniformity of solder paste thickness in the solder paste printing process is feasible.

This study revised the TRIZ contradiction matrix to investigate the correlation between contradiction matrix parameters and parameters that directly influence the uneven thickness of solder paste in the solder paste printing process, screening the squeegee pressure, ejection speed, squeegee speed, and squeegee angle as the key parameters affecting the quality of SMT solder paste thickness. This is an innovative approach that is empirically shown to be feasible.

Taguchi's method is used to establish an optimal parameter set from the experimental data, with the prediction error rate reaching the required accuracy and delivering real improvements in process capability and product quality. These improvements can help lower the defect rate and reduce production costs, while shortening delivery times and increasing customer satisfaction. These results may help Taiwan's SMT assembly factories to increase product quality, explore further different machines and productivity factors, and compare different level parameters to produce even better process parameters for realizing additional quality improvements.

References

- [1] W.-P. Wang, "Evaluating new product development performance by fuzzy linguistic computing," *Expert Systems with Applications*, vol. 36, no. 6, pp. 9759–9766, 2009.
- [2] A. R. Yildiz and K. Saitou, "Topology synthesis of multicomponent structural assemblies in continuum domains," *Journal of Mechanical Design*, vol. 133, no. 1, Article ID 011008, 2011.
- [3] T. Yang, T.-N. Tsai, and J. Yeh, "A neural network-based prediction model for fine pitch stencil-printing quality in surface mount assembly," *Engineering Applications of Artificial Intelligence*, vol. 18, no. 3, pp. 335–341, 2005.
- [4] T.-N. Tsai, "Modeling and optimization of stencil printing operations: a comparison study," *Computers and Industrial Engineering*, vol. 54, no. 3, pp. 374–389, 2008.
- [5] Y.-S. Lai and T. H. Wang, "Optimal design towards enhancement of board-level thermomechanical reliability of wafer-level chip-scale packages," *Microelectronics Reliability*, vol. 47, no. 1, pp. 104–110, 2007.
- [6] A. R. Yildiz, "Hybrid taguchi-harmony search algorithm for solving engineering optimization problems," *International Journal of Industrial Engineering: Theory Applications and Practice*, vol. 15, no. 3, pp. 286–293, 2008.
- [7] A. R. Yildiz, "Optimization of cutting parameters in multi-pass turning using artificial bee colony-based approach," *Information Sciences*, vol. 220, pp. 399–407, 2013.
- [8] I. Durgun and A. R. Yildiz, "Structural design optimization of vehicle components using Cuckoo search Algorithm," *Materials Testing*, vol. 54, no. 3, pp. 185–188, 2012.
- [9] A. R. Yildiz and K. N. Solanki, "Multi-objective optimization of vehicle crashworthiness using a new particle swarm based approach," *International Journal of Advanced Manufacturing Technology*, vol. 59, no. 1-4, pp. 367–376, 2012.
- [10] B. Andersen and T. Fagerhaug, *Root Cause Analysis: Simplified Tools and Techniques*, American Society for Quality, Milwaukee, Wis, USA, 2006.
- [11] V. E. Kane, "Process capability indices," *Journal of Quality Technology*, vol. 18, no. 1, pp. 41–52, 1986.
- [12] G. S. Altshuller, *Creativity as an Exact Science*, Gordon & Breach Science, New York, NY, USA, 1984.
- [13] M. Sawaguchi, "A study of systematic innovation based on an analysis of big hits," in *Proceedings of the ETRIA TRIZ Future Conference*, pp. 143–151, Bergamo, Italy, 2010.
- [14] G. Altshuller, *40 Principles: TRIZ Keys to Technical Innovation*, Technical Innovation Center, 1998.
- [15] H. T. Loh, C. He, and L. Shen, "Automatic classification of patent documents for TRIZ users," *World Patent Information*, vol. 28, no. 1, pp. 6–13, 2006.

- [16] T. Nakagawa, "Overall dataflow structure for creative problem solving in triz/usit," in *Proceedings of the 7th TRIZCON Conference*, 2005.
- [17] G. E. P. Box, J. S. Hunter, and W. G. Hunter, *Statistics for Experimenters: An Introduction to Design, Data Analysis, and Model Building*, John Wiley & Sons, New York, NY, USA, 2nd edition, 2010.
- [18] A. R. Yildiz, "A new hybrid particle swarm optimization approach for structural design optimization in automotive industry," *Journal of Automobile Engineering*, vol. 226, pp. 1340–1351, 2012.
- [19] G. Taguchi, S. Chowdhury, and Y. Wu, *Taguchi's Quality Engineering Handbook*, John Wiley & Sons, New York, NY, USA, 2004.
- [20] J. Z. Zhang, J. C. Chen, and E. D. Kirby, "Surface roughness optimization in an end-milling operation using the Taguchi design method," *Journal of Materials Processing Technology*, vol. 184, no. 1-3, pp. 233–239, 2007.
- [21] A. R. Yildiz, "A new hybrid artificial bee colony algorithm for robust optimal design and manufacturing," *Applied Soft Computing*, vol. 13, no. 5, pp. 2906–2912, 2013.
- [22] A. R. Yildiz, "Hybrid Taguchi-differential evolution algorithm for optimization of multi-pass turning operations," *Applied Soft Computing Journal*, vol. 13, pp. 1433–1439, 2012.
- [23] C.-T. Su, C.-M. Lin, and C.-C. Hsu, "Optimization of the optical whiteness ratio for flexible display by using Taguchi's dynamic approach," *IEEE Transactions on Semiconductor Manufacturing*, vol. 25, no. 1, pp. 2–15, 2012.
- [24] C.-W. Hong, "Using the Taguchi method for effective market segmentation," *Expert Systems with Applications*, vol. 39, no. 5, pp. 5451–5459, 2012.
- [25] H. J. Celani de Souza, C. B. Moyses, F. J. Pontes et al., "Molecular assay optimized by Taguchi experimental design method for venous thromboembolism investigation," *Molecular and Cellular Probes*, vol. 25, no. 5-6, pp. 231–237, 2011.
- [26] A. R. Yildiz, "A new design optimization framework based on immune algorithm and Taguchi's method," *Computers in Industry*, vol. 60, no. 8, pp. 613–620, 2009.
- [27] H. H. Lee, *Quality Management*, Tsang Hai Book Publishing, Taipei, Taiwan, 2009.
- [28] S. H. Sheu, *The Management and Control of Quality*, Future Career Publishing Corporation, Taipei, Taiwan, 2007.
- [29] S. F. Yang, *Quality Management*, Hwa Tai Publishing, Taipei, Taiwan, 2006.
- [30] A. R. Yildiz, "Comparison of evolutionary based optimization algorithms for structural design optimization," *Engineering Applications of Artificial Intelligence*, vol. 26, no. 1, pp. 327–333, 2013.
- [31] S.-H. Hsiang and Y.-W. Lin, "Optimization of the extrusion process for magnesium alloy sheets using the fuzzy-based Taguchi method," *Arabian Journal for Science and Engineering*, vol. 34, no. 1, pp. 175–185, 2009.
- [32] C.-T. Su and C.-J. Yeh, "Optimization of the Cu wire bonding process for IC assembly using Taguchi methods," *Microelectronics Reliability*, vol. 51, no. 1, pp. 53–59, 2011.
- [33] C. T. Su, *Quality Engineering*, Chinese Society for Quality, Taipei, Taiwan, 2009.
- [34] P. J. Ross, *Taguchi Techniques for Quality Engineer*, McGraw-Hill, New York, NY, USA, 1996.
- [35] Y. M. Chen, *Taguchi Methods*, Tingmao, Taipei, Taiwan, 2012.
- [36] K. Tatebayashi, *Introduction Taguchi Method*, Union of Japanese Scientists and Engineers, Tokyo, Japan, 2004.

Research Article

Modelling of Ballistic Impact over a Ceramic-Metal Protection System

Leandro Neckel,¹ Dachamir Hotza,² Daniel Stainer,³
Rolf Janssen,⁴ and Hazim Ali Al-Qureshi⁵

¹ Universidade do Extremo Sul Catarinense (UNESC), Unidade Acadêmica de Ciências, Engenharias e Tecnologia, 88806-000 Criciúma, SC, Brazil

² Universidade Federal de Santa Catarina (UFSC), Centro Tecnológico, Departamento de Engenharia Química, 88040-900 Florianópolis, SC, Brazil

³ Construções Mecânicas Cocal Ltda, 88845-000 Cocal do Sul, SC, Brazil

⁴ Hamburg University of Technology (TUHH), Institute of Advanced Ceramics, 21073 Hamburg, Germany

⁵ Universidade Federal de Santa Catarina (UFSC), Centro de Engenharia da Mobilidade, 89218-000 Joinville, SC, Brazil

Correspondence should be addressed to Dachamir Hotza; dhotza@gmail.com

Received 24 February 2013; Revised 26 September 2013; Accepted 1 October 2013

Academic Editor: Augusto Deus

Copyright © 2013 Leandro Neckel et al. This is an open access article distributed under the Creative Commons Attribution License, which permits unrestricted use, distribution, and reproduction in any medium, provided the original work is properly cited.

The behavior of ceramic-metal protection against a projectile impact is modeled. The model takes into account the mass and velocity for each stage of the phenomenon. A former model was modified considering more realistic parameters such as geometries and deformation profile. To analyze the model, simulations on different parameters have been run. The impact results of different ballistic projectiles were simulated, and the movement was plotted. In addition, a deterministic simulation on the mechanical properties of the back metal plate properties was done.

1. Introduction

Gonçalves et al. [1] have developed a mathematical approach to the behavior of a two-layer system protection of ceramic-metal system against high speed impact. The scheme of the protection is presented in Figure 1. The ceramic layer erodes the projectile, and the back metal plate is responsible for absorbing the remaining energy by plastic deformation. The mathematical model separates the penetration into three different stages and proposes a deterministic equation that explains the deflection of the metal plate. The movement equations were manipulated to find a single problem for velocity and mass separately for each stage. The data and initial parameters provided by the original work [1] were used for the differential equations found. The metal deformity was reevaluated by deducing the deterministic equation. A more realistic shape parameter was considered for the postimpact curvature, and the volume approach was improved. Finally, the solution was plotted and compared to former results [1].

The model was better understood once the solutions were used to simulate different impacts over the system. Initially, properties of some ballistic projectiles were used to prevent the shock absorption. In addition, the mechanical properties of the metallic plate were modified intending to observe the effect on the final deformation.

A previous work [2] has focused on the study of the movement evolution of the projectile. This work has continued to analyze the penetration of the projectile searching for the understanding of the final deformation.

The set of data generated in the simulations together with the newly developed equations for impact and shock absorption were, in conclusion, observed as an advance for the understanding of high speed impact phenomena.

2. Materials and Methods

The software Maplesoft Maple V12 was used to solve the system. Gonçalves et al. work [1] provided all materials,

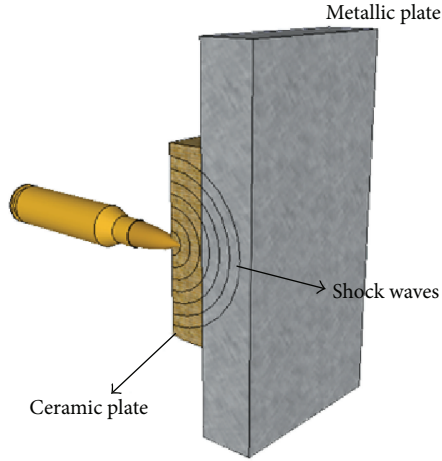


FIGURE 1: Proposal of a two-layer protection made by Gonçalves et al. [1].

constant values, and initial parameters necessary. Moreover, the projectile specifications used were from rifle bullets.

The mathematical model of the penetration process is divided into three stages. The first represents the initial impact and erosion of the head of the projectile. In this situation there is no penetration into the protection. The force against the projectile is

$$m(t) \frac{d}{dt} v(t) = -YA_p, \quad (1)$$

and the variation in the geometry is given by

$$\frac{d}{dt} m(t) = -A_p \rho_p v(t), \quad (2)$$

where Y is the dynamic yielding of the projectile and A_p is the effective contact area of the projectile. Also, ρ_p is the density of the projectile's material. According to Tabor [3], the dynamic hardness of a metal is the pressure with which it resists local indentation by a rapidly moving indenter. The first approximation for the Y value is a constant and not necessarily the same as the static pressure necessary to cause plastic flow. The actual value of the dynamic yield pressure strongly depends on the velocity of the impact and the projectile geometry. Tabor [3] also cites different methods to estimate this value. For simplification, following the original work [1], this value will be considered a fraction of the static hardness of the projectile material.

The impact generates a shock wave that travels through the material and reflects back cracking the ceramic plate. This shock wave is extremely fast and runs through the protection in a small fraction of a second. Theoretically, the sum of the incoming with the returning wave generates a region of high stress. This region is easily observed as a cone in the solids, which fits with the cracking region. Figure 2 demonstrates a single scheme for the initial impact and the propagating shock waves.

The shape and size of the ceramic tile can also affect the protection performance. The crack cone formation allows the

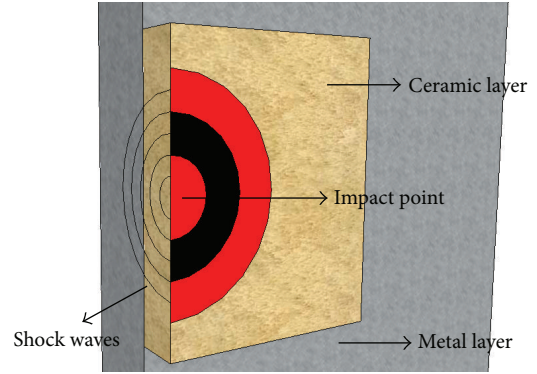


FIGURE 2: First stage of the impact. The collision generates a shock wave that travels through the armor.

necessary scattering to provide enough ceramic particles for the projectile erosion. With smaller geometry, the crack cone would not be properly formed once the constructive interference of the shock waves would not only occur longitudinally but also transversally. Those considerations were not taken into account in this model.

In the second stage the penetration starts pushing an interface projectile-ceramic with velocity $u(t)$. This interface is a small portion of ceramic in contact with the projectile which moves together but with different initial velocity. Thus, the force against the projectile is the same, but the difference of the velocities $v(t)$ and $u(t)$ gives the erosion ratio:

$$\frac{d}{dt} m(t) = -A_p \rho_p (v(t) - u(t)). \quad (3)$$

It is important to note that the erosion ceases when $u(t)$ is equal to $v(t)$. In this moment, the interface reaches the same velocity as the projectile. With this, if there is no difference between both velocities, there is no stress applied in the projectile or interface material.

The modified hydrodynamic theory given by Tate [4] introduced the dynamic yielding (Y) and the resistance against penetration (R) adopted for the ceramic in this case. Tate's law is given by

$$Y + \frac{1}{2} \rho_p (v(t) - u(t))^2 = R + \frac{1}{2} \rho_c u(t)^2, \quad (4)$$

where ρ_c is the density of the ceramic material. Tate's equation is used as an important auxiliary equation to solve the model. This will be present in the next section of this work.

The second stage ends when $v(t) = u(t)$. After this, the final fraction of the movement is given by

$$m_{pr} \frac{d}{dt} v(t) = -RA_p, \quad (5)$$

where m_{pr} is the remaining mass of the projectile. The metal plate absorbs the final kinetic energy by plastic deformation. Simultaneously to the penetration of the projectile, the metallic base will move and will be deformed elastically. However, the energy produced by this elastic energy will

be low and will be neglected [1]. Once the first and second stage end, the main part of the projectile kinetic energy is absorbed by ceramic scattering and projectile erosion and can be computed using m_{pr} and the velocity obtained in the beginning of the third stage. Due to the deceleration of the bullet caused by the ceramic layer, the metallic plate may not be perforated. In this case, the secondary layer will suffer plastic deformation, and the plastic energy consumed by the plate can be expressed in terms of effective stress and strain as

$$E_p = \int_v \left(\int_0^{\bar{\varepsilon}} \bar{\sigma} d\bar{\varepsilon} \right) dV. \quad (6)$$

It is considered a stress-strain curve given by the power law

$$\bar{\sigma} = A \cdot (\bar{\varepsilon})^n \quad (7)$$

and the deflection profile of the plate given by

$$w(r) = w_0 e^{(-kr/D)}, \quad (8)$$

where w_0 is the maximum deflection of the dimple shape, D (m) is the radius of the projectile, k (dimensionless) is a deflection profile constant that can be determined experimentally, and r (m) is the radial distance of the impacting projectile center.

Assuming that the material will be bulged in an axis symmetric mode, the effective strain can be written in terms of the radial strain as

$$\bar{\varepsilon} = 2\varepsilon_r. \quad (9)$$

For a small displacement, the radial strain can be approximated to [1, 5, 6]

$$\varepsilon_r = \frac{1}{2} \left(\frac{\partial}{\partial r} w(r) \right)^2. \quad (10)$$

Considering a geometry of a small dimple given by $2\pi r h \delta r$, where h is the thickness of the plate [7, 8], the manipulation of the equations gives

$$E_p = \frac{2\pi h A}{n+1} \left(-\frac{k w_0}{D} \right)^{2(n+1)} \int_0^\infty e^{[-kr(2n+2)/D]} r \partial r. \quad (11)$$

Considering the physical nature of most constants, it is possible to suppress the negative sign generated by the derivation demonstrated in (11). Also, the radial variation of the deflection profile is mirrored in the x -axis, which demonstrates that this ratio can be used as its own module. Now it gives

$$E_p = \frac{2\pi h A}{n+1} \left(\frac{k w_0}{D} \right)^{2(n+1)} \int_0^\infty e^{[-kr(2n+2)/D]} r \partial r. \quad (12)$$

The solution for the expression is given by

$$E_p = \frac{1}{2} \frac{\pi h A (k/D)^{2n} w_0^{2(n+1)}}{(n+1)^3}. \quad (13)$$

After the initial impact, the movement of the interface starts deforming the metallic plate. It can be argued that, initially, the metal layer is compressed due to high pressure generated by the impact. In addition, the plate does not move significantly because of the low interface velocity. In this way, it is possible to affirm that the deflection of stainless steel plate starts at the end of the second stage of penetration.

Considering that the plastic energy absorbed by the metal plate is equal to the kinetic energy of the projectile in the end of the second stage, it is possible to write the final deflection of the plate as

$$w_0 = \left(\frac{m_{pr} v_p^2 (n+1)^3}{\pi h A (k/D)^{2n}} \right)^{1/(2n+2)}, \quad (14)$$

where v_p is the velocity of the projectile at the end of the second stage.

3. Results and Discussion

The movement solutions were obtained divided by the stages and by mass and velocity. The equations needed to be manipulated together to find a unique solvable problem for mass and velocity for each stage. First it was necessary to find a differential equation with a unique function. For the first stage it was

$$\frac{d^2}{dt^2} v(t) = -\frac{\rho_p v(t) ((d/dt) v(t))^2}{Y} \quad (15)$$

for the velocity and

$$\frac{d^2}{dt^2} m(t) = \frac{Y A^2 \rho_p}{m(t)} \quad (16)$$

for the mass. The auxiliary Tate's equation was used in the manipulation to formulate a second degree equation with the function $u(t)$ as a result. Naturally, one of the results was not considered due to its particularity for being a complex solution, which does not have a physical interpretation. The $u(t)$ written as a function of $v(t)$ could be used to formulate the second stage equations. These sentences are given by

$$\begin{aligned} & \frac{d^2}{dt^2} v(t) \\ &= \left(\rho_p \left(\frac{d}{dt} v(t) \right)^2 \right. \\ & \quad \times \left(v(t) (2\rho_p - \rho_c) \right. \\ & \quad \left. \left. + \sqrt{2\rho_p R - 2\rho_p Y + 2\rho_c Y - 2\rho_c R + \rho_c \rho_p v(t)^2} \right) \right) \\ & \quad \times \left(Y (\rho_c - \rho_p) \right)^{-1} \end{aligned} \quad (17)$$

for the velocity and

$$\begin{aligned} & \frac{d^2}{dt^2} m(t) \\ &= - \left(YA^2 \rho_c \rho_p \right. \\ & \quad \left. \times \left(m(t) \left(-\rho_c + \frac{((d/dt) m(t)) \rho_c \rho_p}{\sqrt{((d/dt) m(t))^2 \rho_c \rho_p - 2\rho_c \rho_p^2 A_p^2 R + 2\rho_c \rho_p^2 A_p^2 Y}} \right) \right)^{-1} \right) \end{aligned} \quad (18)$$

for the mass. For the deflection of the metal plate, the new deflection profile was adopted considering the null derivative in $r = 0$:

$$w(r) = w_0 e^{(-k_{\text{mod}} r^2/D)}, \quad (19)$$

where w_0 is the maximum deflection of the dimple shape, D (m) is the radius of the projectile, k_{mod} (m^{-1}) is a modified deflection profile constant, which is determined experimentally, and r (m) is the radial distance of the impacting projectile center.

Also, the dimple shape after the impact, shown by Figure 3, was then approximated to the volume of a small paraboloid given by

$$dV = \frac{4}{3} \pi r h dr. \quad (20)$$

The newly deduced metal final deformity equation is now given by

$$\begin{aligned} w_0 = & \left(D \left(\frac{1}{2} (m_{pr} v_{pr}^2 (n+1)) \right. \right. \\ & \times \left(A\pi h \cdot \Gamma \left(n + \frac{5}{2} \right) \right. \\ & \quad \left. \left. \cdot \left(\frac{2k_{\text{mod}} (n+1)}{D} \right)^{-n-(5/2)} \right)^{-1} \right)^{1/(2n+2)} \\ & \times (2k_{\text{mod}})^{-1}, \end{aligned} \quad (21)$$

where k_{mod} is the modified profile constant and Γ is the mathematical gamma function, which is an extension of the factorial function, with its argument shifted down by 1, to real and complex numbers.

In addition, for a solid two-layered system, it is necessary to consider the time needed for the generated wave to reflect in the back part of the protection and return to the initial point and, furthermore, start to crack the ceramic layer. The time needed for the wave to travel and reflect back is given by

$$t_i = \frac{2e_c}{c_c} + \frac{2e_m}{c_m}, \quad (21)$$

where e_c and c_c are, respectively, the thickness and the longitudinal velocity of sound for the ceramic material and e_m and c_m are the same constants for the metallic material. It is known that the shock wave travels with the longitudinal

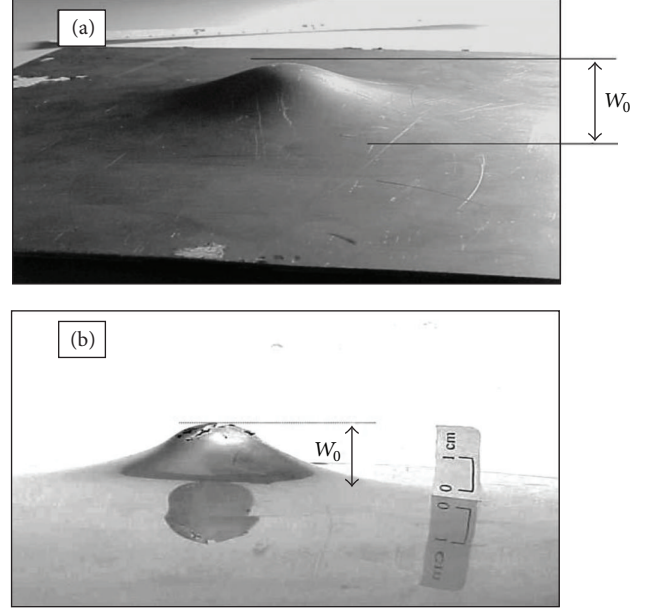


FIGURE 3: Shape of the metallic plate after impact.

TABLE 1: Properties of the steel nucleus of the projectile.

Property	Value
Initial velocity (m/s)	835
Mass (g)	9.54
Vicker's hardness (HV)	8175
Dynamic yield stress (GPa)	2.82
Density (g/cm^3)	8.41
Diameter (mm)	7.62

velocity of sound in the solid, and this velocity can be calculated by [9]

$$c = \sqrt{\frac{E}{\rho}}, \quad (22)$$

where E is the elastic modulus of the material.

The substitution of (22) in (21) gives

$$t_i = 2e_c \sqrt{\frac{\rho_c}{E_c}} + 2e_m \sqrt{\frac{\rho_m}{E_m}}, \quad (24)$$

where E_c and E_m are the elastic modulus for the ceramic and metallic material, respectively.

The first results were obtained using the projectile and system data presented in the former work [1]. Table 1 presents the projectile data. In the former work, basically two different compositions were used for the ceramic plate during the experimental tests. The composition and reference properties of the ceramic plates are shown in Tables 2 and 3, respectively.

In Figures 4(a) and 4(b), the upper curve, $v(t)$, corresponds to the projectile velocity and the lower curve, $u(t)$,

TABLE 2: Ceramic compositions.

Composition	Al ₂ O ₃ A-1000SG (wt.%)	Al ₂ O ₃ Tubular T-60 (wt.%)	TiO ₂ (wt.%)
B	90	8	2
C	85	13	2

TABLE 3: Mechanical and physical properties of the ceramic plates.

Property	Composition	
	B	C
Weibull modulus (m)	8.4	8.8
Mean strength parameter, σ_{50} (MPa)	175.0	171.3
Reference rupture strength, σ_0 (MPa)	182.8	178.5
Vicker's hardness (HV)	1551.4	1259.8
Resistance against penetration on ceramic, R_c (GPa)	4.43	3.60
Density (g/cm ³)	3.90	3.80
Average grain size (μm)	18 ± 8	22 ± 9

TABLE 4: Fraction of loss of velocity, mass and energy of the projectile in the three stages (adapted from previous work [2]).

Stage	Velocity loss (%)	Erosion (%)	Absorbed energy (%)
1st	10.62	19.18	35.73
2nd	30.27	40.77	50.32
3rd	59.10	—	13.93

shows the equivalent results obtained in a previous work [1, 2]. Figure 4(a) presents the results obtained in this work, and Figure 4(b) shows the former work [1] results.

In both graphs it is possible to observe the different stages of penetration in the graph. During the first stage, there is no interface velocity. In the beginning of the second stage, the interface begins to move tending to reach the same velocity as the projectile. The third and final stage begins with the projectile and interface velocities equalized. During this final fraction of the movement, both projectile and interface decelerate together. With the solutions it is possible to estimate the fraction of mass, velocity, and energy lost in each stage. These values are presented in Table 4.

There were more two ceramic compositions presented in the material selection. However, both of these structures were not stable enough to be molded in the system.

The values of the constants were given by the former work [1] together with the initial velocities and mass. The different ceramic plate thicknesses tested by the authors of the former work are also declared in the table. In addition, the first stage duration, calculated using (24), is also presented due to the different thickness and composition. Most of the constants and mechanical properties [10, 11] used in the model are presented in Table 5.

These data (21) together with the solved movement equations can give the results for the maximum deflection

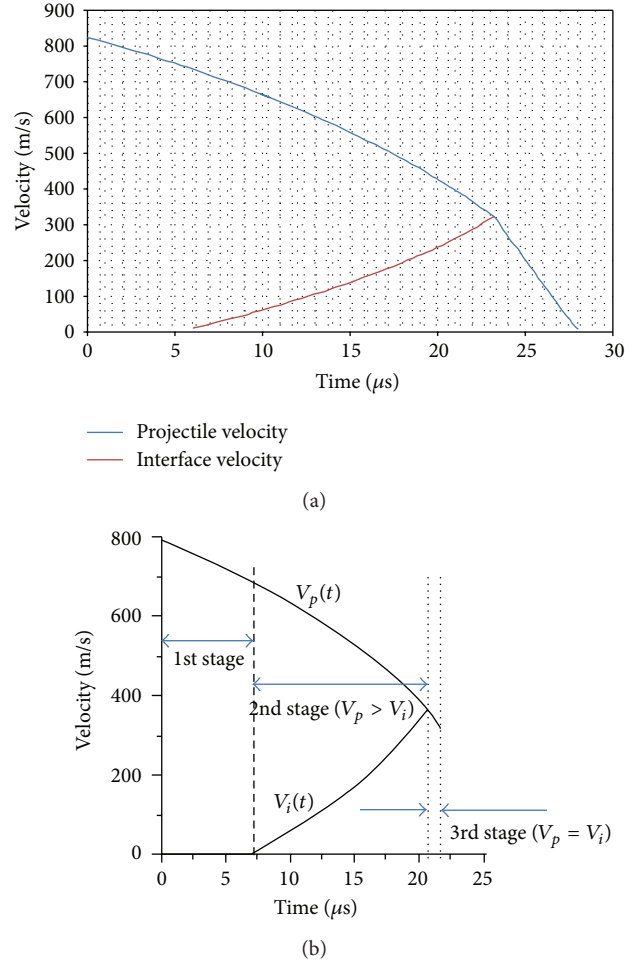


FIGURE 4: Velocity against time for (a) this work and (b) previous work [1, 2], respectively.

of the back metal plate. The comparisons are presented in Table 6. It is possible to note that the proportional errors both in the original and in the modified theory (OT and MT) are of the same magnitude. This fact is related to the simplicity of the model and the amount of neglected variable in the energy absorption, such as impact angle, ceramic porosity, and metal grain size, among others.

However, the results of the maximum deflection showed that the new theories can generate good results not only for the high speed impacts, but also for lower velocities, differently from the former theory. Simulations for different calibers [12] were performed using the new developed theory. The tested calibers with their specification are shown in Table 7. The movement evolutions for the different calibers are presented in Figure 5. Finally, the results are presented in Table 8. In addition, Table 8 also presents the penetration into the ceramic layer by each simulated caliber. This can be calculated by numeric integration of second stage movement equations, considering that the main penetration occurs in this stage.

TABLE 5: Values of the constants used in the modified model.

Symbol	Property	Value	
ρ_c	Ceramic density (g/cm ³)	Composition B 3.9	Composition C 3.8
E_c	Ceramic elastic modulus (GPa)	300	
e_c	Ceramic thickness (mm)	11.3	9.3
R_c	Resistance against penetration on ceramic (GPa)	Composition B 4.43	Composition C 3.60
ρ_m	Metal density (g/cm ³)	7.77	
E_m	Metal elastic modulus (GPa)	193	
e_m and h	Metal thickness (mm)	15	
A	Metal strength (MPa)	935	
n	Metal hardening exponent	0.29	
k_{mod}	Metal modified deflection profile constant (m ⁻¹)	0.0018	
Y	Projectile dynamic yielding (GPa)	2.82	
ρ_p	Projectile density (g/cm ³)	8.41	

TABLE 6: Comparison of the former and new results.

Composition	Thickness (mm)	Duration of the 1st stage (μ s)	Impact velocity (m/s)	Maximum deflection			Errors	
				Experimental data (mm)	Original theory, OT (mm)	Modified theory, MT (mm)	OT (%)	MT (%)
B	11.3	8.6	792.7	16.5	17.0	17.2	2.9	4.3
C	11.3	8.7	858.2	20.0	17.6	18.4	13.6	8.8
B	9.3	8.2	628.9	18.0	17.8	18.8	1.1	4.2
C	9.3	8.2	651.1	17.5	17.7	18.3	1.1	4.3
B	7.3	7.7	428.8	15.5	17.3	14.6	10.4	6.0
C	7.3	7.8	448.4	13.0	16.6	13.0	21.7	0

In Figure 5 it is possible to observe the marked region. This region in the graph corresponds to the probable area of velocity and time where the erosion does not occur. In addition, the shifts in the curvatures of the velocities represent the beginning of the third stage. This helps to investigate the effect of the ceramic's characteristics in the impact absorption and in the erosion. This graph and this model of simulation can be used to search for specific properties in the ceramic plate and/or to improve its shock absorption property.

The not highlighted region in Figure 5 represents a penetration stage where projectile erosion and ceramic scattering occur. If it is desired not to have a large deformation in the metallic plate, it is necessary to improve ceramic impact absorption. These improvements will affect R_c , e_c , and E_c , which will also modify the graph.

Considering the back metal plate as another important energy absorber and integrity maintainer for the system, a deterministic simulation was run using the new deformation

law together with the deflection profile function. Then it gives

$$\begin{aligned}
 w(r) = & \left(d \left(\left(\frac{1}{2} \right) m_{pr} v_{pr}^2 (n+1) \right. \right. \\
 & \times \left(A\pi h \cdot \Gamma \left(n + \frac{5}{2} \right) \right. \\
 & \left. \left. \left. \cdot \left(\frac{2k_{\text{mod}} (n+1)}{d} \right)^{-n-(5/2)} \right)^{-1} \right)^{1/(2n+2)} \right) \\
 & \times (2k_{\text{mod}})^{-1} \\
 & \cdot e^{-(k_{\text{mod}} r^2)/d}.
 \end{aligned} \tag{23}$$

The variable r is the radial distance of the projectile impact. The maximum deflection as a function of the hardening exponent n and the radial distance r is presented in Figure 6. In addition, the effect of the thickness h of the

TABLE 7: Specifications of the different calibers used in the simulation.

Type	Specification	Bullet diameter (mm)	Mass (g)	Initial velocity (m/s)
II	.357 Magnum	9.07	10.2	453
IIA	9 mm	9	8	373
IIA	.40 S&W	10.2	12	300
IIIA	.357 SIG	9.07	8.1	440
IIIA	.44 Magnum	11.2	16	460

TABLE 8: Results of the simulation for several different calibers.

Type	Specification	Third stage velocity (m/s)	Third stage mass (g)	Final deflection value (mm)	Penetration in the ceramic (%)
II	.357 Magnum	170	6.66	19.48	87.5
IIA	9 mm	129	5.80	18.71	41.4
IIA	.40 S&W	104	9.45	18.63	49.6
IIIA	.357 SIG	163	5.36	17.40	84.4
IIIA	.44 Magnum	197	10.38	20.15	90.1

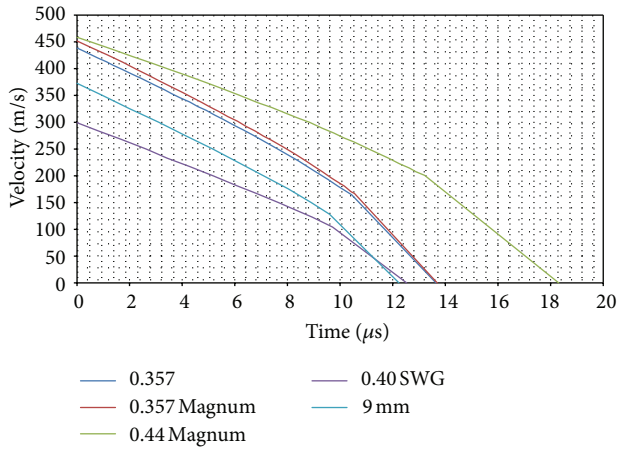


FIGURE 5: Movement evolution for the simulation on different calibers.

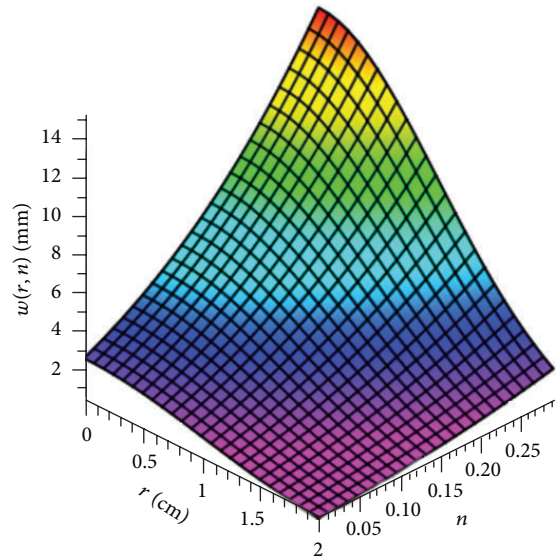


FIGURE 6: Deformation w in function of the radial distance r and the hardening exponent n .

plate together with the radial distance of the impact center is presented in Figure 7.

Based on Figures 6 and 7, it is possible to affirm that the mechanical property n and the thickness h of the metal layer have an important effect on the maximum deflection. The n constant demonstrates the ductile behavior of the material. However, if a lower deflection is required, it is important to note that a harder material could shear more easily depending on the energy of the projectile. Moreover, a change in the thickness of the metal plate will certainly affect the structure weight, which could be an aggravating factor in the carrier’s mobility.

4. Conclusions

The values obtained from the model demonstrate how important the ceramic plate is in the protection, responsible for absorbing approximately 85% of the total energy. Moreover, the value for the deflection of the metal plate was close to

the experimental data, which validates the model. Together with the optimized deflection equation the model could also prevent the effects of different projectile impacts.

In addition, the simulation demonstrated different aspects of the model and some predictable effects in collision phenomena. The control of the properties and its effects were analyzed with the developed computational method. Some of the effects predicted by the program could not be studied experimentally. However, future studies can use the presented results to validate the theory and, then, analyze some internal phenomena in a deeper way.

The present work is a theoretical analysis of the impact phenomenon in a specified type of protection. In the future studies, the current model and its solutions and simulations can be used to perform experimental test to evaluate the

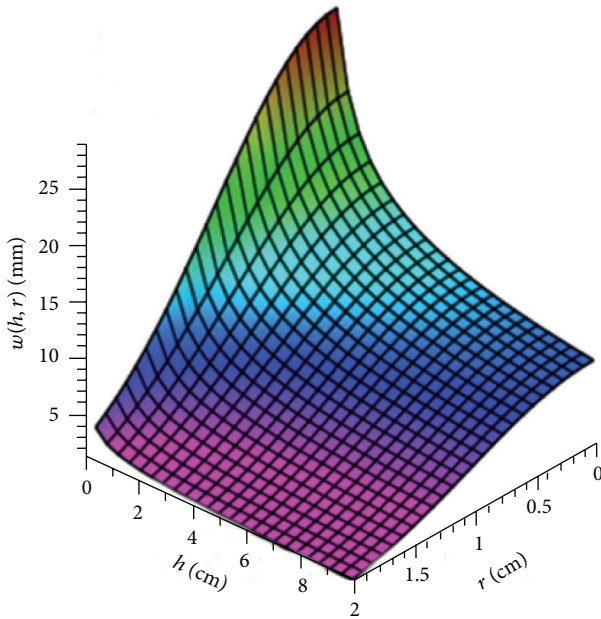


FIGURE 7: Deflection of the metallic plate w in function of the metal thickness h and radial distance r .

reliability of the model. Also, if the model can be considered valid for the impact, the considerations and formulations can be kept or improved to a more advanced modeling as finite element modeling (FEM). In addition, the experimental confirmation of the presented modeling also permits deeper investigation of the impact phenomenon, such as the effect of the interfacial friction between the projectile and sheared surfaces.

Acknowledgments

The authors wish to thank CAPES and CNPq for supporting this work.

References

- [1] D. P. Gonçalves, F. C. L. de Melo, A. N. Klein, and H. A. Al-Qureshi, "Analysis and investigation of ballistic impact on ceramic/metal composite armour," *International Journal of Machine Tools and Manufacture*, vol. 44, no. 2-3, pp. 307–316, 2004.
- [2] L. Neckel, D. Hotza, D. Stainer et al., "Solutions for impact over aerospace protection," *Key Engineering Materials*, vol. 488-489, pp. 25–28, 2012.
- [3] D. Tabor, *The Hardness of Metals*, Oxford University Press, 1951.
- [4] A. Tate, "A theory for the deceleration of long rods after impact," *Journal of the Mechanics and Physics of Solids*, vol. 15, no. 6, pp. 387–399, 1967.
- [5] R. Hill, *The Mathematical Theory of Plasticity*, Oxford University Press, 1950.
- [6] H. A. Al-Qureshi and J. D. Bressan, "Investigation of the degree of biaxiality on the limit strains in sheet metal stretching," in *Proceedings of the 9th North American Manufacturing Research Conference (NAMRC '81)*, pp. 538–541, 1981.
- [7] D. Ishikura and H. A. Al-Qureshi, "An investigation of perforation of metallic and composite plates by projectiles," in *Proceedings of the 5th Pan-American Congress of Applied Mechanics (PACAM '97)*, pp. 194–197, 1997.
- [8] M. L. Wilkins, "Mechanics of penetration and perforation," *International Journal of Engineering Science*, vol. 16, no. 11, pp. 793–807, 1978.
- [9] D. Halliday, R. Resnick, and J. Walker, *Fundamentals of Physics*, vol. 2, John Wiley & Sons, New York, NY, USA, 4th edition, 1996.
- [10] Accuratus, "Aluminum oxide, ceramic properties," <http://accuratus.com/alumox.html>.
- [11] Azom Materials, "Stainless steel, grade 304," <http://www.azom.com/article.aspx?ArticleID=965>.
- [12] U.S. National Institute of Justice, "Ballistic resistance of body armor," NIJ Standard–0101.06, 2008.

Research Article

Modelling the Influence of Manufacturing Process Variables on Dimensional Changes of Porcelain Tiles

Dolly Santos-Barbosa,^{1,2} Dachamir Hotza,¹ Juan Boix,³ and Gustavo Mallo³

¹ Programa de Pós-Graduação em Ciência e Engenharia de Materiais (PGMAT), Universidade Federal de Santa Catarina (UFSC), 88040-900 Florianópolis, SC, Brazil

² Departamento de Ingeniería Química y Ambiental, Universidad Nacional de Colombia, 111321 Bogotá, Colombia

³ Instituto de Tecnología Cerámica (ITC), Asociación de Investigación de las Industrias Cerámicas, Universitat Jaume I, 12006 Castellón, Spain

Correspondence should be addressed to Dachamir Hotza; dhotza@gmail.com

Received 24 February 2013; Revised 9 September 2013; Accepted 10 September 2013

Academic Editor: Augusto Deus

Copyright © 2013 Dolly Santos-Barbosa et al. This is an open access article distributed under the Creative Commons Attribution License, which permits unrestricted use, distribution, and reproduction in any medium, provided the original work is properly cited.

A model to study the influence of main process variables (powder moisture, maximum compaction pressure, and maximum firing temperature) on the intermediate variables (mass, dry bulk density, size, and thickness) and the final dimensions of porcelain tiles is proposed. The properties of dried and fired bodies are basically determined by the process parameters when the physical, chemical, and mineralogical characteristics of the raw material are kept constant. For a given set of conditions, an equation could be sought for each property as a function of raw materials and processing. In order to find the relationship between moisture content and compaction pressure with dry bulk density, springback, and drying and firing shrinkage, a laboratory experimental design with three factors and four levels was applied. The methodology was validated in lab scale for a porcelain tile. The final size and thickness were estimated, and the influence of the main process variables was analysed.

1. Introduction

The integration of systems as a requisite to permit a multistage control in the ceramic industry has advanced in the last decades, but it is still behind the traditional chemical industry [1–3]. This is partly because the ceramic sector works with solids, and the level of knowledge in unit operations involving solids has progressed far less than in fluids [4]. The second point that makes automatic control difficult stems from the structural nature of the ceramic product, making the required end characteristics to be multiple and complex, unlike most of the chemical processes in which the most important feature is usually the chemical composition, as revised by Mallo [5]. In the case of ceramic tiles, the end product must meet a number of requirements that range from purely technical characteristics (low porosity and wear resistance) to aesthetic qualities (gloss and design), often restricting the implementation of control systems. Finally, another aspect that makes automation difficult in this type of industry is the wide variety of products that the same company usually needs to produce.

An implementation of techniques of control and automation in the ceramic tile industry would be justified for high value products, which must present a strict tolerance of properties, particularly regarding geometrical dimensions. Among the different types of ceramic tiles that are produced, as defined by the Spanish Ceramic Tile Manufacturers' Association [6], the porcelain tiles best meet these requirements. A porcelain tile is characterized by low water absorption, usually less than 0.5% for the BIa group [7], high mechanical strength and frost resistance, high hardness, and high chemical and stain resistance, with a broad spectrum of aesthetic possibilities (body colouring with soluble stains, pressed relief, polishing, glazing, etc.), according to a recent review [8].

The usual industrial wet-route processing of porcelain tile covers three main stages: (1) milling/mixing and spray drying of the raw materials, (2) pressing, drying, and decorating of the green body, and (3) firing and classifying of the finished product. The first stage starts with the homogenization and wet milling of raw materials, followed by spray-drying of

the resulting suspension. In the second stage, the spray-dried powder with moisture content between 0.05 and 0.07 kg water/kg dry solids is pressed using uniaxial presses at a maximum pressure from 40 to 50 MPa. In the sequence, the resulting body is dried and decorated. Finally, in the third stage, the decorated body is fired in a single-layer roller kiln, using cycles of 40 to 60 min at a maximum temperature from 1180 to 1220°C for obtaining the maximum densification. After firing, the tiles are classified according to aesthetic properties and dimensional aspects, which are naturally related to processing and composition characteristics [9]. Some industries comprise in a single plant the Steps (1) to (3); other ones purchase the granulated powder from a third part processing unit, being restricted to Steps (2) and (3). The latest approach is followed in this paper.

One of the main concerns is related to the dimensional uniformity of the tile (size and form). In the case of size, the manufacturers generally divide the standard tolerance into different categories. The challenge of dimensional control is to produce the highest amount of tiles within a standardized specification to reduce storage lots.

The dimensional changes of ceramic tiles have been broadly studied in the last decades, using different approaches. The final size of fired bodies has been related to the composition of raw materials and/or processing parameters, including preparation, forming, and firing steps. Some of these works could be associated with tentative approaches to provide data for future-automated control of unit operations in the ceramic tile industry. Particularly, pressing and firing steps have been studied more deeply.

The characteristics of an industrial powder and the influence of its particle size distribution on the wet and fired densities were studied by Amorós et al. [10]. Extensive density and porosity measurements were carried out both in the green and the fired states. A proposal was made for the optimization of pressing conditions, including adjustment of pressure if the humidity changes [11]. Any excessive deviation from required dimensions of the fired product might be corrected by adjusting the green density and density distribution, with the help of experimentally determined dependence on moisture content and compacting pressure and on the basis of the relationship between green density and firing shrinkage [12]. Dimensional variations of only 0.1% are enough to cause significant deformations on large tiles. This fault was traced to nonuniform temperature in the preheating zone [13].

A system for effective control of pressing was proposed by Amorós et al. [14], based on modifying maximum pressing pressure to correct the variations in spray-dried powder moisture content, which needs to be measured on line in the pressed bodies. The validity of this method was verified, and it was shown that the maximum fluctuations of moisture content in typical tile manufacturing conditions sometimes exceed the admissible variation for this variable. De Noni Jr. et al. [15] applied a mathematical modelling to quantify the influence of process control variables on the length of fired tile manufactured from raw materials and processes, used by two floor-tile producers. Nevertheless, the influence of the main process variables (compaction pressure and powder moisture) on the final and intermediate characteristics of

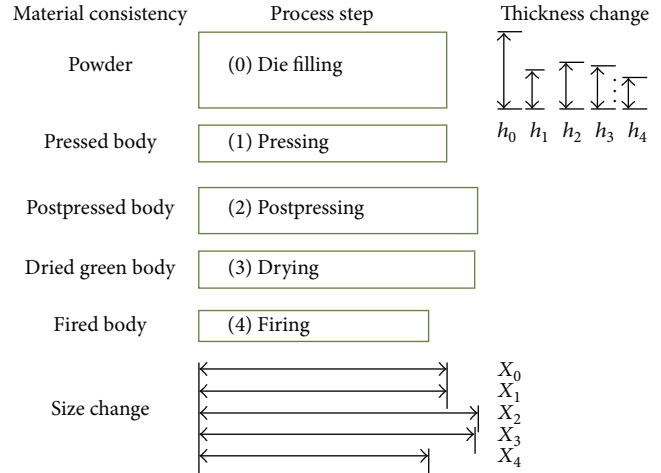


FIGURE 1: Dimensional changes through the process of porcelain tiles.

the tiles (mass, size, and thickness) was not yet accomplished in the literature considering the tile manufacturing process as a whole.

The scope of this work is developing empirical relationships to obtain a model for predicting the final dimensions of tiles (diameter and thickness) in lab scale, taking into account the dimensional changes experienced along the manufacturing steps.

2. Ceramic Tile Manufacturing Process and Variables

During the manufacturing process, ceramic tiles suffer from dimensional changes in different stages, as shown in Figure 1. Step 0 corresponds to die filling, in which the dimensions (thickness, h , and diameter or length, X) are related to the matrix volumes (h_0 and X_0). In pressing, Step 1, compaction occurs, the volume decreases, and the body dimensions correspond to h_1 and X_1 , where $X_1 = X_0$. After pressing, Step 2, an expansion—also known as springback—takes place. The thermal treatments—drying and sintering (Steps 3 and 4, resp.)—lead to shrinkages.

The dimensional changes experienced by tiles after pressing and drying (postpressing expansion and drying shrinkage, resp.) are determined for a given composition by pressing conditions (powder moisture and maximum compaction pressure, primarily), according to Amorós [16]. The dry bulk density of the tile (directly related to the maximum pressure and powder moisture) and the maximum firing temperature determine the dimensional changes experienced by the tile during firing (firing shrinkage), after studies of Escardino et al. [17]. An equation was obtained by Amorós et al. [18], which calculates the final size of the pieces from their dry bulk density and maximum firing temperature, taking into account the firing shrinkage.

Studies usually focus their attention on the largest of the tile dimensions, the length (X), because it features one of the main properties of the final product's size. However, since the shrinkage occurs in three dimensions, the final thickness

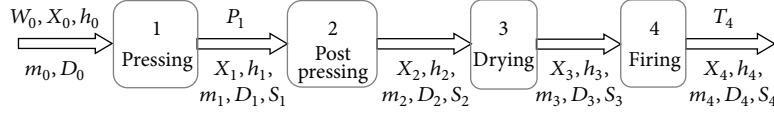


FIGURE 2: Flow diagram and variables of porcelain tile fabrication process.

of tiles (h_4) is affected by the process variables as well. This parameter is conditioned not only by the dimensional changes experienced by the compacted tile during manufacture (Figure 1), but also by the initial thickness of the bed in the press (h_0), that is, the spray-dried powder mass deposited in the press before compacting. Studies have shown the influence of the fill density of press powder beds, which will further affect the final thickness of the ceramic tile [19].

In Figure 2, different variables are shown, which will be taken into account to analyse the volume changes that were undertaken by the ceramic bodies along the processing steps, according to Figure 1.

In Figure 2, the processing variables are

- W_0 : dry-basis spray-dried moisture content (%),
- X : general characteristic size (mm); in lab-scale it corresponds to diameter of a cylindrical sample and in industrial scale to width or length of rectangular tiles,
- h : thickness (mm),
- m : mass (g),
- D : density (kg/m^3),
- P_1 : maximum compaction pressure (MPa),
- S : linear dimensional change based on length or diameter (%),
- T_4 : maximum firing temperature ($^{\circ}\text{C}$).

The subscripts stand for the sequential number related to the respective unit operation. In this work, the variables over the arrow in Figure 2 correspond to independent ones, whose values are fixed, while the variables under the arrow are the dependent ones, whose values are estimated.

The sample dimensional changes, namely, springback, after pressing and shrinkage after drying and firing, were calculated in percentage as

$$S_i = \frac{100(X_{i-1} - X_i)}{X_{i-1}}, \quad (1)$$

where the subscript corresponds to the stage number.

The lateral dimensions of the body associated with compaction pressing are considered unchanged since the powder compact is limited by the matrix physical boundaries. The springback effect corresponds to an expansion after removing the body from the press (S_2 is negative). Following drying and firing, respective shrinkages occur (S_3 and S_4 are positive). Applying (1) to the processing steps, the following equation is obtained:

$$R_4 = (100 - S_2)(100 - S_3)(100 - S_4) 10^{-6} R_1, \quad (2)$$

where R_1 : length/diameter or thickness after pressing (mm), R_4 : length/diameter or thickness after firing (mm).

In this case, it is assumed that the expansion (S_2) and shrinkages (S_3 or S_4) are independent of the direction. Thus, the body final dimension (R_4) may be obtained from the body dimensions after pressing (Step 1), when the values of S_2 , S_3 , and S_4 are known.

For a given composition, springback (S_2) and drying shrinkage (S_3) are basically dependent on powder moisture (W_0) and maximum compaction pressure (P_1). Firing shrinkage (S_4) is mainly a function of dry bulk density (D_3) and maximum firing temperature (T_4), and D_3 depends on W_0 and P_1 . These relationships might be obtained empirically for each composition as follows:

$$S_2 = f(W_0, P_1), \quad (3)$$

$$S_3 = f(W_0, P_1), \quad (4)$$

$$S_4 = f(D_3, T_4), \quad (5)$$

$$D_3 = f(W_0, P_1). \quad (6)$$

Thus, S_2 , S_3 , S_4 , and D_3 may be calculated for a certain composition from the independent variables W_0 , P_1 , and T_4 , using (3) to (6).

Considering that after pressing and before mould extraction the body length or diameter (X_1) is the same mould dimension (X_0), the equation to calculate the characteristic size of the body after firing (X_4) may be written as

$$X_4 = (100 - S_2)(100 - S_3)(100 - S_4) 10^{-6} X_0. \quad (7)$$

Equations (7) and from (3) to (6) allow estimating the final size of bodies as a function of independent variables W_0 , P_1 , T_4 , and X_0 . Similarly, to calculate the body thickness after firing (h_4), (2) may be rewritten as

$$h_4 = (100 - S_2)(100 - S_3)(100 - S_4) 10^{-6} h_1. \quad (8)$$

Equation (8) is not directly applied, since the thickness after pressing (h_1) is not the same thickness of the powder bed (h_0), which is the independent variable. To calculate h_1 , it is assumed that the body mass (m) is changed only during drying (9), so that the density definition after each i step is considered (10), where A_i is the body area (m^2) after Step i . Consider

$$m_0 = m_1 = m_2, \quad (9)$$

$$D_i = \frac{m_i}{h_i A_i}. \quad (10)$$

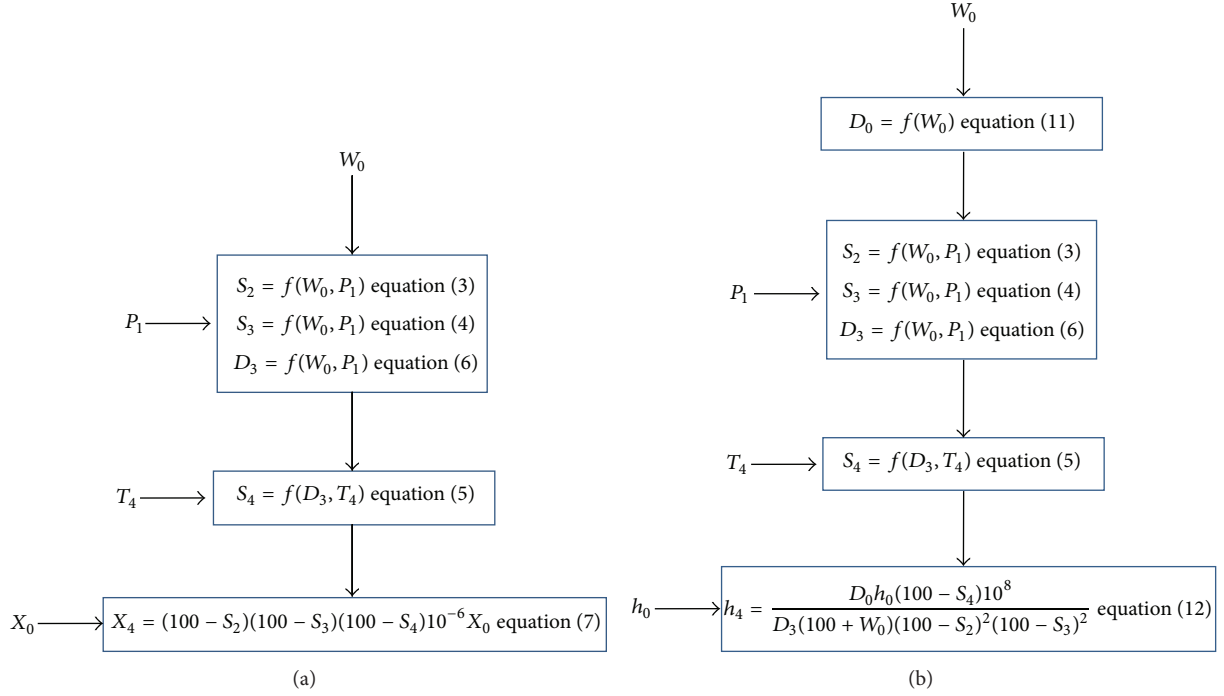


FIGURE 3: Flow charts for calculating the dimensional changes of ceramic tiles: (a) final length or diameter (X_4) and (b) final thickness (h_4).

The fill density, D_0 , is fundamentally affected by the way the powder is prepared, since the preprocessing steps define the particle or granule size distribution as well as their shape and moisture content. For spray-dried powders, whose size and shape are maintained relatively constant, D_0 depends solely on the moisture content (11). This equation is also empirically obtained for a specific powder bed. Consider

$$D_0 = f(W_0). \quad (11)$$

After previous assumptions, (8) might be redefined as

$$h_4 = \frac{h_0 D_0 (100 - S_4) 10^8}{D_3 (100 + W_0) (100 - S_2)^2 (100 - S_3)^2}, \quad (12)$$

where (h_4): final thickness. From (12), the final body thickness may be calculated directly from independent variables (h_0 and W_0) and from dependent variables (S_2 , S_3 , S_4 , D_0 , and D_3), which by their turn may be obtained from (3) to (6) and (11).

Figure 3 presents flow charts, indicating the sequential steps to calculate the dimensional changes of ceramic tiles (X_4 and h_4) from independent variables (X_0 , h_0 , W_0 , P_1 , and T_4), and from (3) to (7), (11), and (12).

As stated before, the scope of this work is developing empirical relationships for S_2 , S_3 , S_4 , D_0 , and D_3 to obtain a model for predicting the final dimensions of tiles (diameter and thickness) in lab scale, taking into account the dimensional changes experienced along the manufacturing steps. Furthermore, the influence of the main process variables (compaction pressure and powder moisture) on the final and intermediate characteristics of the tiles (mass, size, and thickness) will be also accomplished.

TABLE 1: Chemical analysis of spray-dried powder.

Chemical compound	Mass (%)
SiO ₂	65.8
Al ₂ O ₃	20.6
Fe ₂ O ₃	0.66
CaO	0.66
MgO	1.34
Na ₂ O	4.48
K ₂ O	1.60
MnO	<0.01
P ₂ O ₅	0.09
Loss on fire at 1025°C	3.91

3. Materials and Methods

3.1. Raw Materials. A spray-dried powder with standard porcelain tile composition was used. The particle size distribution is represented in Figure 4. The larger fraction (~60%) corresponds to particles between 300 and 500 μm , as usually employed in the porcelain tile industry.

The chemical analysis and X-ray diffraction pattern of the studied ceramic powder are shown in Table 1 and Figure 5, respectively. The main crystalline phases were identified. From the mineralogical and chemical analysis of the samples, a rational analysis was carried out, according to the method developed by Coelho et al. [20]. The percentages of crystalline phases so obtained are presented in Table 2.

3.2. Experimental Design. Experiments were performed in order to find the regression equations, relating the fill density (D_0), dry bulk density (D_3), springback (S_2), and drying

TABLE 2: Rational mineralogical analysis of spray-dried powder.

Crystalline phase	Mass (%)
Albite	38
Quartz	24
Kaolinite	18
Muscovite/illite	14
Chlorite	5
Other	1

TABLE 3: Factor levels of processing parameters: powder moisture (W_0), compaction pressure (P_1), and firing temperature (T_4).

Factors	Levels			
	1	2	3	4
W_0 (%)	3.11	4.59	5.67	7.18
P_1 (MPa)	16.61	29.42	39.23	49.03
T_4 (°C)	1150	1176	1200	1220

and firing shrinkage (S_3 and S_4) of porcelain tiles to the independent variables—powder moisture (W_0), compaction pressure (P_1), and firing temperature (T_4)—under constant raw material characteristics. In other words, the aim is to define the functions of (3) to (6) and (12).

An experimental design with 4 levels was initially used to characterize the nonlinear relationship among variables, as shown in Table 3. For each thermal treatment, a combination of pressure and moisture content was applied, and three cylindrical test bodies were pressed.

Since three factors (W_0 , P_1 , and T_4) and four levels were chosen, a complete experimental design would require 64 experiments without replicates. Considering that the output variables D_0 , D_3 , S_2 , and S_3 are related to W_0 and P_1 but not to T_4 , a reduced experimental set comprising two factors and four levels was applied.

Test bodies were simultaneously used to find the relation between S_4 and the output variables D_3 and T_4 . After drying, all samples were reorganized in four groups, one for each level of temperature. A selection was done, so that each group contained pieces within all ranges of dry bulk density.

3.3. Processing. The processing methodology used closely follows the conventional porcelain tile industrial practice, from pressing to firing stages. However, since the decorating stage is not significant to the dimensional changes, it was not included.

The industrial standard powder was separated into four bags. Each one had the moisture content, adjusted by adding water or drying in a muffle oven. For each W_0 and P_1 , shown in Table 3, three cylindrical specimens (40×7 mm) were formed by uniaxial pressing in a hydraulic laboratory press with electronic pressure control (Nannetti), using about 20 g of material for each specimen. Right after body pressing, the sample was weighted, marked, and carefully placed into a bag for 30 min. Then, the diameter, thickness, and bulk density were measured.

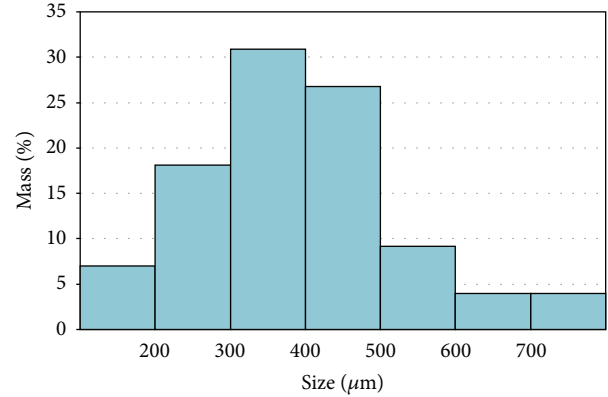


FIGURE 4: Granule size distribution for spray-dried powder.

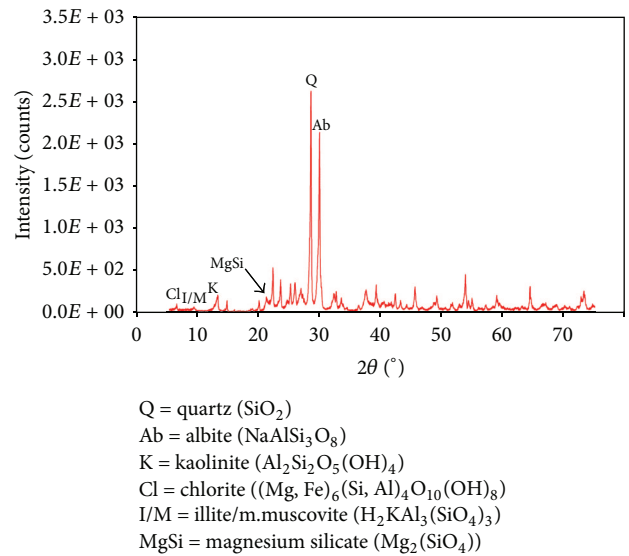


FIGURE 5: X-ray diffraction pattern for spray-dried powder.

After compaction, the test pieces were oven dried at $110 \pm 5^\circ\text{C}$ until reaching a constant mass. The moisture content of the bodies was calculated as a difference of mass before and after drying. Afterwards, they were fired in a laboratory electrical kiln (Pirometrol, maximum operating temperature range 1250°C), using heating cycles similar to the industrial practice (fast heating to 500°C and at $25^\circ\text{C}/\text{min}$ from 500°C until reaching the maximum temperatures, shown in Table 3). The pieces were kept to the maximum temperature during 6 min. Afterwards, they were cooled with forced air using a fan. The mass, dimensions, and bulk density of the dried and fired samples were measured. The water absorption of the fired bodies was measured additionally. The apparent densities (D_2 , D_3 , and D_4) of the bodies were measured by the Archimedes immersion method.

The linear shrinkage was calculated from the change in diameter (measured with 0.02 mm resolution digital calliper) of the cylindrical test pieces. Water absorption was determined after immersion in boiling water for 2 h and using a digital analytical scale with a resolution of 0.03 g. The mass of the tiles was measured both before and after immersion to determine the percentage of water absorption.

For determining fill density, the industrial standard powder was adjusted to the selected highest water content by moisturizing. The graduated cylinder was filled by pouring the powder, and the fill density was calculated as the ratio of mass to the cylinder volume. Then, the moisture content was reduced by natural drying. For each value of moisture content, the weighing was made three times with different powders to calculate the experimental error.

3.4. Modelling and Analysis. When the physical, chemical, and mineralogical characteristics of the raw material are kept constant, the properties of dried and fired bodies are basically determined by the process conditions. For a given set of raw materials and processing conditions, an equation could be sought for each property, relating that property with such conditions.

Equations for estimating D_3 and S_4 are found in the literature [16, 18]. For the remaining variables, new equations were proposed. After analysing different regressions (polynomial, exponential, and logarithmical), the equation which provided the lowest standard deviation of the residuals was chosen, provided that the expected physical behaviour was adequately described.

For each W_0 and P_1 , the response values used in the experimental design represent the average of three measured values, respectively. A regression was fitted to the experimental values, and the regression adequacy was checked. The assumption of normal distribution was proved when the residuals were uncorrelated and randomly distributed with a zero mean value [21]. In most cases, it was known that there was a relation among the three variables.

The regression uncertainty at 95% confidence level was calculated based on a global experimental error. If it is considered that the experimental error is the same throughout the whole region of interest [22], a weighted average (estimate of the standard deviation of the population) can be calculated based on the local experimental errors and the corresponding degrees of freedom. The value of the variable will be equal to the value predicted by the regression plus or minus the half of the 95% confidence interval ($CI_{95\%}$), calculated as

$$CI_{95\%} = \frac{2ts_G}{\sqrt{n}}, \quad (13)$$

where s_G is the global (or weighted average) experimental error, n is the sample size, and t is the t distribution value as a function of the chosen level of confidence (95%) and the degrees of freedom. The significant digits of the coefficients were adjusted following an error analysis.

4. Results and Discussion

This section is structured in two parts. In the first one, (3) to (6) and (11) are presented, which characterize the behaviour of the studied composition in each manufacturing step where dimensional changes occur. In the second one, those equations are used to predict the final diameter (X_4) and thickness (h_4) in lab scale and to analyse the influence of main process variables (powder moisture (W_0) and maximum compaction

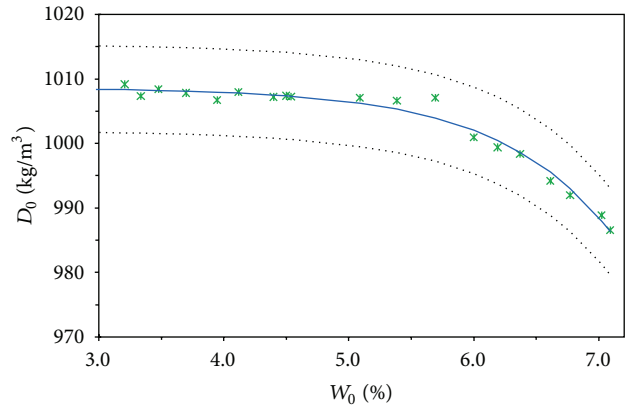


FIGURE 6: Fill density (D_0) as a function of the powder moisture content (W_0) with $CI_{95\%}$.

pressure (P_1)) on the intermediate variables (mass, size, and thickness) and the final dimensions of ceramic tiles.

4.1. Equations in Lab Scale. Measured values for D_0 , S_2 , D_3 , and S_4 were obtained at the different levels of the three factors W_0 , P_1 , and T_4 , shown in Table 3. The regression equations from (3) to (6) and (11), were fitted with these values, and confidence intervals ($CI_{95\%}$) were calculated. The final results are analysed as follows.

4.1.1. Die Filling. The way how the moisture content, W_0 , affects the fill density, D_0 , (11) is presented in Figure 6. Experimental values of D_0 were correlated to W_0 by the following exponential equation:

$$D_0 = B + C \exp(EW_0), \quad (14)$$

where B , C , and E are adjusting experimental parameters.

Equation (15) represents the regression obtained for the particular composition of porcelain tile used in this work with a correlation coefficient, R^2 , of 0.9887. Consider

$$D_0 = 1008.6 - 8.1000 \times 10^{-3} \exp(1.1171W_0). \quad (15)$$

The estimation of the fill density corresponding to the 95% confidence level is defined by (16). In Figure 6, the upper and lower limits of the curves that correspond to the 95% confidence for the regression are presented as well. Consider

$$D_0|_{95\%} = \frac{D_0 \pm CI_{95\%}}{2} = D_0 \pm 7 \text{ kg/m}^3. \quad (16)$$

The experimental data are well adjusted by (15). Moreover, the constant B corresponds to the fill density, so that when $W_0 = 0$, $D_0 \approx B$. From Figure 6, the density decreases as the moisture increases, which is more noticeable for moisture contents $>5\%$. In practice, the mould volume is constant, so that a moisture increase is related to a decrease in the dry powder feed to the mould, especially for $W_0 > 5\%$, which is the usual working range for this kind of ceramic tiles. According to Reed [23], the fill density depends directly on the granule density and the packing behaviour.

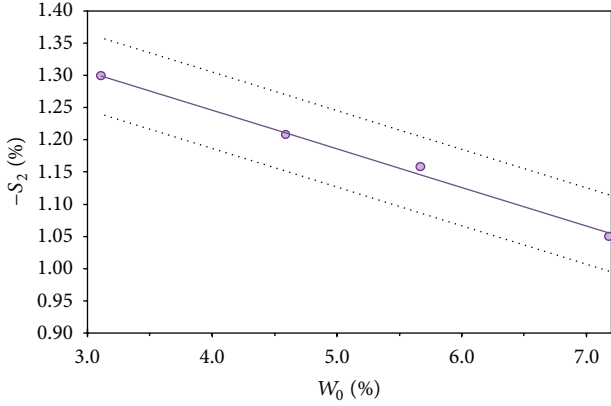


FIGURE 7: Springback (S_2) as a function of the powder moisture content (W_0) at compaction pressure (P_1) of 49.03 MPa with $CI_{95\%}$ (dotted lines).

4.1.2. Pressing. In this section, the adjusted equations corresponding to springback ($S_2 = f(P_1, W_0)$) and compaction diagram ($D_3 = f(P_1, W_0)$) are included. Although D_3 is the dry bulk density of the green and dried body, that is, after drying, the depending variables in this case are P_1 and W_0 , that is, pressing-related variables. The pressing stage mainly determines D_3 , so that drying operating parameters (time and temperature) have minor influence [24].

Elastic energy stored in the compacted powder produces an increase in the dimensions of the pressed tile on an ejection, called springback (S_2), which may cause compact defects on ejection when in excess. The springback experimental values for the porcelain tile powder used in this study are presented in Table 4 and Figure 7, in which, for convenience, $-S_2$ was used. Those values were measured, considering the difference between the tile size after being taken out from the mould and the pressing matrix constant dimensions.

It is observed from Table 4 that, as expected, the springback ($-S_2$) increases when P_1 is raised and W_0 is reduced. The results are consistent with the literature; for the same compaction pressure, $-S_2$ decreases when W_0 is increased up to a level of 9% due to the influence of the moisture over the mechanical properties of the spray-dryer granules [16]. It is expected that $-S_2$ rises with increasing values of P_1 , but this effect is less pronounced at higher W_0 .

A linear relationship between $-S_2$ and W_0 can be established, and changes of P_1 affect the intercept and slope of this regression. An adequate correlation of the three variables (17) was found corresponding to a residual standard deviation of 0.017%. Consider

$$-S_2 = (-3.999 \times 10^{-4} P_1 - 0.04025) W_0 + 4.926 \times 10^{-3} P_1 + 1.244. \quad (17)$$

With a global experimental error of 0.023%, the estimation of the springback with a 95% confidence level will be defined by

$$-S_2|_{95\%} = \frac{-S_2 \pm CI_{95\%}}{2} = -S_2 \pm 0.06\%. \quad (18)$$

TABLE 4: Experimental values of springback (S_2) as a function of the powder moisture content (W_0) and compaction pressure (P_1) with the data interval error at 95% confidence level.

$-S_2$ (%)	W_0 (%)			
	3.11	4.59	5.67	7.18
P_1 (MPa)				
19.61	1.21 ± 0.05	1.08 ± 0.04	1.07 ± 0.01	1.00 ± 0.02
29.42	1.23 ± 0.09	1.14 ± 0.04	1.10 ± 0.01	1.02 ± 0.06
39.23	1.27 ± 0.02	1.14 ± 0.09	1.14 ± 0.13	1.03 ± 0.06
49.03	1.29 ± 0.01	1.21 ± 0.04	1.16 ± 0.04	1.05 ± 0.02

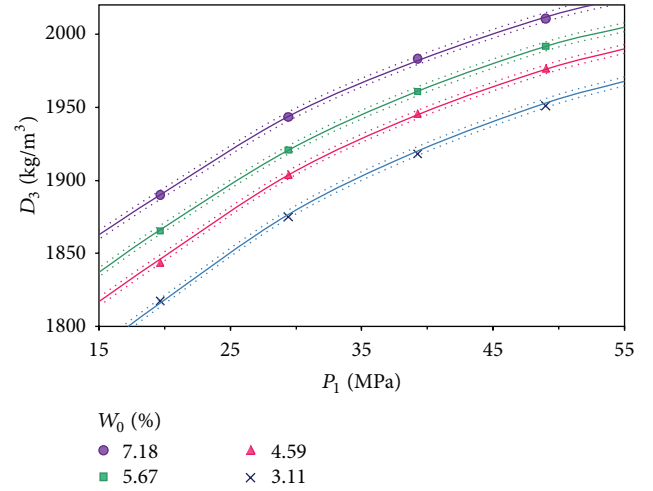


FIGURE 8: Dry bulk density (D_3) as a function of the compaction pressure (P_1) and powder moisture content (W_0) with $CI_{95\%}$ (dotted lines).

For easy visualization, the relationship between S_2 and W_0 is shown only at one compaction pressure (for 49.03 MPa) in Figure 7. Upper and lower limits of the curves that correspond to the 95% confidence for the regression at 49.03 MPa are presented as well. Similar curves might be built for remaining pressures from Table 4 and (17) and (18).

4.1.3. Compaction Diagram. For a fixed composition, D_3 depends on P_1 and W_0 , according to a relation known as compaction diagram [25], which might be expressed as

$$D_3 = QW_0^q \ln P_1 + RW_0^r, \quad (19)$$

where Q , q , R , and r are empirical constants dependent on powder composition. The experimental data and the respective regression curves are shown in Figure 8.

The results show a significant influence of W_0 on D_3 . To analytically express the influence of P_1 on D_3 , the following equation was fitted. Consider

$$D_3 = 174.85W_0^{-0.1324} \ln P_1 + 1219.2W_0^{0.10188}. \quad (20)$$

Equation (21) is used to estimate D_3 within a 95% confidence level. The curves corresponding to a $CI_{95\%}$ for each P_1 are also shown in Figure 8. Consider

$$D_3|_{95\%} = \frac{D_3 \pm CI_{95\%}}{2} = D_3 \pm 3 \text{ kg/m}^3. \quad (21)$$

The residuals of the correlation shown in (20) have a mean of -0.39 kg/m^3 and a standard deviation of 0.19 kg/m^3 , values that validate the normality hypothesis.

4.1.4. Drying. Linear drying shrinkage (S_3) occurs, as the liquid between the particles is removed and the interparticle separation decreases, and a linear correlation between S_3 and W_0 might be expected [16]. Shrinkage significantly increases when W_0 is raised and slightly decreases when the pressure is increased.

The maximum experimental mean value of S_3 was 0.04%, while the standard deviation ranged between 0.01% and 0.07%, resulting in large residual standard deviation (RSD) values, varying between 35 and 1054%. On this basis, the experimental error was considered relatively high.

Additionally, by comparing the orders of magnitude of S_2 , S_3 , and S_4 , it is concluded that the contribution of S_3 to the dimensional change is not significant. This result is consistent with the literature data that reports a volume shrinkage in the range of 3–12% for extruded and slip cast parts but 0 for dry-pressed and injection-moulded parts [23].

4.1.5. Firing. As shown in Figures 9 and 10, for constant D_3 , when T_4 is increased, the linear firing shrinkage (S_4) reaches a maximum value and then decreases. The maximum value is reached at a higher temperature as D_3 decreases. The same tendency was observed elsewhere [17, 26], owing to the sintering mechanism of porcelain tiles, which includes the decomposition of some clay components generating gases inside the samples causing swelling. After a certain extent, S_4 decreases during sintering, since the gases are released [27, 28]. Likewise, for the same T_4 , S_4 increases proportionally to D_3 , that is, according to the initial porosity. Although only six curves are present in Figure 9, eleven different dry densities were taken into account to adjust the equation.

Porcelain tiles are required to have water absorption values lower than 0.5% [7] as well as to keep the dimensional changes with temperature within a specific range, so that a compromise must be found combining those two properties according to T_4 and D_3 . Lower absorption values are obtained at higher values of T_4 and D_3 .

An adequate correlation of the variables S_4 , T_4 , and D_3 was found with a residual standard deviation of 0.07% and a residual mean of nearly zero (-0.02%). The mathematical regression and the corresponding graphical representation are shown in (22) and Figure 9, respectively. Three-dimensional response surface showing the expected S_4 as a function of T_4 and D_3 is presented in Figure 10. Consider

$$S_4 = (3.9389 \times 10^{-7} T_4^2 - 1.07704 \times 10^{-7} T_4 + 0.70975) D_3 - 1.44726 \times 10^{-3} T_4^2 + 3.711346 T_4 - 2334.5. \quad (22)$$

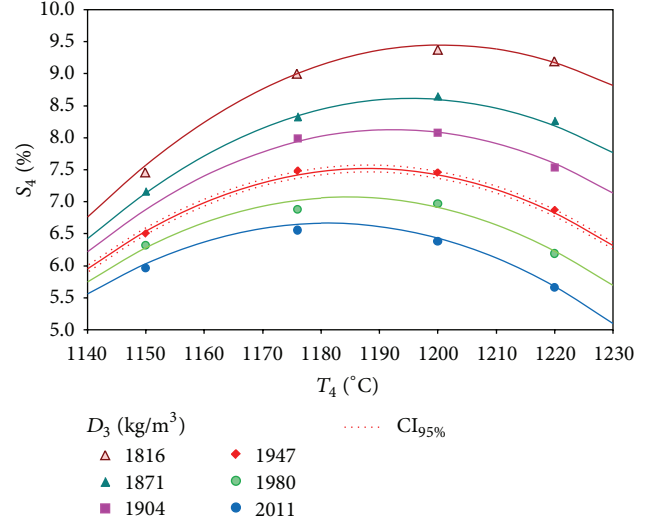


FIGURE 9: Linear firing shrinkage (S_4) as a function of the maximum firing temperature (T_4) and dry bulk density (D_3).

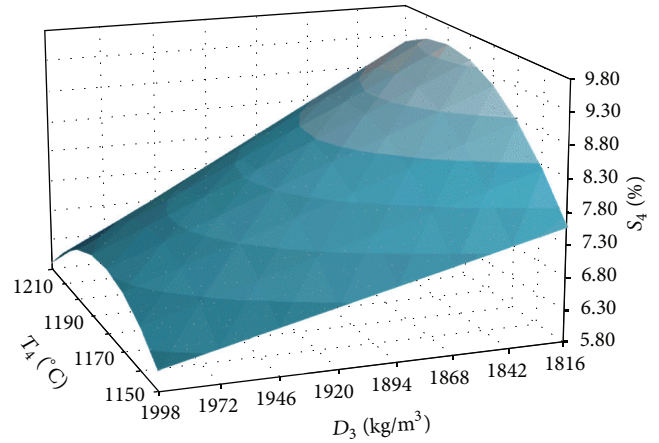


FIGURE 10: Three-dimensional response surface: linear firing shrinkage (S_4) as a function of the maximum firing temperature (T_4) and dry bulk density (D_3).

According to the regression and for a dry bulk density of 1947 kg/m^3 , a confidence interval of 0.20% was found with a weighted average experimental error of 0.042%. The curves corresponding to the upper and lower limits of the confidence interval (for $D_3 = 1947 \text{ kg/m}^3$) are shown in Figure 9.

4.2. Estimation of Tile Dimensions in Lab Scale and Behaviour Analysis of Intermediate Variables. In this section, the influence of main process variables (W_0 and P_1) on the intermediate variables (mass, size, and thickness) and on the final dimensions of ceramic tiles was analysed following the study of the model adequacy to estimate the final dimensions (h_4 and X_4) of ceramic tiles in lab scale.

4.2.1. Estimation of Tile Dimensions in Lab Scale. Using the proposed equations (Section 4.1) and following the scheme presented in Figure 3, the final piece dimension (h_4 and X_4) was estimated. Those values were calculated for each one

TABLE 5: Experimental and estimate errors in final diameter and thickness estimation.

	Residuals mean (mm)	Residuals standard deviation (mm)	Experimental absolute error (mm)	Mean absolute error (mm)
X_4	0.01	0.04	0.02	0.03
h_4	0.00	0.18	0.50	0.14

of the operational conditions (W_0 , P_1 , and T_4 , presented in Table 3) and the matrix dimensions ($h_0 = 14.27$ mm and $X_0 = 40.01$ mm). The estimated values were compared with measured values. To validate the assumption of normality, the residues were uncorrelated and randomly distributed with a standard deviation and mean value slightly over zero, as presented in Table 5. To validate the methodology, the average of the absolute value of the residuals (the mean absolute error, MAE) was also calculated and compared with the experimental absolute error (EAE). Their values are also presented in Table 5. EAE was calculated as an error associated with the half of the confidence interval with the same probability used through this work (0.95).

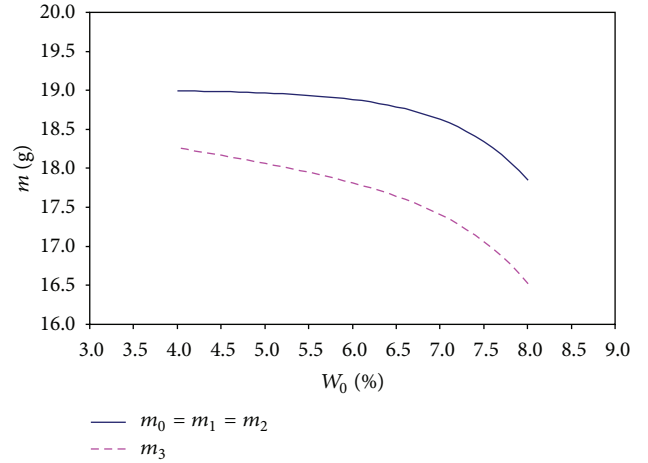
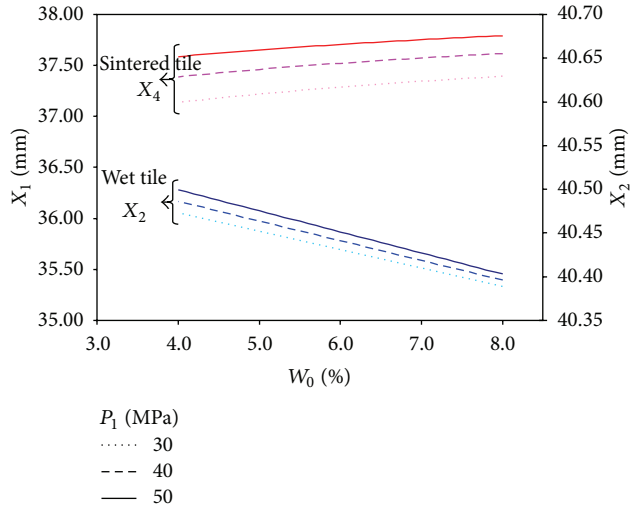
The regression can be considered adequate if the mean absolute error is smaller than the experimental absolute error. That is the case for h_4 . Although the MAE, for X_4 , is larger than EAE, its values are close.

4.2.2. Behaviour Analysis of Intermediate Variables. The influence of P_1 and W_0 on the mass, size, and thickness of the porcelain tile through the manufacturing process was studied following the methodology proposed with the previous equations (Section 4.1). For calculations, the values of h_0 and X_0 were assumed to be typical lab-scale values (15 mm and 40 mm, resp.).

(1) Influence of Powder Moisture on Tile Mass. According to (14), W_0 affects D_0 . During industrial pressing, the volume of the press matrices (X_0, h_0) is kept constant, so that the variations in D_0 will modify the amount of feed powder (m_0) and the mass of the green pressed and sintered tile. P_1 does not affect the tile mass during the manufacturing process.

In Figure 11, it can be observed that m_0 and the dried tile mass (m_3) are lower due to the higher W_0 and consequent lower D_0 , caused by the reduced flowability of the powder. This effect is more pronounced for higher moistures, especially for m_0 , since the variation in bed density is summed up with the water loss after drying. A change in $\pm 0.5\%$ in moisture content, which is usual in industrial practice, will cause a variation of $\pm 0.5\%$ in m_0 , considering the range of operation moistures to be usually employed (5–7%).

(2) Influence of Powder Moisture and Pressing Pressure on Tile Dimensions. W_0 and P_1 will affect the size of the wet tile after pressing (X_2), the size of the dried tile (X_3), and the size of the sintered tile (X_4), since $X_1 = X_0$. Moreover, considering that $X_2 \approx X_3$, the influence of W_0 and P_1 on those values is practically the same. In Figure 12, the variation of X_2 and X_4 is presented as a function of W_0 for 3 different P_1 . For a certain moisture and pressure, the wet tile size is larger than the sintered tile size due to the higher shrinkage (7–8%) compared

FIGURE 11: Influence of spray-dried powder moisture (W_0) on the fill mass (m_0) and tile masses (m_1 , m_2 , and m_3).FIGURE 12: Influence of spray-dried powder moisture (W_0) and maximum pressing pressure (P_1) on wet and sintered tile sizes (X_2 and X_4).

to the springback (1–1.5%). The influence of W_0 is much larger on X_4 than on X_2 , being in both cases a practically linear dependency, in the range of studied powder moisture. The effect of W_0 is opposite when wet and sintered tiles are compared: for higher moisture X_2 is diminished, while X_4 is augmented. In wet bodies, water works as a binder of particles, reducing the elastic response after pressing (lowering the springback) and enhancing D_3 . When S_2 is reduced, the wet bodies present a lower size. When D_3 is increased, the bodies present a lower initial porosity, so that sintering shrinkage is lower, and the final dimensions of tiles are higher.

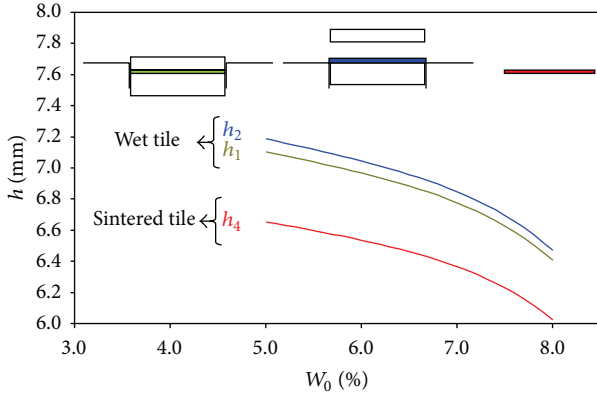


FIGURE 13: Influence of the powder moisture (W_0) on the tile thickness (h) along the fabrication steps, for a maximum pressure of 40 MPa.

The effect of P_1 is similarly much higher on the sintered tiles when compared to the wet tiles. Nevertheless, the influence is directly proportional in both cases, for wet and sintered tiles, in contrast to the effect of W_0 .

(3) *Influence of Powder Moisture and Pressing Pressure on Tile Thickness.* In Figure 13, the variation of h_1 , h_2 , and h_4 as a function of W_0 is shown for a P_1 of 40 MPa.

As mentioned before, for this particular composition $h_2 \cong h_3$, so that the effect of W_0 and P_1 will be similar. For higher W_0 , the tile thickness is reduced, being this effect similar for h_1 , h_2 , and h_4 , since the curves present the same trend. This behaviour is markedly different from the one observed for the size (Figure 12). The variation of the thickness of tiles with W_0 seems to depend to a greater extent on the mass variations of the powder fed to the matrix during filling. Indeed, the trends of curves in Figures 13 and 11 are comparable. This indicates that m_0 into the press matrix has a larger effect on h than S_2 and S_4 , explaining the behaviour observed in Figure 13.

Figure 14 shows the variation of h as a function of W_0 for 3 different P_1 (30, 40, and 50 MPa). For convenience, only the results for h_2 and h_4 are presented, since h_1 values are similar to those of h_2 .

For a certain W_0 , when P_1 is increased, the tile thickness is reduced, both for a wet body (h_2) and for a sintered body (h_4). The effect of pressure is decreased for higher pressure values, since the particles are closer. The influence of pressure on the thickness is higher for the wet body than for the sintered body, since the curves are closer in this case when compared to the curves of the wet body.

5. Conclusions

Empirical equations were obtained correlating the dependent properties to independent variables for fixed raw materials composition and processing conditions.

It was observed that S_2 , S_3 , and S_4 presented different orders of magnitude, suggesting that the contribution of S_3 to the dimensional change is not significant under the studied experimental conditions. The correlations were chosen by the lowest deviation standard value, implying minimal lack of fit

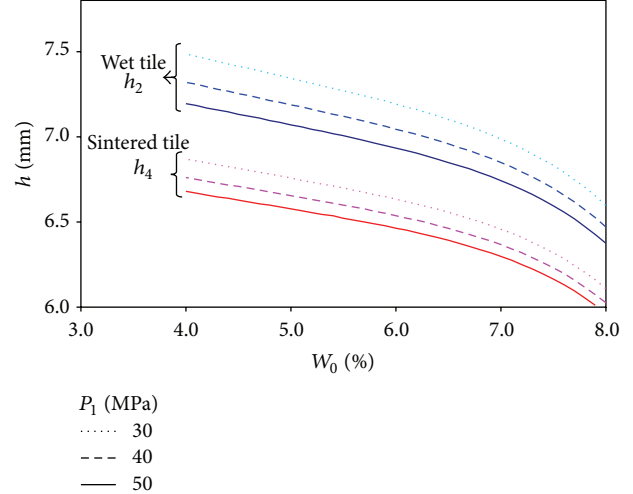


FIGURE 14: Influence of powder moisture (W_0) and pressing pressure (P_1) on tile thickness (h).

and experimental errors. In all cases, the residuals could be considered randomly distributed around a zero mean value, corresponding to a common constant variance and normal distribution.

On the basis of the statistical analysis, the regression equations obtained were accepted to describe the effect of

- (i) powder moisture content (W_0) on fill density (D_0),
- (ii) powder moisture content (W_0) and compaction pressure (P_1) on springback (S_2),
- (iii) powder moisture content (W_0) and compaction pressure (P_1) on dry bulk density (D_3),
- (iv) maximum firing temperature (T_4) and dry bulk density (D_3) on firing shrinkage (S_4).

A computational model that permits predicting the intermediate variables of ceramic tiles during their processing (mass, dry bulk density, size, and thickness) and their final dimensions' properties (size and thickness) was obtained. The multivariable model found makes use of both material balance equations and correlated equations. The used methodology proved to be a useful tool for planning and analysing experiments to find the influence of the mean press operational conditions on the variables of the empirical relationships needed to complete the calculation model. The analysis of the data obtained shows that

- (i) when the powder moisture (W_0) is increased, the amount of powder fed into the press (m_0) is decreased. The same effect, with a higher intensity, is also observed for the dried mass of compacted tiles (m_3);
- (ii) the sizes of green bodies (X_2 and X_3) are slightly reduced when the powder moisture (W_0) is increased, and they augment for higher pressing pressure (P_1) as a result of the springback (S_2);
- (iii) the final tile size (X_4) is larger for higher powder moisture contents (W_0) and the pressing pressure values (P_1) due to the increase of density (D_3).

The effect of both variables on X_4 is higher than that on X_2 and X_3 ;

- (iv) the thickness of both green (h_1 , h_2 , and h_3) and sintered tiles (h_4) decreases for lower powder moisture (W_0) and pressing pressure (P_1).

For the operational conditions considered, the regression equations represent the behaviour of the studied variables at lab scale within a high confidence level. Therefore, before using them to evaluate different press control conditions and strategies, their efficiency should be verified to reproduce industrial data. This is going to be accomplished in a further work, including a computational model to be established according to pressing operational conditions and control strategies in industrial scale. The aim is that the variables of the final product, particularly the tile thickness and size, are kept within a specific quality range.

Acknowledgments

Capes (Coordenação Geral de Aperfeiçoamento de Pessoal de Nível Superior, Brazil), DGU (Dirección General de Universidades, Spain), ERDF (European Regional Development Found), and IMPIVA (Instituto de la Mediana y Pequeña Industria Valenciana, Spain) are acknowledged for financial support as well the Spanish producer of ceramic tiles ROCERSA (Roig Cerámica S. A.) for providing raw materials.

References

- [1] A. Azadeh, M. Moghaddam, P. Geranmayeh, and A. Naghavi, "A flexible artificial neural network-fuzzy simulation algorithm for scheduling a flow shop with multiple processors," *International Journal of Advanced Manufacturing Technology*, vol. 50, no. 5–8, pp. 699–715, 2010.
- [2] J. A. Heredia and M. Gras, "Empirical procedure for modeling the variation transmission in a manufacturing process," *Quality Engineering*, vol. 22, no. 3, pp. 150–156, 2010.
- [3] J. A. Heredia and M. Gras, "Statistical estimation of variation transmission model in a manufacturing process," *International Journal of Advanced Manufacturing Technology*, vol. 52, no. 5–8, pp. 789–795, 2011.
- [4] T. F. Edgar, "Control of unconventional processes," *Journal of Process Control*, vol. 6, no. 2–3, pp. 99–110, 1996.
- [5] G. Mallol, "Control y automatización en la industria cerámica: evolución y perspectivas," in *9º Congreso Mundial de la Calidad del Azulejo y del Pavimento Cerámico (Qualicer '06)*, pp. 47–72, Castellón, Spain, 2006.
- [6] ASCER, *Guía de la Baldosa Cerámica*, Instituto Valenciano de la Edificación, Castellón, Spain, 2006.
- [7] ISO13006, "Ceramic tiles—definitions, classification, characteristics and marking," 1998.
- [8] E. Sánchez, J. García-Ten, V. Sanz, and A. Moreno, "Porcelain tile: almost 30 years of steady scientific-technological evolution," *Ceramics International*, vol. 36, no. 3, pp. 831–845, 2010.
- [9] A. de Noni Jr., D. Hotza, V. C. Soler, and E. S. Vilches, "Influence of composition on mechanical behaviour of porcelain tile—part I: microstructural characterization and developed phases after firing," *Materials Science and Engineering A*, vol. 527, no. 7–8, pp. 1730–1735, 2010.
- [10] J. L. Amorós, A. Blasco, J. E. Enrique, and A. Escardino, "Estudio de la compactación de soportes cerámicos (bizcochos) de pavimento y revestimiento-I: influencia del tamaño de gránulo de atomizado," *Boletín de la Sociedad Española de Cerámica y Vidrio*, vol. 21, no. 4–5, pp. 245–250, 1982.
- [11] J. L. Amorós, V. Beltrán, F. Negre, and A. Escardino, "Estudio de la compactación de soportes cerámicos (bizcochos) de pavimento y revestimiento-II: influencia de la presión y humedad de prensado," *Boletín de la Sociedad Española de Cerámica y Vidrio*, vol. 22, no. 1, pp. 8–18, 1983.
- [12] J. L. Amorós, A. Escardino, V. Beltrán, and J. E. Enrique, "Quality control in tile production," *Interceram*, vol. 33, no. 2, pp. 50–54, 1984.
- [13] J. L. Amorós, A. Escardino, E. Sánchez, and F. Zaera, "Stabilità delle dimensioni nelle piastrelle porose monocotte," *Cerám Información*, vol. 324, pp. 56–67, 1993.
- [14] J. L. Amorós, G. Mallol, A. Mezquita et al., "Melhoria da estabilidade dimensional de peças de grés porcelânico através da medida contínua da umidade dos suportes prensados," *Ceramics International*, vol. 9, no. 2, pp. 6–15, 2004.
- [15] A. de Noni Jr., C. Modesto, A. P. N. de Oliveira, and D. Hotza, "Dimensional modeling and control of ceramic tile," *American Ceramic Society Bulletin*, vol. 85, no. 11, pp. 9201–9207, 2006.
- [16] J. L. Amorós, *Pastas cerámicas para pavimentos de monococción—influencia de las variables de prensado sobre las propiedades de la pieza en crudo y sobre su comportamiento durante el prensado y la cocción [Ph.D. thesis]*, Universitat Jaume I, Castellón, Spain, 1987.
- [17] A. Escardino, J. L. Amorós, and J. E. Enrique, "El diagrama de gresificación en la fabricación de pavimentos de gres," *Cerám Información*, vol. 84, pp. 211–220, 1981.
- [18] J. L. Amorós, A. Escardino, V. Beltrán, and J. E. Enrique, "Control de la compactación durante el proceso de fabricación de pavimentos y revestimientos cerámicos," *Técnica Cerámica*, vol. 118, pp. 1307–1314, 1983.
- [19] J. L. Amorós, A. Blasco, J. E. Enrique, and F. Negre, "Características de polvos cerámicos para prensado," *Boletín de la Sociedad Española de Cerámica y Vidrio*, vol. 26, no. 1, pp. 31–37, 1987.
- [20] C. Coelho, C. A. Scopel, N. Roqueiro, and D. Hotza, "Quantitative mineralogical analysis of ceramic raw materials: an alternative approach," *Journal of Materials Science Letters*, vol. 20, no. 11, pp. 1041–1042, 2001.
- [21] D. C. Montgomery, *Design and Analysis of Experiments*, John Wiley & Sons, New York, NY, USA, 5th edition, 2001.
- [22] O. L. Davies, *Métodos Estadísticos Aplicados a la Investigación y a la Producción con Especial Referencia a la Industria Química*, Aguilar, Madrid, Spain, 2nd edition, 1965.
- [23] J. C. Reed, *Introduction to the Principles of Ceramics Processing*, Wiley Interscience, New York, NY, USA, 2nd edition, 1993.
- [24] D. Santos-Barbosa, B. Vicente, D. Hotza, and R. A. F. Machado, "Análisis de los parámetros de proceso sobre la media y la variabilidad de la densidad aparente pos secado de revestimientos cerámicos," in *11º Congreso Mundial de la Calidad del Azulejo y del Pavimento Cerámico (Qualicer '10)*, Castellón, Spain, 2010.
- [25] J. L. Amorós, A. Blasco, J. E. Enrique, V. Beltrán, and A. Escardino, "Variables en la compactación de soportes cerámicos de pavimento y revestimiento," *Técnica Cerámica*, vol. 105, pp. 792–812, 1982.

- [26] J. L. Amorós, A. Moreno, M. J. Orts, and A. Escardino, "La operación de prensado en la fabricación de pavimentos por monococción-II: influencia de la naturaleza del polvo de prensas sobre las propiedades de las piezas en cocido," *Boletín de la Sociedad Española de Cerámica y Vidrio*, vol. 29, no. 3, pp. 151–158, 1990.
- [27] V. Bagán, *Efecto de las condiciones de operación en las diferentes etapas del proceso sobre las propiedades y características de un pavimento de muy baja porosidad [Ph.D. thesis]*, Universitat Jaume I, Castellón, Spain, 1991.
- [28] M. J. Orts, *Sinterización de piezas de pavimento gresificado [Ph.D. thesis]*, Universitat Jaume I, Castellón, Spain, 1991.

Research Article

Geometry Optimization Calculations for the Elasticity of Gold at High Pressure

E. Güler and M. Güler

Hitit University, Department of Physics, 19030 Corum, Turkey

Correspondence should be addressed to E. Güler; eguler71@gmail.com

Received 2 May 2013; Revised 18 September 2013; Accepted 23 September 2013

Academic Editor: Augusto Deus

Copyright © 2013 E. Güler and M. Güler. This is an open access article distributed under the Creative Commons Attribution License, which permits unrestricted use, distribution, and reproduction in any medium, provided the original work is properly cited.

We present embedded atom method based geometry optimization aspects of pressure effect on some elastic and mechanical properties of gold. During study, we determined the pressure dependency of equilibrium volume, typical cubic elastic constants, bulk modulus, shear modulus, young modulus, and elastic wave velocities of the considered metal with varying pressure between 0 GPa and 1000 GPa. Finally, we carried out a benchmark between our results and other available theoretical calculations and experimental data. The results of the study mutually agree with the previous findings and provide a deeper outlook for high pressure behavior of the studied metal.

1. Introduction

The effect of pressure on the propagation of elastic waves in materials is essential for predicting and understanding some physical properties comprising the interatomic forces, mechanical stability, phase transition mechanisms, dynamic fracture, earthquakes, and the internal structures of Earth. Unfortunately, there is not much experimental information about the elasticity of solids at high pressure, since measurement of the elastic constants is challenging under high pressure.

The two traditional experimental methods for moderate pressures are ultrasonic technique and Brillouin spectroscopy measurements. From these methods, ultrasonic methods utilize a few gigapascals (GPa) where Brillouin spectroscopy measurements are limited to 25 GPa [1]. Furthermore, gold (Au) is often used as an internal pressure calibrant for high pressure studies, because of its stable nature over wide temperature and pressure ranges. Au is also chemically inert, compressible, and displays a simple X-ray diffraction pattern. However, as reported by Matsui there has been much debate especially on the pressure-volume-temperature (P - V - T) equation of state (EOS) of Au, even at room temperature. Also, estimated pressure differences between proposed EOSs often reach more than 10% with respect to experiments

[2]. Therefore, to overcome the experimental limitations, computational researches on the high pressure characteristics of Au are particularly critical for ongoing academic studies and still current research topics [3–6].

Over the past few decades, computer simulation techniques have become an important tool in science as an aid to the interpretation of experimental data for yielding an atomic level model [7]. Notably, two popular calculation methods, namely, classical physics based molecular dynamics (MD) and quantum-mechanics based density functional theory (DFT) methods, play a major role on the materials science and condensed matter scene to get reliable results on the physical properties of metals being dependent to accurate interatomic potentials [8]. For instance, embedded atom method (EAM) and its potentials are well-known schemes for the atomistic simulations of metallic materials [9–11]. In the early 1980s, Daw and Baskes introduced EAM for calculating the ground state properties of realistic metal systems to remove the insufficiency of pairwise potentials [12], and, afterwards, researchers applied this semiempirical method extensively with various types of many improved body potentials for distinct physical problems in metallic systems. Exemplarily, Finnis-Sinclair type EAM potentials adequately explain the elastic and defect properties of base centered cubic (bcc) metals [13, 14], whereas Sutton-Chen

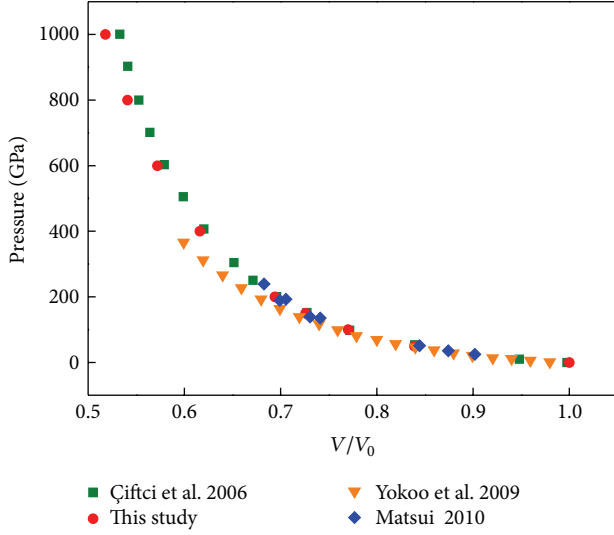


FIGURE 1: A comparison for the P - V equation of state for Au between 0 GPa and 1000 GPa.

type EAM is a proper alternative for face centered cubic (fcc) metals for atomistic calculations [15]. Noteworthy to mention here, the use of EAM with geometry optimization calculations with General Utility Lattice Program (GULP) code reveals veracious research results on some versatile features of metals such as bulk modulus, elastic constants, and elastic moduli [16, 17].

In the present study, we focus on clarifying the individual high pressure elastic constants of Au by EAM based geometry optimization calculations. The main purpose of this study is not only to provide results that can be used to evaluate quantitatively the high pressure elasticity of Au from 0 GPa up to 1000 GPa, but also to contribute to enlightening the abovementioned doubts on Au.

2. Computational Procedure

During this computational study, we performed all calculations using General Utility Lattice Program (GULP) code 4.0. This simulation code allows performing wide-range property calculations for 3D periodic solids, 2D surfaces and gas phase clusters, and so forth. Besides, this code also allows the use of two-body, three-body, four-body, six-body, and many body (EAM) potentials depending on demands of research. Most calculations in GULP code consist of the optimization of a trial structure to the local energy minimum, under given conditions of pressure and temperature. Moreover, several types of standard minimization techniques are available in GULP. The two common techniques are to optimize the related structures at constant pressure, in which all internal and cell variables are included or at constant volume, where the unit cell remains frozen [16, 17]. So, we applied a constant pressure optimization for the Au. The geometry of the studied cells was optimized by the Newton-Raphson method [21] based on the Hessian matrix calculated from the second derivatives. The Hessian matrix is recursively updated during

optimization using the Broyden-Fletcher-Goldfarb-Shanno algorithm [22–25]. We employed Sutton-Chen type EAM potential to study fcc Au metal, under periodic boundary conditions with a temperature configuration at $T = 0$ Kelvin. Then, we increased the pressure from 0 GPa to 1000 GPa in the steps of 200 GPa with a lattice constant $a_0 = 4.08 \text{ \AA}$ for Au. Following the EAM based optimization results for Au, we particularly concentrated on some elastic parameters such as typical cubic elastic constants (C_{11} , C_{12} , and C_{44}), bulk modulus (B), shear modulus (G), young modulus (E), longitudinal sound velocity (V_L), and shear velocity (V_T) of this metal for the studied pressure range where all these physical parameters are circumstantiated in very recent study of authors [26]. At the end of our calculations we presented a benchmark between our results and earlier experimental and DFT findings of fcc Au.

3. Results and Discussion

Since it is not possible get data on the EOS of Au up to 1000 GPa experimentally, we deliberately focused on the former theoretical results from the literature. Figure 1 shows P - V diagram of Au. In Figure 1 the circle symbols represent our present calculation data where squares show the molecular dynamics results of Çiftci et al. [5]. In addition, diamonds symbols stand for Matsuis data [2], and triangles belong to Yokoo et al. calculations [27]. As it is obvious from Figure 1, our present results on the P - V diagram of Au are very close to molecular dynamics data in [5] and cover both the Matsuis findings and Yokoo's data in which Yokoo and his coworkers calculations also subsumed the electronic-free energy contribution. As a result, our data strongly supports previous findings on the EOS of Au and show significant similarities on the P - V curve.

Figure 2 represents the typical elastic constants (C_{11} , C_{12} , and C_{44}) of Au at the pressure interval between 0 GPa and 150 GPa where the authors could be able to make a comparison between current results and former experimental data and DFT values. The closed circles in Figure 2 indicate the present calculations while open-crossed circles denote experimental data of Duffy et al. [28] and squares show Greeff and Graf DFT data [29]. It is quite clear in Figure 2 that our elastic constant data, appears in the range of both experimental and DFT data except the little disagreement of C_{44} . Additionally, Figure 3 outlines the pressure dependency of the elastic constants in the 0 GPa–1000 GPa range obtained during this research. As seen in Figure 3, the calculated values of C_{11} , C_{12} , and C_{44} elastic constants are positive and exhibit a smooth increment as a function of the increasing pressure. Besides, the increment of the elastic constant C_{11} is higher than both elastic constants C_{12} and C_{44} . Physically, C_{11} describes the longitudinal elastic behavior, whereas C_{12} and C_{44} portray the off-diagonal and shear elastic characteristic of cubic crystals related with shearing, respectively. So, a longitudinal strain produces a change in volume without a change in shape. This volume change is highly related to pressure and thus reflects a large change in C_{11} . On the other hand, a transverse strain or shearing causes a change in shape

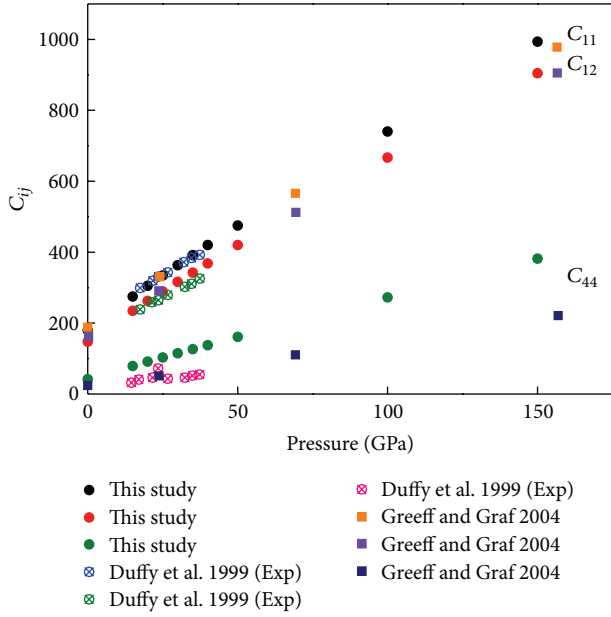


FIGURE 2: Comparing typical cubic elastic constants of Au as a function of pressure.

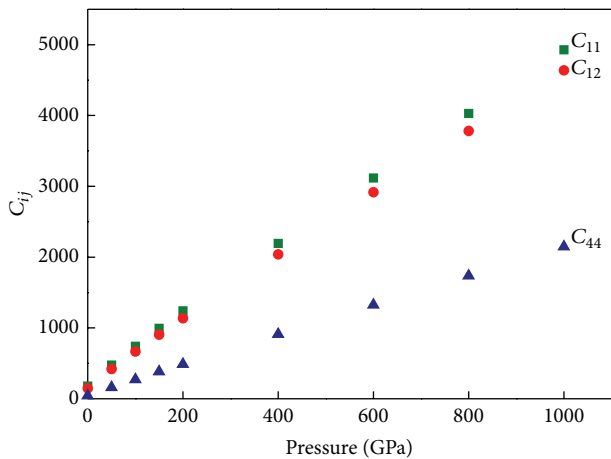


FIGURE 3: Typical cubic elastic constants of Au from 0 GPa to 1000 GPa.

without a change in volume. Therefore, C_{12} and C_{44} are less sensitive to pressure when compared with C_{11} .

Figure 4 displays the behavior of three elastic moduli (B , G , and E) of Au for the applied pressure range. From the prevalent physical definition of bulk modulus $B = \Delta P / \Delta V$, an increment for B is expected due to its direct proportionality to applied pressure. Thus, it is visible in Figure 4 that bulk modulus of Au represents a straight increment as expected. In this regard, the other elastic moduli G and E depending strictly on bulk modulus also expose similar behavior in Figure 4. The behavior of these curves is also consistent within the former results of moderating pressures in metals and alloys.

Pressure effect on the longitudinal sound velocity (V_L) and shear velocity (V_T) of Au up to 1000 GPa can be seen in

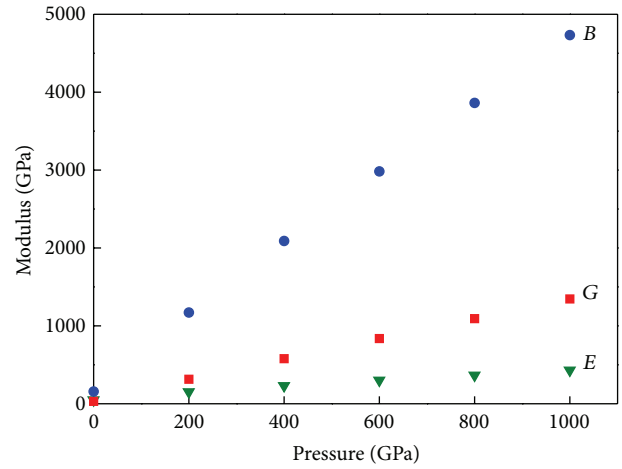


FIGURE 4: Bulk modulus, shear modulus, and young modulus of Au as a function of studied pressure range.

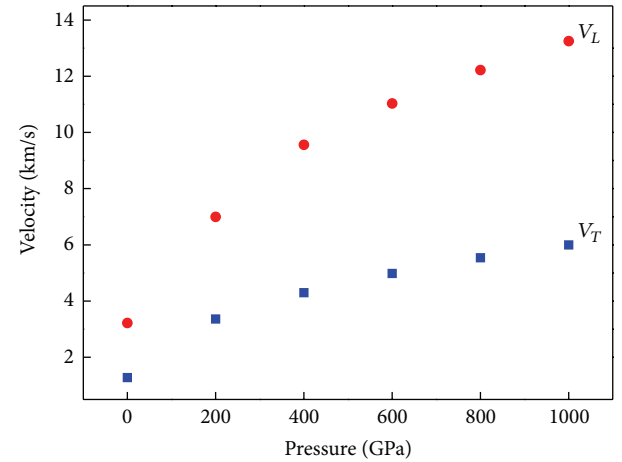


FIGURE 5: V_L and V_T behavior of Au under pressure up to 1000 GPa.

Figure 5. Under high pressure both of the sound velocities display an increment trend with the increasing of pressure; this characteristic confirms the former findings of pressure effect on both V_L and V_T [30]. When compared with each other V_L has a more uniform increasing fashion than V_T .

An additional comparison is given in Tables 1 and 2 for the present typical cubic elastic constants C_{11} , C_{12} , and C_{44} and other calculated parameters, respectively. As seen in Table 1, our obtained values for C_{11} , C_{12} , and C_{44} are reasonable when compared with the experimental measurements. On the other hand, Table 2 summarizes the present and former experimental results (originally extrapolated from 4 Kelvin measurements) of B , G , E , V_L , and V_T constants for $T = 0$ Kelvin and $P = 0$ GPa. From a more physical perspective, from Tables 1 and 2, it is easy to see the existence of traditional Born mechanical (dynamical) stability conditions ($P = 0$ GPa); $C_{11} > 0$, $C_{44} > 0$, $C_{11} - C_{12} > 0$, $C_{11} + C_{12} > 0$, and $C_{12} < B < C_{11}$ [18] for Au over the entire pressure range.

TABLE 1: Comparing previous experimental results and present calculation data for C_{11} , C_{12} , and C_{44} constants of Au.

Elastic constants	Reference [18] (Exp)	Reference [19] (Exp)	This study
C_{11} (GPa)	186.0	190.0	179.8
C_{12} (GPa)	157.0	161.0	147.7
C_{44} (GPa)	42.0	42.3	42.1

TABLE 2: Comparing earlier experimental data of B , E , G , V_L , and V_T values for Au with our results.

Elastic parameters	Reference [20] (Exp)	This study
B (GPa)	180.32	158.4
G (GPa)	29.23	31.6
E (GPa)	83.19	46.5
V_L (km/s)	3.35	3.22
V_T (km/s)	1.22	1.28

Apparently our presently calculated data shows a fair consistency again for all considered parameters and their related characteristics under high pressures.

4. Conclusion

In summary, we surveyed the effect of pressure on several mechanical and elastic properties of Au metal with embedded atom model by geometry optimization calculations. As an outcome, the obtained findings put forth reasonable results for the high pressure behavior of Au when compared with the other experimental, molecular dynamics, and density functional results. We found that the calculated P - V EOS of Au (Figure 1) up to 1000 GPa is fully consistent with the former data of available experiments and theoretical results. From the high pressure point of view, with the increasing of pressure, all the elastic constants (Figures 2 and 3) and other elastic parameters (Figures 4 and 5) increased almost linearly. This finding is also compatible with the foregoing studies (Tables 1 and 2) of the considered metal. Finally, as it is obvious from all figures and tables, EAM based geometry optimization provides satisfactory results for the concerned study parameters and a convenient alternative for atomistic modeling.

References

- [1] H. Kimikuza, S. Ogata, J. Li, and Y. Shibusaki, "Complete set of elastic constants of α -quartz at high pressure: a first principles study," *Physical Review B*, vol. 75, no. 5, Article ID 054109, 6 pages, 2007.
- [2] M. Matsui, "High temperature and high pressure equation of state of gold," *Journal of Physics*, vol. 215, no. 1, Article ID 012197, 2010.
- [3] S.-H. Shim, T. S. Duffy, and K. Takemura, "Equation of state of gold and its application to the phase boundaries near 660 km depth in Earth's mantle," *Earth and Planetary Science Letters*, vol. 203, no. 2, pp. 729–739, 2002.
- [4] C. V. Pandya, P. R. Vyas, T. C. Pandya, N. Rani, and V. B. Gohel, "An improved lattice mechanical model for FCC transition metals," *Physica B*, vol. 307, no. 1–4, pp. 138–149, 2001.
- [5] Y. Ö. Çiftci, K. Çolakoğlu, S. Kazanç, and S. Özgen, "The effect of pressure on the elastic constants of Cu, Ag and Au: a molecular dynamics study," *Central European Journal of Physics*, vol. 4, no. 4, pp. 472–480, 2006.
- [6] P. I. Dorogokupets and A. R. Oganov, "Ruby, metals, and MgO as alternative pressure scales: a semiempirical description of shock-wave, ultrasonic, x-ray, and thermochemical data at high temperatures and pressures," *Physical Review B*, vol. 75, no. 2, Article ID 024115, 2007.
- [7] J. D. Gale, "Molecular modeling theory: applications," in *The Geosciences*, C. R. Timothy and J. D. Kubicki, Eds., chapter 2, p. 37, Mineralogical Society of America, Washington, DC, USA, 2001.
- [8] A. Budi, D. J. Henry, J. D. Gale, and I. Yarovsky, "Comparison of embedded atom method potentials for small aluminium cluster simulations," *Journal of Physics Condensed Matter*, vol. 21, no. 14, Article ID 144206, 2009.
- [9] R. B. Wilson and D. M. Riffe, "An embedded-atom-method model for alkali-metal vibrations," *Journal of Physics. Condensed Matter*, vol. 24, no. 33, Article ID 335401, 2012.
- [10] M. A. Tschopp, K. N. Solanki, M. I. Baskes, F. Gao, X. Sun, and M. F. Horstemeyer, "Generalized framework for interatomic potential design: application to Fe-He system," *Journal of Nuclear Materials*, vol. 425, no. 1–3, pp. 22–32, 2012.
- [11] X. J. Zhang and C. L. Chen, "Phonon dispersion in the Fcc metals Ca, Sr and Yb," *Journal of Low Temperature Physics*, vol. 169, pp. 40–50, 2012.
- [12] M. S. Daw and M. I. Baskes, "Semiempirical, quantum mechanical calculation of hydrogen embrittlement in metals," *Physical Review Letters*, vol. 50, no. 17, pp. 1285–1288, 1983.
- [13] M. W. Finnis and J. E. Sinclair, "A simple empirical N-body potential for transition metals," *Philosophical Magazine A*, vol. 50, no. 1, pp. 45–55, 1984.
- [14] E. Güler and M. Güler, "A benchmark for some bulk properties of bcc iron," *The International Journal of Multiphysics*, vol. 7, pp. 95–100, 2013.
- [15] A. P. Sutton and J. Chen, "Long-range Finnis-Sinclair potentials," *Philosophical Magazine Letters*, vol. 61, pp. 139–146, 1990.
- [16] J. D. Gale, "GULP: a computer program for the symmetry-adapted simulation of solids," *Journal of the Chemical Society*, vol. 93, no. 4, pp. 629–637, 1997.
- [17] J. D. Gale and A. L. Rohl, "The General Utility Lattice Program (GULP)," *Molecular Simulation*, vol. 29, no. 5, pp. 291–341, 2003.
- [18] H. B. Huntington, *The Elastic Constants of the Crystals*, Academic Press, New York, NY, USA, 1958.
- [19] E. A. Brandes and G. B. Brook, *Smithells Metals Reference Book*, Butterworth-Heinemann, Oxford, UK, 7th edition, 1992.
- [20] T. M. Flynn, *Cryogenic Engineering*, CRC Press, 2nd edition, 2004.
- [21] M. B. Taylor, G. D. Barrera, N. L. Allan, and T. H. K. Barron, "Free-energy derivatives and structure optimization within quasiharmonic lattice dynamics," *Physical Review B*, vol. 56, no. 22, pp. 14380–14390, 1997.
- [22] C. G. Broyden, "The convergence of a class of double-rank minimization algorithms I. General considerations," *IMA Journal of Applied Mathematics*, vol. 6, no. 1, pp. 76–90, 1970.
- [23] F. R. Fletcher, "New approach to variable metric algorithms," *Computer Journal*, vol. 13, no. 3, pp. 317–322, 1970.

- [24] D. Goldfarb, "A family of variable metric updates derived by variational means," *Mathematics of Computation*, vol. 24, pp. 23–26, 1970.
- [25] D. F. Shanno, "Conditioning of quasi-Newton methods for function minimization," *Mathematics of Computation*, vol. 24, pp. 647–656, 1970.
- [26] M. Güler and E. Güler, "Embedded atom method based geometry optimization aspects of body centered cubic metals," *Chinese Physics Letter*, vol. 30, no. 5, Article ID 056201, 2013.
- [27] M. Yokoo, N. Kawai, K. G. Nakamura, K.-I. Kondo, Y. Tange, and T. Tsuchiya, "Ultrahigh-pressure scales for gold and platinum at pressures up to 550 GPa," *Physical Review B*, vol. 80, no. 10, Article ID 104114, 2009.
- [28] T. S. Duffy, G. Shen, D. L. Heinz et al., "Lattice strains in gold and rhenium under nonhydrostatic compression to 37 GPa," *Physical Review B*, vol. 60, no. 22, pp. 15063–15073, 1999.
- [29] C. W. Greeff and M. J. Graf, "Lattice dynamics and the high pressure equation of state of Au," *Physical Review B*, vol. 69, no. 5, Article ID 054107, 10 pages, 2004.
- [30] H. Wang and M. Li, "The elastic stability, bifurcation and ideal strength of gold under hydrostatic stress: an ab initio calculation," *Journal of Physics Condensed Matter*, vol. 21, no. 45, Article ID 455401, 2009.

Research Article

Modelling of Hybrid Materials and Interface Defects through Homogenization Approach for the Prediction of Effective Thermal Conductivity of FRP Composites Using Finite Element Method

C. Mahesh,¹ K. Govindarajulu,² and V. Balakrishna Murthy¹

¹ Department of Mechanical Engineering, V.R. Siddhartha Engineering College, Vijayawada 520 007, India

² Department of Mechanical Engineering, JNT University Anantapur, Anantapur 521 501, India

Correspondence should be addressed to C. Mahesh; mahesh_chindanuru@rediffmail.com

Received 30 May 2013; Accepted 12 September 2013

Academic Editor: Martha Guerrero

Copyright © 2013 C. Mahesh et al. This is an open access article distributed under the Creative Commons Attribution License, which permits unrestricted use, distribution, and reproduction in any medium, provided the original work is properly cited.

Finite element method is effectively used to homogenize the thermal conductivity of FRP composites consisting of hybrid materials and fibre-matrix debonds at some of the fibres. The homogenized result at microlevel is used to determine the property of the layer using macromechanics principles; thereby, it is possible to minimize the computational efforts required to solve the problem as in state through only micromechanics approach. The working of the proposed procedure is verified for three different problems: (i) hybrid composite having two different fibres in alternate layers, (ii) fibre-matrix interface debond in alternate layers, and (iii) fibre-matrix interface debond at one fibre in a group of four fibres in one unit cell. It is observed that the results are in good agreement with those obtained through pure micro-mechanics approach.

1. Introduction

Composite materials are extensively used in many fields of engineering such as aerospace, electronic packaging, reactor vessels, and turbines, due to light weight, high strength, long durability, stability against chemical reaction, tailorable properties, and so forth. FRP composites can be designed as heat conductors for enhancing heat transfer rate and also for insulation purpose; this depends on the thermal properties, volume fraction, orientation, and so forth, of each constituent of the composite. The effective thermal conductivity and other thermophysical properties of composites have been a topic of considerable theoretical, experimental, and numerical interest from long period.

Composite materials are nonhomogeneous and exhibit anisotropic response due to structural and thermal loads. Analysis of a composite structure as in state of heterogeneity by providing the material properties of constituent materials is mathematically complex, and therefore theories such as micromechanics and macromechanics are developed for

the theoretical analysis. The homogenized properties of a composite lamina obtained from micromechanical theories are used for the macromechanical analysis of a composite made of several individual laminas stacked in a specified manner.

The micromechanical theories select a particular portion of the composite known as “Representative Volume Elements” (RVE) and find the properties of RVE which are considered to be lamina properties. In this approach, there are many assumptions such as fibres which are arranged in a particular pattern (square/hexagonal) in a matrix, no voids in the matrix, all fibres are of uniform cross-section and perfectly aligned, the interface between the fibre and matrix is perfectly or totally debond; this leads to much deviation of theoretical and experimental results. Numerical approaches such as Finite Element Method (FEM) are developed to overcome some of the assumptions of micromechanical theories but still not explored in addressing many complexities in micromechanical approach. Though FEM is an

approximate method, it can be effectively used after proper mesh refinement and validation.

Aligned fibre composite laminates are frequently used in beam, plate, or shell form. The axial thermal conductivity (in the fibre direction) of each lamina is satisfactorily predicted by a simple rule of mixtures Chawla [1]. Prediction of through-thickness thermal conductivity is more problematic. Yet this is important, since heat sources one side of the laminate often create a through-thickness temperature gradient.

Earlier several researchers studied thermal conductivities of composites by experimental, theoretical, and numerical approaches. Prediction of effective transverse thermal conductivity of fibre reinforced composites is made for several models, such as experimental determination of effective thermal conductivity of aligned fibre composite of Chamis [2], thermal conductivity of constituents of FRCL by backout method of Al-Sulaiman et al. [3], simple thermal resistance models of Chawla, Springer and Tsai [1, 4], as well as sophisticated conduction models of Rayleigh and Lu [5, 6] and interface resistance models of Hasselman and Johnson, Farmer and Covert, Zou et al., Benveniste [7–10], 2D numerical model of Islam and Pramila, [11], 3D numerical model of Rao et al. [12], 2D thermal contact resistance model of Ramani and Vaidyanathan, [13]. Hybrid composites are also playing a dominant role by adding desirable properties which are lagging with monofibre composites by Jawaid and Abdul Khalil [14].

In the present analysis, a 3D FEM is proposed to address various nonsimilarities in the unit cells at microlevel and developing equivalence between micro- and macromechanical approaches through some of the examples of heat conduction. Three cases are considered for present study: case (i) hybrid composite constituting two different thermal conductivity fibres and matrix, case (ii) composite with alternate layers of fibres fully debonded, and case (iii) composite with one in set of four fibres of a unit cell is fully debonded.

2. Problem Modelling

2.1. Geometric Modelling. Figures 1, 3, and 5 represent the microlevel view of case (i) hybrid composite constituting two different thermal conductivity fibres and matrix, case (ii) composite with alternate layers of fibres fully debonded, and case (iii) composite with one in set of four fibres of a unit cell debonded, respectively. Because of high degree of symmetry in the alignment of fibres, thermal loading, one-fourth model is used for the analysis as shown in Figures 2 and 4. For case (iii), even though material and geometric symmetry exists, due to non-symmetric thermal loading a full model is taken for the analysis as shown in Figure 6. Dimensions considered for the analysis are $a = 100$ units, $b = 100$ units, radius of fibres corresponds to volume fractions ranging from 0.1 to 0.7.

In macromechanics approach for first two cases, two blocks are modelled one over the other. For case (i) one block represents fibre1 and matrix portion and the other block is for fibre2 and matrix portion. Case (ii) one block represents total debonded fibre matrix and other perfectly bonded fibre matrix, whereas for case (iii) four blocks are modelled in

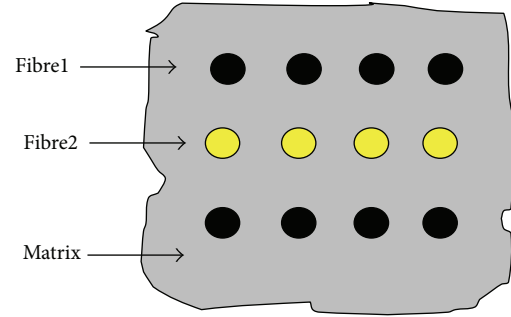


FIGURE 1: Concept of square unit cell for aligned pattern of hybrid composite with two different types of fibres.

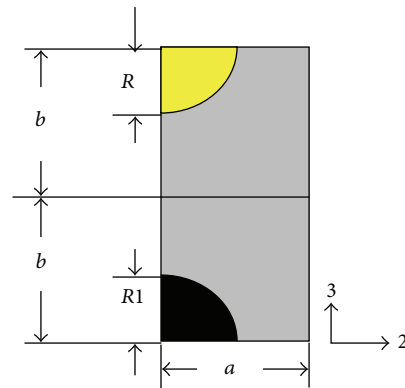


FIGURE 2: One-fourth model of unit cell for aligned pattern of fibres.

square pattern. One block represents debonded fibre and matrix portion and other three blocks for perfectly bonded fibre matrix. Surfaces at the junction of blocks are merged for heat transfer connectivity without any interfacial thermal barrier.

2.2. Finite Element Modelling. The problem is modelled in commercial Finite Element Software ANSYS 12 [15]. A 3D quadratic brick element having 20 nodes with a single degree of freedom (temperature) at each node, named SOLID90, is used for discretization of the constituents. For hybrid composite two material properties are assigned for fibre1 and fibre2, whereas for case (ii) and case (iii) only one material property is assigned for fibres. CONTA174 and TARGE170 elements of ANSYS software are used for studying interface thermal contact behaviour between fibre and matrix. The finite element mesh is properly refined, and converged results are verified with Hasselman-Johnson and Farmer-Covert models for perfect bond and total debond at fibre-matrix interfaces. Results are present in Section 3. Figure 7 represents the Geometry and FE mesh of a 3D model for case (i) and case (ii) and Figure 8 represents the Geometry and FE mesh of a 3D model for case (iii).

2.3. Boundary Conditions. Temperature difference (dT) of 100°C is maintained on two isothermal surfaces perpendicular to heat flow direction. All other surfaces are subjected to insulation boundary conditions. For debond between fibre

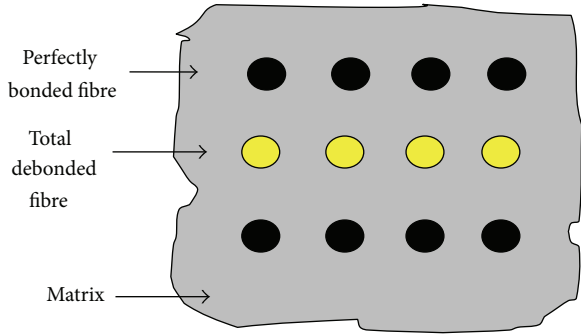


FIGURE 3: Concept of square unit cell for aligned pattern of composite with alternate layers of debonded fibres.

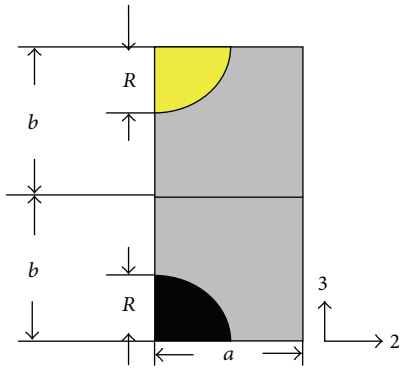


FIGURE 4: One-fourth model of unit cell for composite with alternate layers of debonded fibres.

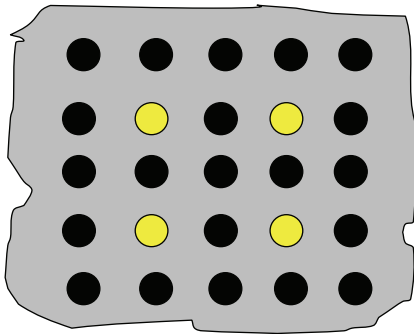


FIGURE 5: Concept of square unit cell for aligned pattern of composite with one in set of four fibres of unit cell totally debonded.

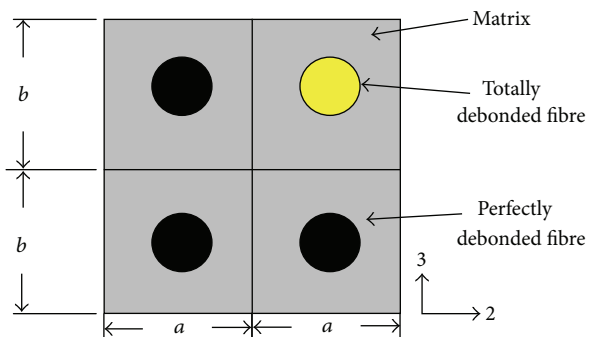


FIGURE 6: Full model for aligned pattern of composite with one in set of four fibres of unit cell totally debonded.

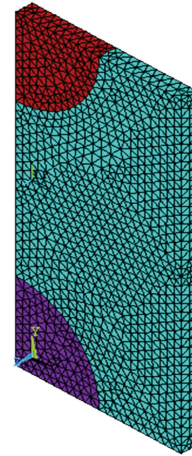


FIGURE 7: Geometry and FE mesh of a 3D model for case (i) and case (ii).

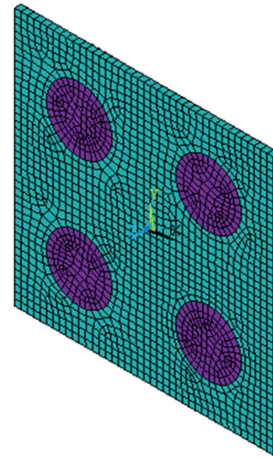


FIGURE 8: Geometry and FE mesh of a 3D model for case (iii).

and matrix contact conductance $h_c = 1E - 6$ and for perfect contact between fibre and matrix contact conductance $h_c = 1E6$ are taken.

2.4. *Material Properties.* For the validation of the models developed in the present analysis, the following properties of fibres and matrix [2] are considered.

Polyimide matrix with thermal conductivity $K_m = 0.19$ W/mK.

(T-300) Carbon fibre with thermal conductivity $K_{f1} = 8.365218$ W/mK.

For all the three cases of the study, matrix is polyimide matrix.

For the hybrid model, fibre1 : fibre2 : matrix thermal conductivity ratios used are 100 : 10 : 1, 80 : 8 : 1, 60 : 6 : 1, and 40 : 4 : 1.

For the debond models, fibre thermal conductivities range from 0.14 W/mK to $1E6$ W/mK.

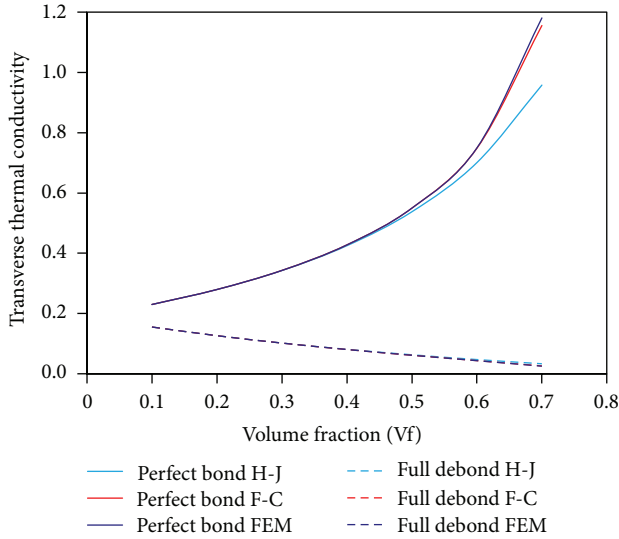


FIGURE 9: Variation in transverse thermal conductivity with respect to Vf for perfect bond and total debond conditions.

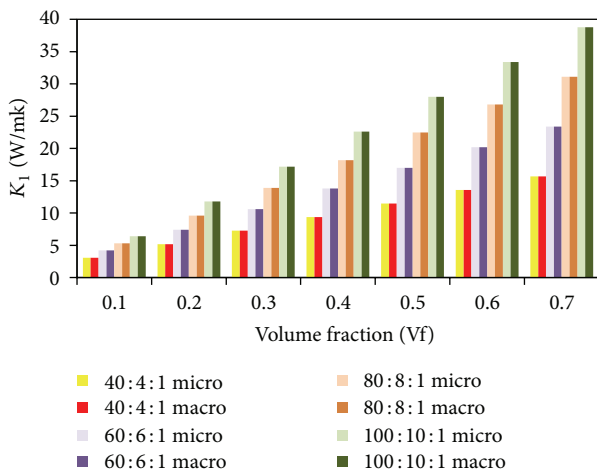


FIGURE 10: Variation in K_1 of hybrid composite with respect to Vf for different $K_{f1} : K_{f2} : K_m$.

3. Discussion of Results

The analytical solution for 1D heat conduction in homogeneous slabs is readily available. However, the analytical solution for 1D heat conduction is quite complex for heterogeneous materials such as fibre reinforced composite materials. Thus, the numerical finite element models have been developed to suit the different cases under consideration for this study. The models are first tested for mesh-independent solution by imposing earlier stipulated boundary conditions; then with the heat flux obtained from ANSYS software, effective thermal conductivity of composite is found by Fourier's law of heat conduction [3],

$$q = -K \frac{dT}{dx}, \quad (1)$$

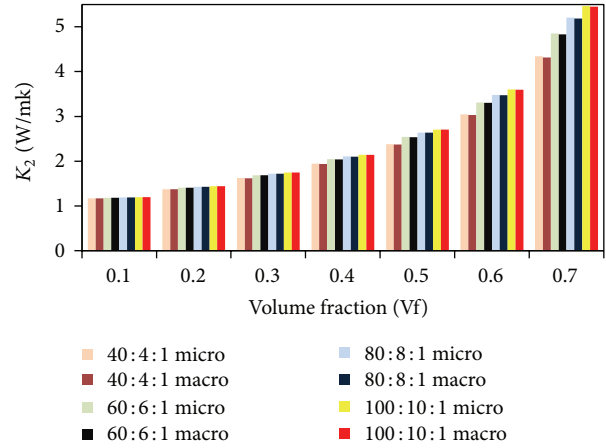


FIGURE 11: Variation in K_2 of hybrid composite with respect to Vf for different $K_{f1} : K_{f2} : K_m$.

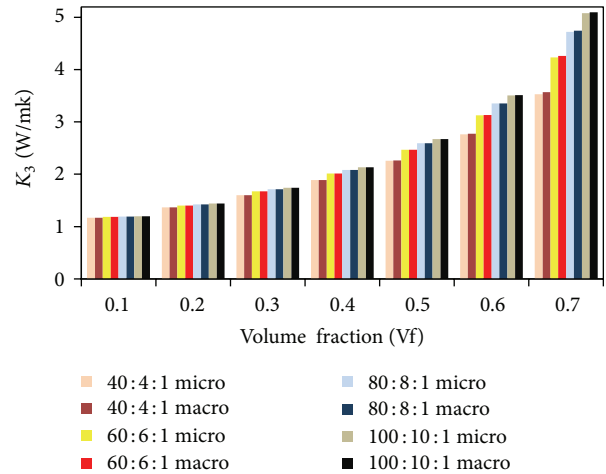


FIGURE 12: Variation in K_3 with respect to Vf of hybrid composite for different $K_{f1} : K_{f2} : K_m$.

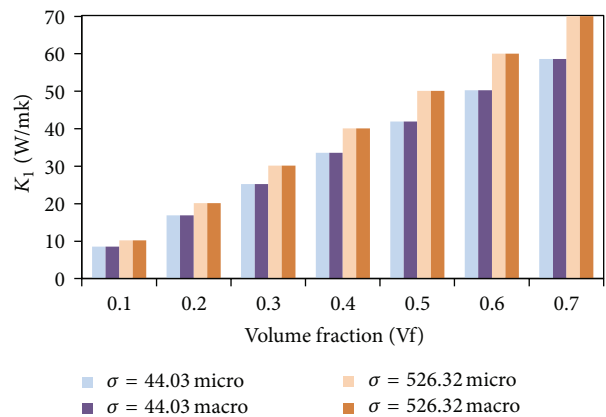


FIGURE 13: Variation in K_1 with respect to Vf of a composite with alternate layers of fibres fully debonded.

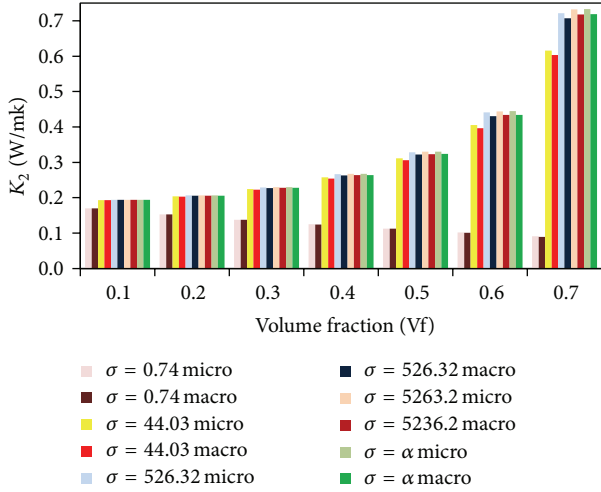


FIGURE 14: Variation in K_2 with respect to Vf of a composite with alternate layers of fibres fully debonded.

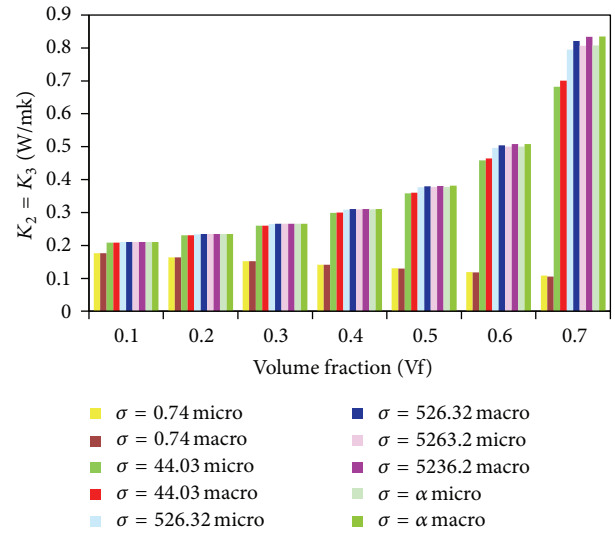


FIGURE 17: Variation of $K_2 = K_3$ with respect to Vf for a composite with one in four fibres in unit cell fully debonded.

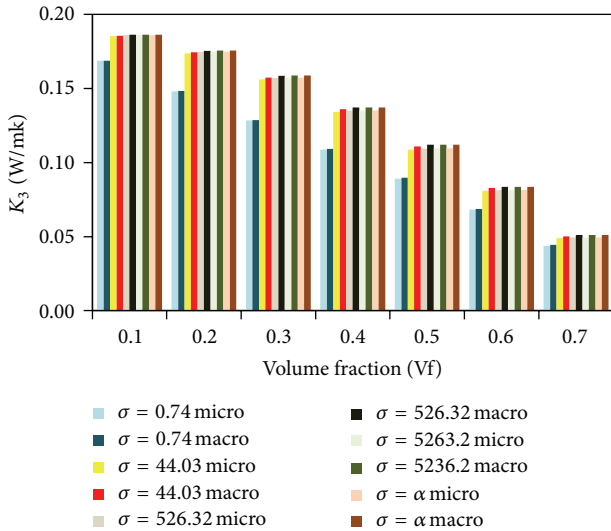


FIGURE 15: Variation in K_3 with respect to Vf of a composite with alternate layers of fibres fully debonded.

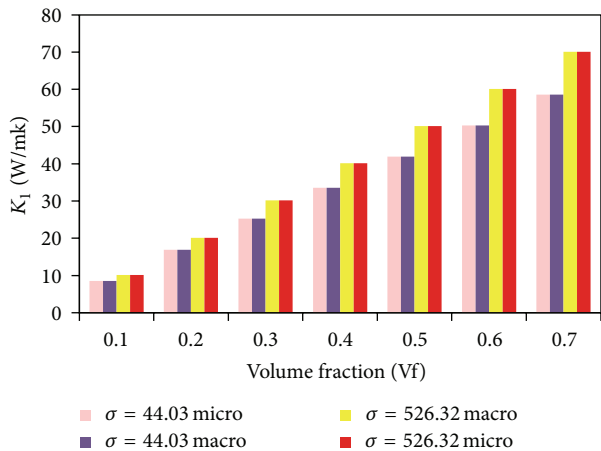


FIGURE 16: Variation in K_1 with respect to Vf for a composite with one in four fibres in unit cell fully debonded.

where dT/dx is temperature gradient between two isothermal surfaces. q is the heat flux W/m^2 .

FE model developed in ANSYS is first validated with the Hasselman and Johnson model (H-J) [7] and Farmer and Covert model (F-C) [8]. Figure 9 shows the comparison of results between Hasselman-Johnson model, Farmer-Covert model, and FEM model. It reveals that the results predicted by FE model for full debond case exactly match for complete range of volume fraction and up to nearly 50% Vf for perfect bond condition with both H-J and F-C models and deviation with H-J model from 50% Vf is due to assumptions made in the model and quite coherent with the higher order F-C model.

Figures 10, 11, and 12 show variation in principal thermal conductivities with respect to volume fraction and fibre1 : fibre2 : matrix thermal conductivity ratios for case (i).

Figures 13, 14, and 15 show variation in principal thermal conductivities with respect to volume fraction and fibre-matrix thermal conductivity ratios for case (ii).

Figures 16 and 17 show variation in principal thermal conductivities with respect to volume fraction and fibre-matrix thermal conductivity ratios for case (iii).

Table 1 represents % error between micro- and macromechanics approaches for case (i).

Table 2 represents % error between micro- and macromechanics approaches for case (ii).

Table 3 represents % error between micro- and macromechanics approaches for case (iii).

Effective longitudinal thermal conductivity for three cases matches with the simple rule of mixtures and increases in linear manner with the increase in Vf (Figures 10, 13, and 16) since the fibre thermal conductivity dominates the matrix thermal conductivity. K_1 increases with increase in fibre1 : fibre2 : matrix thermal conductivity ratios and its effect is significant at higher Vf. As low and high K_f/K_m values prevent better pictorial visibility, in Figures 13 and

TABLE 1: % Error between macro- and micromechanics approach results for case-(i) hybrid composite.

Vf	100 : 10 : 01		80 : 08 : 01		60 : 06 : 01		40 : 04 : 01	
	K_2 % Error	K_3 % Error						
0.1	0.025	0.022	0.008	0.010	0.000	0.003	0.000	0.010
0.2	0.021	0.013	0.007	0.024	0.028	0.006	0.029	0.022
0.3	0.017	0.009	0.029	0.016	0.065	0.004	0.074	0.057
0.4	0.037	0.028	0.057	0.038	0.093	0.060	0.160	0.095
0.5	0.085	0.037	0.125	0.046	0.173	0.097	0.294	0.177
0.6	0.136	0.103	0.193	0.143	0.269	0.230	0.440	0.389
0.7	0.212	0.369	0.273	0.502	0.371	0.708	0.521	1.092

TABLE 2: % Error between macro- and micromechanics approaches for composite with alternate layers of fibres fully debonded.

Vf	$K_f/K_m = 0.74$		$K_f/K_m = 4.03$		$K_f/K_m = 526.32$		$K_f/K_m = 5263.2$		$K_f/K_m = \alpha$	
	K_2 % Error	K_3 % Error	K_2 % Error	K_3 % Error	K_2 % Error	K_3 % Error	K_2 % Error	K_3 % Error	K_2 % Error	K_3 % Error
0.1	0.01	0.02	0.10	0.10	0.07	0.12	0.09	0.11	0.09	0.10
0.2	0.01	0.13	0.37	0.34	0.35	0.43	0.35	0.43	0.34	0.44
0.3	0.06	0.26	0.82	0.77	0.82	0.88	0.82	0.88	0.82	0.88
0.4	0.20	0.41	1.37	1.34	1.38	1.51	1.39	1.51	1.40	1.51
0.5	0.31	0.88	1.89	1.93	1.92	2.27	1.93	2.28	1.94	2.28
0.6	0.75	0.87	2.24	2.30	2.28	2.53	2.30	2.54	2.30	2.54
0.7	1.45	1.82	2.03	2.08	1.97	3.08	1.96	3.09	1.97	3.09

TABLE 3: % Error between macro- and micromechanics approach results for composite with one out of four fibres of unit cell fully debonded.

Vf	$K_f/K_m = 0.74$	$K_f/K_m = 44.03$	$K_f/K_m = 526.32$	$K_f/K_m = 5263.2$	$K_f/K_m = \alpha$
	$K_2 = K_3$ % Error				
0.1	0.01	0.01	0.03	0.01	0.01
0.2	0.01	0.02	0.06	0.06	0.08
0.3	0.03	0.10	0.15	0.15	0.15
0.4	0.15	0.26	0.36	0.37	0.35
0.5	0.34	0.61	0.79	0.79	0.78
0.6	0.93	1.27	1.54	1.56	1.56
0.7	2.08	2.65	3.23	3.28	3.28

16 plots for K_f/K_m values of 44.03 and 526.32 are made, as the focus of this paper is comparison between micro- and macromechanics approaches. Also for the three cases, % error between micro- and macromechanics results is zero, so % error for effective longitudinal thermal conductivity is not shown in tables given below.

Transverse thermal conductivities K_2 and K_3 for case (i) vary nonlinearly with the variation in Vf, at low values of Vf a gradual rise in K_2 and K_3 and at higher Vf beyond 0.6 a steep rise in K_2 and K_3 is observed (Figures 11 and 12). Fibrel : fibre2 : matrix thermal conductivity ratio is not significant at lower Vf and an increasing trend with respect to K_f/K_m is observed at higher Vf. % error between micro- and macromechanics approaches for K_2 and K_3 lies between 0.01 and 1.09 (Table 1).

For case (ii) inplane thermal conductivity K_2 and case (iii) both transverse thermal conductivities K_2 and K_3 vary nonlinearly with volume fraction, and behaviour is similar to case (i) for K_f/K_m values greater than unity, but these properties decrease linearly with increase in Vf for K_f/K_m value less than unity. Thermal conductivity mismatch ratio is significant at higher volume fractions. % error between micro- and macromechanics approaches for K_2 lies between 0.01 and 3.09 (Table 2).

For case (ii) through-thickness thermal conductivity K_3 decreases almost linearly with increase in Vf, and there is no significant effect of thermal conductivity mismatch ratio at all volume fractions. % error between micro- and macromechanics approaches for K_2 lies between 0.01 and 3.28 (Table 3).

4. Conclusions

Applicability of homogenization technique by using finite element method is successfully tested for predicting effective thermal conductivities of a hybrid and thermal contact resistance models for different volume fractions within practically possible range of 10% to 70% and thermal conductivity mismatch ratio 0.74 to α . It is evident from the results that macro-mechanics approach yields minimal errors with minimum effort. The same can be extended to composite with more other kinds of dissimilarities which is quite difficult with pure micromechanical models.

References

- [1] K. K. Chawla, *Composite Materials, Science and Engineering*, Springer, New York, NY, USA, 1987.
- [2] C. C. Chamis, "Simplified composite micromechanics equations for hygral, thermal and mechanical properties," NASA Technical Memorandum 83320, 1983.
- [3] F. A. Al-Sulaiman, Y. N. Al-Nassar, and E. M. A. Mokheimer, "Prediction of the thermal conductivity of the constituents of fiber-reinforced composite laminates: voids effect," *Journal of Composite Materials*, vol. 40, no. 9, pp. 797–814, 2006.
- [4] G. S. Springer and S. W. Tsai, "Thermal conductivities of unidirectional materials," *Journal of Composite Materials*, vol. 1, pp. 166–173, 1967.
- [5] L. Rayleigh, "On the influence of obstacles arranged in rectangular order upon the properties of a medium," *Philosophical Magazine*, vol. 34, p. 481, 1982.
- [6] S.-Y. Lu, "Effective thermal conductivities of composites with 2-D arrays of circular and square cylinders," *Journal of Composite Materials*, vol. 29, no. 4, pp. 483–506, 1995.
- [7] D. P. H. Hasselman and L. F. Johnson, "Effective thermal conductivity of composites with interfacial thermal barrier resistance," *Journal of Composite Materials*, vol. 21, no. 6, pp. 508–515, 1987.
- [8] J. D. Farmer and E. E. Covert, "Transverse thermal conductance of thermosetting composite materials during their cure," in *Proceedings of the 34th AIAA/ASME/ASCE/AHS/ASC Structures, Structural Dynamics, and Materials Conference*, pp. 2337–2347, April 1993, paper 93.
- [9] M. Zou, B. Yu, and D. Zhang, "An analytical solution for transverse thermal conductivities of unidirectional fibre composites with thermal barrier," *Journal of Physics D*, vol. 35, no. 15, pp. 1867–1874, 2002.
- [10] Y. Benveniste, "Effective thermal conductivity of composites with a thermal contact resistance between the constituents: nondilute case," *Journal of Applied Physics*, vol. 61, no. 8, pp. 2840–2843, 1987.
- [11] R. Islam and A. Pramila, "Thermal conductivity of fiber reinforced composites by the FEM," *Journal of Composite Materials*, vol. 33, no. 18, pp. 1699–1715, 1999.
- [12] G. S. Rao, T. Subramanyam, and V. B. Murthy, "3-D finite element models for the prediction of effective transverse thermal conductivity of unidirectional fibre reinforced composites," *International Journal of Applied Engineering Research*, vol. 3, no. 1, pp. 99–108, 2008.
- [13] K. Ramani and A. Vaidyanathan, "Finite element analysis of effective thermal conductivity of filled polymeric composites," *Journal of Composite Materials*, vol. 29, no. 13, pp. 1725–1740, 1995.
- [14] M. Jawaid and H. P. S. Abdul Khalil, "Cellulosic/synthetic fibre reinforced polymer hybrid composites: a review," *Carbohydrate Polymers*, vol. 86, no. 1, pp. 1–18, 2011.
- [15] ANSYS Reference Manuals, 2011.

Research Article

Calculation of Liquidus Temperature for Aluminum and Magnesium Alloys Applying Method of Equivalency

Mile B. Djurdjević,¹ Srećko Manasijević,² Zoran Odanović,¹ and Natalija Dolić³

¹IMS Institute, Bulevar Vojvode Mišića 43, 11 000 Belgrade, Serbia

²Lola Institute, Kneza Višeslava 70a, 11 000 Belgrade, Serbia

³Faculty of Metallurgy, University of Zagreb, Aleja Narodnih Heroja 3, 44 103 Sisak, Croatia

Correspondence should be addressed to Srećko Manasijević; srecko.manasijevic@li.rs

Received 29 May 2013; Accepted 3 September 2013

Academic Editor: Martha Guerrero

Copyright © 2013 Mile B. Djurdjević et al. This is an open access article distributed under the Creative Commons Attribution License, which permits unrestricted use, distribution, and reproduction in any medium, provided the original work is properly cited.

The purpose of this paper is to develop a mathematical equation, which will be able to accurately predict the liquidus temperature of various aluminum and magnesium cast alloys on the basis of their known chemical compositions. An accurate knowledge of liquidus temperature permits a researcher to predict a variety of physical parameters pertaining to a given alloy. The analytical expressions presented in this paper are based on the “method of equivalency.” According to this concept, the influence of any alloying element on the liquidus temperature of an aluminum and/or magnesium alloy can be translated into the equivalent influence of a reference element. Silicon as a reference element has been chosen for aluminum alloys and aluminum for magnesium alloys. The sum of the equivalent concentrations for other elements, when added to the influence of the actual reference element is used to calculate the liquidus temperature of the alloy. The calculated liquidus temperatures for wide ranges of alloy chemical compositions show a good correlation with corresponding measured liquidus temperatures.

1. Introduction

In order to predict the various physical parameters of a solidifying aluminum and magnesium alloys (e.g., fraction solid), the liquidus temperatures of these alloys must be known with the highest possible degree of accuracy. Unfortunately, only few equations are reported in the literature that relate the compositions of many commercially important nonferrous [1, 2] and ferrous [3] alloys to their liquidus temperatures. Moreover, some of these equations are not sufficiently verified by experimental data. For the binary aluminum and magnesium alloys, liquidus temperature/composition relations can easily be derived from highly accurate binary diagrams. These are based on experimental data obtained under equilibrium solidification conditions [4, 5].

The Al-Si phase diagram is the base component system for the Al-Si series of alloys. As Figure 1 shows, it is a binary eutectic type phase diagram with limited aluminum and silicon solubility. The melting temperature of pure aluminum is 660°C. The solubility of silicon in the aluminum melt reaches

a maximum of 1.6 wt.% at the 577°C eutectic temperature. The maximum solubility of aluminum in silicon at the eutectic temperature is still questionable, and according to some literature data, it is approximately 0.015 wt.% [6]. The concentration of silicon, which corresponds to the eutectic reaction, is still not accurately defined or accepted among researchers, despite the fact that this diagram has been investigated often. In the available literature the following values for eutectic concentration of silicon were found: 11.9 wt.% [7], 12.2 wt.% [6], 12.3 wt.% [8] and 12.6 wt.% [9] In this work the value of 12.3 wt.% of Si will be used as the eutectic concentration of silicon as well as 577°C as the temperature at which eutectic reaction occurs.

The cast aluminum-silicon alloys are widely used in many automotive components. These alloys are characterized by their low density, light weight, relative low melting temperatures, negligible gas solubility (with the exception of hydrogen), excellent castability, good corrosion resistance, electrical, and thermal conductivity and good machinability. Major alloying elements, Si, Cu, and Mg, are primarily

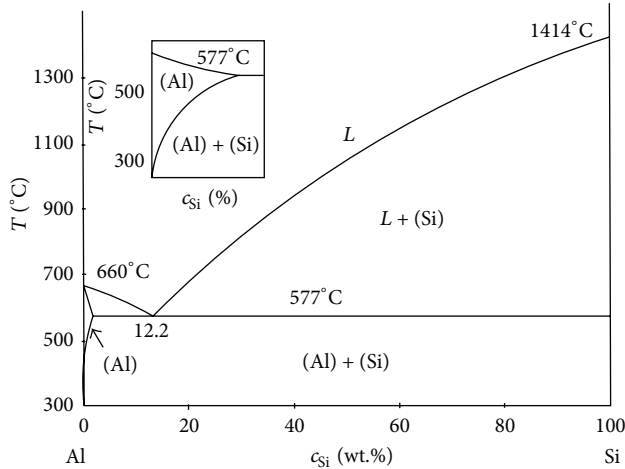


FIGURE 1: The Al-Si phase diagram [6].

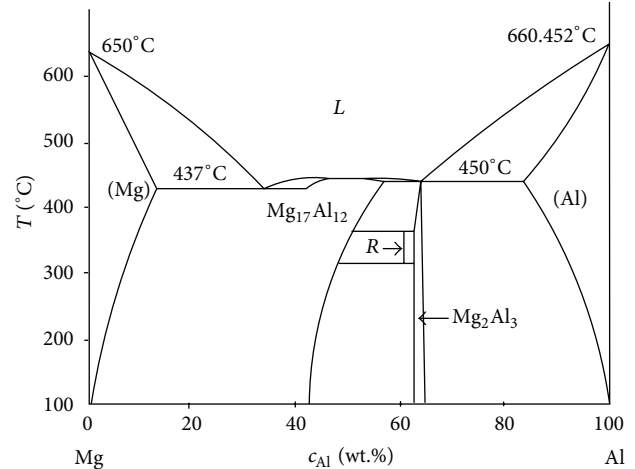


FIGURE 2: The Mg-Al binary phase diagram [10].

responsible for defining the microstructure of the aluminum alloy.

Mg-Al alloys are light metallic structural materials with a unique combination of properties, which are very attractive in such applications as the automobile, aerospace, and electronics industries. The use of magnesium alloys has become significant due to a one-third lower density of magnesium compared with aluminum, improved damping ability, a higher resistance to corrosion and better mechanical properties. In lightweight magnesium alloys, aluminum constitutes the main alloying element, chiefly because of its low price, availability, low density, and the advantageous effects on corrosion, and strength properties. Figure 2 shows the binary Mg-Al phase diagram with limited Al and Mg solubility [10]. The melting temperature of pure magnesium is 650°C. The solubility of magnesium in the aluminum melt reaches a maximum of 18.9 at.% at the 450°C eutectic temperature. The maximum solubility of aluminum in magnesium at the eutectic temperature is 11.8 at.% [11]. In this work, the value of 32.0 wt.% of Al will be used as the eutectic concentration of aluminum as well as 473°C as the temperature at which eutectic reaction occurs.

The modeling and control of the casting processes have remained a topic of active interest for several decades, and the availability of numerous software packages (MAGMA [12], Thermo-Calc [13], Pandat [14], FactSage [15], Pro-Cast [16], Calphad [17], WinCast [18], etc.) on the market a good indication of the interest that casting industries and researchers have in this field. Most of the data used in the above listed software packages are based on binary or multicomponent phase diagrams, but unfortunately, except for binary diagrams, many of the ternary or higher order phase diagrams are still not accurate enough for this purpose. Keeping in mind that most aluminum and magnesium binary systems are very well established, the transferring of a multicomponent system into a well-known Al- X_i "quasi-binary" system has a great industrial and research potential. This type of system could be used to calculate several thermo-physical and solidification process parameters of multicomponent

aluminum alloys in either cast or melt treated conditions. In order to calculate the various thermophysical and metallurgical parameters of solidifying aluminum casting alloys, the characteristic solidification temperatures of the alloys must be known with the highest possible degree of accuracy.

The purpose of this paper is to develop the general method for the calculation of the characteristic liquidus temperatures of the multicomponent aluminum-silicon and magnesium-aluminum alloys based on their known chemical composition. The accuracy of the developed algorithms will be determined by comparing the calculated values of the liquidus temperatures with the measured values obtained using the thermal analysis technique as with the calculated values obtained using Thermo-Calc software program.

2. Modeling the Liquidus Temperature of Multicomponent Al and Mg Alloys

2.1. Development of the Algorithm of Equivalency. Figures 3 and 4 show several phase diagrams of selected aluminum and magnesium binary alloys. From most of them, it is visible that their liquidus temperatures decrease uniformly with the increase in the amount of the added alloying element and reach the minimum at the corresponding eutectic composition. Mathematically, the liquidus line of any eutectic binary Al- X_i and/or Mg- X_i phase diagrams from Figures 3 and 4 can be accurately expressed by the second order polynomial as follows:

$$T_{\text{liq}}^{\text{Al-}X_i} = A - BX_i - CX_i^2, \quad (1a)$$

$$T_{\text{liq}}^{\text{Mg-}X_i} = A - BX_i - CX_i^2, \quad (1b)$$

where $T_{\text{liq}}^{\text{Al-}X_i}$ and $T_{\text{liq}}^{\text{Mg-}X_i}$ are the liquidus temperatures of the observed binary system in °C, X_i is the amount of the alloying element in wt.%, A is the melting point of pure aluminum/magnesium, 660°C and 650°C, respectively, and B , and C are polynomial coefficients.

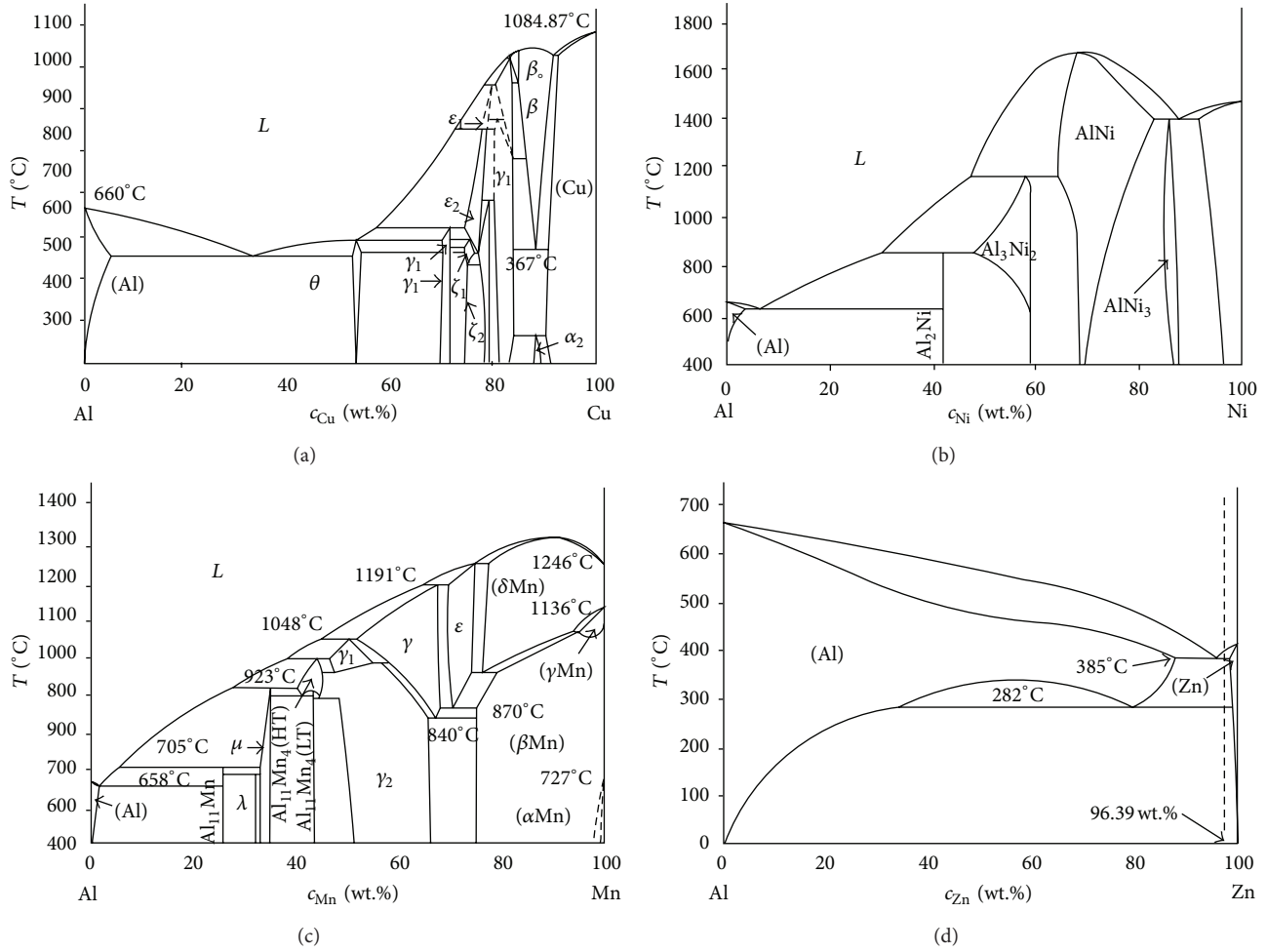


FIGURE 3: Binary phase diagrams of major aluminum alloying elements [13].

Therefore, the liquidus line for the Al-Si binary system can be expressed, respectively, as follows:

$$T_{\text{liq}}^{\text{Al-Si}} = 660.0 - 6.11\text{Si} - 0.057\text{Si}^2. \quad (2a)$$

Applying the same approach from (1a) and (1b), the liquidus line of the Mg-Al binary system can be written as

$$T_{\text{liq}}^{\text{Mg-Al}} = 650.0 - 4.987\text{Al} - 0.047\text{Al}^2. \quad (2b)$$

The visual analysis of the two liquidus lines of the binary systems, Al reference element and Al- X_i as presented in Figure 5, shows that the “equivalent effect” on the liquidus temperature of the aluminum alloy can be obtained by using “equivalent” concentrations of the reference element and X_i alloying elements.

This means that the influence of any alloying X_i element in the aluminum or magnesium melt on its liquidus temperature can be expressed as the effect of an “equivalent amount” of reference element, expressed in wt.%. Silicon as a major alloying element for Al-Si series of alloys was chosen as the reference element. It is also known to have the most

significant influence on the casting properties of Al-Si family of alloys (e.g., fluidity, latent heat, and shrinkage).

In lightweight magnesium alloys, aluminum is the mainly alloying element, chiefly because of its low price, availability, low density, and the advantageous effects on corrosion and strength properties. The AZ91 alloy (contains about 9 wt.% Al and 1wt.% Zn) is the most widely used magnesium alloy exhibiting a good combination of high strength at room temperature, good castability, and excellent corrosion resistance. Therefore, by magnesium alloys, aluminum has been chosen as a reference element.

The isothermal concentration difference between the reference element (Si or Al) and the X_i alloying elements can be mathematically expressed as follows:

$$\text{Si}_{\text{EQ},@T=\text{CONSTANT}}^{X_i} = \text{Si (wt.\%)} - X_i \text{ (wt.\%)}, \quad (3a)$$

$$\text{Al}_{\text{EQ},@T=\text{CONSTANT}}^{X_i} = \text{Al (wt.\%)} - X_i \text{ (wt.\%)}. \quad (3b)$$

Taking into consideration the whole temperature range between the melting temperature of the pure reference element (Si or Al) and the corresponding eutectic temperature

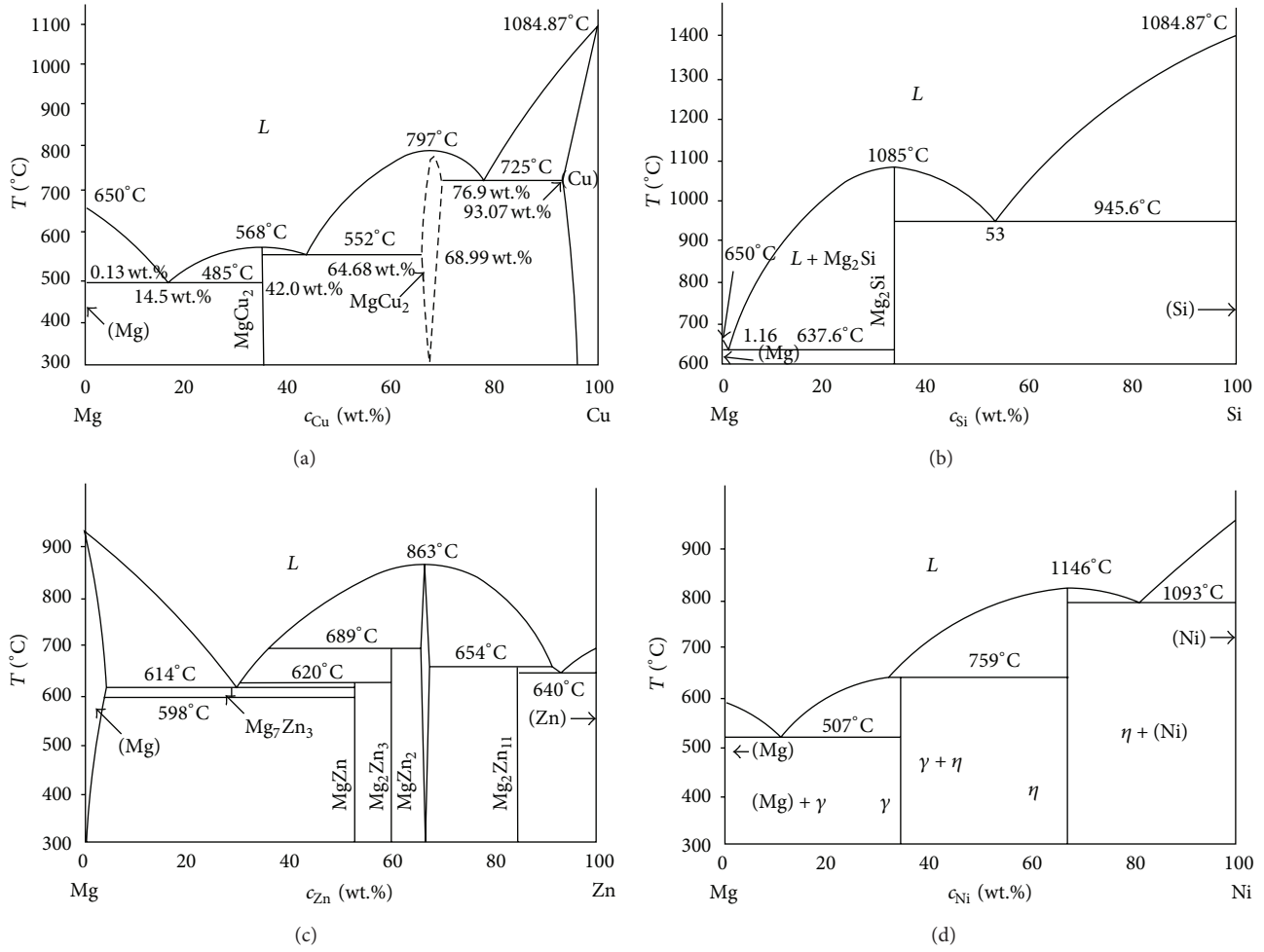
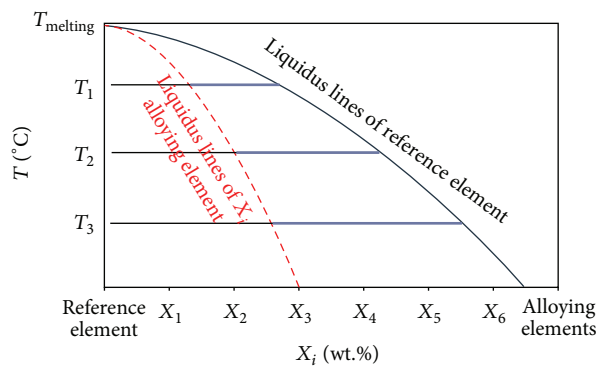


FIGURE 4: Binary phase diagrams of selected magnesium alloys [10, 13].

FIGURE 5: Superimposed liquidus lines of the reference element and X_i alloying elements in any binary system.

of an observed binary alloy (Al-Si or Mg-Al), the following relationship can be established between $Si_{EQ}^{X_i}$, $Al_{EQ}^{X_i}$ and the concentration of the alloying element X_i :

$$Si_{EQ}^{X_i} = a_o^{X_i} + b_o^{X_i} X_i + c_o^{X_i} X_i^2, \quad (4a)$$

$$Al_{EQ}^{X_i} = a_o^{X_i} + b_o^{X_i} X_i + c_o^{X_i} X_i^2, \quad (4b)$$

where $Si_{EQ}^{X_i}$ is the silicon equivalent for any alloying element expressed in wt.%, $Al_{EQ}^{X_i}$ is the aluminum equivalent for any alloying element expressed in wt.%, $a_o^{X_i}$, $b_o^{X_i}$, and $c_o^{X_i}$ are polynomial coefficients of the quadratic equation which describe the relationship between $Si_{EQ, @T=CONSTANT}^{X_i}$ or $Al_{EQ, @T=CONSTANT}^{X_i}$ and considered the alloying elements for at least three various temperatures, and X_i is the concentration of the alloying elements in wt.%.

The coefficients for the particular alloying elements (a_o , b_o , and c_o) from (4a) and (4b) are found in Table 1.

The Si_{EQ} and/or $Al_{EQ}^{X_i}$ for the alloying elements as well as for some impurity elements can be determined as the sum of individual contributors ($\sum Si_{EQ}^{X_i}$, $\sum Al_{EQ}^{X_i}$) plus the effect of the silicon/aluminum itself, and can be expressed as follows:

$$Si_{EQ} = Si + \sum Si_{EQ}^{X_i}, \quad (5a)$$

$$Al_{EQ} = Al + \sum Al_{EQ}^{X_i}. \quad (5b)$$

TABLE 1: Polynomial coefficients for the $\text{Si}_{\text{EQ}}^{X_i}$ and $\text{Al}_{\text{EQ}}^{X_i}$ function ((4a) and (4b)).

Elements X_i	Coefficients for the $\text{Si}_{\text{EQ}}^{X_i}$			Coefficients for the $\text{Al}_{\text{EQ}}^{X_i}$		
	a_o	b_o	c_o	a_o	b_o	c_o
Si	1.0	0.0	0.0	0.0	0.5111	-0.1458
Al				1.0	0.0	0.0
Cu	0.0	0.35	-0.027	0.0	-0.4161	0.0069
Mg	0.0	0.0258	0.0088			
Zn	0.0	0.1227	-0.0002	0.0	-0.4983	0.0047
Ni	0.0	0.5644	-0.0285			
Mn	0.0	0.8221	-0.0349			
Fe	0.0	0.6495	0.0003			
Y				0.0	-0.5695	0.0040

The characteristic liquidus temperatures for multi component Al-Si and Mg-Al series of alloys can be calculated using following equations:

$$T_{\text{LIQ}}^{\text{Al-Si} \sum X_i} = 660.0 - 6.110\text{Si}_{\text{EQ}} - 0.057\text{Si}_{\text{EQ}}^2, \quad (6a)$$

$$T_{\text{LIQ}}^{\text{Mg-Al} \sum X_i} = 650.0 - 4.987\text{Al}_{\text{EQ}} - 0.047\text{Al}_{\text{EQ}}^2. \quad (6b)$$

Equations (6a) and (6b) are valid for the following concentrations of key elements (expressed in wt.%):

For aluminum alloys,

$$\begin{aligned} \text{Si} \leq 12.6, \quad \text{Cu} \leq 10.0, \quad \text{Mg} \leq 10.0, \\ \text{Zn} \leq 10.0, \quad \text{Ni} \leq 2.0, \quad \text{Mn} \leq 2.0, \quad \text{Fe} \leq 1.0. \end{aligned} \quad (7)$$

For magnesium alloys,

$$\begin{aligned} \text{Al} \leq 32.0, \quad \text{Zn} \leq 45.0, \quad \text{Si} \leq 1.5, \\ \text{Cu} \leq 33.0, \quad \text{Y} \leq 24.0. \end{aligned} \quad (8)$$

3. Results and Discussion

The validity of the calculation procedure presented above was determined by comparing the calculated liquidus temperatures with the experimentally determined and computed (using Thermo-Calc software package) liquidus temperatures of aluminum and magnesium alloys. These comparisons are presented in Tables 2 and 3.

The slight discrepancies between measured and calculated values of liquidus temperatures (Tables 2 and 3) for aluminum and magnesium hypoeutectic cast alloys are related to the fact that the interaction among alloying elements from aluminum and magnesium melts has not been taken into consideration in (6a) and (6b). The analytical approach of this work is based on binary alloying systems (Figures 3 and 4), and no other interactions between three or more elements have been taken into consideration for the Si_{EQ} and Al_{EQ} methods. By allowing these parameters of interaction among of at least three elements (taken from ternary systems) from

aluminum and magnesium melts might bring the calculated values closer to the measured ones.

Figure 6 depicts a plot of the predicted liquidus temperature for each of the aluminum and magnesium alloys presented in Tables 2 and 3 versus their experimentally determined counterparts. Measured liquidus temperatures have been determined experimentally using the thermal analysis technique. According to the available literature data, the accuracy of the applied thermal analysis technique was between ± 0.5 and 1°C . All calculated liquidus temperatures have been computed using the method of equivalency expressed in this work through (6a) and (6b).

Figure 6 together with Table 4 demonstrate the pretty fair accuracy of the predictions made by the procedure developed in this study in comparison with the measured liquidus temperatures taken from the literature and calculated with Thermo-Calc software.

Table 4 displays that both approaches (the method of equivalency and the Thermo-Calc software) are used to calculate the liquidus temperatures of Al and Mg alloys according to R^2 criteria which shows pretty fair predictions. Statistical analysis reveals that application of (6a) for the calculation of liquidus temperatures results in lower standard deviations and lower scatter (minimum and maximum values) in the predictions compared to the results obtained using Thermo-Calc software package. Regarding Mg alloys, applying either (6b) or Thermal-Calc software, the statistical analysis shows almost the same results, that is, the same accuracy in comparison to measured liquidus temperature independent from applied procedures.

The main advantage of the method of equivalency has been recognized in its simplicity and straightforward application. Using chemical compositions of corresponding aluminum and/or magnesium alloys, their liquidus temperatures can be calculated using known polynomial coefficients for the Si_{EQ} and Al_{EQ} . This method can be in the future simply applied for any multicomponent metallic system that satisfies the following assumptions.

- (1) The melting point of reference element is known and constant.
- (2) The considered binary systems (reference element- X_i) are eutectic or peritectic.
- (3) Any addition of alloying elements to the reference element decreases the liquidus temperature to its eutectic temperature (peritectic type of reaction negative sign needs to be inserted in front the of corresponding polynomial coefficients from (4a) and (4b)).
- (4) For the multicomponent alloys, the equivalent concentration of the reference element needs to be considered as additive.

The accuracy of the calculated liquidus temperature in the proposed model (6a) and (6b) is dependent solely on the accuracy of the coefficients, by means of which the corresponding alloy content is converted into an equivalent silicon/aluminum weight percent. However, these coefficients are derived from the liquidus lines in the respective binary systems, and their reliability is closely related to the accuracy

TABLE 2: Chemical composition of aluminum alloys (wt.%) calculated liquidus temperatures using (6a), Thermo-Calc, and the measured.

Number	Chemical composition, wt.%							$T_{\text{LIQ}}/^{\circ}\text{C}$		
	Si	Cu	Mg	Zn	Fe	Mn	Ti	Equation (6a)	Thermo-Calc	Measured [Ref]
1	7.03	0.01	0.30	0.019	0.08		0.12	614.2	616	614.2 [19]
2	6.80	0.04	0.35	0.01	0.08		0.15	615.8	618	615.8 [9]
3	7.80							609.3	611	609.4 [7]
4	5.80	0.05						623.1	624	623.1 [20]
5	7.00	0.05	0.51	0.02	0.05	0.01	0.05	614.5	615	614.5 [21]
6	5.75	3.01	0.30	0.04	0.31	0.05	0.07	616.2	614	616.2 [22]
7	5.10	2.93	0.23	0.04	0.31	0.05	0.17	620.7	621	620.7 [23]
8	7.02	0.24	0.37	0.17	0.18	0.03	0.14	613.1	615	613.1 [24]
9	6.91	0.24	0.39	0.15	0.18	0.03	0.14	613.8	616	613.8 [25]
10	4.85	1.03	0.14	0.01	0.09	0.01	0.06	626.6	628	626.8 [25]
11	5.01	2.06	0.14	0.01	0.09	0.01	0.06	622.8	623	623.8 [25]
12	4.94	2.98	0.21	0.01	0.07	0.01	0.06	620.0	621	622.9 [25]
13	4.89	3.85	0.16	0.01	0.09	0.01	0.09	618.3	619	622.4 [25]
14	5.90	1.07	0.14	0.01	0.07	0.01	0.06	622.4	620	619.7 [25]
15	5.91	1.83	0.15	0.01	0.11	0.01	0.06	618.9	618	618.1 [25]
16	5.82	3.03	0.15	0.01	0.06	0.01	0.06	614.8	615	617.1 [25]
17	7.13	0.96	0.28	0.01	0.12	0.01	0.06	613.3	612	611.2 [25]
18	7.05	1.98	0.28	0.01	0.13	0.01	0.08	610.3	609	609.8 [25]
19	6.95	3.05	0.26	0.01	0.14	0.01	0.08	607.4	607	608.8 [25]
20	6.75	4.38	0.29	0.01	0.12	0.01	0.09	604.6	603	608.9 [25]
21	8.03	1.09	0.28	0.01	0.14	0.01	0.09	600.7	605	604.5 [25]
22	8.14	1.93	0.27	0.01	0.12	0.01	0.08	601.7	602	602.2 [25]
23	8.03	2.96	0.29	0.01	0.14	0.01	0.09	600.5	599	601.3 [25]
24	7.84	4.31	0.31	0.01	0.14	0.01	0.09	596.8	595	601.2 [25]

TABLE 3: Chemical composition of magnesium alloys (wt.%) calculated liquidus temperatures using (6b), Thermo-Calc, and the measured.

Number	Alloy	Chemical composition, wt.%					$T_{\text{LIQ}}/^{\circ}\text{C}$		
		Al	Zn	Ca	Mn	Cu	Equation (6b)	Thermo-Calc	Measured [Ref]
1	AZC911						603.1	592	600.0 [26]
2	AMC502	5.11		1.63	0.32		623.1	615	625.0 [26]
3	AMC503	5.37		2.89	0.30		621.7	610	615.0 [26]
4	AZ62	6.61	1.32		0.24		618.2	610	608.0 [27]
5	AZ91	8.67	0.63		0.21		604.0	601	598.0 [27]
6	AM60	6.50	0.22		0.13		616.1	615	615.0 [28]
7	AZ91	9.70	0.35		0.13	0.10	598.3	596	595.0 [28]
8	AM50	5.25	0.01		0.37		622.5	622	625.1 [29]
9	AZ91D	9.71	0.35		0.15	0.03	598.2	596	598.0 [18]
10	AM60B	6.51	0.20		0.24	0.01	616.0	615	615.0 [18]
11	AM50A	5.41	0.21		0.26	0.01	622.1	621	620.0 [18]
12	AM20	2.50	0.20		0.33	0.08	638.0	636	638.0 [18]
13	AE42	4.51	0.20		0.15	0.01	627.0	626	626.0 [18]

with which the liquidus curves are experimentally determined and numerically fitted. Therefore, some inaccuracy is also observed by applying this method. In order to exclude this source of error, a reexamination of the liquidus lines on the silicon/aluminum rich sides of the respective binary systems, or even better for the ternary Al-Si- X_i /Mg-Al- X_i systems, would be necessary.

The model has been developed using binary phase diagrams of Al- X_i and Mg- X_i alloys. For all the considered binary phase diagrams, the liquidus lines have been mathematically described until their corresponding eutectic concentrations. The concentration limits for the key elements have been established by either using the maximal concentration of key element at eutectic temperature (for major

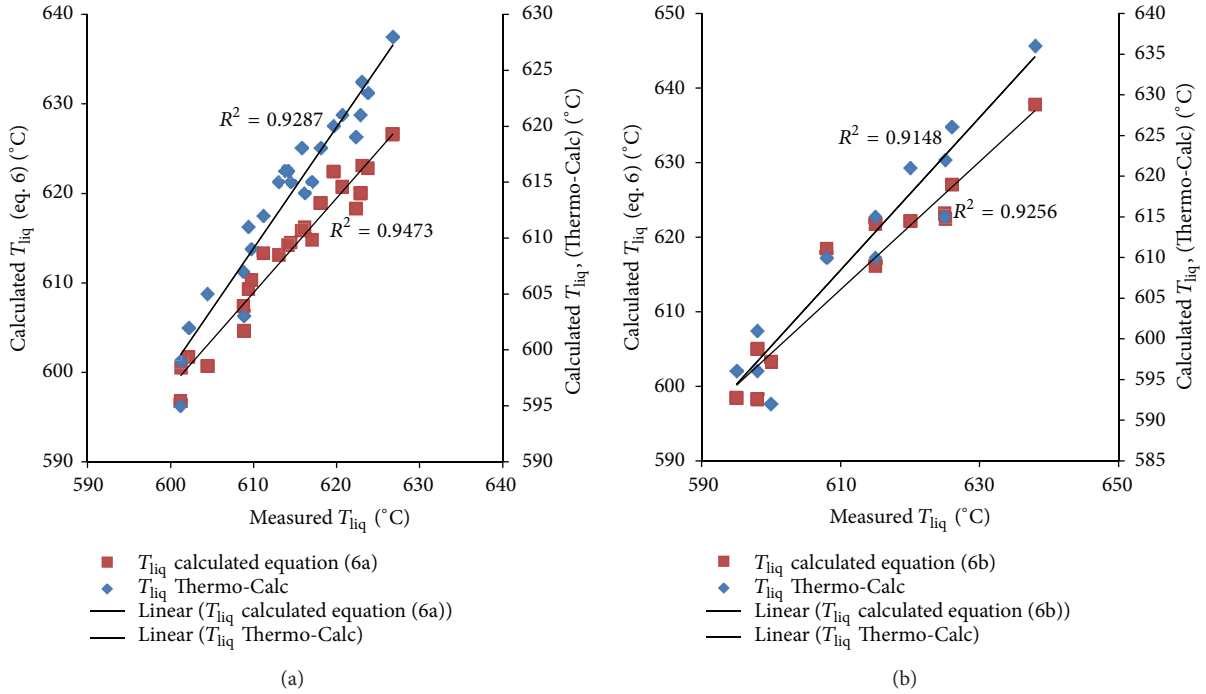


FIGURE 6: Predicted versus measured liquidus temperatures calculated applying the method of equivalency, (a) aluminum alloys (6a) and (b) magnesium alloys (6b).

TABLE 4: Regression coefficients, standard deviations and average values of differences calculated between measured and analytically determined liquidus temperatures using method equivalency and Thermo-Calc software.

Statistical data	Al-alloys		Mg-alloys	
	Equation (6a)	Thermo-Calc	Equation (6b)	Thermo-Calc
R^2	0.946	0.928	0.925	0.914
Standard deviations	1.901	2.309	-2.451	1.777
Average value	0.821	0.563	3.736	3.879
Minimum	-2.700	-2.200	-10.501	-3.000
Maximum	4.400	6.200	2.665	10.000

alloying elements such as Si in Al-Si alloys and Al in Mg-Al alloys) or setting the maximal concentrations of other minor alloying elements that can be found in typical hypoeutectic Al and Mg alloys [30]. It means that, theoretically, the established liquidus equations for Al and Mg alloys are usable up to the eutectic concentrations of any elements present in these alloys. Tables 2 and 3 show only those alloys that are found in the available literature with measured liquidus temperatures. In addition, the higher cooling rates applied in the experimental data presented in Tables 2 and 3 are a potential source of inaccuracy that cannot be disregarded.

Another advantage of a new equivalency method can be recognized in its general application to calculate the liquidus temperatures of other alloys. Potentially, a similar approach could be used to develop an algorithm for the calculation of the solidus temperature of other light alloys.

4. Conclusion

In this paper, a new method of equivalency has been developed that is able to predict the liquidus temperatures of multicomponent aluminum and magnesium alloys based on known aluminum and magnesium binary phase diagrams. The new method of equivalency expresses the amounts of major and minor alloying elements in the aluminum/magnesium melts through an “equivalent” amount of a reference element. Statistical analysis of the results obtained for a wide range of alloy chemical compositions shows a very good correlation between the calculated and experimentally determined data. The newly developed method can be applied to calculate other characteristic solidification temperatures of nonferrous and ferrous multicomponent alloys.

Acknowledgment

This work is financially supported by the Ministry of Science and Technical Development, Serbia, Projects ON: 172005 and TR: 35023.

References

- [1] G. Drossel, “Der einfluss von schmelzebehandlungen auf die dichteit von gusskoerpon aus Al-Si Gusslegierungen,” *Giessereitechnik*, vol. 27, pp. 7–12, 1981.
- [2] R. Vijayaraghavan, N. Pelle, J. Boileau, J. Zindel, R. Beals, and F. Bradley, “A micro model for aluminium-silicon alloys,” *Scripta Materialia*, vol. 35, pp. 861–867, 1996.

- [3] E. Schürmann, M. Djurdjevic, and L. Nedeljkovic, "Calculation of liquidus temperature of low and high alloyed iron base melts from their chemical composition by means of the equivalence factors," *Steel Research*, vol. 68, no. 3, pp. 101–106, 1997.
- [4] ASM Handbook, *Alloy Phase Diagrams*, vol. 3, ASM International, Metals Park, Ohio, USA, 1992.
- [5] J. Barthel, E. Buhrig, K. Hein, and L. Kucl, *Kristallisation aus der Schmelze*, VEB Deutscher Verlag für Grundstoffindustrie, Leipzig, Germany, 1983.
- [6] V. S. Zolotarevsky and N. I. Belov, *Casting Aluminum Alloys*, Elsevier, Amsterdam, The Netherlands, 2007.
- [7] A. R. E. Singer and S. A. Cottrell, "Properties of aluminum-silicon alloys at temperatures in the region of the solidus," *Journal of the Institute of Metals*, vol. 73, pp. 33–73, 1947.
- [8] O. Berthon, G. Petot-Ervas, C. Petot, and P. Desre, "Thermodynamics of Al-Si Alloys containing from 2 to 35 at.%Si," *Comptes Rendus de l'Académie des Sciences*, vol. 268, pp. C1939–C1942, 1969.
- [9] L. Backerud, G. Chai, and J. Tamminen, *Solidification Characteristics of Aluminum Alloys*, vol. 2, AFS Skanaluminium, Schaumburg, Ill, USA, 1990.
- [10] J. L. Murray, "The Al-Mg (Aluminum-Magnesium) system," *Bulletin of Alloy Phase Diagrams*, vol. 3, no. 1, pp. 60–74, 1982.
- [11] A. A. Nayeb-Hashemi and J. B. Clark, *Phase Diagrams of Binary Magnesium Alloys*, ASM International, Metals Park, Ohio, USA, 1998.
- [12] <http://www.magmasoft.de/de/>.
- [13] <http://www.thermocalc.com/>.
- [14] W. Cao, S. L. Chen, F. Zhang et al., "PANDAT software with pan engine, pan optimizer and pan precipitation for multi-component phase diagram calculation and materials property simulation," *Calphad*, vol. 33, no. 2, pp. 328–342, 2009.
- [15] <http://www.factsage.com/>.
- [16] <http://www.esi-group.com/products/casting/procast>.
- [17] <http://www.calphad.org/>.
- [18] <http://www.rwp-simtec.de/index.php?id=12>.
- [19] S.-C. Jeng and S.-W. Chen, "Determination of the solidification characteristics of the A356.2 aluminum alloy," *Materials Science Forum*, vol. 217–222, no. 1, pp. 283–288, 1996.
- [20] K. Kobayashi, P. H. Shingu, and R. Ozaki, "Shift of aluminium liquidus in Al-Si system due to the sodium addition," *Scripta Metallurgica*, vol. 10, no. 6, pp. 525–527, 1976.
- [21] B. P. Winter, T. R. Ostram, T. A. Sleder, P. K. Trojan, and R. D. Pehlke, "Mould dilation and volumetric shrinkage of aluminum alloys in green and dry sand molds," *AFS Transactions*, vol. 87, p. 259, 1993.
- [22] A. Kearney, "Thermatest thermal analysis system for quality control of molten aluminum," in *Proceedings of the Conference on Thermal Analysis of Molten Aluminum*, p. 169, Rosemont, Ill, USA, 1984.
- [23] J. Carbonier and C. Rechiney, "Foundry monitoring of aluminum alloys using thermal analysis," in *Proceedings of the Conference on Thermal Analysis of Molten Aluminum*, p. 121, Rosemont, Ill, USA, 1984.
- [24] J. Morice, "History of thermal analysis and its application to aluminum alloy castings," in *Proceedings of the Conference on Thermal Analysis of Molten Aluminum*, p. 37, Rosemont, Ill, USA, 1984.
- [25] M. B. Djurdjevic, S. Manasijevic, Z. Odanovic, and R. Radisa, "Influence of different contents of Si and Cu on the solidification pathways of cast hypoeutectic Al-(5–9)Si-(1–4)Cu (wt.%) alloys," *International Journal of Materials Research*, no. 9, pp. 865–873, 2013.
- [26] S. M. Liang, R. S. Chen, J. J. Blandin, M. Sueryand, and E. H. Han, "Thermal analysis and solidification pathways of Mg-Al-Ca system alloys," *Materials Science and Engineering A*, vol. 480, pp. 365–372, 2008.
- [27] M. Ohno, D. Mirkovic, and R. Schmid-Fetzer, "Liquidus and solidus temperatures of Mg-rich Mg-Al-Mn-Zn alloys," *Acta Materialia*, vol. 54, no. 15, pp. 3883–3891, 2006.
- [28] H. E. Friedrich and B. L. Mardike, *Magnesium Technology*, Springer, Heidelberg, Germany, 2006.
- [29] W. Kasprzak, J. H. Sokolowski, M. Sahoo, and L. A. Dobrzański, "Thermal and structural characteristics of the AM50 magnesium alloy," *Journal of Achievements in Materials and Manufacturing Engineering*, vol. 28, no. 2, pp. 131–138, 2008.
- [30] M. B. Djurdjevic, W. T. Kierkus, G. E. Byczynski, and J. H. Sokolowski, "Calculation of liquidus temperature for the Aluminum 3XX series of alloys," *AFS Transactions*, vol. 47, pp. 143–147, 1998.

Research Article

Effect of Mandrel on Cross-Section Quality in Numerical Control Bending Process of Stainless Steel 2169 Small Diameter Tube

Jun Fang,^{1,2} Shiqiang Lu,² Kelu Wang,² Jianmei Xu,² Xiaomei Xu,² and Zhengjun Yao¹

¹ Institute of Materials Science and Technology, Nanjing University of Aeronautics and Astronautics, Nanjing 210016, China

² School of Materials Science and Engineering, Nanchang Hangkong University, Nanchang 330063, China

Correspondence should be addressed to Shiqiang Lu; niatusq@126.com

Received 15 May 2013; Accepted 5 September 2013

Academic Editor: Augusto Deus

Copyright © 2013 Jun Fang et al. This is an open access article distributed under the Creative Commons Attribution License, which permits unrestricted use, distribution, and reproduction in any medium, provided the original work is properly cited.

The tube numerical control (NC) bending process is a much complex physical process with multifactors coupling interactive effects. The mandrel is the key to improve forming quality and to enhance forming limit. In this study, based on the platform of ABAQUS/Explicit, a 3D elastic-plastic finite element model of NC bending process of 2169 (0Cr21Ni6Mn9N) stainless steel tube was established, key technological problems were solved, and its reliability was validated. Then, simulation and analysis of the processes were carried out, and the influence laws of mandrel types and mandrel parameters on cross-section quality were obtained. The results show that the wall thinning or cross section deformation is serious at the middle part and small in the vicinity of the bending plane or initial bending plane; the wall thinning degree increases or the cross section deformation degree decreases with the increase of mandrel diameter or mandrel extension length; the effect of bulb mandrel on the cross section quality is more significant than that of cylinder mandrel. And the reasonable mandrel types and mandrel parameters are chosen for the 2169 high-pressure hydraulic tube with small diameter. The results may lead to better understanding of mandrel role in the improvement of forming quality and forming limit in the NC bending process.

1. Introduction

Tube bending parts have many desirable features, such as reducing the weight, strengthening the structure, and absorbing the impact energy and shock. As a result, they have been attracting more and more applications in aviation, aerospace, automobile, and ship [1]. The rapid development has posed an urgent requirement for the exploitation of advanced plastic-forming technology to bend high-quality tube parts. Among the various bending processes, the NC bending process, based on a rotary draw bending method, has become one of the advanced technologies satisfying the above requirements, due to its many unique advantages, such as high efficiency, economy, process stability, and easier to enable digital precision forming process and mass production [2].

However, in the NC bending process of stainless steel 2169 tube with small diameter, the tube is subjected to tension stress on extrados, compression stress on intrados, and compression stress in the radial direction, respectively,

so that there is thinning or even cracking on extrados and thickening or even wrinkling on intrados. Meanwhile, the centripetal resultant forces make the tube cross section to be distorted. Cracking and wrinkling can be avoided, but the wall thinning and the cross section deformation are inevitable. Thus, both the cracking and wrinkling should be avoided firstly; then, the wall thinning and the cross section deformation should be controlled to some acceptable extent in the NC bending process.

In order to reduce the wrinkling risk and cross section deformation degree, it is considered to fill the tube with fine sand, fluid, or rosin-cerate [3]. But it is known that filling the mediums such as sands or fluid may decrease the forming precision in production process and add pretreatment and posttreatment processes such as sealing, removing sealing, and cleaning, thus, increasing forming cost and environmental pollution, and so on, which seems difficult to satisfy the requirements of advanced NC bending process. While the mandrel can conquer the above problems due to its advantages of design ability, much flexibility, and relatively

little cost. The mandrel plays an important role in improving both the forming quality and forming limit. So the research on the effect of mandrel on cross section quality is of great significance in the tube NC bending process.

Many scholars have carried out the researches on the wall thickness change and cross section deformation of tubes during bending process using theoretical analysis, experimental research, and the finite element method (FEM) simulation. By using plastic-deformation theory, Tang [4] derived the formulas for wall thickness change and cross section deformation. Strano [5] presented the expression for the maximal cross section deformation degree based on the experimental data of steel tube bending. Veerappan and Shanmugam [6] gave a mathematical relationship among the pressure ratio, ovality, thinning, tube ratio, and bend ratio. Wang and Agarwal [7] predicted the cross section deformation and wall thickness change of tubes in bending process under axial force and internal pressure. Pan and Stelson [8] used energy principle to solve the cross section deformation and wall thickness change of plastic tube bending. But, using the above formulas, it is difficult to find the characteristics in wall thickness change and cross section deformation of tube NC bending process.

By FE and experimental analysis, Zhan et al. [9] studied the various in wall thickness and cross-section under various operating parameters and mandrel parameters for the NC bending of TA18 tubes and presented a method for quickly determining the range of the axial mandrel feed. Li et al. [10–14] researched the deformation behavior of wall thickness and cross-section of NC bending of stainless steel and aluminum alloy tubes under different bending conditions, including the bending for the tube with large diameter and/or small bending radius [10, 11], the push assistant loading conditions [12], the role of mandrel [13], and different clearance between tube and dies [14]. Yang et al. [15] addressed the effect of frictions on cross section quality of thin-walled tube NC bending and obtained the reasonable friction conditions in the process. Jiang et al. [16] revealed the laws of cross section deformation and wall thickness change during NC bending of TA18 tubes with different bending radii. Yang et al. [17–19] experimentally investigated the influence of process parameters and geometric parameters on forming quality of thin-walled NC bending tube. Though the above researches mainly focus on the effect of process parameters and geometric parameters on forming quality of thin-walled tube NC bending, and study on the effect of mandrel on cross section quality is still scant [9, 13, 17], they could provide a reference for relevant investigation of stainless steel 2169 small diameter tube NC bending.

Therefore, in the study, a 3D elastic-plastic FE model of the NC bending process is established using the dynamic explicit FE code ABAQUS/Explicit (ABAQUS, 2011); then, the effect of mandrel on cross section quality of the tube NC bending has been studied. The achievements of this study are useful to select reasonable mandrel types and parameters in the process, and the method of numerical simulation can be used to study the influences of other parameters on the forming quality and forming limit of tube NC bending process.

2. Forming Principle of Tube NC Bending and Its Cross Section Quality

Figure 1 shows the sketch of the NC bending process and stress strain state. As shown in Figure 1(a), bending die is fixed on the major axes of machine tool and revolves together with the major axes. The pressure die is set on outer part, the wiper dies set on inner part of tube bending, and the mandrels set in the tube at the tangent point between the tube and bending die. Pulled by bending die and clamp die, the tube goes past the tangent point and rotates along the groove of bending die to desired bending angle and bending radius; then, the mandrel retracts, and the tube is unloaded.

Figure 1(b) shows the stress strain state of bent tube during NC bending process. Node A in the extrados is under tension stress in both tangent and hoop directions and compressive stress in radial direction; meanwhile, node B in the intrados is under 3D compressive stress state. This will lead to thinning or even cracking on extrados and thickening or even wrinkling on intrados. Meanwhile, both the composite force of tangent stress of outer part and that of inner part point to the center of the cross section of the tube, which causes the cross section deformation as shown in Figure 2(a).

The essential dies and the cooperation between them are needed to accomplish the tube bending process to ensure the free-wrinkling and allowed wall thinning and cross section deformation degrees. The pressure die is to apply enough pressure force and bending moment to the tube and push it against the wiper die tightly ensuring the free-wrinkling bending tube. At same time, the moving pressure die helps pushing the materials into bending regions reducing the wall thinning degree. The wiper die and mandrel are used to prevent the tube from wrinkling and over cross section deforming; especially the mandrel extension length plays an important role in that. The mandrel extension length e refers to the mandrel body extension length exceeding the bending tangent point (the point where the tube will begin to bend) as shown in Figure 1(a). The wiper die neck in the bending die grooves with its very thin tip extending to the bending tangent point. In doing so, it fills up the gap normally left by the bending die. Thus, the tube is completely confined and does not have space to wrinkle.

A few indices are used to measure the wall thinning degree and cross section deformation degree of NC bending of 2169 stainless steel tubes; the ratio of wall thinning (Δt) is expressed as

$$\Delta t = \frac{t - t'}{t} \times 100\%, \quad (1)$$

where t is the initial wall thickness of the tube; t' is the wall thickness at the thinnest point along the tube extrados after bending deformation as shown in Figure 2(b).

Due to the boundary constraints shown in Figure 2(b), the tube is constrained in transverse direction by bending die groove and under free deformation conditions in vertical direction. Thus, in NC bending process, the cross section

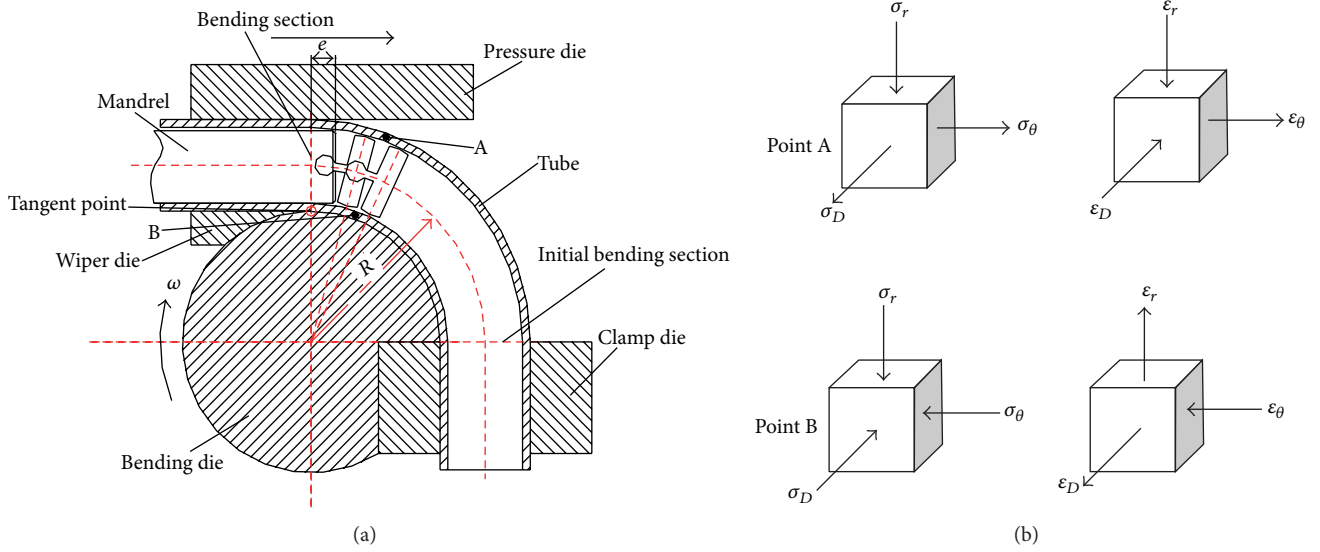


FIGURE 1: Sketch of the NC bending process (a) and stress strain state (b).

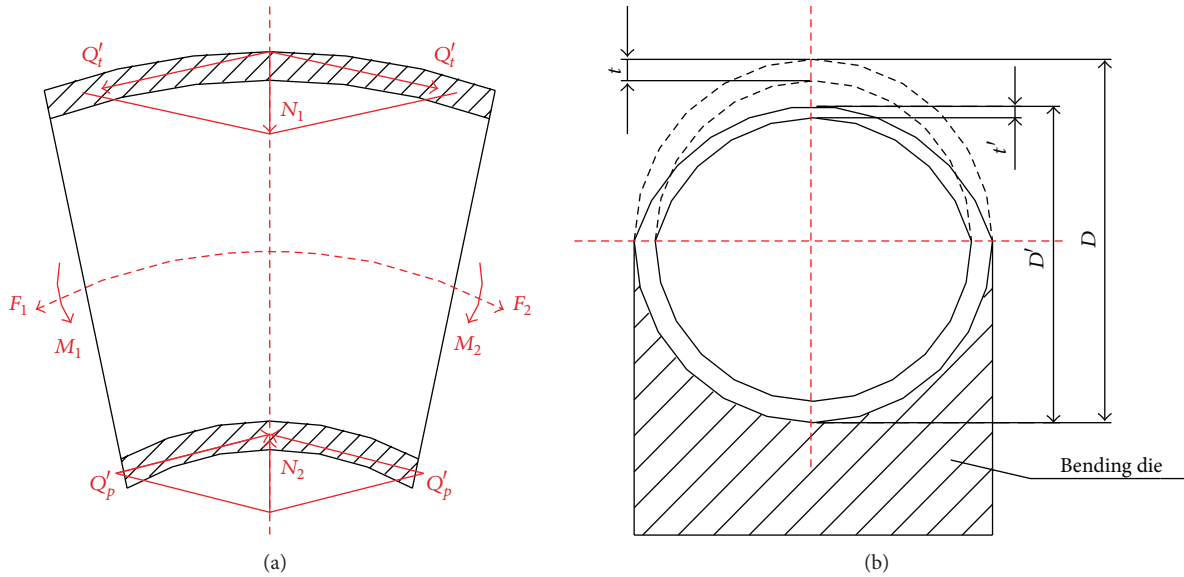


FIGURE 2: Cross section deformation and wall thinning of tube NC bending.

deformation (ΔD) can be determined by the changing ratio of the vertical magnitude of the cross section as

$$\Delta D = \frac{D - D'}{D} \times 100\%, \quad (2)$$

where D is tube initial outer diameter; D' is the cross section length in the vertical direction after bending as shown in Figure 2(b).

3. FEM Modeling and Key Technologies Resolved

Compared with the static implicit algorithm, the dynamic explicit finite element algorithm is the main method for simulating the 3D metal plastic forming process because of the unique advantages such as lower solution cost, few difficulties in simulating the complex contact and large deformation in metal forming process, and also ability of predicting wall thinning and cross section deformation phenomena directly, without iteration and convergence tolerance. So,

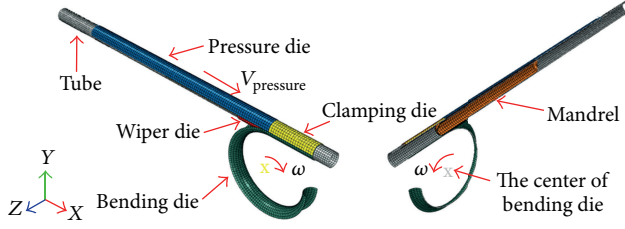


FIGURE 3: Finite element model for NC bending process of 2169 small diameter tube.

the elastic-plastic dynamic explicit finite element algorithm is chosen for simulating the NC tube bending.

Based on the above analysis and the platform of ABAQUS/Explicit (ABAQUS, 2011), a 3D elastic-plastic finite element model of the NC tube bending process is established (shown in Figure 3). To simulate the quasi-static metal forming process using the explicit algorithm exactly, the key technologies such as element type, friction condition, materials properties, and contact condition are resolved reasonably.

3.1. Geometry Modeling and Element Type Selection. Figure 3 shows a representative finite element model for NC bending of small diameter tube. In this model, tube is a deformable body. Forming dies, including bending die, clamp die, wiper die, pressure die, and mandrel, are simplified as rigid bodies for improving computational precision and efficiency.

The four-node doubly curved thin shell S4R is adapted to describe the tube with the following features: reduced integration and hourglass control. Five integration points are selected across the thickness to describe the tube bending deformation better. The rigid body surfaces of dies are described by four-node 3D bilinear quadrilateral rigid element R3D4 to simulate smooth contact geometry curved face. The mesh size of tube is 0.8×0.8 mm and that of rigid body surfaces is 1×1 mm.

3.2. Material Model. Correct material model determines the credibility of the finite element simulation. The material used in the simulations is an isotropic, homogeneous, elastic-plastic material following the von Mises yield criterion, with isotropic work hardening. The uniaxial tension test is used to obtain the mechanical properties of 2169 stainless steel tube (shown in Table 1) according to the GB/T228-2002 [20] using a WDW-100 electronic universal testing machine. And the Ludwigs model is used to describe the strain-hardening of austenitic stainless steel tube material as follows:

$$\bar{\sigma} = K\bar{\epsilon}^n + e^{(a-b\bar{\epsilon})}, \quad (3)$$

where a, b are constants.

3.3. Friction Model. In the tube NC bending process, the friction has an important influence on the deformation, so it is necessary to select a proper friction model into the finite element simulation. As there is a relative sliding phenomenon

TABLE 1: Material properties of 2169 stainless steel tube.

Material parameters	Value
Young's modulus E (GPa)	197
Poisson's ratio ν	0.29
Initial yield stress $\sigma_{0.2}$ (MPa)	987
Hardening exponent n	0.177
Strength coefficient K (MPa)	1796.5
Ultimate tension strength σ_b (MPa)	1112
Extensibility δ (%)	22
Density ρ (kg/m ³)	7830
Constant a	5.7
Constant b	27.4

TABLE 2: Friction coefficients in various contact interfaces.

	Contact interface	Friction coefficients
1	Tube-bending die	0.1
2	Tube-pressure die	0.25
3	Tube-clamp die	Rough
4	Tube-wiper die	0.1
5	Tube-mandrel	0.05

between the different contact interfaces, including tube-bending die, tube-clamp die, tube-wiper die, tube-pressure die, and tube-mandrel. So the Coulomb friction model is chosen to represent the friction behaviors between tube and dies. And the different friction coefficients have been assigned to the different contact interfaces as shown in Table 2. The friction coefficient between tube and clamp die is assigned a large value to satisfy the no slipping in the clamp interface. In ABAQUS, so-called "rough" friction with coefficient ∞ is available, where it is assumed that there is no bound on the shear stress, and thus, no relative motion can occur as long as the surfaces are in contact.

3.4. Dynamic Boundary Constraints and Loadings. For contact pairs, the "surface-to-surface contact" method is used to define the contact between tube and dies. "Kinematic constraints" method is used to describe mechanical constraints for contact pairs except for the tube-mandrel interface which is simulated with "penalty method." Moreover, according to the real conditions, the sliding formulation for every contact interfaces is the "Finite sliding" except the one for tube-clamp die contact pair with the "Small sliding," namely, not being allowed for sliding between the tube and the clamp die.

The boundary constraints and loadings are applied by two approaches: "Displacement/rotation" and "Velocity/angular velocity." For the NC bending process with the bending radius 19.05 mm and the bending angle 180 degree, the bending time needed is 7.85 s at the bending angular velocity of 0.4 rad/s.

Both bending die and clamp die are constrained to rotate along the global Z -axis, while the pressure die is constrained to translate only along the global X -axis with the same linear speed as the centerline bending speed of the bending die. The wiper die is constrained along all degrees of freedom. The mandrel is fixed from all degrees of freedom

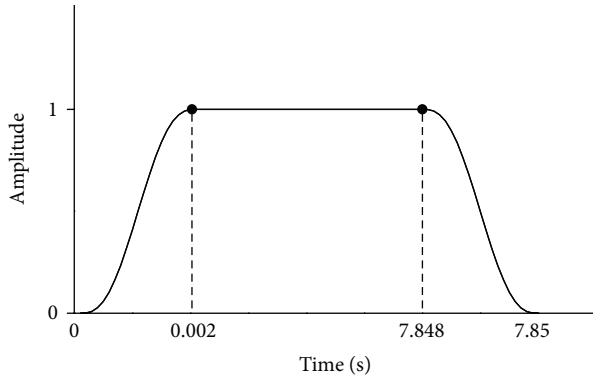


FIGURE 4: Smooth step amplitude curves.

in the tube bending process. After the bending process is finished, the mandrel will be withdrawn along the global X -axis. The smooth step amplitude curves are defined describing the change of the velocity with time as smooth as possible to ensure little inertial effects in explicit finite element simulation of quasi-static process as shown in Figure 4.

3.5. Finite Element Model Validation. In order to validate the 3D elastic-plastic finite element model of NC bending process, simulations for TA18 titanium alloy tube with the size of 14×1.35 mm (denoted $D \times t$, where D and t are the tube diameter and tube wall thickness, respectively) have been carried out based on the experimental conditions in [21]. The comparison of simulation result with the experimental result gotten in [21] is shown in Figure 5. From Figure 5, it is discovered that the result of simulation and that of experimental agree with each other. The maximum relative error of wall thinning degree between the simulation and the experimental result is less than 2% as shown in Figure 5(a), and the maximum relative error of cross section deformation degree between the simulation and the experimental result is less than 8% as shown in Figure 5(b). So it indicates that the 3D elastic-plastic finite element model built above is credible.

4. Results and Discussion

Using the established 3D elastic-plastic finite element model, the effect of the mandrel on cross section quality has been revealed. Using the hard mandrel (cylinder mandrel and bulb mandrel are shown in Figure 6) or without mandrel during small diameter tube bending process in general. Thus, the effect of mandrel types on cross section quality is modeled, and the appropriate mandrel is chosen based on the simulation results firstly. Then, the effects of the diameter and the extension length of mandrel on cross section quality are modeled based on the appropriate mandrel. The diameters of mandrel are 5.43 mm, 5.33 mm, and 5.23 mm, respectively, the mandrel extension lengths are selected as 0 mm, 1 mm, and 2 mm, respectively, and the fillet radius of the cylinder mandrel is 0.5 mm. Other parameters are shown in Tables 1, 2, and 3. Cracking and wrinkling are not found in

the simulation, which provides the basis for the further research on the wall thinning and cross section deformation.

4.1. Effect of Mandrel Types on Cross Section Quality. The bending processes without mandrel or with cylinder mandrel and bulb mandrel have been simulated, respectively. The mandrel diameter is 5.43 mm, and the mandrel extension length is 2 mm.

Figure 7(a) shows the wall thinning degree without mandrel or with various mandrels. It can be seen that the wall thinning is serious at the middle part and small in the vicinity of the bending plane or initial bending plane. The wall thinning degree firstly increases then hardly changes and finally decreases along the bending direction from the bending plane to the initial bending plane. The maximum wall thinning degree without mandrel is 6.94%, while the maximum wall thinning degree with cylinder mandrel or bulb mandrel is 12.1%, 13.6%, respectively. It is because that mandrel-tube contact will produce friction force, which baffles the flowing of material and accordingly causes larger tangent strain and more serious tube wall thinning. The more the contact surface between mandrel and tube is, the larger friction force is. Thus, the maximum wall thinning degree with bulb mandrel is the largest.

The cross section deformation degree without mandrel or with different mandrels is shown in Figure 7(b). It is found that the cross section deformation is serious in the midst of the bending deformation area and small near the initial bending plane and bending plane. This is because sections near the bending plane are supported by mandrel and restrained by mold cavity and sections in the vicinity of the initial bending plane are restrained by mold cavity, while sections in the midst of the bending deformation zone lie in the suspended state. When the mandrel is not used, the section, located at the angle of 50° with the bending plane, distorts most seriously and its cross section deformation degree is about 10.9%, which exceeds the requirement of the aerial standard. When the cylinder mandrel or bulb mandrel is used, the section, located at the angle of 30° with the bending plane, distorts most seriously and its cross section deformation degree is about 3%, 1.8%, respectively, which satisfies the requirement of the aerial standard. From the above results, it can be found that mandrel improves the cross section deformation significantly. This is because of the support of mandrel, and the bulb mandrel can support a wider range of curved surface of the bent tube. Therefore, taking both thinning and cross section deformation into consideration, the bulb mandrel was chosen properly in this paper.

4.2. Effect of Mandrel Diameter on Cross Section Quality. The mandrel diameter is a significant dimension parameter since it greatly influences the cross section quality of the bent tube. In this paper, the finite element simulation of the bending processes with the mandrel diameters of different sizes 5.23 mm, 5.33 mm, and 5.43 mm have been carried out, respectively. The bulb mandrel is used, and the mandrel extension length is 2 mm.

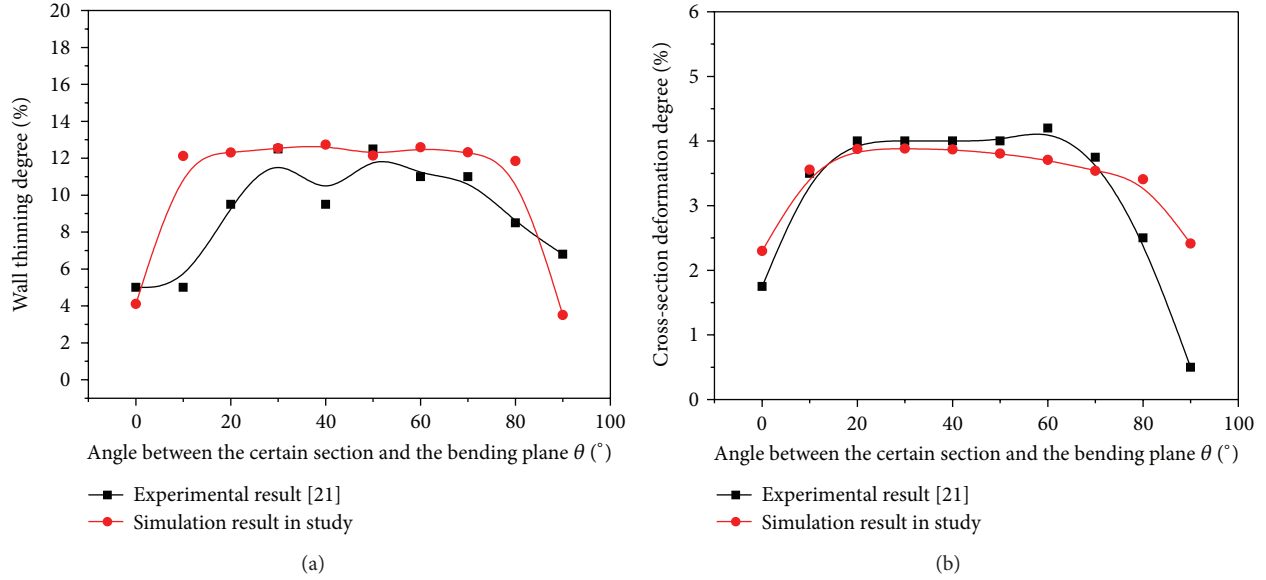


FIGURE 5: Comparison of simulation result with experimental result [21]: (a) wall thinning; (b) cross section deformation.

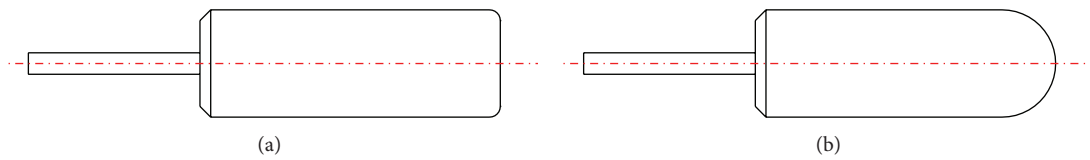


FIGURE 6: Types of the hard mandrel: (a) cylinder mandrel; (b) bulb mandrel.

TABLE 3: Simulation parameter.

Tube diameter D (mm)	Tube wall thickness t (mm)	Bending radius R (mm)	Bending angle θ (deg)	Bending angular velocity ω (rad/s)	Clearance between tube and dies ΔC (mm)
6.35	0.41	19.05	180	0.4	0.1

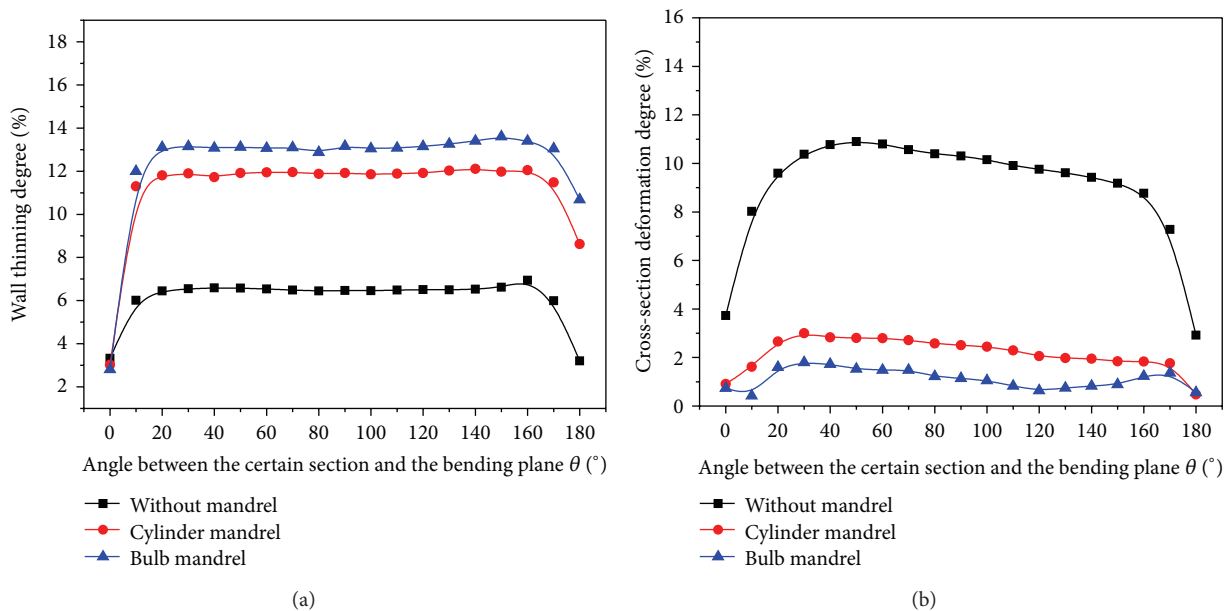


FIGURE 7: Effect of mandrel type on cross section quality: (a) wall thinning; (b) cross section deformation.

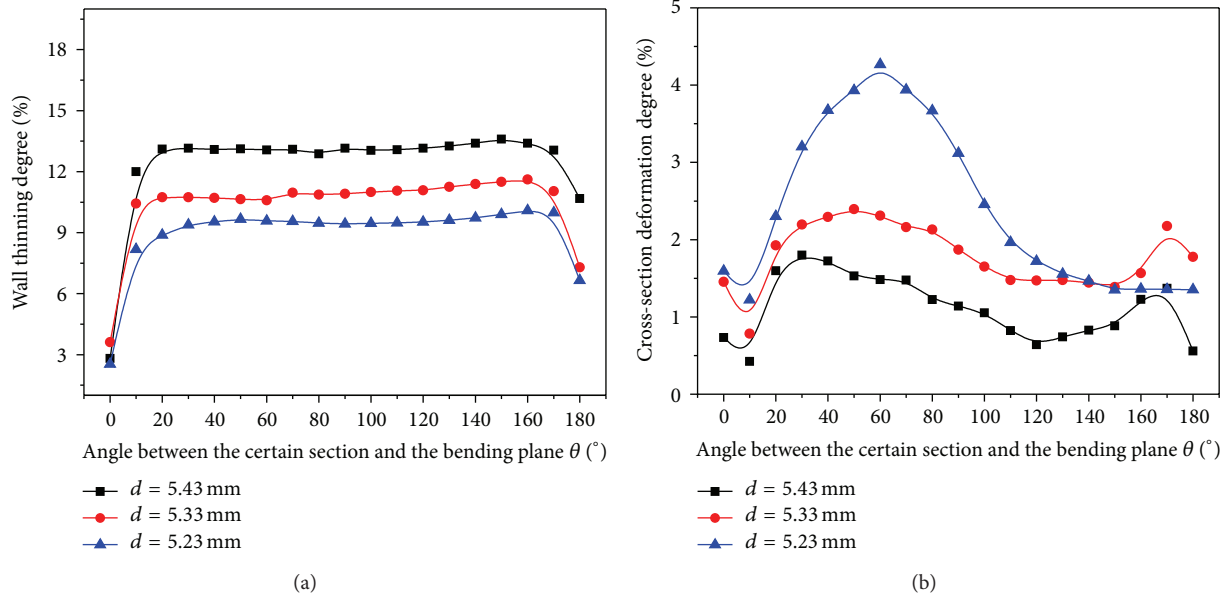


FIGURE 8: Effect of mandrel diameter on cross section quality: (a) wall thinning; (b) cross section deformation.

The wall thinning degree with different mandrel diameters is shown in Figure 8(a). It is found that the larger the mandrel diameter is, the larger the wall thinning degree of bent tube is. These results are similar to those of the NC bending for TA18 tube [9], but the effects of the mandrel diameter on wall thinning are more obvious in this work. The maximum wall thinning degree with mandrel diameter of 5.23 mm, 5.33 mm, and 5.43 mm is 10.1%, 11.6%, and 13.6%, respectively. This is because the large mandrel diameter increases the friction between the mandrel and the inside wall of tube and accordingly causes larger tangent strain and more serious wall thinning of bent tube.

Figure 8(b) shows the cross section deformation degree with various mandrel diameters. It can be seen from Figure 8(b) that the larger the mandrel diameter is, the smaller the cross section deformation degree is. These results are similar to those of the NC bending for TA18 tube [9], but the effects of the mandrel diameter on cross section deformation are more obvious in this work. And the peak of 2169 tube deflects toward the bending plane as mandrel diameter increases, which is different from that of the NC bending for TA18 tube [9]. The maximum cross section deformation degree with mandrel diameter of 5.23 mm is more than 4.2%, while the maximum cross section deformation degree with mandrel diameter of 5.43 mm is less than 1.8%. Although the difference between the two diameters is only 0.2 mm, the difference of the cross section deformation degree is 2.4%. So, it can be concluded that the large mandrel diameter can support the inside wall of tube more effectively to improve cross section deformation.

4.3. Effect of Mandrel Extension Length on Cross Section Quality. The mandrel extension length is an important parameter in the tube bending processes. Wrinkling may occur when

the mandrel extension length is too small, while the outside of the tube may crack with overlarge mandrel extension length. In this paper, the bending processes with the mandrel extension lengths of 0 mm, 1 mm, and 2 mm have been simulated, respectively. The bulb mandrel is used, and the diameter is 5.43 mm. In the simulation, it is found that the wrinkling or cracking does not occur in all cases.

Figure 9(a) shows the tube wall thinning degree with various mandrel extension lengths. It is found that the larger the mandrel extension length, the more serious the wall thinning degree. These results are similar to those of the NC bending for TA18 and 5052O tubes [9, 17], but when the bending angle reaches the critical value, the wall thinning is of a platform deforming characteristic with little change, which differ from those of the NC bending for 5052O alloy thin-walled tube [17]. When the length is 0 mm, the maximum wall thinning degree is 9.5%; when the length is 1 mm, the maximum wall thinning degree is 10.7%; and when the length is 2 mm, the maximum wall thinning degree is 13.6%. It is because that larger mandrel extension length increases the friction between the mandrel front-end and inside wall of tube to prevent the material from flowing, which leads to tangent strain and wall thinning degree increasing. Overlarge length may cause hump, overthinning, or even cracking.

In order to avoid over-thinning, appropriate mandrel extension length should be chosen in the bending processes. A formula to calculate the maximum mandrel extension length is put forward in [3]:

$$e_{\max} = \sqrt{2 \left(R + \frac{D_1}{2} \right) z - z^2}, \quad (4)$$

$$z = D_1 - d,$$

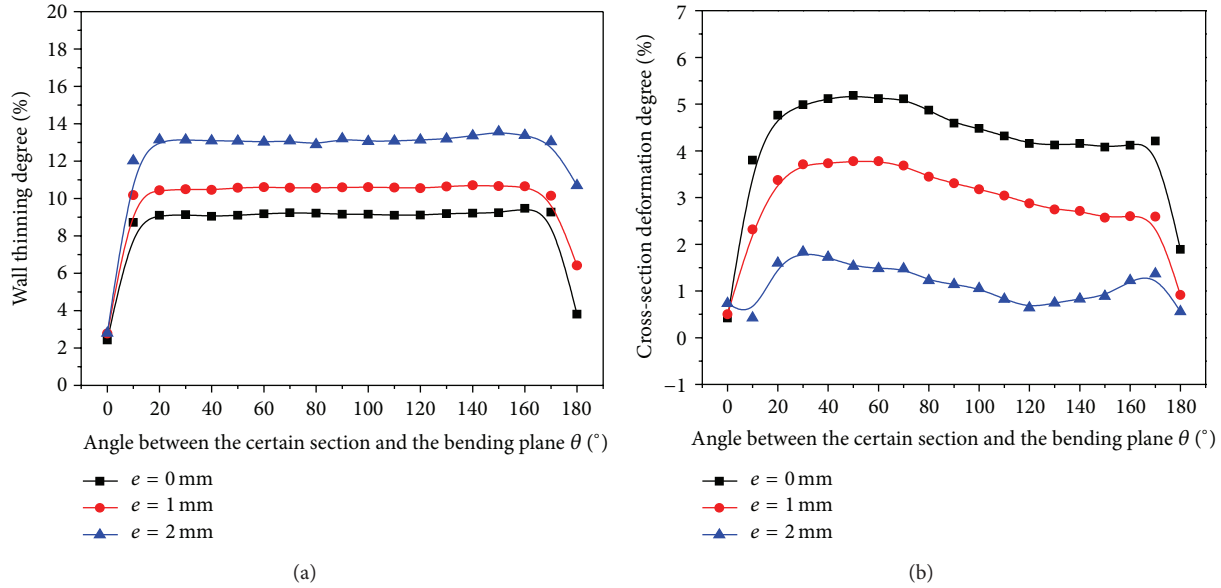


FIGURE 9: Effect of mandrel extension length on cross section quality: (a) wall thinning; (b) cross section deformation.

where D_1 is the inner diameter of the tube; R is the centerline bending radius; d is the mandrel diameter; and z is the clearance between inside wall of tube and mandrel.

In practical production, because of the tubes with relatively low elongation percentage, testing bending after calculating mandrel extension length by the equation is needed. Otherwise, hump or cracking may easily occur. In this paper, the calculated value of the maximum mandrel extension length is 2.1 mm, which is in agreement with the simulation conditions.

Figure 9(b) shows the cross section deformation degree with different mandrel extension lengths. It can be seen from Figure 9(b) that the cross section deformation of bending tube decreases with the increase of the mandrel extension length, which is similar to that of the NC bending for TA18 tube [9]. When the length is 0 mm, the maximum cross section deformation degree is 5.2%; when the length is 1 mm, the maximum cross section deformation degree is 3.8%; and when the length is 2 mm, the maximum cross section deformation degree is 1.8%. It is because that the sections are supported more effectively, which causes the inside wall of tube to undergo larger pressure stress from mandrel.

4.4. Selection of Reasonable Mandrel Parameters. According to the different usage of the bent tube, the requirements on the section quality are different. In practical production, except that the wall thinning and the cross section deformation must satisfy the requirements, the cost of production should be minimized. In the aviation technical standards, the requirements on section quality is that wall thinning degree does not exceed 25% and cross section deformation degree does not exceed 5% for high-pressure hydraulic tube. In order to gain qualified high-pressure 2169 stainless steel bent tube with diameter of 6.35 mm, wall thickness of 0.41 mm, and bending radius of 19.05 mm, the bulb mandrel and the diameter of

5.43 mm should be selected and the mandrel extension length should be set as 2 mm according to the above research results.

5. Conclusions

- (1) The 3D elastic-plastic finite element model of NC bending process of 2169 stainless steel tube with small diameter is established based on the platform of ABAQUS/Explicit, the key technological problems are solved, and its reliability is validated.
- (2) The mandrel type has a significant effect on cross section quality during tube NC bending. The wall thinning or cross section deformation is serious at the middle part and small in the vicinity of the bending plane or initial bending plane. The maximum wall thinning without mandrel is 6.94%, while the maximum wall thinning with cylinder mandrel or bulb mandrel is 12.1%, 13.6%, respectively. When the mandrel is not used, the section, located at the angle of 50° with the bending plane, distorts most seriously and its cross section deformation degree is about 10.9%, which exceeds the requirement of the aerial standard. When the cylinder mandrel or bulb mandrel is used, the section, located at the angle of 30° with the bending plane, distorts most seriously and its cross section deformation degree is about 3%, 1.8%, respectively, which satisfies the requirement of the aerial standard. Therefore, taking both thinning and cross section deformation into consideration, the bulb mandrel was chosen properly in this paper.
- (3) The mandrel parameters have a great influence on the cross section quality of the bent tube. The larger the mandrel diameter or the mandrel extension length is, the larger the wall thinning degree of bent tube is. The larger mandrel diameter or the mandrel extension

length is, the smaller the cross section deformation is. Overlarge mandrel extension length may cause hump, overthinning, or even cracking.

- (4) In order to gain qualified high-pressure 2169 stainless steel bent tube with diameter of 6.35 mm, wall thickness of 0.41 mm, and bending radius of 19.05 mm, the bulb mandrel and the diameter of 5.43 mm should be selected and the mandrel extension length should be set as 2 mm.

Acknowledgment

The authors would like to thank the National Natural Science Foundation of China (Grant no. 51164030) for the support given to this research.

References

- [1] H. Yang, Z. Sun, Y. Lin, and M. Li, "Advanced plastic processing technology and research progress on tube forming," *Journal of Plasticity Engineering*, vol. 8, no. 2, pp. 83–85, 2001 (Chinese).
- [2] J. Yan, H. Yang, M. Zhan, and H. Li, "Forming limits under multi-index constraints in NC bending of aluminum alloy thin-walled tubes with large diameters," *Science China Technological Sciences*, vol. 53, no. 2, pp. 326–342, 2010.
- [3] T. H. Wang, *Tube Plastic Processing Technology*, China Machine Press, Beijing, China, 1998, (Chinese).
- [4] N. C. Tang, "Plastic-deformation analysis in tube bending," *International Journal of Pressure Vessels and Piping*, vol. 77, no. 12, pp. 751–759, 2000.
- [5] M. Strano, "Automatic tooling design for rotary draw bending of tubes," *International Journal of Advanced Manufacturing Technology*, vol. 26, no. 7-8, pp. 733–740, 2005.
- [6] A. R. Veerappan and S. Shanmugam, "Analysis for flexibility in the ovality and thinning limits of pipe bends," *Journal of Engineering and Applied Sciences*, vol. 3, no. 1, pp. 31–41, 2008.
- [7] J. Wang and R. Agarwal, "Tube bending under axial force and internal pressure," *Journal of Manufacturing Science and Engineering*, vol. 128, no. 2, pp. 598–605, 2006.
- [8] K. Pan and K. A. Stelson, "On the plastic deformation of a tube during bending," *Journal of Engineering for Industry*, vol. 117, no. 4, pp. 494–500, 1995.
- [9] M. Zhan, T. Huang, Z. Q. Jiang, P. P. Zhang, and H. Yang, "Determination of process parameters for the NC bending of a TA18 tube," *The International Journal of Advanced Manufacturing Technology*, vol. 68, no. 1–4, pp. 663–672, 2013.
- [10] H. Li, H. Yang, J. Yan, and M. Zhan, "Numerical study on deformation behaviors of thin-walled tube NC bending with large diameter and small bending radius," *Computational Materials Science*, vol. 45, no. 4, pp. 921–934, 2009.
- [11] H. Li, H. Yang, M. Zhan, and R.-J. Gu, "Forming characteristics of thin-walled tube bending process with small bending radius," *Transactions of Nonferrous Metals Society of China*, vol. 16, supplement 2, pp. s613–s623, 2006.
- [12] H. Li, H. Yang, M. Zhan, and Y. L. Kou, "Deformation behaviors of thin-walled tube in rotary draw bending under push assistant loading conditions," *Journal of Materials Processing Technology*, vol. 210, no. 1, pp. 143–158, 2010.
- [13] L. Heng, Y. He, Z. Mei, S. Zhichao, and G. Ruijie, "Role of mandrel in NC precision bending process of thin-walled tube," *International Journal of Machine Tools and Manufacture*, vol. 47, no. 7-8, pp. 1164–1175, 2007.
- [14] H. Li and H. Yang, "A Study on multi-defect constrained bendability of thin-walled tube NC bending under different clearance," *Chinese Journal of Aeronautics*, vol. 24, no. 1, pp. 102–112, 2011.
- [15] H. Yang, R.-J. Gu, M. Zhan, and H. Li, "Effect of frictions on cross section quality of thin-walled tube NC bending," *Transactions of Nonferrous Metals Society of China*, vol. 16, no. 4, pp. 878–886, 2006.
- [16] Z. Jiang, M. Zhan, H. Yang, X. Xu, and G. Li, "Deformation behavior of medium-strength TA18 high-pressure tubes during NC bending with different bending radii," *Chinese Journal of Aeronautics*, vol. 24, no. 5, pp. 657–664, 2011.
- [17] C. Li, H. Yang, M. Zhan, X.-D. Xu, and G.-J. Li, "Effects of process parameters on numerical control bending process for large diameter thin-walled aluminum alloy tubes," *Transactions of Nonferrous Metals Society of China*, vol. 19, no. 3, pp. 668–673, 2009.
- [18] G. X. Wang, H. Yang, H. Li, M. Zhan, and R. J. Gu, "Experimental study of the influence of process parameters on forming quality of thin-walled NC bending tube," *Mechanical Science and Technology*, vol. 24, no. 8, pp. 995–998, 2005 (Chinese).
- [19] Y.-L. Kou, H. Yang, M. Zhan, Y.-B. Yue, and H. Li, "Experimental study on cross-section ovalization of thin-walled tube in NC bending process," *Journal of Plasticity Engineering*, vol. 14, no. 5, pp. 26–31, 2007 (Chinese).
- [20] GB/T228-2002, "Metallic materials-tensile testing at ambient temperature [S]".
- [21] Y. B. Yue, *Numerical simulation and experiment study on Ti-Alloy tube NC bending process [M.S. thesis]*, Northwestern Polytechnical University, 2009, (Chinese).

Research Article

Neuro-Fuzzy Model for the Prediction and Classification of the Fused Zone Levels of Imperfections in Ti6Al4V Alloy Butt Weld

Giuseppe Casalino,¹ Sabina Luisa Campanelli,¹ and Fabrizio Memola Capece Minutolo²

¹ Department of Mechanics, Mathematics and Management, Politecnico di Bari, Viale Japigia 182, 70126 Bari, Italy

² Department of Materials and Production Engineering, University of Naples Federico II, Piazzale Tecchio 80, 80125 Naples, Italy

Correspondence should be addressed to Sabina Luisa Campanelli; campanel@poliba.it

Received 10 May 2013; Accepted 3 September 2013

Academic Editor: Martha Guerrero

Copyright © 2013 Giuseppe Casalino et al. This is an open access article distributed under the Creative Commons Attribution License, which permits unrestricted use, distribution, and reproduction in any medium, provided the original work is properly cited.

Weld imperfections are tolerable defects as stated from the international standard. Nevertheless they can produce a set of drawbacks like difficulty to assembly, reworking, limited fatigue life, and surface imperfections. In this paper Ti6Al4V titanium butt welds were produced by CO₂ laser welding. The following tolerable defects were analysed: weld undercut, excess weld metal, excessive penetration, incomplete filled groove, root concavity, and lack of penetration. A neuro-fuzzy model for the prediction and classification of the defects in the fused zone was built up using the experimental data. Weld imperfections were connected to the welding parameters by feed forward neural networks. Then the imperfections were clustered using the C-means fuzzy clustering algorithm. The clusters were named after the ISO standard classification of the levels of imperfection for electron and laser beam welding of aluminium alloys and steels. Finally, a single-value metric was proposed for the assessment of the overall bead geometry quality. It combined an index for each defect and functioned according to the criterion “the-smallest-the-best.”

1. Introduction

Titanium and its alloys are considered as one of the best engineering metals because of the combination of properties such as elevated strength-to-weight ratio, high fatigue life, toughness, excellent resistance to corrosion, and good fatigue properties. High-strength-to-weight ratio and superior corrosion resistance make titanium attractive for many chemical, marine, and military applications. The compatibility with carbon fibre composite makes titanium alloys also suitable for aeronautical applications. Ti6Al4V is presently one of the most widely used titanium alloy, accounting for more than 50% of all titanium tonnage in the world, and to date no other titanium alloy has been a threat to its dominant position.

Titanium alloys may be joined by a wide variety of conventional and solid-state processes although their chemical reactivity requires special precautions to avoid contamination of the fusion and heat-affected zones both on the face and root sides. The fusion welding of titanium is performed

principally in inert gas-shielded arc and high-energy beam welding processes.

Gas-shielded laser welds are produced with very interesting results concerning both the weld bead morphology and the mechanic properties. Both Helium and Argon shielding gases are commonly used, and Helium proved to be more performing with respect to Argon [1].

Unfortunately, welds are not perfect and defect-free. Weld undercut, excess weld metal, excessive penetration, incomplete filled groove, root concavity, and lack of penetration can alter the form of the bead. These kinds of defect can cause a set of drawbacks that require reworking and also limited fatigue life, difficulty to assembly, and consequences of failure.

In the last two decades laser welding has received increasing confidence from worldwide manufacturers. Deep penetration, flexibility, precision, narrow heat affected zones are among its most effective features. Laser beam welding can produce high quality titanium weld by controlling the welding parameters [2].

Statistical or evidence-based artificial intelligence (AI) use optimization techniques to obtain high software performance that are based on evidence present in experimental data. Over the years, these techniques have given various solutions to modelling and optimization problems [3–5]. Among the available applications it is worth to highlight some works in the field of titanium laser manufacturing such as a model for the evaluation of laser welding efficiency and quality [6] and the capability of confirming the statistical significance of some welding parameters and their interactions using both the ANOVA and Taguchi approaches [7]. In this way, artificial neural networks have well established themselves as an optimisation technique in laser welding investigations [8].

In the case of titanium alloys the neural networks have been used for modelling the correlations in the properties [9] and to link the welding parameters to the metallurgical, the mechanical, and the weld geometry [10, 11].

Fuzzy logic has been widely utilised in the classification of the weld defects using the nondestructive method. By this method, the defects were classified to the right quality level. Compared with the ordinary ones, this method has higher accuracy and better robustness [12].

In this paper a large number of welds of the Ti6Al4V titanium alloy were produced by CO₂ laser and then cut, etched and observed using an optical microscope. Six imperfections of the fused zone were measured and analysed.

Artificial neural networks (ANN) were implemented to connect the weld defects to the laser parameters. A supervised back-propagation type neural network was used and applied to the experimental data. The optimal network topology was obtained by an iterative algorithm which allows to test a large number of networks with varying quantities of neurons in each layer and varying numbers of epochs before choosing the network with the minimum error rate. The prerequisite for successfully testing such a large number of networks lay in using the Levenberg-Marquardt algorithm. In a direct approach the weld imperfections were calculated for the process parameters, and in a reverse one the latter were calculated for the former.

Then the Bezdek fuzzy logic [13] was used to calculate the upper limits of three clusters each significant imperfection. The clusters were named stringent, intermediate, and moderate and included smallest, average, and largest defects, respectively. The nomenclature used is compliant with the ISO standard for steel and aluminium welds. Therefore it was possible to assign each measure to a cluster, which determines the quality score for that tolerable defect.

Some difficulties can arise for the evaluation of the defectiveness of the bead geometry when several imperfections are considered together [14]. Therefore, a single-value metric was calculated, and following the-smallest-the-best criterion it was possible to give a single score to the weld imperfection.

Figure 1 shows the flow charts for how to use the neuro-fuzzy model. When the process parameters are known it is possible to calculate and classify the weld tolerable imperfections and then the laser welding capability (flow chart a). On the other hand when the specifications for the levels of the weld imperfections are known it is possible to

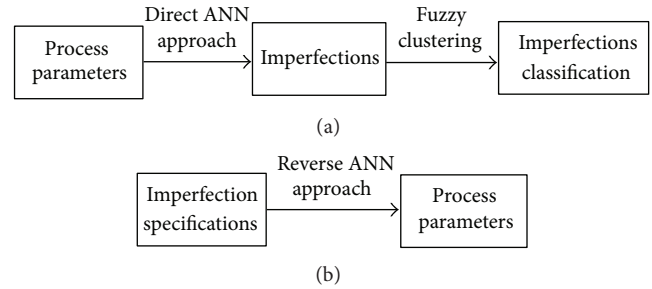


FIGURE 1: Flow charts for the application of the neuro-fuzzy model.

TABLE 1: Weld group and laser parameters.

Group no.	Thickness (mm)	Laser power (W)	Welding speed (mm/s)	Sample size
1.0	2.61–2.62	1500–2000	25–120	19
1.1	2.81–2.89	1500–2500	35–140	17
1.2	2.54–2.61	1500–2500	50–120	21
1.3	1.36–1.39	800–2000	30–160	21
1.4	0.92–0.97	600–1200	40–140	9

calculate the process parameters that can generate those levels (flow chart b).

2. Welding Conditions

A mod. DC 025 Rofin Sinar CO₂ laser was used operating in continuous wave regime to produce laser beam butt welds using Ti6Al4V grade 5 annealed sheets whose thickness varied between 0.92 and 2.89 mm.

The laser source characteristics were 2.5 kW max power level, slab type, and radio frequency. A polished copper, 200 mm focal length parabolic mirror was used as a laser beam focusing system. In order to move the work piece speeds ranged from 40 to 160 mm/s using a 10 mm/s step. Cleaning and polishing the parts to be joined avoided the porosity of the bead.

The pieces were lapped with SiC abrasive papers (grit numbers 600 and 800) followed by washing in ethyl alcohol. Chemical etching was performed with Keller's reagent: 2 mL HF + 10 mL HNO₃ + 88 mL deionized H₂O.

The morphological aspects of each weld were then numerically evaluated using a metallographic microscope, Nikon Eclipse, connected to a Nikon digital camera. To highlight the welding morphological characteristics, the cross-sections of the beads were subjected to microscope observation measuring for each sample. Helium covering gases was used. Three cross-sections for each welding condition were considered to evaluate the bead imperfections.

Groups were set up for different weld thicknesses and welding conditions. Table 1 shows at a glance the process parameters and welds groups.

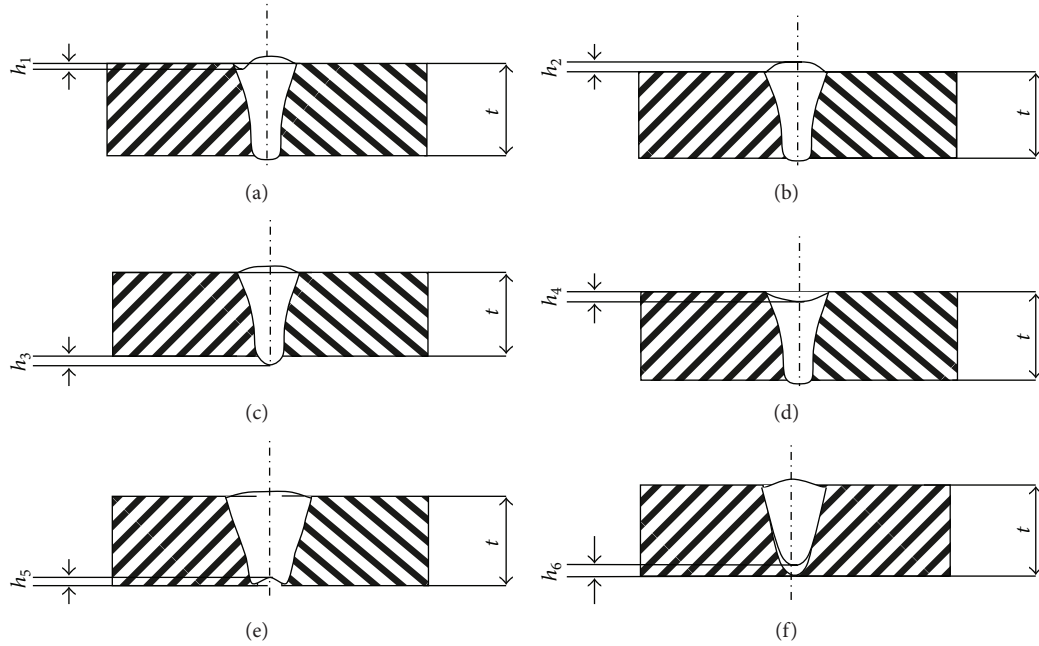


FIGURE 2: Geometrical imperfection considered for the analysis: (a) weld undercut h_1 , (b) excess weld metal h_2 , (c) excessive penetration h_3 , (d) incomplete fill groove h_4 , (e) root concavity h_5 , and (f) lack of penetration h_6 .

3. Imperfection Evaluation

3.1. Imperfection Description. The EN ISO 13919 guidance on the levels of tolerable defects (imperfections) in electron and laser beam welded joints in steel and Aluminium was used as a reference for the imperfections nomenclature [15, 16].

The three levels included in the ISO standard are defined in such a way to allow application to a wide range of welded fabrications. The levels refer to the production quality as opposed to the fitness for purpose of the product manufactured. The levels are moderate, intermediate, and stringent.

When significant deviations from the joint geometries and dimensions stated in the ISO standard are present in the welded product, it is necessary to evaluate to what extent the provisions of this standard can apply. Metallurgical and hardness aspects are not covered by this standard.

The imperfections analysed included weld undercut (Figure 2(a)), excess weld metal (Figure 2(b)), excessive penetration (Figure 2(c)), incomplete filled groove (Figure 2(d)), root concavity (Figure 2(e)), and lack of penetration (Figure 2(f)).

3.2. Imperfection Analysis. The average values of each imperfection measure observed for the different groups are reported in Table 2. An imperfection was deemed significant if it was detected in more than 10% of the sample size. When an imperfection typology was absent or present in less than 10% of the sample size, the result was not reported in Table 2. The sample variability within each group was also calculated by either the standard deviation or the range, which is more suitable for sample size less than 10 (Table 3).

TABLE 2: Average values of the imperfections' performance measures (mm).

Group no.	h_1	h_2	h_3	h_4	h_5	h_6
1.0	—	0.136	—	—	—	0.910
1.1	—	0.193	0.215	—	—	0.368
1.2	—	0.160	0.133	—	—	0.320
1.3	0.032	0.100	0.085	—	—	0.325
1.4	0.016	0.085	0.016	—	—	0.197

TABLE 3: Standard deviations of the levels for imperfections.

Group no.	h_1	h_2	h_3	h_4	h_5	h_6
1.0	—	0.038	—	—	—	0.47
1.1	—	0.035	0.069	—	—	0.203
1.2	—	0.050	0.059	—	—	0.118
1.3	0.025	0.010	0.069	—	—	0.215
1.4	0.007*	0.023*	0.007	—	—	0.088*

*Range (mm).

Most of the welds did not show incomplete filled grooves (h_4) and root concavities (h_5); as a consequence, these imperfections were neglected in the classification algorithm. Weld undercut (h_1) was frequently revealed in the He-shielded thin plates in the butt configuration and overlap welds.

The average levels for the remaining imperfections grew proportionally to the thickness of the butt welds when Helium gas was used for shielding. Argon gas seemed to produce lower levels of imperfections. In fact, neither excess weld metal nor lack of penetration was observed.

The average lack of penetration (h_6) was up to 35% for Ar-shielded welds and up to 15% for He-shielded ones.

The use of Argon seems to produce fewer imperfections, both in number and size, than the use of Helium. Higher power levels can improve penetration while keeping low the levels of other imperfections when Argon is used.

He-shielded overlap welds showed weld undercut (h_1), excess weld metal (h_2), and excessive penetration (h_3). Thick overlap welds also showed lack of penetration (h_6).

Standard deviations and ranges were high for butt welds and low for overlap welds.

Based on the welds' analysis, the levels of imperfection from groups 2.1 to 2.4 were used to build a fuzzy model with the aim to classify those imperfections.

4. Neural Network Prediction Model

The used neural network was the multilayer feed forward type (MFNN). This kind of network is frequently used due to the fact that it acts as a universal interpolator in a wide range of cases in which input variables are to be related to a set of output variables.

This network is a supervised learning type, in that the input/output relation can only be learned based on a set of training data and then validated by means of a second set of data, which is called validation set.

The typical architecture of an MFNN is shown in Figure 3. It includes an input layer (x), one or more hidden layers, and an output layer.

The input value for each neuron is determined as the weighted average of the output values of the neurons in the previous layer (1), whereas the output value is based on a sigmoidal or hyperbolic tangent activation function (2)

$$\text{net}_i^{l+1} = \sum_i^N w_{ij} \cdot x_i, \quad (1)$$

$$\text{out}_i^{l+1} = f(\text{net}_i^{l+1}). \quad (2)$$

The test data available from the macroanalysis was subdivided into two sets: the training set, which included 62 examples, and the test set, which included 25 examples.

In the direct approach the networks were characterised by a three neurons layer input (power rating, thickness, and speed), a hidden layer, and by one output value for each network, which was the single imperfection. Therefore, four independent networks were trained and validated.

In the reverse approach the networks were characterised by a three neurons layer input (weld's imperfections), a hidden layer, and by a single output, which was either the welding speed or laser power. Therefore, two independent networks were trained and validated.

In order to investigate the network response in more detail a regression analysis between the network response and the corresponding targets was performed after the training and the validation sessions.

The more the regression slope (m) is next to one the better is the fit, which outputs exactly equal to targets. Moreover, the correlation coefficient (R) between the outputs and targets

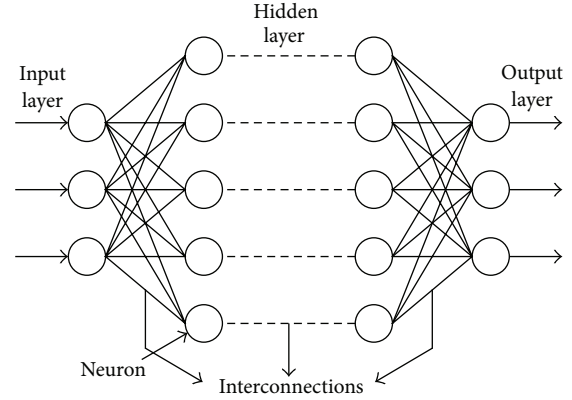


FIGURE 3: Network architecture.

was calculated. It is a measure of how well the variation in the output is explained by the targets. If this number is equal to 1, then there is perfect correlation between targets and outputs.

Tables 4 and 5 report the better architecture and the performance data for the direct and the reverse approach, respectively. In this example we can see that the numbers of the regression slope and correlation coefficient are very close to 1, which indicates a very good fit for the training and the validation sets.

5. Fuzzy Model

The fuzzy C-means clustering is a clustering algorithm for experimental data wherein a data point belongs to a cluster to a degree specified by a membership grade. It is an improvement over hard C-means clustering, and it provides a concise representation of a system's behaviour [17]. It uses an optimisation technique to solve the fuzzy classification task, and it is one of the most precise approaches to the classification problem. Recent results have shown that this grouping method performs much better than the neural network classification algorithm [18].

The fuzzy C-means algorithm is used to find a fuzzy partition so that the parameters under investigation can be classified into fuzzy subsets. Each partition of the data set into a subset can be described by a membership function.

The C-mean routine starts with an initial guess for the cluster centre, which is intended to mark the mean location of each cluster. By iteratively updating the cluster centres and the membership degrees for each data point, the calculation iteratively moves the cluster centres to the "right" location within the data set.

This iteration is based on minimizing an objective function that represents the distance from any given data point to a cluster centre weighted by that data point's membership degree. The fuzzy logic toolbox of Matlab can be used to perform the calculation [19].

In this application the data set consisted of the levels for imperfections h_1 , h_2 , h_3 , h_6 . For each kind of imperfection three centres were calculated.

TABLE 4: Neural network architecture and performance for the direct approach.

Imperfection	Neurons in the input layer	Neurons in the hidden layer	Neurons in the output layer	Regression slope for training	Regression slope for validation	Correlation coefficient
h_1	3	6	1	0.994	0.962	0.912
h_2	3	8	1	0.996	0.972	0.922
h_3	3	9	1	0.989	0.976	0.938
h_6	3	8	1	0.991	0.981	0.921

TABLE 5: Neural network architecture and performance for the reverse approach.

Process parameters	Neurons in the input layer	Neurons in the hidden layer	Neurons in the output layer	Regression slope for training	Regression slope for validation	Correlation coefficient
Laser power	3	11	1	0.976	0.942	0.907
Welding speed	3	14	1	0.986	0.952	0.904

TABLE 6: Centres for imperfection clusters (mm).

	Lower	Middle	Upper
Undercut (h_1)	0.012	0.033	0.071
Excess metal (h_2)	0.054	0.116	0.194
Excessive penetration (h_3)	0.035	0.134	0.243
Lack of penetration (h_6)	0.198	0.457	0.66

TABLE 7: Limits for imperfections for quality levels (mm).

	Stringent	Intermediate	Moderate
Undercut (h_1)	$0 \div 0.012$	$0.012 \div 0.033$	$0.033 \div 0.071$
Excess metal (h_2)	$0 \div 0.054$	$0.054 \div 0.116$	$0.116 \div 0.194$
Excessive penetration (h_3)	$0 \div 0.035$	$0.035 \div 0.134$	$0.134 \div 0.243$
Lack of penetration (h_6)	$0 \div 0.198$	$0.198 \div 0.457$	$0.457 \div 0.66$

The different categories were named “stringent,” “intermediate,” and “moderate” according to the EN ISO 13919 that assign to the “moderate” class the higher level of tolerable defects, to the “intermediate” the average level of imperfection, and to the “stringent” the lower one.

The calculated positions of the cluster centre are listed in Table 6. The “stringent” cluster has the minimum value for each kind of imperfection.

On the basis of the calculated centres it is possible to select the limits for imperfections for quality levels. Table 7 shows the limits that the authors calculated using the Matlab fuzzy logic toolbox.

The three sets of limits can be used for a selection that can be made for each particular application. Levels should be prescribed before the start of production, preferably at the inquiry or order stage. For special purposes, additional details may need to be prescribed.

6. Single Score Metric

The definition of three quality levels produced by the fuzzy logic application enabled a convenient classification of the level of imperfection for each given fused zone defect. Maintaining separated information about each quality feature ensures a higher detailed evaluation when some specification

has to be either communicated among parties involved in the production or tested on the welds produced. However difficulties can arise when the welds have to be compared to each other since the minimisation of the different kinds of imperfection can conflict together. In this case the synthesis of quality information in a single metric represents a convenient solution.

With the aim of classifying the global quality level of a titanium alloy laser welded joint, a numerical index, named R_{tot} , was developed. It was a “the-smaller-the-better” type index, and it took into account the membership of an imperfection to one of the levels previously defined. It is defined as follows:

$$R_{\text{tot}} = \sqrt{\sum_{i=1}^l R_i^2}, \quad (3)$$

where l is the number of imperfections considered and R_i a standardized index relative to the i th feature. This score was obtained using a piecewise linear model based on the cluster centre values. In each interval, the starting point coincided with the ending point of the previous interval, and the slope of the model curve was equal to the width of the interval. The starting point of the first interval was assumed equal to zero. Finally, the score obtained was standardized by dividing the absolute maximum of the curve, which was the value corresponding with the highest cluster centre. Let c_j be the bounds of the quality intervals, with $j = 0, 1, 2, 3$, x the quality measurement relative to the i th feature, and $c_0 = 0$. Then R_i was expressed as follows:

$$R_i = \begin{cases} \frac{(c_1 - c_0)(x - c_0)}{(c_1 - c_0)^2 + (c_2 - c_1)^2 + (c_3 - c_2)^2} & c_0 \leq x \leq c_1 \\ \frac{(c_1 - c_0)^2 + (c_2 - c_1)(x - c_1)}{(c_1 - c_0)^2 + (c_2 - c_1)^2 + (c_3 - c_2)^2} & c_1 < x \leq c_2 \\ \frac{(c_1 - c_0)^2 + (c_2 - c_1)^2 + (c_3 - c_2)(x - c_2)}{(c_1 - c_0)^2 + (c_2 - c_1)^2 + (c_3 - c_2)^2} & c_2 < x \leq c_3. \end{cases} \quad (4)$$

TABLE 8: R_{tot} values calculated for some samples.

Sample no.	h_1	h_2	h_3	h_6	R_1	R_2	R_3	R_6	R_{tot}
8	0.0503	0.1972	0.0294	0	—	NC	—	—	NC
10	0	0.1606	0.2114	0	0	0.7972	0.8496	0	1.1651
33	0.0318	0.1481	0	0.474	0.2759	0.7213	0	0.744	1.0723
40	0	0.0652	0	0.729	—	—	—	NC	NC
52	0	0.1708	0	0	0	0.8591	0	0	0.85911
59	0	0	0	0.2918	0	0	0	0.4305	0.43051
72	0.0317	0.1051	0	0	0.2749	0.4737	0	0	0.54767
74	0.0067	0.11	0.1732	0	0.0396	0.4974	0.6679	0	0.83365

(NC: not classifiable).

This kind of model ensured a progressive increase in the metric as the magnitude of the related imperfection increases. Moreover, since the wider was the interval the higher was the slope, a higher penalization was given to the values belonging to the wider intervals that meant a more severe distinction was possible between values belonging to the presumably most populated intervals.

Relatively to the analysis conducted in this paper, four features from the initial six ones were considered in the R_{tot} evaluation since incomplete fill groove and root concavity proved not to be significant imperfections. The fact that the lack of penetration was opposed to the excessive penetration did not create any issue in the R_{tot} calculation since the contribution of a lacking imperfection was null. For these reasons it was possible to consider l equal to 3. As from its definition, the R_{tot} index varied in a finite interval ($[0; \sqrt{3}]$) and presented two critical values which are 1 and $\sqrt{2}$. R_{tot} values higher than 1 indicated the presence of at least two imperfections, values higher than $\sqrt{2}$ revealed the presence of three of imperfections.

It should be noted that it was not possible to apply the R_{tot} index when an imperfection measurement exceeded the lowest quality limit for that imperfection, which was the largest centre value determined by the fuzzy logic. In these cases, the overall quality of the joint can be considered not satisfactory, which is indicated as not classifiable (NC). Table 8 shows the values of R calculated for some welds.

7. Conclusion

In this paper a model for the prediction and the evaluation of the levels for imperfections for the fused zone of Ti6Al4V titanium alloy laser butt weld was proposed. It was based on multiple neural network mapping followed by a fuzzy logic clustering of the process parameters, and the tolerable levels for the weld imperfections. The calculation of a single score for the quality comparison between the welds was presented. It followed the-smaller-the-better criterion.

Both the prediction and the classification of the imperfections were based on a structured and objective model, which was built straight from experimental data.

The neural network connections were built both in the direct and inverse approaches.

The calculation of three quality clusters enabled a convenient classification and evaluation of each tolerable defect. When the quality of the beads was to be compared to each other the single metric evaluation criterion proved a better solution.

The use of this neuro-fuzzy method gives the opportunity to predict the quality of the fused zone which can make the titanium welding more suitable for the severe standard of the aeronautical and modern automotive industries for the weld imperfections.

References

- [1] F. Caiazzo, F. Curcio, G. Daurelio, and F. M. C. Minutolo, "Ti6Al4V sheets lap and butt joints carried out by CO₂ laser: mechanical and morphological characterization," *Journal of Materials Processing Technology*, vol. 149, no. 1–3, pp. 546–552, 2004.
- [2] A. Squillace, U. Prisco, S. Ciliberto, and A. Astarita, "Effect of welding parameters on morphology and mechanical properties of Ti-6Al-4V laser beam welded butt joints," *Journal of Materials Processing Technology*, vol. 212, no. 2, pp. 427–436, 2012.
- [3] A. G. Olabi, G. Casalino, K. Y. Benyounis, and A. Rotondo, "Minimisation of the residual stress in the heat affected zone by means of numerical methods," *Materials and Design*, vol. 28, no. 8, pp. 2295–2302, 2007.
- [4] A. G. Olabi, G. Casalino, K. Y. Benyounis, and M. S. J. Hashmi, "An ANN and Taguchi algorithms integrated approach to the optimization of CO₂ laser welding," *Advances in Engineering Software*, vol. 37, no. 10, pp. 643–648, 2006.
- [5] S. L. Campanelli, G. Casalino, A. D. Ludovico, and C. Bonserio, "An artificial neural network approach for the control of the laser milling process," *International Journal of Advanced Manufacturing Technology*, vol. 66, no. 9–12, pp. 1777–1784, 2013.
- [6] G. Casalino and F. M. C. Minutolo, "A model for evaluation of laser welding efficiency and quality using an artificial neural network and fuzzy logic," *Proceedings of the Institution of Mechanical Engineers B*, vol. 218, no. 6, pp. 641–646, 2004.
- [7] G. Casalino, F. Curcio, and F. M. C. Minutolo, "Investigation on Ti6Al4V laser welding using statistical and Taguchi

- approaches,” *Journal of Materials Processing Technology*, vol. 167, no. 2-3, pp. 422–428, 2005.
- [8] K. Y. Benyounis and A. G. Olabi, “Optimization of different welding processes using statistical and numerical approaches—a reference guide,” *Advances in Engineering Software*, vol. 39, no. 6, pp. 483–496, 2008.
- [9] S. Malinov and W. Sha, “Application of artificial neural networks for modelling correlations in titanium alloys,” *Materials Science and Engineering A*, vol. 365, no. 1-2, pp. 202–211, 2004.
- [10] Y. Wei, H. K. D. H. Bhadeshia, and T. Sourmail, “Mechanical property prediction of commercially pure titanium welds with artificial neural network,” *Journal of Materials Science and Technology*, vol. 21, no. 3, pp. 403–407, 2005.
- [11] A. Khorram, M. R. Soleymani Yazdi, M. Ghoreishi, and M. Moradi, “Using ANN approach to investigate the weld geometry of Ti 6Al 4V titanium alloy,” *International Journal of Engineering and Technology*, vol. 2, no. 5, pp. 491–498, 2010.
- [12] L. Tao, T. J. Sun, and Z. H. Li, “Rough set based intelligent welding quality classification,” *World Academy of Science, Engineering and Technology*, vol. 60, pp. 211–214, 2011.
- [13] J. C. Bezdek, *Pattern Recognition with Fuzzy Objective Function Algorithms*, Plenum Press, New York, NY, USA, 1981.
- [14] P. Sathiya and M. Y. Abdul Jaleel, “Grey-based Taguchi method for optimization of bead geometry in laser bead-on-plate welding,” *Advances in Production Engineering & Management*, vol. 5, no. 4, pp. 225–234, 2010.
- [15] EN ISO 13919-1 Electrons and laser beam welded joints, Guidance on the levels for imperfections, part 1: steel, 1996.
- [16] EN ISO 13919-2 Electrons and laser beam welded joints, Guidance on the levels for imperfections, Part 2: aluminum and its weldable alloys, 2001.
- [17] H. J. Zimmermann, *Fuzzy Set Theory and Its Application*, Kluwer Academic, London, UK, 1991.
- [18] Y. S. Tarnag, H. L. Tsai, and S. S. Yeh, “Modeling, optimization and classification of weld quality in tungsten inert gas welding,” *International Journal of Machine Tools and Manufacture*, vol. 39, no. 9, pp. 1427–1438, 1999.
- [19] *MATLAB Fuzzy Logic Toolbox the MathWorks Inc*, Prentice Hall, Englewood Cliffs, NJ, USA, 1998.